



# THÈSE

en vue de l'obtention du

## DOCTORAT DE L'UNIVERSITÉ DE TOULOUSE

*délivré par*

*IMT - École Nationale Supérieure des Mines d'Albi-Carmaux*

---

présentée et soutenue par

Thomas DELEAU

le 2 Décembre 2020

## Mass transfer and thermodynamics phenomena in high pressure two-phase microflows

---

**École doctorale et discipline ou spécialité :**

ED MEGEP : Génie des procédés et de l'Environnement

**Unités de recherche :**

Centre RAPSODEE, UMR CNRS 5302, IMT Mines Albi  
Laboratoire de Génie Chimique LGC, UMR CNRS 5503, Toulouse

**Directrices de thèse :**

Fabienne ESPITALIER, Professeure, IMT Mines Albi (*Directrice*)  
Joëlle AUBIN, Directrice de recherche, LGC Toulouse (*Co-Directrice*)

**Autres membres du jury :**

Charlotta TURNER, Professeure, Lund University, Sweden (*Rapportrice*)  
Pawel SOBIESZUK, Professeur, Warsaw University of Technology, Poland (*Rapporteur*)  
Samuel MARRE, Directeur de recherche, ICMCB Bordeaux (*Président*)  
Christophe COQUELET, Professeur, CTP Mines-ParisTech (*Examineur*)  
Séverine CAMY, Professeure, LGC Toulouse (*Encadrante*)  
Jean-Jacques LETOURNEAU, Maître assistant, IMT Mines Albi (*Encadrant*)  
Andreas.S. BRAEUER, Professeur, TU Bergakademie Freiberg, Germany (*Invité*)







# Scientific productions

## Publication:

T. Deleau, M.H.H. Fechter, J-J. Letourneau, S. Camy, J. Aubin, A.S. Braeuer, F. Espitalier  
**"Determination of mass transfer coefficients in high-pressure two-phase flows in capillaries using Raman spectroscopy"** *Chemical Engineering Science* vol. 228, December 31<sup>st</sup> 2020. <https://doi.org/10.1016/j.ces.2020.115960>

## Communication:

T.Deleau, **"A Transparent Micro-Device to Study Mass Transfer and Thermodynamics in Two-Phase Flows at High Pressure"** The European Summer School in High Pressure Technology (ESS-HPT), July 8<sup>th</sup>- July 22<sup>nd</sup> 2018, Maribor (Slovenia), Graz (Austria). <http://dx.doi.org/10.3217/978-3-85125-619-2>

T. Deleau, J-J. Letourneau, S.Camy, J.Aubin, F.Espitalier, H. Helouvry, N. Macedo Portela da Silva, **"A Transparent Micro-Device to Study Mass Transfer and Thermodynamics in Two-Phase Flows at High Pressure"** 12<sup>th</sup> International Symposium on Supercritical Fluids (ISASF), April 22<sup>nd</sup>- April 25<sup>th</sup> 2018, Antibes (France). Extended Abstract (hal-01858138).

## Poster communications:

T. Deleau, J-J. Letourneau, S.Camy, J.Aubin, F.Espitalier, H. Helouvry, N. Macedo Portela da Silva, **"A Transparent Micro-Device to Study Mass Transfer and Thermodynamics in Two-Phase Flows at High Pressure"** 12<sup>th</sup> International Symposium on Supercritical Fluids (ISASF), April 22<sup>nd</sup>- April 25<sup>th</sup> 2018, Antibes (France)

T.Deleau, J-J. Letourneau, S.Camy, J.Aubin, F.Espitalier, **"Measurement of mass transfer coefficient in gas-liquid Taylor flow at high pressure"** Sendai Albi Knowledge Engineering Seminar (SAKES), October 8<sup>th</sup>- October 22<sup>nd</sup> 2019, Albi (France).



# Contents

<i>Scientific productions</i> . . . . .	i
<i>Contents</i> . . . . .	iii
<hr/>	
<b>Acknowledgements</b> . . . . .	1
<b>Résumé long en Français</b> . . . . .	3
Introduction . . . . .	3
Projet MuSyS et description de la thèse . . . . .	4
Chapitre 1 . . . . .	6
Chapitre 2 . . . . .	10
Chapitre 3 . . . . .	12
Chapitre 4 . . . . .	13
Chapitre 5 . . . . .	14
Conclusions et perspectives . . . . .	15
<b>Introduction</b> . . . . .	17
General context . . . . .	17
Thesis objectives and manuscript organization . . . . .	19
<b>1 State of the art</b> . . . . .	21
Introduction . . . . .	21
1.1 Supercritical Fluids . . . . .	22
1.1.1 Supercritical fluids properties . . . . .	22
1.1.2 Applications of supercritical fluids . . . . .	24
1.2 From Microtechnology to Microfluidics . . . . .	26
1.2.1 Microfluidics . . . . .	27
1.2.2 Application of microfluidics in chemical engineering . . . . .	28
1.2.3 High pressure and high temperature micro-systems . . . . .	30
1.3 Gas-liquid two phase flow in microsystems . . . . .	38
1.3.1 Flow regime map . . . . .	39
1.3.2 Hydrodynamics of Taylor flow . . . . .	42
1.4 Mass Transfer in Taylor flow . . . . .	49
1.4.1 Plug flow unit-cell model . . . . .	50
1.4.2 Volumetric mass transfer coefficient ( $k_L a_L$ ). . . . .	51
1.4.3 High-pressure mass transfer studies in two-phase segmented micro-flows . . . . .	58
Conclusion . . . . .	60

---

<b>2 Thermodynamics and mass transfer in high-pressure microchannel flows</b>	61
Introduction	61
2.1 Changes in bubble volume in high-pressure flows	62
2.2 Thermodynamic study of $CO_2$ - $H_2O$ , $CO_2$ - $EtOH$ and $CO_2$ - $BMimPF_6$ systems	65
2.2.1 Mutual solubility of $CO_2$ - $H_2O$ , $CO_2$ - $EtOH$ and $CO_2$ - $BMimPF_6$ systems	66
2.2.2 Physical properties of pure water, carbon dioxide, $EtOH$ and $BMimPF_6$ at high-pressure	71
2.2.3 Physical properties of $CO_2$ - $H_2O$ , $CO_2$ - $EtOH$ and $CO_2$ - $BMimPF_6$ mixtures	75
2.2.4 Impact of evolving physical properties along the microchannel	82
2.3 Mass transport modelling	82
2.3.1 Two-phase mass transport	83
2.3.2 Mass transfer model for high-pressure two-phase segmented micro-flow	86
2.4 Conclusion	91
<b>3 Microreactor design and manufacturing process</b>	93
Introduction	93
3.1 Microreactor elements and manufacturing tools	96
3.2 Frame manufacturing	99
3.3 Assembly and integration of capillary tubes in the frame	100
3.4 Casting of the resin	102
3.5 Manufacturing time	102
3.6 Manufacture of the temperature-controlled chamber	104
3.7 Pressure and temperature resistance tests	106
Conclusion	107
<b>4 Determination of mass transfer coefficients using Raman Spectroscopy</b>	109
Introduction	110
4.1 Raman spectroscopy	113
4.1.1 Raman Effect	113
4.1.2 Principle of Raman spectroscopy	113
4.1.3 Calibration step	115
4.1.4 Raman spectra of pure $CO_2$ and pure $H_2O$	116
4.1.5 Raman spectra of $CO_2$ and $H_2O$ liquid mixture	117
4.2 Experimental method	119
4.2.1 Experimental setup	119
4.2.2 Operating conditions	123
4.2.3 Raman spectroscopy measurement setup	124
4.2.4 Raman spectra measurements	126
4.3 Determination of mass transfer	127
4.3.1 Determination of $C_{CO_2}$	127
4.3.2 Determination of the volumetric mass transfer coefficient $k_L a_L$	129
4.4 Application of the experimental method to $CO_2$ - $H_2O$ mass transfer under high pressure	130
4.4.1 Concentration profiles	130
4.4.2 Effect of flow rate conditions on $k_L a_L$	133
Conclusion	136
<b>5 Determination of liquid mass transfer coefficients in a <math>CO_2</math>-<math>H_2O</math> system using a colorimetric method</b>	137

Introduction . . . . .	137
5.1 Experimental method . . . . .	139
5.1.1 Experimental setup . . . . .	139
5.1.2 Operating conditions . . . . .	144
5.1.3 Image acquisition setup . . . . .	146
5.1.4 Calibration of the method . . . . .	151
5.1.5 Image processing and analysis . . . . .	154
5.2 Determination of liquid-side volumetric mass transfer coefficients . . . . .	161
5.2.1 Determination of $C_{CO_2}$ . . . . .	161
5.2.2 Determination of the volumetric mass transfer coefficient $k_L a_L$ . . . . .	164
5.3 Application of the experimental method to $CO_2$ - $H_2O$ mass transfer under high pressure . . . . .	165
5.3.1 Characteristics of the gas-liquid flow . . . . .	165
5.3.2 Concentration profiles . . . . .	175
5.3.3 Effect of flow rate conditions on $k_L a_L$ . . . . .	176
Conclusion . . . . .	179
<b>General conclusion and outlooks . . . . .</b>	<b>181</b>
Summary . . . . .	181
Outlooks . . . . .	183
<b>Nomenclature . . . . .</b>	<b>187</b>
<hr/>	
<b>A Straight reactor dimensions and drilling parameters . . . . .</b>	<b>193</b>
<b>B Fast Fourier Transform method . . . . .</b>	<b>197</b>
<b>C Raman spectroscopy method supplements . . . . .</b>	<b>201</b>
<b>D Uncertainty calculations . . . . .</b>	<b>203</b>
D.1 Uncertainty calculations on the $CO_2$ concentrations in the Raman spectroscopy method . . . . .	203
D.2 Uncertainty calculations on the $z$ -axis position in the capillary in the Raman spectroscopy method . . . . .	205
D.3 Uncertainty calculations on the $CO_2$ concentrations in the colorimetric method . . . . .	206
D.4 Uncertainty calculations on the $z$ -axis position in the capillary in the colorimetric method . . . . .	207
<b>E Colorimetric method supplements . . . . .</b>	<b>209</b>
E.1 Operating Conditions . . . . .	209
E.2 Choice of BPB concentration . . . . .	210
E.3 Output files of the Matlab software . . . . .	212
E.4 Images of two-phase segmented flow of $CO_2$ and $H_2O$ . . . . .	214
<b>F Chemical Engineering Science, Deleau et al. (2020) . . . . .</b>	<b>217</b>
<hr/>	
<b><i>List of Figures . . . . .</i></b>	<b>233</b>
<b><i>List of Tables . . . . .</i></b>	<b>245</b>
<b><i>Bibliography . . . . .</i></b>	<b>247</b>





# Acknowledgements

Le travail effectué durant ces trois années de thèse et présenté dans ce manuscrit est le fruit du travail d'une seule et unique personne, MOI ! De plus, aucun soutien n'a été nécessaire pour son accomplissement.

Bon. Pour bien faire, peut être devrais-je mentionner mon équipe d'encadrement : Jean-Jacques, Fabienne, Séverine et Joëlle. Jean Jacques a été présent au quotidien durant ces trois années de thèse (incluant week-ends et jours fériés) ! Il m'a pris sous son aile et m'a accordé une confiance sans borne dès les premiers mois de thèse, en me confiant des enseignements et en me laissant une grande liberté dans l'approche de ma problématique de recherche. J'ai appris énormément de choses à ses côtés, en thermodynamique, en calculs scientifiques et dans bien d'autres domaines<sup>1</sup>. Pour ceci, mais aussi pour sa bonne humeur et ses blagues quotidiennes, je l'en remercie. Fabienne, ma directrice de thèse, a été d'une aide sans faille tout au long de ma thèse. Je souhaite la remercier pour sa bienveillance, sa gentillesse et ses conseils avisés. Je n'aurai pas pu rêver mieux comme directrice de thèse ! Je souhaite aussi remercier Séverine et Joëlle. Merci de m'avoir soutenu tout au long de la thèse, pour les longues heures de corrections que vous m'avez accordées et pour vos conseils éclairés. Merci de votre gentillesse et pour votre patience lorsque, têtue, je commençais par dire non avant de me rendre compte que finalement votre idée était la bonne ;-). Un grand merci à vous quatre, une vraie team de choc !

Ah oui, il est aussi vrai que sans l'aide de Séverine, Sylvie, Laurent, Philippe, Mickael et Pierre, le dispositif expérimental de cette thèse ressemblerait plus à une pile patate qu'à une plateforme microfluidique fonctionnelle. Un grand merci aux techniciens du laboratoire Rapsodee qui sont toujours à l'écoute des doctorants et toujours prêts à les aider. Je remercie aussi Jacques et Martial, avec qui j'ai beaucoup ri (et travaillé bien sûr) au congrès sur les fluides supercritiques à Antibes.

---

<sup>1</sup>J'inclus l'utilisation des notes en bas de page pour faire des blagues douteuses et parfois censurées lors de l'écriture du manuscrit... oups

---

Merci à Andreas Brauer pour m'avoir accueilli dans son laboratoire à Freiberg, ainsi qu'à Mickael, Marina, Mirko et Zheng avec qui j'ai adoré travailler (et boire des bières).

Pendant ces trois ans, j'ai eu la chance d'effectuer le trajet quotidien Toulouse-Albi en bonne compagnie en covoiturant avec Rachel, Séverine, Jean-Jacques, Laura et Sébastien<sup>2</sup>. Je vous remercie pour ces trajets dans la joie et dans la bonne humeur dont je garderai un très bon souvenir ! Je ne rentrerai pas dans plus de détails... secret du covoiturage oblige.

J'ai partagé de très bons moments en compagnie des doctorants du centre Rapsodee et du LGC. Si j'en oublie certains, merci de ne pas m'en tenir rigueur, c'est le risque quand on tente d'être exhaustif... Merci à Alexandre, Astrid, Bhianca, Carla, Claire, Emilien, Gweni, Hélène, Karline, Laura, Léa, Lori, Marco, Marine, Martin, Pauline, Roger, Sagar, Thibaut et Yi. Mention spéciale à Emilien, alias Caius, mon binôme de choc à la salle de sport, aux afterwork, en road-trip et dans d'autres aventures...

Durant ces trois ans, j'ai eu la chance d'avoir un soutien indéfectible de ma famille. En particulier, mes parents, qui ont toujours cru en moi, qui m'ont soutenu pendant ces trois ans, mais aussi depuis ma naissance, en mettant tout en œuvre pour me fournir le kit de survie de la vie, comportant une bonne éducation, la possibilité de m'épanouir dans de multiples activités et enfin, une très grande dose d'amour. Mon talentueux petit frère Théo, qui m'a toujours soutenu pendant mes études, et qui j'en suis sûr, a devant lui un bel avenir. Enfin, je souhaiterais remercier celle qui m'a à la fois soutenu et supporté au quotidien pendant ces trois années de thèse (et ce ne fût pas une mince affaire), Alice, avec qui j'ai la chance de partager ma vie.

Pour finir, je souhaiterais aussi remercier la Région Occitanie pour avoir financé cette thèse et l'école doctorale MeGeP pour avoir financé ma mobilité en Allemagne. Merci à Catherine et Kamila qui font un boulot formidable pour les doctorants de l'école doctorale.

Vous l'aurez donc compris, ce travail est le fruit non pas d'une personne, mais s'inscrit dans une pluralité indéniable ! Rien n'aurait été possible sans l'aide et le soutien de toutes les personnes citées plus haut (et d'autres que je risque d'avoir oublié par mégarde...). Pour leur aide, leur soutien, leur gentillesse et leur bienveillance, je leur adresse un infini merci.

---

<sup>2</sup>Pas tous en même temps, cela ne rentre pas dans une petite voiture de doctorant :-).





# Résumé long en Français

## Introduction

Entre 2014 et 2016, le ministère de l'économie, de l'industrie et du numérique a demandé une étude sur les solutions réelles d'innovations à l'horizon 2020. Cette étude a montré que les procédés de chimie verte et la microfluidique sont des réelles innovations et des atouts potentiels pour les industries en France. La microfluidique propose des avantages en termes de contrôle et de réduction de consommation d'énergie et de matières premières. De plus, elle permet de réduire les coûts d'investissement et opératoires tout en améliorant les conditions de sécurité et de contrôle des déchets lors de la manipulation des appareils. Ces avantages permettent donc d'inscrire parfaitement la microfluidique dans le domaine de la chimie verte et de l'intensification de procédés.

En parallèle, l'émergence des fluides supercritiques comme nouveaux types de solvants pour le développement de procédés et de matériaux plus propres pour l'environnement voit le jour. Un fluide est supercritique lorsque sa pression et sa température dépassent à la fois la pression et la température du point critique de ce fluide. Dans ces conditions, le fluide n'est ni un gaz ni un liquide. Cependant, ce fluide possède une masse volumique proche d'un liquide et une viscosité proche d'un gaz. Ces propriétés permettent notamment un transport facile (faible viscosité) et d'y solubiliser d'autres composés en grande quantité. Ces fluides apparaissent comme une alternative à des solvants dangereux utilisés dans l'industrie. Le cas du dioxyde de carbone en est l'exemple même. Il est intéressant de par son faible coût, son abondance et sa non toxicité. De nombreuses utilisations du dioxyde de carbone ont déjà montré leur efficacité dans l'industrie, comme par exemple dans la décaféination du café où le dioxyde de carbone vient remplacer le chloroforme, le trichloréthylène ou bien encore le dichlorométhane. De plus, les conditions critiques du dioxyde de carbone, 304 K et 74 bar, facilement atteignables expérimentalement, en font un fluide à coût énergétique modéré. Ainsi, l'utilisation de dioxyde de carbone et d'eau, deux produits environnementalement intéressants, dans des procédés verts et à faibles coûts énergétiques, couplée avec les avantages de la microfluidique, apparaît comme prometteur pour le développement de procédés verts

---

intensifiés.

## Projet MuSyS et description de la thèse

C'est dans un contexte de préservation de l'environnement que le projet MuSyS (MycroSystèmes pour les fluides Supercritiques) a vu le jour. Ce projet est porté par le laboratoire RAPSODEE (Recherche d'Albi en génie des Procédés des Solides Divisés, de l'Énergie et de l'Environnement) à IMT Mines Albi-Carmaux (Albi) et par le LGC (Laboratoire de Génie Chimique) à l'Institut National Polytechnique (Toulouse), financé par l'Université de Toulouse et la région Occitanie. Ce projet vient à la suite des travaux de thèse de Martin (2016) et de Silva (2014) effectués respectivement dans les laboratoires LGC et RAPSODEE. Le projet MuSyS mutualise donc les connaissances ainsi que les moyens techniques des deux laboratoires. Ce projet se décompose en trois étapes majeures.

La première étape consiste en la fabrication d'une plateforme microfluidique permettant de résister à l'utilisation de dioxyde de carbone à l'état supercritique ( $T > 304\text{ K}$  et  $P > 74\text{ bar}$ ) dans le but d'étudier des écoulements diphasiques avec le dioxyde de carbone comme phase dispersée. Une particularité supplémentaire que doit posséder cette plateforme est un accès optique transversal, afin de pouvoir utiliser des méthodes optiques de suivi en ligne le long de l'écoulement (ombroscopie, spectrophotométrie, spectroscopie Raman etc.). Cette plateforme dans laquelle le réacteur a une taille caractéristique d'une centaine de micromètres vient remplacer les appareils de tailles macroscopiques où l'étude de mélange sous pression nécessite de forts investissements en termes de coûts mais aussi de temps de mesure. Ainsi, la dernière contrainte de cette plateforme est son coût, qui doit être moindre que les appareils de mesure sous haute pression conventionnels (cellules PVT, autoclaves haute pression etc.).

La deuxième étape consiste à comprendre les phénomènes de transferts de matière dans les écoulements diphasique à haute pression, afin de modéliser leur comportement. Plus particulièrement, cette étude se fait dans les écoulements de type segmentés, autrement nommés écoulements de Taylor, qui se présentent comme une alternance de bouchons de phase dispersée et de phase continue avec potentiellement un film liquide autour de la phase dispersée. Un tel écoulement est présenté dans la Figure 1.28 de la thèse. Dans un écoulement diphasique de type Taylor contenant une phase de dioxyde de carbone et une phase liquide, plusieurs phénomènes peuvent influencer sur la taille des bouchons de la phase dispersée. Dans un but de simplification, appelons un bouchon de phase dispersée une « bulle », même si les conditions de température et de pression peuvent donner présence à une goutte à la place. Si le  $\text{CO}_2$  se dissout dans la phase continue, la taille de la bulle de  $\text{CO}_2$  va diminuer en progressant dans le tube. Dans le cas contraire, si la phase continue tend à changer de phase, la taille de la bulle va augmenter. De plus, si une perte de charge est présente le long du réacteur, la taille de la bulle augmente du fait de la diminution de pression même si aucun transfert entre les phases n'a lieu. Il n'est donc pas évident de relier une évolution de taille

de bulle à un transfert entre les phases le long de l'écoulement. De plus, le transfert entre les phases peut faire varier les propriétés physiques de celles-ci, comme la viscosité et la masse volumique. Ces changements sont globalement peu présents lors des études à pression atmosphérique, mais deviennent beaucoup plus significatifs à haute pression. Par exemple, dans le cas d'un écoulement de dioxyde de carbone et de liquide ionique ( $BMimPF_6$ ), étudié dans les travaux de thèse de Silva (2014), ce changement de propriétés est très significatif. Pour un écoulement à 120 bar 30°C, la viscosité de la phase continue est divisée par dix entre le moment où elle entre en contact avec le dioxyde de carbone et le moment où l'équilibre thermodynamique est atteint. La masse volumique quant à elle, est multipliée par 1,7. Ces changements de propriétés physiques de la phase continue (mais parfois aussi de la phase dispersée) vont fortement influencer l'hydrodynamique et le transfert de matière le long de l'écoulement. Il est donc nécessaire de repenser les modèles de transfert de matière élaborés pour des conditions de pression atmosphérique pour pouvoir les appliquer à des écoulements sous haute pression, en incluant ces changements de propriétés physiques.

Enfin, la dernière étape du projet MuSyS, consiste à mutualiser les deux étapes précédentes dans le but de concevoir une méthode pour la mesure de coefficients de transfert de matière dans les écoulements diphasiques à haute pression. La plateforme microfluidique couplée à des méthodes en ligne non intrusives (ombroscopie, spectroscopie Raman) ouvre la possibilité d'acquérir rapidement des données précises de transfert de matière via la détermination des coefficients de transfert de matière. L'obtention de ces coefficients permet d'envisager de multiples perspectives : la mesure de la performance de l'intensification du transfert de matière dans les microréacteurs, avec notamment une application dans des réacteurs de types monolithes composés de dizaines de micro-canaux, mais aussi dans un but plus ambitieux de calculer des coefficients de diffusion, qui sont des données indépendantes de l'échelle, et donc utilisables pour les dimensionnements de procédés de taille industrielle.

Les thèses de Silva (2014) et Martin (2016) ont développé les bases de la plateforme microfluidique du projet MuSyS, en mettant en évidence la problématique de fabrication de microréacteurs « faits maison » résistants à la pression et peu coûteux. Ces thèses ont aussi montré que les écoulements de types Taylor à haute pression ont des comportements différents de ceux observés à pression atmosphérique du fait du changement des propriétés physiques (masse volumique, viscosité, tension interfaciale) des phases en présence entre le moment où elles entrent en contact et le moment où l'équilibre thermodynamique est atteint.

La thèse présentée ici possède quatre objectifs qui sont présentés dans la Table 1. Le premier objectif, décrit dans le chapitre 1, concerne la réalisation d'un état de l'art sur l'hydrodynamique et le transfert de matière dans les écoulements diphasique. Un accent est mis sur les études à haute-pression. Il est à noter que dans le cadre de cette thèse, les systèmes étudiés sont isothermes et non-réactifs. De ce fait, l'étude bibliographique ne traite pas les aspects thermique et réactionnel que certains écoulements diphasiques en microréacteurs peuvent présenter. Cette étude bibliographique permet aussi de mettre en exergue la non

---

applicabilité des modèles de transfert de matière valables à pression atmosphérique pour des écoulements diphasiques à haute-pression. Une fois ce manque présenté, le chapitre 2 concerne la reformulation des modèles à pression atmosphérique en prenant en compte la dépendance des propriétés physiques des phases de l'écoulement avec une augmentation de la pression. Dans ce chapitre, l'étude des propriétés physiques (masse volumique, viscosité et tension interfaciale) de trois systèmes binaires, choisis pour leurs comportements caractéristiques,  $CO_2$ -éthanol,  $CO_2$ - $BMimPF_6$  et  $CO_2$ -eau, est présentée. Ces trois systèmes possédant des comportements différents à haute-pression, ils permettent en premier lieu de discuter les hypothèses du modèle de transfert de matière présenté, mais aussi de montrer son applicabilité à plusieurs systèmes binaires. Le chapitre 3 présente la fabrication d'un réacteur « fait maison », ne nécessitant pas de contraintes de fabrication élevée (pas besoin de salle blanche ni d'instrumentations coûteuses), résistant à la haute-pression (jusqu'à 25 MPa) et compatible à l'utilisation de  $CO_2$  supercritique. Ce chapitre est construit de sorte que le lecteur puisse reproduire un tel réacteur, avec une description étape par étape de la fabrication, avec les difficultés rencontrées et donc de ce fait, de potentielles erreurs à éviter lors de celle-ci. Enfin, les chapitres 4 et 5 présentent deux méthodes pour des mesures quantitatives de composition des phases dans un écoulement diphasique à haute pression. La première méthode est basée sur de la spectroscopie Raman là où la seconde est basée sur de la colorimétrie. Ces deux méthodes permettent donc de répondre au quatrième objectif de la thèse et à l'objectif majeur du projet MuSyS, qui est de développer des méthodes permettant de mesurer des coefficients de transfert de matière dans un écoulement diphasique à haute-pression. L'applicabilité de ces deux méthodes est présentée pour le système binaire  $CO_2$ -eau, et les résultats obtenus par les deux méthodes sont comparés.

La fabrication peu coûteuse du dispositif microfluidique résistant à la pression ainsi que le développement de deux méthodes non intrusives pour la mesure de coefficients de transfert de matière à haute-pression constituent la nouveauté de ce travail de recherche. De plus, contrairement aux méthodes classiques de mesure de coefficients de transfert de matière « moyens » entre l'entrée et la sortie du réacteur où a lieu l'écoulement diphasique, les méthodes présentées dans cette thèse permettent de mesurer des coefficients de transfert de matière à chaque position entre l'entrée et la sortie du réacteur. Ces nouvelles méthodes ont permis de mettre en évidence que ces coefficients de transfert de matière ne sont pas constants le long de l'écoulement. Cette mise en évidence ouvre la porte à de nouvelles études concernant l'intensification du transfert de matière en écoulement diphasique haute pression, mais aussi à pression atmosphérique, au sein d'un microréacteur.

## Chapitre 1

Le chapitre 1, portant sur l'état de l'art est décomposé comme suit : Une première partie présente la notion de fluide supercritique et des applications industrielles de ces fluides. Une seconde partie présente l'historique de la naissance de la microfluidique, descendante directe

de la microtechnologie. Des applications en génie chimique de la microfluidique sont présentées et plus particulièrement les applications à haute pression. Dans une troisième partie, l'étude de l'hydrodynamique des écoulements diphasiques en microréacteurs est présentée, en mettant l'accent sur les écoulements segmentés, dits de Taylor. Enfin, dans une dernière partie, les modèles classiques de quantification du transfert de matière dans les écoulements de Taylor sont détaillés, ainsi que les expériences répertoriées dans la littérature. Dans cette partie sont présentées les méthodes existantes pour la mesure des coefficients de transfert de matière à pression atmosphérique, mais aussi les études portant sur des écoulements diphasiques à pression plus élevée, où la quantification du transfert de matière n'est pas ou peu étudiée.

Dans la première partie, la Figure 1.1 présente le diagramme de phases dans le plan (pression, température) d'un fluide quelconque. Dans cette figure, le domaine supercritique est présenté, délimité par une pression supérieure à celle du point critique et une température supérieure à celle du point critique. Le domaine supercritique dépend donc du point critique, qui est différent en fonction du fluide étudié. La Table 1.1 présente la pression et la température critique du dioxyde de carbone, de l'éthane, du propane, de l'eau et de l'ammoniac. On constate par exemple qu'il sera plus facile expérimentalement d'obtenir du dioxyde de carbone supercritique (304 K, 7.4 MPa) que de l'eau supercritique (647 K, 22.1 MPa). Comme présenté plus haut, un fluide supercritique possède la masse volumique proche de celle d'un liquide et la viscosité proche de celle d'un gaz. Il est aussi notable que la diffusivité d'un fluide supercritique est intermédiaire entre celle d'un gaz et d'un liquide (Table 1.2). Autour du point critique, une faible variation en pression donne lieu à une importante variation en densité, ce qui résulte en une importante variation du « pouvoir de solubilisation » du fluide. C'est autour de cette propriété spécifique que sont par exemple basés les procédés de génération de particules assistées par fluide supercritique (notamment du dioxyde de carbone supercritique). Dans les procédés RESS (*rapid expansion of supercritical solutions*), PGSS (*particle generation from gas saturated solutions*) et SAS (*supercritical anti-solvent power*), le fluide supercritique joue un rôle majeur. Dans le procédé RESS (Figure 1.2), la substance d'intérêt est dissoute dans le fluide supercritique avant d'être cristallisée lors d'une forte dépressurisation. Dans le procédé PGSS (Figure 1.3), un liquide est saturé par un fluide supercritique puis détendu à travers un orifice pour former des particules solides. Enfin, dans le procédé SAS (Figure 1.4), le fluide supercritique est utilisé comme anti-solvant pour la fabrication de particules solides. Les fluides supercritiques sont aussi employés dans des procédés d'extraction ou de réactions polyphasiques. Cette variété d'utilisation des fluides supercritiques dans divers procédés démontre la nécessité de connaître les propriétés thermodynamiques de ces fluides et de leurs mélanges avec d'autres composés (masse volumique et viscosité de mélange, tension interfaciale, coefficients de diffusion) afin de dimensionner de nouveaux procédés ou d'optimiser les procédés déjà existants (Reverchon et al. (1997), Hassim et al. (2019), Lebedev et al. (2015)). Cependant, ces mesures de propriétés ont un coût non négligeable lié à la haute pression, qui impose des installations résistantes et des appareils de mesure spécifiques. A cela s'ajoutent des temps de mesure longs pour atteindre l'équilibre thermodynamique dans ces appareils de mesure. En effet, les temps

---

caractéristiques de transfert de matière et de transfert thermique sont proportionnels à la dimension caractéristique de l'appareil au carré. Pour un autoclave de deux litres, le temps nécessaire pour atteindre l'équilibre thermodynamique se compte en heures. Dans un appareil de taille caractéristique de l'ordre de plusieurs centaines de micromètres, ce temps est divisé par 105. De ce fait, dans un microréacteur, l'équilibre thermodynamique est atteint presque instantanément, diminuant grandement la durée des campagnes d'expérimentation.

La deuxième partie du chapitre présente l'étude des écoulements dans des réacteurs de taille caractéristique de l'ordre de plusieurs centaines de micromètres : la microfluidique. La microfluidique a été définie par Whitesides (2006) et Tabeling (2015) de deux manières différentes, mais leurs définitions s'entendent sur la suivante : On désigne par microfluidique « La science ou la technologie des systèmes où au moins une des dimensions est de l'ordre du micromètre ». La microfluidique est de plus en plus présente dans les publications scientifiques comme le montre la Figure 1.5. Le changement d'échelle de réacteur a un effet direct sur la géométrie, mais aussi sur les phénomènes physiques en présence comme expliqué plus haut, les temps de transfert thermique et de matière, mais aussi les forces d'inertie, les forces visqueuses et même les temps de réaction chimique (Table 1.3) sont fortement impactés. L'utilisation de la microfluidique permet donc de réduire le volume de produit utilisé, tout en augmentant la rapidité pour obtenir des résultats expérimentaux. Un paramètre important est la surface spécifique, soit le rapport de la surface sur le volume du réacteur. Dans le cas d'un microréacteur, ce ratio est multiplié par mille par rapport aux appareils de taille macroscopique. Plus ce ratio est élevé, plus le transfert thermique et le transfert de matière sont performants. En conséquence de cela, il est plus facile de contrôler les effets thermiques au sein d'un microréacteur, ce qui est par exemple nécessaire lors de l'étude de réactions fortement exothermiques. Une autre différence notable entre les écoulements en microréacteurs comparés aux écoulements en réacteurs de taille macroscopique est la concurrence entre les forces inertielles et les forces visqueuses et de tension interfaciale. Dans les microréacteurs, les forces inertielles sont dominées par les forces visqueuses et de tension de surface. C'est pour cette raison que l'on obtient la plupart du temps des écoulements de type laminaire en microréacteurs. La perspective de coupler les avantages de la microfluidique avec les avantages que procure l'utilisation des fluides supercritique est rapidement parue comme une évidence. Ces avantages mis en commun, comme par exemple les nombreux procédés supercritiques existants couplés avec un contrôle précis des conditions opératoires en microfluidique, ont permis de développer des microréacteurs supercritiques performants, notamment en extraction, en chimie organique, en génération de nanomatériaux et en acquisition de données thermodynamiques (voir section 1.2.3).

Dans la troisième partie du premier chapitre, l'étude spécifique des écoulements diphasiques en microfluidique est présentée. Plusieurs types d'écoulements diphasiques sont observables à l'intérieur des microréacteurs en fonction des débits volumiques entrant (voir Figure 1.16). Parmi ces écoulements on retrouve les écoulements de type « dispersés », où de nombreuses bulles de petites tailles sont dispersées dans une phase continue ; les écoulements

aits « à bulle », où l'on observe une distribution de bulles irrégulières avec une longueur caractéristique comparable à celle du canal dans lequel s'écoulent les fluides ; les écoulements à « bulles confinées » où les bulles sont quasiment sphériques ; les écoulements segmentés ou de Taylor où les bulles sont sous forme de bouchons avec une partie cylindrique et deux hémisphères en amont et en aval ; ou bien encore des écoulements « annulaires » où la phase dispersée forme un tunnel au centre de l'écoulement de la phase continue. Ces types d'écoulements sont représentés sur des cartes d'écoulements, tracées soit en fonction des débits volumiques, soit en fonction de nombres adimensionnels (Weber, Reynolds) ou bien encore dans des diagrammes de phase de type (pression, composition) ou (température, composition). Ces cartes d'écoulement permettent de localiser les conditions opératoires où l'on obtient tel ou tel type d'écoulement. Ces cartes sont très utiles lorsque l'on cherche à se placer préférentiellement dans un écoulement plutôt qu'un autre, ce qui est le cas dans cette thèse. Le type d'écoulement que l'on souhaite étudier est l'écoulement de type segmenté, dit de « Taylor ». Cet écoulement a comme spécificité sa régularité dans les tailles de bouchons de la phase dispersés et de la phase continue. S'ajoute à cela des propriétés de mélange intéressantes au niveau des recirculations dans la phase continue. Cette partie traite des publications de la littérature concernant l'étude de la zone de génération des bulles, du film liquide autour des bouchons de la phase dispersée ainsi que des recirculations dans les bouchons de la phase continue. L'étude de l'hydrodynamique de ce type d'écoulement permet d'éclairer de potentiels phénomènes de transfert de matière qui ont lieu entre la phase continue et la phase dispersée. Par exemple, une recirculation plus intense dans la phase continue donne lieu à un transfert de matière plus performant entre les deux phases en présence.

Enfin, la dernière partie de ce chapitre porte sur l'étude du transfert de matière dans les écoulements de Taylor. Concernant les études expérimentales, deux types d'études sont à différencier : Les études dites « entrée/sortie » où les phases sont échantillonnées à la sortie du réacteur pour connaître la quantité qui a transféré, et les études dites « en ligne » où l'information de la composition d'au moins une des phases est connue tout au long du réacteur. Concernant la modélisation du transfert de matière, la plupart des études de la littérature sont basées sur le modèle « plug-flow unit-cell ». Ce modèle, présenté dans la partie 1.4.1 du chapitre, est basé sur le principe et les hypothèses suivantes : une cellule unitaire « unit-cell » est composée d'un bouchon de la phase dispersée et d'un bouchon de la phase continue (Figure 1.27). Il est pris comme hypothèse qu'il n'y a pas de transfert entre deux cellules unitaires consécutives. Ainsi, le transfert n'a lieu qu'au niveau de l'interface des deux bouchons d'une même cellule unitaire. Le volume du bouchon de la phase continue est supposé constant le long du réacteur et les deux bouchons sont supposés comme étant parfaitement mélangés (concentrations uniformes dans chaque bouchon). Il est aussi supposé que le transfert n'a lieu que de la phase dispersée vers la phase continue (réduisant ainsi grandement le nombre de systèmes binaires pouvant être étudiés). En supposant que le produit du coefficient de transfert de matière local de la phase continue (ici liquide)  $k_L$  et l'aire spécifique  $a_L$  (défini comme l'aire de l'interface de transfert sur le volume du bouchon de la phase continue) est constant, on obtient l'équation 1.15 pour le calcul du coefficient de

---

transfert de matière volumique de la phase liquide  $k_L a_L$ . Cette équation est utilisée dans la majorité des études à pression atmosphérique pour le calcul de  $k_L a_L$ . Ainsi, à partir de cette équation et des données expérimentales de concentrations dans la phase continue obtenues par les méthodes « entrée/sortie » ou « en ligne »,  $k_L a_L$  est obtenu. Les mesures de  $k_L a_L$  sont ensuite traitées pour former des corrélations adimensionnelles avec les nombres de Sherwood (Sh), Reynolds (Re), Capillaire (Ca) et Schmidt (Sc) comme pour l'équation 1.20, ou alors des corrélations empiriques faisant intervenir des variables observées comme la longueur de bulle  $L_B$ , la longueur de bouchon liquide  $L_S$  et la vitesse de l'écoulement diphasique  $U_{TP}$  comme dans l'équation 1.17. Les hypothèses de travail du modèle de cellule unitaire présent dans la littérature ne conviennent pas à l'étude des écoulements à haute pression, et notamment les hypothèses de concentrations uniformes dans les phases en présence, de volume constant des bouchons de la phase continue ou encore de coefficient de transfert de matière volumique de la phase liquide  $k_L a_L$  constant le long de l'écoulement.

## Chapitre 2

Le chapitre 2 de ce travail de thèse présente une méthodologie permettant d'adapter le modèle de cellule unitaire valable à pression atmosphérique uniquement, à une étude d'un écoulement diphasique à haute pression. Cette méthodologie se découpe en trois étapes, et forme ainsi les trois parties de ce chapitre. En première partie, l'évolution de la taille des bouchons de la phase dispersée et de la phase continue le long de l'écoulement est discutée en fonction du binaire employé pour l'étude. Dans une deuxième partie, les propriétés thermodynamiques (masse volumique et viscosité de mélange, tension interfaciale) des trois binaires  $CO_2$ -éthanol,  $CO_2$ - $BMimPF_6$  et  $CO_2$ -eau sont présentées dans le but de discuter les hypothèses du modèle de cellule unitaire présentées dans la dernière partie du chapitre 1. Enfin, dans une dernière partie, le modèle de cellule unitaire pour le calcul du coefficient de transfert de matière volumique dans la phase liquide  $k_L a_L$  est reconstruit à partir d'un bilan local dans la phase liquide, afin de discuter étape par étape, les hypothèses pouvant être gardées et celles devant être rejetées, jusqu'à l'expression analytique de  $k_L a_L$ .

La première partie décrit l'évolution de la taille des bouchons de la phase dispersée et de la phase continue en fonction de la solubilité mutuelle des constituants du système binaire. Cette étape est importante car la technique la plus employée pour quantifier le transfert de matière est l'analyse de photos de l'écoulement, et plus précisément de l'évolution de la taille du bouchon de la phase dispersée le long de l'écoulement. Cependant, l'évolution de sa taille n'est pas facilement corrélable avec les quantités transférées entre les deux phases. Par exemple, si le transfert a lieu simultanément de la phase continue vers la phase dispersée et de la phase dispersée vers la phase continue, l'évolution du volume ne peut pas être corrélée aux quantités transférées sans l'étude des masses volumiques de mélange des deux phases et sans la connaissance de la composition d'une des phases. La Figure 2.2 présente un diagramme faisant la liste des cas où la taille de la bulle le long de l'écoulement suffit à quantifier le transfert de matière entre les phases. On remarque que ces cas sont rares, surtout



si l'écoulement présente une perte de charge. Le cas de trois mélanges binaires sont présentés,  $CO_2$ -éthanol,  $CO_2$ - $BMimPF_6$  et  $CO_2$ -eau. Dans le cas du  $CO_2$ -éthanol, le  $CO_2$  de la phase dispersée va transférer dans la phase continue riche en éthanol et l'éthanol de la phase continue va transférer dans la phase dispersée riche en  $CO_2$ . Avec ou sans perte de charge, il est impossible de relier l'évolution du volume de la phase dispersée aux quantités d'éthanol et de  $CO_2$  échangées. A cette information il faudrait ajouter la composition d'au moins une des phases, et la connaissance de la masse volumique de mélange des deux phases. Dans le cas du binaire  $CO_2$ - $BMimPF_6$ , le  $CO_2$  de la phase dispersée va transférer dans la phase continue riche en  $BMimPF_6$ . Cependant, le  $BMimPF_6$  de la phase continue ne transfère pas vers la phase dispersée. Dans ce cas précis, il est possible de corréler le changement de volume de la phase dispersée en quantité de dioxyde de carbone transféré dans la phase continue, sous couvert qu'il n'y ait pas de perte de charge. Dans le cas d'une perte de charge non négligeable le long de l'écoulement, la bulle de dioxyde de carbone va s'expanser sous l'effet de la chute de pression et diminuer de taille sous l'effet du transfert. Sans la connaissance de l'évolution de la pression le long de l'écoulement (et donc de la masse volumique du dioxyde de carbone le long de l'écoulement), il n'est pas possible de dissocier le phénomène de changement de taille lié à la perte de charge du phénomène de changement de taille dû au transfert vers la phase continue. Il en est de même pour le binaire  $CO_2$ -eau où l'eau de la phase continue est extrêmement peu soluble dans la phase dispersée (la fraction molaire d'eau dans la phase riche en dioxyde de carbone à l'équilibre est de l'ordre de 0,005 à 10 MPa, 303 K). La Figure 2.3 présente une photo d'écoulement pour chacun de ces binaires. On constate que les caractéristiques géométriques de ces écoulements diffèrent totalement, autant par la forme de la phase dispersée que par son évolution le long de l'écoulement. Les approches de modélisation des phénomènes de transfert pour ces binaires sont donc à différencier.

La deuxième partie de ce chapitre présente la masse volumique et la viscosité de mélange de la phase continue des trois binaires étudiés ainsi que la tension interfaciale entre la phase continue et la phase dispersée de chaque binaire. L'idée est d'observer l'influence qu'aura une dissolution du dioxyde de carbone dans l'éthanol, le  $BMimPF_6$  et l'eau. On constate que la quantité de dioxyde de carbone dissout va avoir une influence différente en fonction du constituant de la phase continue. Si l'on prend l'exemple de la masse volumique, on constate que la présence de  $CO_2$  dans l'eau a peu d'influence (Figure 2.19), la masse volumique augmente de 1%. La présence de  $CO_2$  dans l'éthanol va en premier lieu augmenter la masse volumique, puis la diminuer (Figure 2.20) alors que celle-ci sera augmentée de 65% dans du  $BMimPF_6$  saturé en dioxyde de carbone. Si l'on trace le ratio du volume de la phase continue saturée en dioxyde de carbone sur le volume de cette même phase pure (Figure 2.22), on constate que le volume de la phase riche en  $BMimPF_6$  est inchangé, celui de la phase riche en eau augmente légèrement (1%) et celui de la phase riche en éthanol augmente jusqu'à un facteur 6 en fonction de la quantité de dioxyde de carbone dissout. Cette étude montre par exemple que l'hypothèse de volume constant de la phase continue n'est pas valable pour le binaire  $CO_2$ -éthanol. Cette section a pour but de montrer que pour l'étude du transfert de matière à haute pression, une étude préliminaire de la thermodynamique du

---

binaire étudié est primordiale.

Dans la dernière partie de ce chapitre, le modèle de cellule unitaire est repensé, afin de prendre en compte un éventuel changement de volume de la phase continue, simultanément au changement de volume de la phase dispersée, pour le calcul du coefficient de transfert de matière volumique de la phase continue  $k_L a_L$  à haute pression. De plus, l'hypothèse d'un  $k_L a_L$  constant le long de l'écoulement n'est plus utilisée. On obtient finalement l'équation 2.28, qui permet de calculer  $k_L a_L$ . Cette équation est simplifiée par l'équation 2.32 dans le cas de l'étude de l'écoulement  $CO_2$ -eau, qui est expérimentalement étudié dans ce travail de thèse.

## Chapitre 3

Le chapitre 3 de cette thèse porte sur la fabrication d'un microréacteur capable de résister à la pression (25 MPa) pour une température modérée (testée jusqu'à 333 K). Bien qu'il existe dans le commerce des microréacteurs permettant de résister à des pressions et à des températures supérieures, ces microréacteurs sont bien souvent très chers et avec peu de flexibilité dans le design (taille caractéristique de canaux ou de capillaires, longueur, matériaux, etc...). De plus, à haute pression, le risque d'endommager un microréacteur est plus élevé que lors d'une utilisation à pression atmosphérique. Ainsi, la fabrication présentée dans cette thèse a l'avantage d'être rapide (une fois maîtrisée), avec une durée totale de fabrication de quatre jours pour un réacteur et de cinq jours pour deux réacteurs fabriqués simultanément. Elle possède aussi l'avantage du coût, avec environ 200 euros de matière première pour la fabrication du réacteur. Ce microréacteur est placé dans une enceinte pouvant être connectée à un bain thermostaté afin de maintenir la température du microréacteur constante. L'assemblage des deux est utilisable pour l'expérimentation d'écoulements diphasiques avec des fluides compatibles avec l'acier inoxydable (connectique) et la silice fondue (paroi du microréacteur).

Le chapitre est construit de sorte que le lecteur puisse reproduire le microréacteur tel qu'il est présenté. Pour ce faire, la première partie est consacrée à la liste du matériel et à la liste des outils nécessaires à la conception. La technologie utilisée pour assurer le maintien de la pression dans le microréacteur est celle des capillaires de silices, fabriqués par extrusion et recouverts d'une gaine protectrice en polyimide. Ces capillaires de silice sont capables de résister à des pressions allant jusqu'à 100 MPa. Cependant, avec la gaine protectrice, les capillaires ne permettent pas un accès optique (bien que la gaine soit légèrement transparente). Ainsi, la gaine protectrice est retirée pour permettre un accès optique à l'intérieur du capillaire (là où l'écoulement a lieu). Une fois la gaine retirée, la résistance du capillaire à la pression est fortement diminuée. Pour pallier à cette perte de résistance, le capillaire est plongé dans de la résine époxy, parfaitement transparente, dans le but de conserver l'accès optique.

La fabrication se déroule en trois étapes (Figure 3.1) : la fabrication du châssis dans lequel les capillaires de silice sont insérés, l'assemblage des capillaires de silice dans le châssis, et pour finir le coulage de la résine époxy dans le châssis. Le châssis est usiné à l'aide d'une fraiseuse numérique à partir de deux blocs de PMMA ( $270 \times 140 \times 20 \text{ mm}^3$ ), pour des dimensions finales du microréacteur de  $502 \times 80 \times 20 \text{ mm}^3$ . Des fenêtres traversantes sont creusées où des plaques de verre seront plus tard collées pour offrir un accès optique à l'intérieur du capillaire. Le châssis final est présenté dans la Figure 3.2. Les capillaires sont assemblés à l'aide d'un système de jonction « férule-écrou » pour permettre une résistance à la pression. Le diamètre interne des capillaires de silice utilisés est de 250 micromètres. La Figure 3.5 présente l'assemblage élaboré pour pouvoir injecter la phase dispersée dans la phase continue de manière coaxiale à l'intérieur du microréacteur, tout en gardant un accès optique dans cette zone de mise en contact. Une fois l'assemblage de capillaires placé à l'intérieur du châssis, une colle de type époxy est appliquée pour assurer l'étanchéité au niveau des entrées et sorties du châssis. Une fois cette étape terminée, la résine époxy est coulée pour terminer la fabrication du réacteur. Le résultat final est présenté dans la Figure 3.7. Une fois le réacteur sec, celui-ci est testé (montée en pression et en température) pour s'assurer de son bon fonctionnement. Un tel réacteur peut être utilisé pendant 200 heures d'expériences, si celui-ci est pressurisé et dépressurisé lentement avant (+2 MPa par minute) et après manipulation (-1 MPa par minute) respectivement. Un inconvénient de ce microréacteur serait la limitation de sa tenue en température. Cette limitation est due à la différence de coefficient de dilatation thermique entre le verre, la résine et le PMMA. Ce réacteur est utilisé pour la méthode colorimétrique présentée dans le chapitre 5.

## Chapitre 4

Le chapitre 4 présente une méthode expérimentale pour la mesure de coefficients de transfert de matière dans un écoulement diphasique à haute pression, et plus particulièrement dans le cas présent du coefficient de transfert de matière volumétrique de la phase continue d'un écoulement  $CO_2$ -eau à une pression de 8, 9 et 10 MPa pour une température de 303 K (La méthode permet également de mesurer ce même type de coefficients dans la phase dispersée). Ce chapitre a fait l'objet d'une publication d'article dans Chemical Engineering Science. En utilisant le modèle du chapitre 2 qui prend en compte les potentielles modifications des propriétés physiques des deux phases le long du réacteur, inhérentes au changement de pression dans un écoulement pour lequel le transfert de matière se fait de la phase dispersée vers la phase continue, le coefficient de transfert de matière volumique de la phase dispersée est calculé par l'équation 2.32 du chapitre 2. Dans le cas d'un écoulement de dioxyde de carbone et d'eau, le calcul de coefficient de transfert de matière liquide (la phase continue riche en eau étant liquide) à différentes positions dans le microréacteur nécessite ainsi la connaissance de plusieurs variables. Il nécessite d'une part de connaître la vitesse d'ensemble de l'écoulement,  $U_{TP}$ , qui dépend des débits de dioxyde de carbone et d'eau injectés dans le microréacteur. D'autre part, il est nécessaire de connaître la concentration en dioxyde de carbone à l'équilibre dans la phase riche en eau,  $C_{CO_2}^*$  à la pression et la température de travail, mais aussi, la concentration en dioxyde de carbone dans la phase liquide à chaque

---

position axiale  $z$  dans le microréacteur,  $C_{CO_2}$ , ainsi que la variation de cette concentration par rapport à la position  $z$  dans le microréacteur,  $\frac{dC_{CO_2}}{dz}$ .

La méthode présentée dans ce chapitre est basée sur l'acquisition de spectres Raman de la phase continue (riche en eau) de l'écoulement segmenté et ceci tout au long de l'écoulement (à 10 positions différentes). Après une étape préliminaire de calibration, les données spectrales de la phase continue (comme celles présentées dans la Figure 4.15) sont traduites en terme de fraction molaire de dioxyde de carbone dans la phase continue. Ces fractions molaires, couplées avec la connaissance de la masse volumique du mélange d'eau et de dioxyde de carbone, permettent d'obtenir le profil de concentration de dioxyde de carbone dissout dans la phase continue, et ceci le long de l'écoulement (Figure 4.16). Ces données ponctuelles sont filtrées à l'aide d'une méthode de transformée de Fourier rapide comme présenté dans la Figure 4.17. Les données filtrées permettent d'obtenir avec une meilleure précision la dérivée première de la concentration en dioxyde de carbone dans la phase continue par rapport à la position  $z$  dans le réacteur. A l'aide du modèle développé dans le chapitre 2 et plus particulièrement de l'équation 2.32, la connaissance de la concentration en dioxyde de carbone et de sa dérivée première par rapport à la position permet donc de calculer  $k_L a_L$  le coefficient de transfert de matière volumique de la phase continue riche en eau.

## Chapitre 5

Le chapitre 5 présente une autre méthode expérimentale pour l'acquisition des paramètres nécessaires au calcul du coefficient de transfert de matière liquide à différentes positions  $z$  pour un écoulement diphasique d'eau et de dioxyde de carbone sous pression. Cette méthode est une méthode colorimétrique basée sur le fait que la phase riche en eau est acidifiée par la dissolution du dioxyde de carbone à l'intérieur de celle-ci. Cette acidification diminue fortement le pH de la phase riche en eau, pouvant aller jusqu'à des pH inférieurs à 3. Un indicateur coloré, le bleu de bromophénol (BPB) est mélangé dans l'eau avant la mise en contact avec le  $CO_2$  à l'intérieur du microréacteur qui possède un accès optique. Le contact de la phase riche en  $CO_2$  et de la phase riche en eau forme un écoulement segmenté de type Taylor composé de bouchons riches en eau et de bulles riches en dioxyde de carbone, observés à l'aide d'une caméra rapide. Le bleu de bromophénol possède un spectre d'absorbance dépendant du pH. Ainsi, en plaçant un éclairage en dessous du microréacteur et un filtre passe bande de la longueur d'onde du pic d'absorbance du bleu de bromophénol sur la caméra, il est possible d'observer un changement de niveau de gris le long du microréacteur. Ce changement de niveau de gris, qui correspond à un changement de pH de la phase riche en eau, est obtenu à l'aide d'une courbe d'étalonnage réalisée au préalable à l'aide de solutions tampons. Cette méthode permet donc de déterminer l'évolution du pH dans les bouchons liquides de la phase continue à différentes positions dans le microréacteur.

Cette technique de colorimétrie est utilisée dans ce travail de thèse pour obtenir l'évolution de la concentration en dioxyde de carbone dans la phase riche en eau le long du microréacteur

à une pression de 10 MPa et 303 K. Les paramètres cruciaux pour la mise en œuvre de cette méthode sont : les choix opératoires (débits des deux phases mises en contact), la géométrie du microréacteur (diamètre), la qualité de l'image (ouverture de la caméra), la puissance du système d'éclairage et la concentration en bleu de bromophénol dans l'eau. Ces cinq paramètres sont liés. Par exemple, à une puissance de système d'éclairage donnée, il existe une concentration en BPB à partir de laquelle il n'est plus possible d'observer une variation de niveau de gris (et donc de pH) avec la caméra. Un autre exemple : à un diamètre de réacteur donné, si la concentration en BPB est trop élevée, il n'existe pas d'ouverture de caméra qui permet à la fois d'avoir une image claire et une observation précise de la variation du niveau de gris. La méthode est donc dans un premier temps calibrée afin d'obtenir le jeu de ces cinq paramètres qui permet d'obtenir de manière optimale la variation de pH le long du microréacteur. Une fois ces paramètres fixés, des solutions tampons de différents pH sont préparées à partir de mélanges d'acide citrique et de citrate de sodium. Du bleu de bromophénol est ajouté dans ces solutions tampons (à la concentration préalablement fixée). Ces solutions de BPB à différents pH sont injectées dans le microréacteur où des images en noir et blanc sont acquises par la caméra. Le traitement de ces images permet de tracer une courbe d'étalonnage du pH en fonction du niveau de gris. Le microréacteur est ensuite utilisé pour acquérir les images d'écoulement diphasiques  $CO_2$ -eau à 10 MPa et 303 K aux débits que l'on souhaite étudier. Ces images sont traitées à l'aide d'un programme d'analyse d'images codé avec le logiciel Matlab ©. Ce programme a été développé dans le but d'obtenir les propriétés géométriques des bulles et des bouchons liquides de l'écoulement comme leur taille et leur vitesse le long du microréacteur. Ce programme permet aussi de récupérer le niveau de gris des bouchons liquides le long du microréacteur. A l'aide de la courbe d'étalonnage préalablement établie, l'évolution du pH le long du microréacteur est ainsi obtenue. A l'aide d'un modèle de cinétique chimique adapté aux études à haute pression, le pH est relié à une concentration en  $CO_2$  dans la phase riche en eau. Des courbes de concentrations en  $CO_2$  sont alors obtenues en fonction de la position du bouchon riche en eau dans le microréacteur. Ces courbes sont filtrées à l'aide d'une méthode de transformée de Fourier rapide afin d'obtenir une expression analytique de ces concentrations. Une fois ces expressions obtenues, il est possible de calculer analytiquement leurs dérivées et donc de calculer les coefficients de transfert de matière à l'aide de l'équation 2.32 du chapitre 2. Les résultats obtenus sont présentés dans les sections 5.3.2 et 5.3.3.

## Conclusions et perspectives

Les chapitres 4 et 5 présentent donc deux méthodes différentes pour le calcul du coefficient de transfert de matière volumique dans la phase liquide  $k_L a_L$ , d'un écoulement  $CO_2$ -eau sous pression. L'étude comparative de ces deux méthodes a permis de démontrer leur efficacité, du fait de la similitude des résultats obtenus et de leur confrontation avec la littérature. Bien que le travail de cette thèse soit principalement centré sur le développement des méthodes de mesure, l'influence des débits d'eau et de  $CO_2$  sur  $k_L a_L$  a pu être étudiée. La première observation faite sur  $k_L a_L$  est que celui-ci n'est pas constant le long de l'écoulement. L'utilisation d'un modèle où cette hypothèse est faite donne une erreur relative de 35% sur les valeurs de

---

$k_L a_L$  mesurées ici. Le coefficient de transfert de matière est plus élevé dans la zone de mise en contact des deux phases (zone de génération des bulles). Les valeurs obtenues dans la gamme de débits étudiés sont comprises dans les intervalles  $0,2 \text{ s}^{-1} - 4 \text{ s}^{-1}$  pour la méthode de spectroscopie Raman et de  $1 \text{ s}^{-1} - 13 \text{ s}^{-1}$  pour la méthode colorimétrique. Cet écart est lié aux diamètres employés pour les deux méthodes. Le diamètre utilisé pour la méthode de colorimétrie étant de 250 micromètres contre 300 micromètres pour la méthode de Raman. En effet, un diamètre plus petit a pour effet d'augmenter la vitesse de transfert (le temps de transfert étant proportionnel à la longueur caractéristique du réacteur au carré). De plus, pour des raisons de contraintes techniques, les débits fixés pour la méthode de colorimétrie sont légèrement supérieurs à ceux fixés pour la méthode de spectroscopie Raman.

Les perspectives de ce travail de recherche sont multiples. L'influence des débits sur  $k_L a_L$  n'a pu être que partiellement étudiée. De plus, l'influence des paramètres opératoires tels que la pression, la température et le diamètre interne du réacteur sont encore à explorer. L'étude de ces paramètres opératoires permettrait de développer des corrélations adimensionnelles pour  $k_L a_L$ . Toutefois, contrairement aux corrélations présentes dans la littérature, celles-ci devraient inclure un nombre adimensionnel tenant compte de la distance à la zone de génération des bulles ou de la distance à l'endroit où l'équilibre thermodynamique est atteint (car  $k_L a_L$  n'est pas constant le long du microréacteur). Ces corrélations permettraient d'évaluer le transfert de matière dans les écoulements diphasiques en microréacteurs dans un but d'intensification (en réacteurs monolithes par exemple). Avec une étude en parallèle de l'hydrodynamique, et plus précisément des profils de vitesse au sein de l'écoulement, des mesures de coefficients de diffusion pourraient être effectuées. Ces données de coefficients de diffusion à haute pression sont très rares dans la littérature et sont des paramètres importants lors du dimensionnement ou de la modélisation de procédés de taille industrielle.



# Introduction

## General context

Between 2014 and 2016, the French ministry of Economy, Industry and Digitalisation mandated the Directorate General for Enterprise to identify the Key Enabling Technologies (KET) in France for 2020. Among them, chemical processes using green chemistry and microfluidics appear as innovative solutions for industry in the context of environmental conservation and sustainability. In particular, microfluidics provides advantages in terms of the control and reduction of use of energy and raw materials. Furthermore, microfluidics leads to the reduction of investment and operating costs, as well as improved safety conditions and waste management, which fulfill the requirements of green chemistry and process intensification.

Supercritical fluids are another type of novel solvent that allow the development of cleaner processes and materials with unique and specific properties. A fluid in its supercritical region (temperature and pressure higher than the critical point) has liquid-like properties, such as density, which allows low polar compounds to be solubilized. Such fluids appear as an alternative solution to harmful solvents used in industry. The case of supercritical carbon dioxide is particularly interesting due to its low cost, abundance, and non-toxicity. As a consequence, the utilization of supercritical carbon dioxide and water, both of which are environmentally-friendly substances, in clean and low energy processes coupled with the advantages of microfluidics appears to be a promising route to develop green and intensified chemical processes. It is in this context that the MuSyS project emerged.

The MuSyS project (**M**icro**S**ystèmes pour les Fluides **S**upercritiques), funded by Occitanie region, focuses on the development of a microfluidic platform with the aim of improving and showing the interest of microsystems for the study and the measurement of the dynamic properties of two-phase mixtures at high pressure ( $>7$  MPa). This project follows the studies of Silva (2014) and Martin (2016) carried out at Rapsodee UMR CNRS 5302 (Albi, France) and at the Laboratoire de Génie Chimique UMR CNRS 5503 (Toulouse, France), respectively.

---

These previous studies concerned the development of pressure-resistant microfluidic systems for applications using supercritical carbon dioxide. The MuSyS project combines the expertise and savoir-faire of both research teams for the development of a microfluidic tool that allows the investigation of mass transport under pressure and more precisely, the mass transfer behaviour in a two-phase segmented flow with mixtures containing supercritical carbon dioxide. The project is divided into three steps:

- **Fabrication of a microfluidic platform:** The major requirement of the microfluidic platform is that it resists high pressure ( $>7$  MPa) in order to investigate two-phase flows containing carbon dioxide under supercritical conditions. The device should also allow optical access to the flow in order to investigate hydrodynamics and mass transfer phenomena along the microchannel. This platform should be an alternative to conventional research and development apparatus in which it is difficult to study high pressure mixtures due to non-negligible investment costs and long residence times (for example only two measurements are generally obtained in one day for data solubility acquisition).
- **Understanding and modelling of mass transfer phenomena in high-pressure two-phase flow:** A two-phase segmented flow of carbon dioxide in a liquid under-pressure in a microchannel leads to several opposing phenomena. The size of  $CO_2$  bubbles can be reduced due to the solubilization of  $CO_2$  in the liquid-rich phase. However the bubble size can also increase due to the solubilization of the liquid in the  $CO_2$ -rich phase and/or due to pressure drop along the microchannel. Furthermore, the physical properties, such as density and viscosity, of the  $CO_2$ -rich phase and liquid-rich phase can change significantly between the point of contact of both phases and that where the thermodynamic equilibrium is reached. As an example, the viscosity of an oil-rich phase is drastically decreased by the solubilization of  $CO_2$ . This effect increases with increasing pressure (at 120 bar, the viscosity of a  $CO_2$  saturated oil-rich phase is decreased by more than ten times) and significantly impacts the hydrodynamic behaviour of the flow. All these phenomena render mass transfer phenomena challenging to model. The classical approach consists in the description of a "unit-cell", which is the addition of a  $CO_2$ -rich segment (drop or bubble) and a slug of liquid. A mass balance over the time is performed and a Lagrangian approach allows to translate from temporal space to physical space (i.e. axis location along the microchannel). Previous studies of two-phase flow in microchannels at ambient conditions do not take into account the changes in fluid properties along the microchannel and are therefore generally not suitable for use at high-pressure. One of the ambition of the MuSyS project is thus to investigate models where these changes in fluid properties are taken into account by including thermodynamic models, which are able to describe mixture behavior, and by omitting over-simplifying hypotheses, such as assuming an ideal plug flow behaviour in the microchannel.
- **Determination of mass transfer coefficients in high-pressure two-phase flow:** The understanding and the modelling of mass transfer phenomena at high pressure allows the development of new methods for the determination of mass transfer coefficients



in high pressure two-phase flow. The microfluidic platform coupled with non-intrusive on-line techniques such as spectroscopy and fast screening open the possibility of fast and reliable data acquisition of mass transfer via the determination of global and local mass transfer coefficients. Indeed, the ultimate goal of the MuSyS project will be to determine diffusion coefficients of  $sCO_2$  in liquid solvents that are challenging to obtain at high pressure with adequate precision.

The thesis work of Silva (2014) and Martin (2016) developed the foundations of the microfluidic platform of the MuSyS project, emphasizing the issues of making in-house and inexpensive microsystems that resist high pressure. They also showed that the flow and mass transfer behavior of two-phase systems such as  $CO_2$ - $EtOH$  and  $CO_2$ - $BMimPF_6$  at high pressure are very different to that obtained in similar fluid systems at low pressure due to the significant change in physical properties of the fluids along the microchannel. The  $CO_2$ - $EtOH$  case investigated by Martin (2016) is characterized by the high mutual solubility of compounds at high pressure. Furthermore, the mixture density of  $CO_2$  and  $EtOH$  is highly dependent of the composition of phases. Consequently, standard techniques for measuring mass transfer coefficients, such as those based on the rate of change of bubble (or drop) size are not well adapted. In the case of the  $CO_2$ - $BMimPF_6$  binary system, mass transfer occurs only from the  $CO_2$ -rich phase to the  $BMimPF_6$ -rich phase and the mixture density is easily obtained experimentally. However, the dissolution of a large quantity of  $CO_2$  in the  $BMimPF_6$ -rich phase leads to an important viscosity gradient between the liquid film surrounding the bubbles (or droplets) and the liquid slug bulk. This viscosity gradient renders modelling of mass transfer difficult because it requires a different approach for each of the liquid slug domain and liquid film. These observations lead to the conclusion that mass transfer phenomena occurring at high-pressure in two-phase segmented flow has to be investigated in a fundamental manner to be able to understand and describe such different situations.

## Thesis objectives and manuscript organization

This thesis work has four main objectives, which are presented in Table 1. The first objective, which is the subject of Chapter 1 of the manuscript, is to present a literature review on hydrodynamics and mass transfer studies in two-phase segmented flow, with a focus on studies performed at high-pressure. Chapter 2 focuses on the second objective and consists in demonstrating that the current mass transfer models presented in the literature for the determination of mass transfer coefficient in two-phase segmented flow in microchannels at ambient conditions are not suitable for high-pressure flows. This is particularly due to the impact of pressure on the thermodynamics of binary systems and the very different characteristics (mixture densities and viscosities highly dependent of compositions, mass transfer from both phases, specific thermodynamic laws for phase volume computation) of a large number of binary systems. The binary working systems are classified and the classical "unit-cell" mass transfer model is reformulated to take into account the pressure-dependency

---

of fluid properties. The appropriate simplifying hypotheses for different fluid systems are identified. Chapter 3 describes the fabrication process of an in-house microfluidic platform that resists high-pressure and allows optical access, which is the third objective of this thesis work. The fourth objective consists in the development of two different methods – one based on Raman spectroscopy and the other on a colorimetric method – for the determination of local liquid-side mass transfer coefficients in a two-phase segmented flow at high pressure. Both methods are described in Chapter 4 and Chapter 5, respectively. The first method based on Raman spectroscopy, for which the results have been published in Chemical Engineering Science (Deleau et al. (2020)), provides information on the amount of  $CO_2$  dissolved in the  $H_2O$ -rich phase with a particular Raman setup. The second method that based on the use of a pH-sensitive tracer, allows quantification of the amount of  $CO_2$  dissolved in the  $H_2O$ -rich phase by detecting the acidification via changes in grey-level intensity with a high-speed camera. The  $H_2O$ - $CO_2$  binary system is investigated using both methods and the two measurement methods are compared.

The development of a cost-efficient microfluidic platform and the development of two non-intrusive methods for the determination of mass transfer coefficients at high pressure is the main novelty of this work. In addition, the methods developed in this thesis work enable the mass transfer coefficient to be determined in the two-phase segmented flow at different positions along the length of the microreactor, rather than an average mass transfer coefficient between the inlet and the outlet of the microreactor.

Microfluidic mass transfer investigation of high pressure two-phase segmented flow in microsystems			
To evaluate the applicability of a conventional mass transfer model for two-phase segmented flow to high-pressure flows	To reformulate the model in order to take into account the pressure-dependency of fluid properties, which impacts mass transfer	To design and manufacture a pressure-resistant microfluidic system that enables measurement of mass transfer using optical-based methods	To develop two methods for the determination of local liquid-side mass transfer coefficients in a two-phase segmented flow at high-pressure.

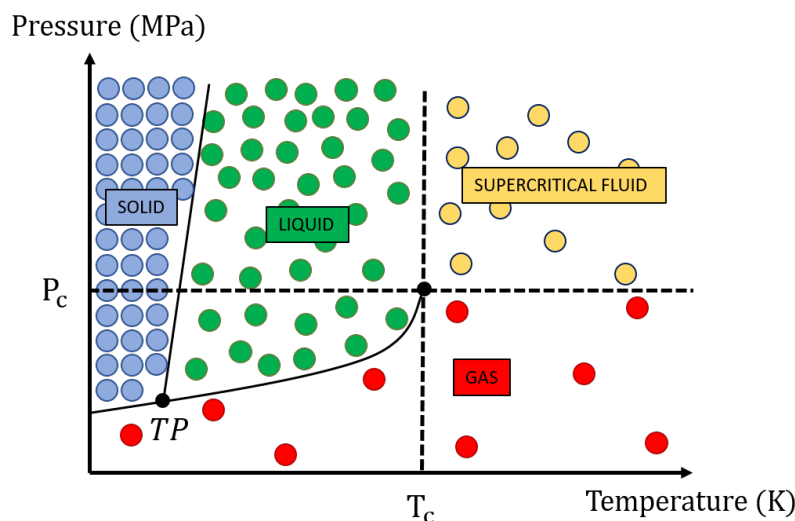
**Table 1** – Objectives of the thesis work.

# State of the art

Introduction . . . . .	21
1.1 Supercritical Fluids . . . . .	22
1.1.1 Supercritical fluids properties . . . . .	22
1.1.2 Applications of supercritical fluids . . . . .	24
1.2 From Microtechnology to Microfluidics . . . . .	26
1.2.1 Microfluidics . . . . .	27
1.2.2 Application of microfluidics in chemical engineering . . . . .	28
1.2.3 High pressure and high temperature micro-systems . . . . .	30
1.3 Gas-liquid two phase flow in microsystems . . . . .	38
1.3.1 Flow regime map . . . . .	39
1.3.2 Hydrodynamics of Taylor flow . . . . .	42
1.4 Mass Transfer in Taylor flow . . . . .	49
1.4.1 Plug flow unit-cell model . . . . .	50
1.4.2 Volumetric mass transfer coefficient ( $k_L a_L$ ). . . . .	51
1.4.3 High-pressure mass transfer studies in two-phase segmented micro-flows . . . . .	58
Conclusion . . . . .	60

## Introduction

This chapter presents the state of the art describing the advantages and challenges of a microfluidic measurement tool for the investigation of dynamic properties of mixtures employing supercritical fluids with a goal of process intensification. The knowledge of such properties is essential for scale-up purposes (Lebedev et al. (2015), Hassim et al. (2019)) and for both modelling and optimization of processes employing supercritical fluids (Reverchon et al. (1997), Diaz et al. (2009)). The first part of this chapter define a supercritical fluid and its specific properties. The second part of the chapter presents microfluidics and applications to the chemical engineering domain, particularly at high-pressure. In the last part of this chapter fundamental knowledge of gas-liquid flows in microfluidic systems is presented. Focus is given to segmented flow, also called Taylor flow, and the hydrodynamics and mass transfer properties are presented. Finally, the different methods described in the literature for the determination of mass transfer coefficients in gas-liquid flow are presented.



**Figure 1.1** – (Pressure, Temperature) diagram of a substance with its three states (solid, liquid, gas) and its supercritical region.

## 1.1 Supercritical Fluids

It is often of interest to carry out chemical processes at pressures and temperatures higher than ambient conditions (pressure of 0.1 MPa and a temperature around 298 K) in order to improve process performance. Under these extreme conditions, it is often not easy to differentiate between a gas and a liquid. The term "fluid" is therefore employed for all the states that are not solid. Furthermore, each fluid has a critical pressure ( $P_c$ ) and a critical temperature ( $T_c$ ). Beyond these conditions, the fluid is called a supercritical fluid.

### 1.1.1 Supercritical fluids properties

A supercritical fluid has physical properties that are between those of a gas and those of a liquid. This can be explained by the observation of the solid-liquid-vapor equilibrium curve of a P-T diagram as presented in Figure 1.1, which shows the separation lines between liquid, solid and gas states. The triple point (TP) corresponds to the pressure and the temperature where the three states coexist. The line that separates the gas and the liquid states corresponds to the pressure and temperature values where the gas and the liquid states are in equilibrium. The end of this equilibrium line is called the critical point, characterized by a critical pressure ( $P_c$ ) and a critical temperature ( $T_c$ ). Above the critical temperature and the critical pressure, the fluid is in the supercritical region. It is therefore possible to transform a compound that is initially in a liquid state to a gas state, without crossing the gas liquid equilibrium boundary by modifying the temperature and pressure. Indeed, the compound is continuously a liquid, a supercritical fluid, and a gas, without crossing any phase boundary. A fluid in its supercritical region therefore has no surface tension since it is not in equilibrium with any other phase. Each fluid has its own critical point and as can be seen in Table 1.1, some are easier to obtain experimentally than others.

**Table 1.1** – Critical points of usual chemical compounds (Smith et al. (2013))

-	$T_c$ [K]	$P_c$ [MPa]
Carbon dioxide	304	7.4
Ethane	305	4.9
Propane	370	4.3
Water	647	22.1
Ammonia	406	11.4

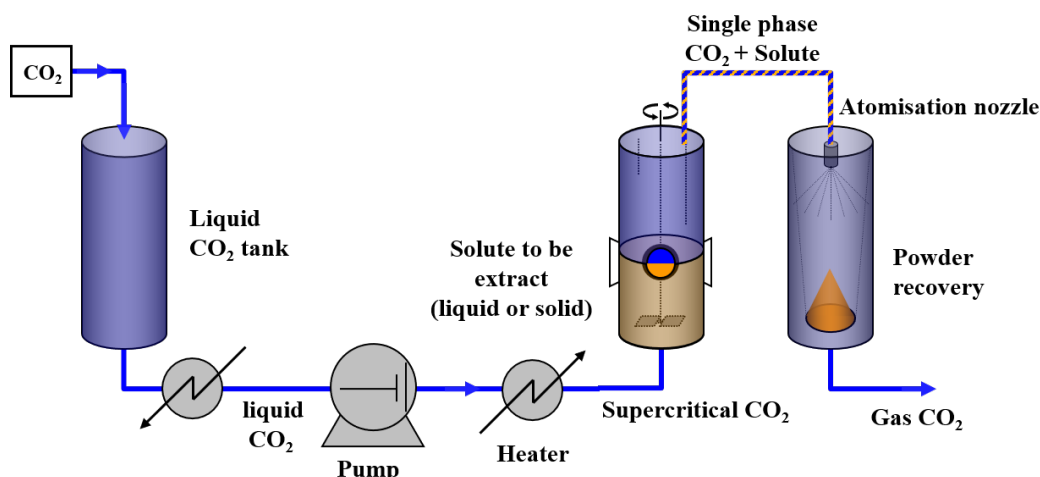
In the supercritical region, a supercritical fluid is a single phase and its physical properties are different from liquids and gases. Table 1.2 presents the order of magnitude of density, viscosity and diffusivity for gases, liquids and supercritical fluids.

**Table 1.2** – Density, viscosity and diffusivity order of magnitude for gas, liquid and supercritical fluids (Smith et al. (2013)).

-	Gas	Supercritical fluid	Liquid
Density ( $kg.m^{-3}$ )	1	500	1000
Viscosity ( $Pa.s$ )	$10^{-5}$	$10^{-4}$ - $10^{-5}$	$10^{-3}$
Diffusivity ( $m^2.s^{-1}$ )	$10^{-3}$	$10^{-5}$ - $10^{-6}$	$10^{-8}$

From the information in Table 1.2, it can be seen that a supercritical fluid is dense like a liquid, which allows the dissolution of many organic compounds, and compressible like a gas. They also possess excellent miscibility with other gases. The low viscosity of a supercritical fluid results in a small pressure drop when it is used in pipeline or packed bed reactors. Furthermore, near the critical point, a small variation in pressure or temperature leads to a significant variation in density and this can result in an important variation in solvent power.

Carbon dioxide ( $CO_2$ ) has a critical point ( $T_c=304.25$  K,  $P_c=7.38$  MPa) that can be "easily" reached experimentally, especially in terms of temperature. Supercritical  $CO_2$  ( $sCO_2$ ) can therefore be employed in processes where substances are heat sensitive. Furthermore,  $CO_2$  is non-toxic, non-flammable, inexpensive and abundant on earth. Consequently, the main applications of supercritical fluids often involve  $CO_2$ .



**Figure 1.2** – Simplified scheme of the Rapid Expansion of Supercritical Solution process (RESS). The solute can be either a liquid or a solid such as drugs, polymers and fat.

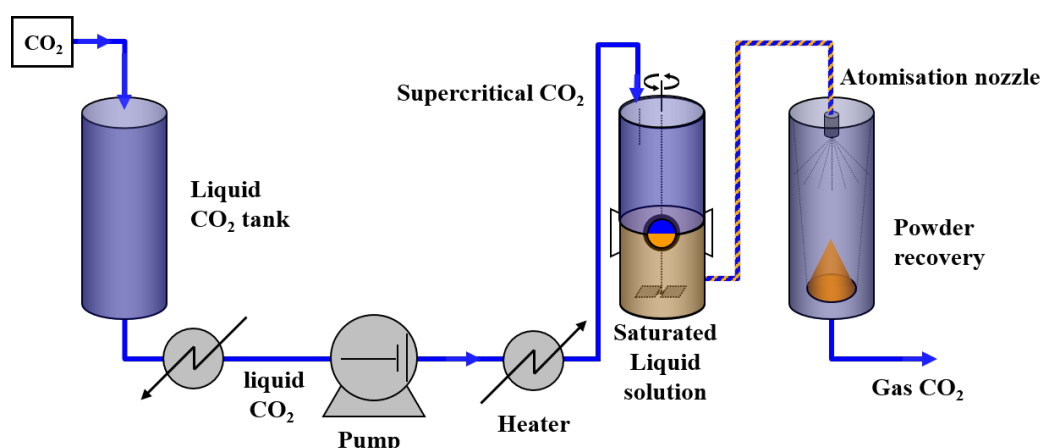
### 1.1.2 Applications of supercritical fluids

The specific properties of supercritical fluids make them attractive for the development of chemical processes. Supercritical fluids, and especially  $CO_2$ , are employed in numerous applications such as fluid extraction, dry cleaning, chemical reactions, nano and micro particle formation, water hydrolysis, oil recovery... Among these, particle generation processes, namely rapid expansion of supercritical solutions (RESS), particle generation from gas saturated solutions (PGSS) and supercritical anti-solvent (SAS) processes are well-known methods that allow the formation of solid particles with controlled size. Although many other application are now developed, including at industrial scale, these processes are presented in the context of this thesis because they include a step in which two phases are brought into contact<sup>1</sup>. Modelling these steps requires thermodynamic data that can be acquired using microfluidic systems, which are described later in this chapter.

#### Rapid Expansion of Supercritical Solutions (RESS)

The Rapid Expansion of Supercritical Solutions (RESS) is divided into two steps: a dissolution step and a crystallization step. The substance of interest is dissolved in the supercritical fluid at high pressure before it is crystallized during a fast de-pressurization step through a nozzle. In the supercritical domain, the fluid is dense and compressible. The significant variation in solvent power of the supercritical fluid by changes in pressure and temperature enables a liquid or a solid to be solubilized in the supercritical fluid. Solids are formed by a simple expansion. The fast and abrupt decrease in pressure coupled with a fast decrease in temperature (due to the Joule-Thomson effect), leads to supersaturation and formation

<sup>1</sup>The choice was made here to give examples of solid generation processes, developed at the RAPSODEE Laboratory, in which at least one step brought several phases into contact. Nevertheless, this particularity is found in many other processes involving supercritical fluids for liquid-fluid extraction as well as multiphase reaction, which are not presented in this thesis work. However, reactions and multiphase extractions are presented in the supercritical microfluidic part.



**Figure 1.3** – Simplified scheme of the Particle Generation From gas Saturated Solution process (PGSS).

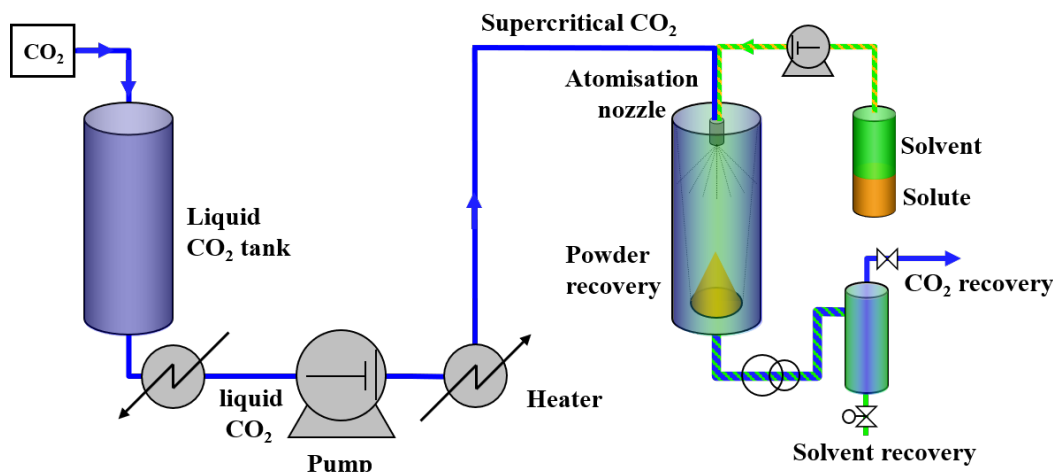
of solids. The process is presented in Figure 1.2. After the fast expansion, the solids are taken from the expansion vessel. In some cases, where fat or polymers are employed, the substance to be solidified can be a non-pure substance. A solid fractionation can occur during the extraction process and this can lead to a variation in the composition of the particles formed during the fast expansion. It is also possible to co-crystallize two compounds when they are both soluble in the supercritical fluid. In industrial applications, it is interesting to recycle the supercritical fluid after the rapid expansion. A minimum pressure is maintained in the expansion vessel but this pressure has to be low enough to reduce the solubility of the substance in the supercritical fluid during formation of particles.

### Particle Generation from gas Saturated Solution (PGSS)

The second process is Particle Generation from Saturated Solution (PGSS), which is presented in Figure 1.3. A supercritical fluid (mainly  $s\text{CO}_2$ ) is dissolved in a liquid at high pressure in a vessel. The liquid can be either a solution, a suspension or a melted polymer. The saturated solution is then transferred to an expansion vessel through a nozzle. Particle generation occurs in the expansion vessel and the particles are collected from the vessel at the end of the process. This process has been initially developed for polymers where significant quantities of  $s\text{CO}_2$  can be dissolved. This dissolution in the polymer reduces its glass transition and fusion temperatures, inflates the polymer and plasticizes it.

### Supercritical Anti-Solvent process (SAS)

Supercritical fluids can act as anti-solvents for some solutes that are solubilized in a solvent. The Supercritical Anti-Solvent (SAS) process has demonstrated its efficiency with supercritical carbon dioxide since many sugars, proteins, polymers and metal oxides are only slightly soluble in the supercritical fluid. In this process, three components are employed: carbon dioxide, a component of interest (solute) and a third component (solvent), which exhibit the following properties:



**Figure 1.4** – Simplified scheme of Supercritical Anti-Solvent process (SAS).

- The solvent has to be a good solvent for the solute.
- The solvent is miscible with the supercritical fluid.
- The solvent has to leave the final crystallized solid easily.

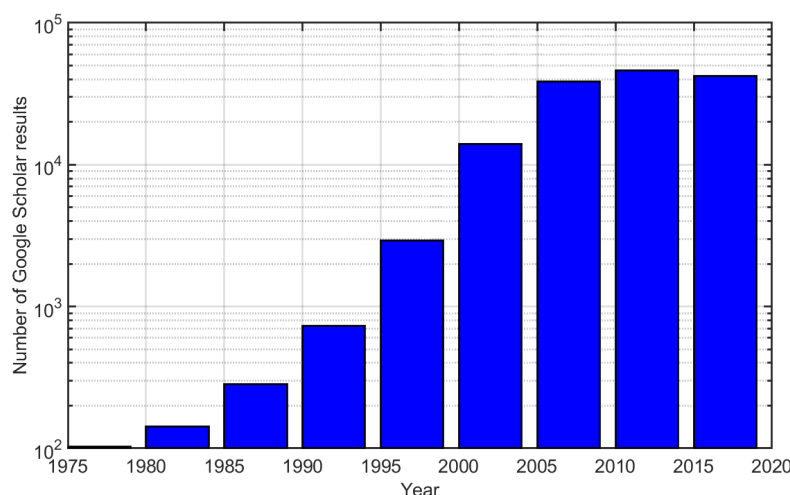
When the solution (i.e. the solvent and the solute) is put into contacts with supercritical carbon dioxide, the latter dissolves in the phase, thereby decreasing the degree of saturation of the solute. Simultaneously, the solvent evaporates in the supercritical phase, which decreases the ratio of solute over solvent in the solution, and therefore leads to the supersaturation of the solute. Both phenomena induce the crystallization of the solute. Moreover, the rapid expansion of the solution fosters the generation of small particles.

The RESS, PGSS and SAS processes all have at least one part of their process that two phase contacting and the optimization of unsteady mass transfer behavior between the two phases requires the knowledge of certain properties such as diffusion coefficients (Reverchon et al. (1997)). Moreover, these properties are essential for process scale-up (Hassim et al. (2019), Lebedev et al. (2015)). Diffusion coefficients are difficult to measure experimentally due to the high investment costs of high pressure apparatus and the long experimental time needed to acquire reliable data. A promising solution to tackle this challenge is microfluidics. As an example, in the work of Zhang (2019) and Zhang et al. (2020), mixing efficiencies of the SAS process are investigated in a high-pressure microreactor.

## 1.2 From Microtechnology to Microfluidics

Microtechnology involves devices or elements in which the characteristic length is in the order of magnitude of a micrometer. The first development of such technology in the 1970s was on the microscopic transistors. Numerous microscopic transistors were mutualized on a single chip and the miniaturization provided benefits in terms of performance, functionality



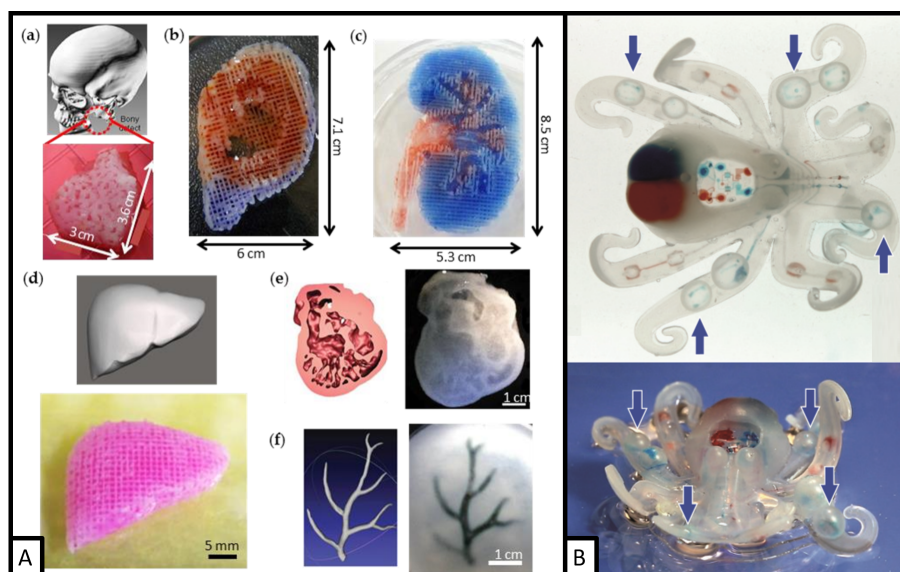


**Figure 1.5** – Number of Google Scholar results per half decade for publications containing the keyword "Microfluidics". The data between 2015 and 2020 are taken at the end of July in 2020.

and reliability with reduced costs. The term of Micro Electro Mechanical Systems (MEMS) appeared in the 1980s and described this new type of systems. The terms Micro System Technology (MST) or micromachines are also employed for such systems. The development of this technology was derived in other fields and especially in fluid mechanics. Utilization of such devices in the field of fluid mechanics led to the development of microfluidics. This section presents a definition of microfluidics and some applications in chemical engineering. Focus is given to microfluidic devices that are able to resist high pressure and high temperature environments, which are adapted to investigations with supercritical fluids.

### 1.2.1 Microfluidics

The term "microfluidics" is defined by Whitesides (2006) as the science and technology of systems that process or manipulate small amounts ( $10^{-9}$  to  $10^{-18}$  liters) of fluid, using channels with dimensions of tens to hundreds of micrometers. Tabeling (2015) defined microfluidics as a domain concerning the study of simple and complex flows that are composed of a single or several phases, inside an artificial micro-system. Microfluidics appears as a science since it includes the study of fluid mechanics at the micro-scale and also as a technique since the term describes an applicability (fabrication of artificial micro-systems). The definition of Tabeling (2015) does not include natural microfluidic systems. In a more general manner, microfluidics can be defined as the science and the technology of systems using fluids where at least one of the dimensions has a micrometer order of magnitude. Figure 1.5 shows the number of Google Scholar results per half decade for publications containing the keyword "microfluidics". The number of results has increased significantly since 1980 and is still important today. Microfluidics is more and more developed since it is considered as the solution for many modern challenges in various topics (including those in medical research,



**Figure 1.6** – [Left] 3D printing of biological constructions with heterogeneous and complex structures. Photographs of the 3D-printed (a) a mandible bone construct, (b) an ear cartilage with ear lobule, (c) a kidney with renal pelvis, (d) a liver, (e) a heart cross-section, and (f) an arterial tree, taken from Yi et al. (2017). [Right] Fully soft and autonomous robot controlled via the embedded microfluidic soft controller and powered by monopropellant decomposition, taken from Wehner et al. (2016).

biomedical engineering, mechanical engineering, materials science, chemical engineering...). Two impressive examples of the potential of microfluidics are manufacturing of biocompatible 3D printed organs with microfluidic systems (H. Sun et al. (2020), Yi et al. (2017)) and the fabrication strategy for entirely soft and autonomous robots (Wehner et al. (2016)) as presented in Figure 1.6.

### 1.2.2 Application of microfluidics in chemical engineering

In the field of chemical engineering, microfluidics also appeared as a solution to many challenges due to the high performance of the miniaturized reactors, called microreactors, in term of chemical conversion and data acquisition (Ehrfeld et al. (2000), Pohar et al. (2009)). They are still developed today in many chemical engineering fields such as electro-chemistry (Mo et al. (2020)), generation of nano-materials (X. Zhao et al. (2020)) and catalysis (Albrand et al. (2020)).

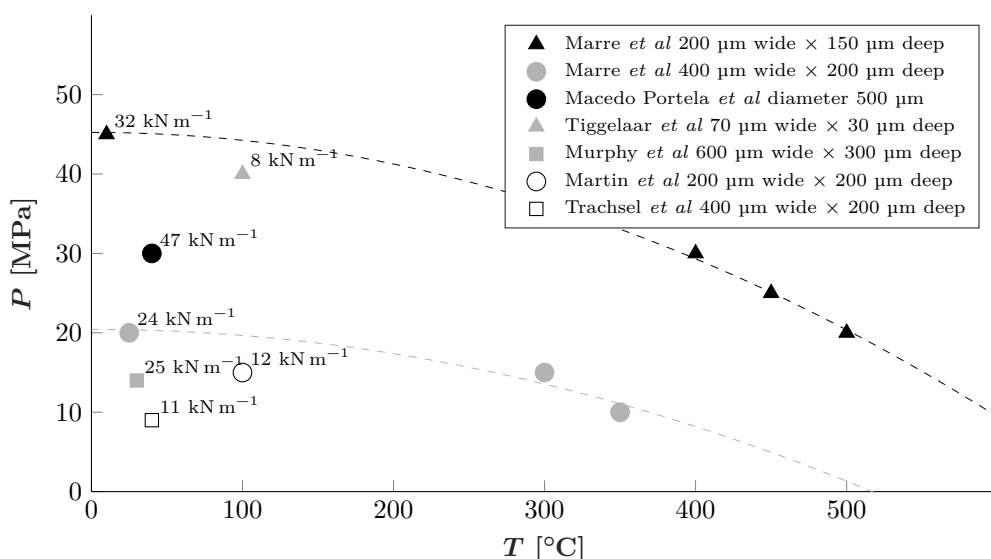
This high performance of microreactors is mainly due to the short characteristic length scale, which allows the characteristic times of heat and mass transport to be drastically reduced. The scale change of microfluidic systems compared with conventional macro-systems used in chemical engineering is the key parameter for understanding the physical and chemical effects in microfluidic systems. Indeed, reaction rates, mass transfer time, heat transfer time,

**Table 1.3** – Scale change effect on geometry, forces and transport properties between conventional macro scale systems and microfluidic systems. The term " $\propto$ " means "proportional to". Adapted from Silva (2014).

	$\mu\text{m}$	cm	m
Length ( $L$ )	$10^{-6}$	$10^{-2}$	1
Surface ( $L^2$ )	$10^{-12}$	$10^{-4}$	1
Volume ( $L^3$ )	$10^{-18}$	$10^{-6}$	1
Specific surface ( $L^{-1}$ )	$10^6$	$10^2$	1
Thermal and mass transport time ( $\propto L^2$ )	$10^{-12}$	$10^{-4}$	1
1st order heterogeneous chemical reaction time ( $\propto L$ )	$10^{-6}$	$10^{-2}$	1
Inertial forces ( $\propto L^4$ )	$10^{-24}$	$10^{-8}$	1
Viscous forces ( $\propto L^2$ )	$10^{-12}$	$10^{-4}$	1
Interfacial tension forces ( $\propto L$ )	$10^{-6}$	$10^{-2}$	1
Viscous forces/Inertial forces ( $\propto L^{-2}$ )	$10^{12}$	$10^4$	1
Interfacial tension forces/Inertial forces ( $\propto L^{-3}$ )	$10^{18}$	$10^6$	1

specific surface, inertial forces, viscous forces, interfacial tension forces and the ratio of these forces are directly dependent of the characteristic length of the system. These dependences are presented in Table 1.3.

The main characteristic of microreactors is that the volumes of fluids employed are small. The analysis of small quantities takes less time than for big volumes. It is therefore possible to analyse a larger number of samples in a fixed amount of time than with conventional techniques. For a fixed sampling time, a larger amount of data is obtained using microfluidics. For a fixed number of samples, the data are obtained in less time with microfluidics. Moreover, the use of small quantities enables the investigation of expensive or dangerous products. Another observation is that the specific surface (i.e. surface to volume ratio) is greatly increased in microreactors. An increase in the specific surface is a key parameter for the enhancement of heat and mass transport driving forces. In macro-scale systems, this surface to volume ratio is limited (being around 1000 times smaller than for microreactors). The enhancement of these driving forces has advantages such as easy heat management of the system (for highly exothermic reaction as an example) and short pathways or response times which also facilitate data acquisition. The ratio between the inertial forces and the viscous forces is greatly decreased in microreactors and leads to the prevalence of laminar



**Figure 1.7** – Maximum experiment pressure and temperature of microreactors providing an optical access, shown in the litterature and their maximum linear strength applied on their inner surfaces. Presentation adapted from Marre et al. (2010).

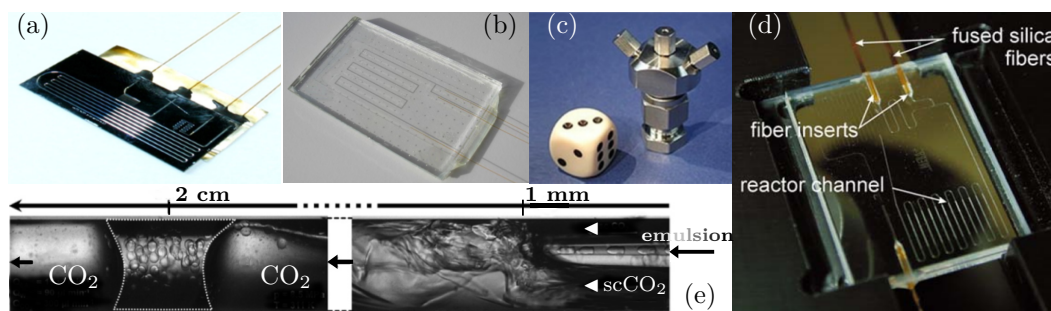
flow instead of turbulent flow<sup>2</sup>. This coupled with the dominance of interfacial tension forces over inertial forces ratio leads to perfectly defined flow characteristics.

The term "Lab on Chip" (LOC), which designates a device that integrates one or several laboratory functions on a single integrated circuit, also appears for microfluidic systems with the fabrication of micro-scale analysis laboratories. Microfluidic LOCs have been used for many applications such as clinical diagnostics (Srinivasan et al. (2004)), water treatment (Song et al. (2012)), and more recently for space technology (Mukhopadhyay (2020)), bio-analysis (Zhukov (2020)) and extraction process (Maurice et al. (2020)). However, as discussed below, microfluidics is not only used for analytical systems but also for the conversion of matter. Some industrial applications in conventional macro-scale reactors are limited by diffusion processes. In microreactors, this limitation is decreased or even eliminated thanks to the high surface to volume ratio and short characteristic length scales. This has also lead to the development of monolith reactors, which unite numerous microchannels in parallel and provide interesting flow properties such as an intermittent series of different fluid phases that enable almost ideal "plug flow" behaviour of tubular reactors in industry. (Ullah et al. (1992), Nijhuis et al. (2001), Avila et al. (2005), Albrand et al. (2020)).

### 1.2.3 High pressure and high temperature micro-systems

The desire of developing industrial applications based on supercritical fluids as presented in Section 1.1 involves the use of new fluid mixtures at various experimental conditions

<sup>2</sup>This property reduces the complexity of flow modelling and in particular computational fluid dynamics studies.



**Figure 1.8** – (a) Silicon/pyrex microreactor for supercritical extraction of vanillin (Assmann et al. (2012)); (b) Glass/ostemer microreactor for gas liquid mass transfer investigation (Martin et al. (2016)); (c) Metal microreactor for liquid fractionation with supercritical carbon dioxide (Campos Domínguez et al. (2016)); (d) Glass/glass microreactor for analytical chemistry (Oosterbroek et al. (2006)); (e) Capillary - An emulsion [ethyl-acetate  $15 \mu\text{L min}^{-1}$  - water  $90 \mu\text{L min}^{-1}$ ] is injected into a flow of supercritical  $\text{CO}_2$   $300 \mu\text{L min}^{-1}$  at 311 K and 8 MPa (Luther et al. (2012)).

(e.g. temperature, pressure, compositions) and therefore knowledge of physical, thermodynamic and kinetic properties such as mixture density, mixture viscosity, surface tension, thermodynamic equilibrium compositions, diffusion coefficient and mass transfer coefficient is required. The data acquisition of these parameters is time consuming with standard techniques. Microfluidic systems therefore appear as a solution for the rapid investigation of such properties. In addition, the advantages of microfluidic systems presented above and the increasing number of supercritical fluid applications in industry sparks a desire to develop micro-scale systems dedicated to supercritical fluids processes. It has been shown that many gas-liquid reactions must be achieved at high-pressure and some extractions or absorptions are improved with a high-pressure system. This improvement coupled with fast heat and mass transfer in microreactors is interesting. As a consequence, the development of microreactors that are able to resist high-pressure and high-temperature is needed.

## Pressure-resistant microfluidic systems

Many microreactors are made with Polydimethylsiloxane (PDMS), which has been a material of choice since the 1990s due to its ease of use and its interesting elastic properties. Nevertheless, such reactors are unsuitable for high-pressure use since PDMS is easily deformed with pressure and is permeable to supercritical fluids. Consequently, alternative technologies have been developed for high-pressure applications: metals, glass/glass, glass/polymer, silicon/Pyrex and capillary microreactors. All of which have advantages and drawbacks. Example of these microreactors are summarized in Figure 1.7 where the maximum linear strength applied on the inner surfaces of the microchannel are calculated<sup>3</sup>. This figure shows the difficulty to reach high-pressure and high-temperature at the same time. This difficulty is due to the weaknesses of the soldering between the microreactor and the connections to the

<sup>3</sup>Calculated with the maximum pressure applied on an equivalent capillary microreactor with the hydraulic diameter,  $d_H = 4A/P$  with  $A$  the area of the channel and  $P$  the perimeter. This value gives a comparison on the forces magnitude applied on the microsystems walls.

---

feeding system. The higher the maximum temperature, the lower the maximum reachable pressure.

Despite this observation, some microreactors are able to resist high-pressure and high-temperature and have demonstrated interesting applications like supercritical extraction, mass transfer investigations, liquid fractionation or analytical chemistry. These microreactors are presented in Figure 1.8.

Metal microreactors (Iglesia et al. (2007), Chambers et al. (2007) and Yao et al. (2017)) are typically fabricated using laser ablation or electrical discharge machining. Some of them are able to withstand pressure up to 1000 bar and temperature up to 500°C but do not allow optical access (Campos Domínguez et al. (2016)). Metal microreactors with optical access are typically made with stainless steel plates to compress glass or polymer wafers (Y. Zhao et al. (2013), Yao et al. (2014b)) but they are limited to pressure of 50 bar and ambient temperature.

Glass/glass microreactors are fabricated using hydrofluoric acid or buffered oxide etchant etching of either borosilicate (Ohashi et al. (2011), Luther et al. (2015)) or soda-lime glass (Mazurczyk et al. (2008)) wafers, which are directly bonded. Commercial glass/glass microreactors, such as those by Dolomite Ltd, withstand pressures up to 100 bar (Ogden et al. (2014), Andersson et al. (2018)). Tiggelaar et al. (2007) and Oosterbroek et al. (2006) developed glass/glass reactors that withstand up to 690 bar at ambient temperature or 400 bar at 100°C. These microreactors have an optical access, are not permeable to common supercritical fluids such as supercritical carbon dioxide ( $\text{sCO}_2$ ). However, the fabrications steps are difficult and require clean room facilities.

Martin et al. (2016) developed inexpensive glass/OSTEMER resin microreactor that does not require clean room facilities. The micro reactor withstands up to 200 bar but is not totally impermeable to  $\text{sCO}_2$  because of weaknesses of the transparent OSTEMER resin. The inexpensive aspect is important for such a microreactor because of its brittleness with high pressure (Andersson et al. (2016)), potential non-reversible clogging, and cleaning difficulties. Therefore, high-pressure microfluidic system need to be disposable devices.

Silicon/Pyrex microreactors seem to be the best means to withstand high pressure and temperature at the same time (Marre et al. (2010), R. Murphy et al. (2007), Keybl et al. (2011) and Assmann et al. (2012)) since the connection system and the microreactor itself are independent<sup>4</sup>. These microreactors are fabricated by dry or wet etching of a silicon wafer, which is bonded (fusion or anodic bonding) to a Pyrex wafer allowing optical access. Anodic bonding allows better pressure resistance than the direct bonding of glass/glass microreactors (Tiggelaar et al. (2007)). Silicon/Pyrex microreactors can also be adapted to new applications such as infra-red spectroscopy (Ari et al. (2020)). Nevertheless, this type of

---

<sup>4</sup>This also renders the microreactors interchangeable.

reactor is still relatively expensive to make and requires clean room facilities.

Silica glass microcapillaries coated with a polyimide protection are also a solution for microreactor fabrication. These microcapillary devices allow an optical access when the coating is removed but this also decreases the pressure resistance. To prevent this drawback, Macedo Portela da Silva et al. (2014) set the unprotected capillary tube with epoxy resin to increase its pressure resistance. In a such way, they developed an inexpensive transparent microreactor that is able to withstand pressures up to 300 bar.

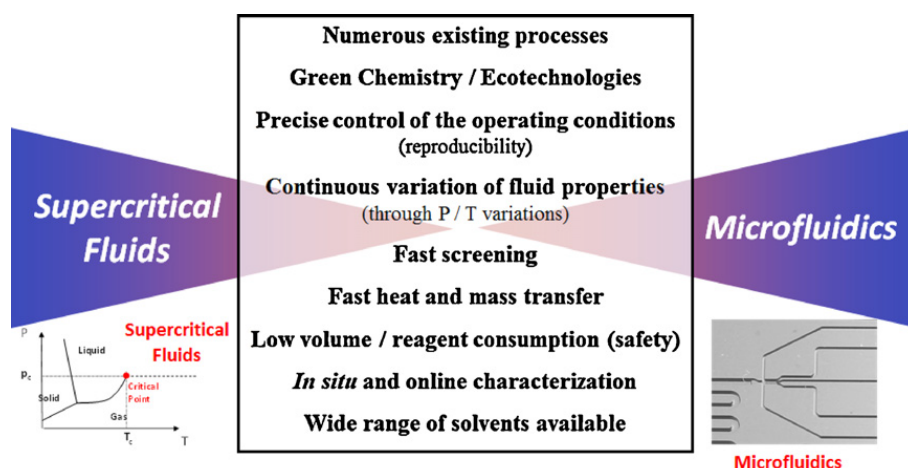
The microreactor resistance is not the only barrier preventing the high pressure investigation. Indeed, above 150 bar, the pressure resistance depends on the quality of connections between the capillary tubes and the microsystem. Two different kinds of connections can possibly be used:

- Permanent integrated connections like epoxy gluing of silica capillaries (Blanch-Ojea et al. (2012), Ogden et al. (2014), Martin et al. (2016), Assmann et al. (2012), Tiggelaar et al. (2007)), PEEK tubes (Yen et al. (2005)) or Teflon tubes (Pattekar et al. (2003)). Other types include metal soldering (Trachsel et al. (2008), R. Murphy et al. (2007)), glass brazing (Yen et al. (2005), Peles et al. (2004)) or anodic bonding of Kevlar tubes to glass (Blom et al. (2001)). These permanent connections can withstand pressure up to 200 bar or more but have a low temperature resistance and complicated fabrication steps.
- Removable connections like compression sealing with O-rings (Marre et al. (2010)), stainless steel junctions (Nittis et al. (2001), Müller et al. (2005), Campos Domínguez et al. (2016)) and commercial interfaces for capillaries can resist high pressure up to 450 bar depending on the design (Stishov et al. (2003)). These non-permanent connections are less time consuming in fabrication and enable high pressure and temperature issues to be decoupled if necessary (Marre et al. (2010)).

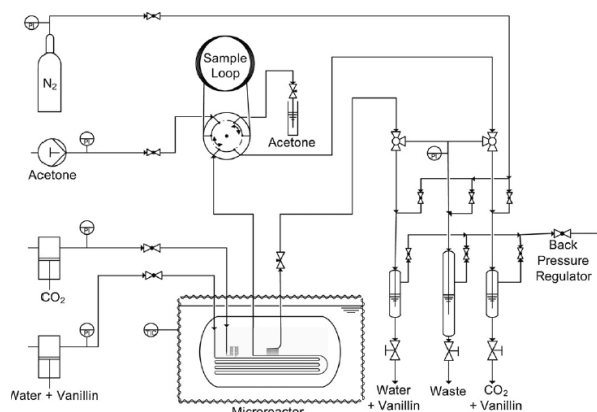
## Supercritical microfluidics applications

The combined advantages of microfluidics and supercritical fluids opens many possibilities in the field of process engineering. Indeed, the definite advantage provided by the use of "green" supercritical fluids as reagents, reaction medium or as a replacement for certain toxic solvents, is increased tenfold by their use in microsystems. Figure 1.9 is from the work of Marre et al. (2012) and shows the different advantages of combining supercritical fluids and microreactors. Among these advantages is the use of fluids under pressure while having increased safety due to their use in small volumes. In addition, the drastically reduced heat and mass transfer times in microreactors reduces the operating times required for the extraction, reaction or particle generation purposes.

Indeed, literature studies have profiled these benefits in areas such as extraction, organic chemistry, generation of nanomaterials and the acquisition of thermodynamic data:



**Figure 1.9** – Summary of the main advantages of combining supercritical fluids to microfluidics systems. Taken from Marre et al. (2012).



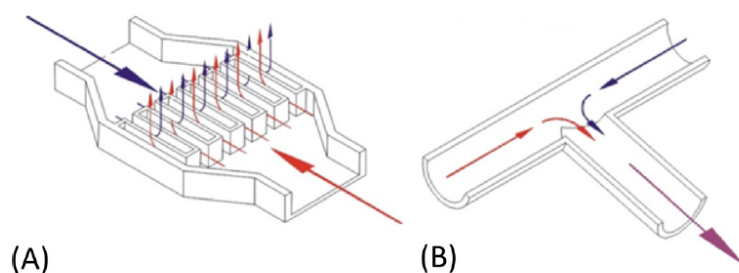
**Figure 1.10** – Schematic diagram of the high pressure plant, into which the microreactor was integrated. It consists of high pressure piston pumps and an elaborated sampling system. Taken from Assmann et al. (2012).

- **Extraction:** As presented before, organic compounds are easily soluble in a supercritical phase and can therefore be extracted from a complex solid or a liquid solution. This type of extraction can be conducted into microfluidic systems. As an example, Assmann et al. (2012) proposed the extraction of vanillin as described in Figure 1.10. The vanillin is extracted from an aqueous solution with supercritical carbon dioxide in a two-phase flow at pressures between 8 MPa and 10 MPa. In this process, the fast mass transfer in the microreactor allows to the residence time to be reduced compared with macro-scale apparatus. In addition, since supercritical carbon dioxide has no surface tension, the aqueous phase is separated from the supercritical carbon dioxide phase (which contains vanillin) with a simple capillary separator.

Another example is the investigation of liquid fractionation with supercritical carbon dioxide in the work of Campos Domínguez et al. (2016) where a continuous extraction of *EtOH* from an aqueous phase is performed with *sCO<sub>2</sub>* at 10.1 MPa and 333 K in two



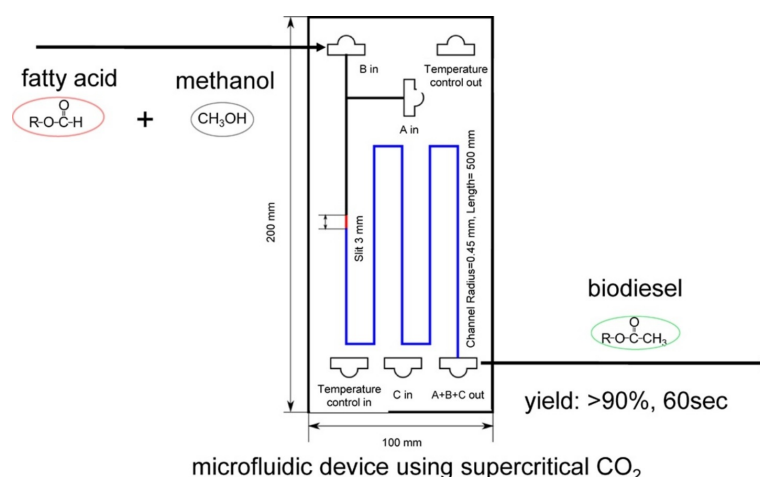
types of micro-mixers, presented in Figure 1.11. They observed that the thermodynamic equilibrium is reached for each type of micro-mixers. This concludes that the extraction *EtOH* of *EtOH-H<sub>2</sub>O* binary mixture with *sCO<sub>2</sub>* can be performed in micro-scale apparatus.



**Figure 1.11** – Description of the mixing principles studied in the work of Campos Domínguez et al. (2016): multi-lamination (A) and T-type lamination (B). Taken from Campos Domínguez et al. (2016).

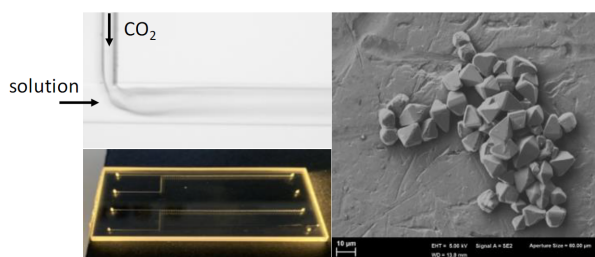
- Organic chemistry:** In macro-scale apparatus, the limitation due to slow diffusion can be a barrier for the performance of chemical reactions, such as hydrogenation reactions. In microreactors, the significant decrease in characteristic length allows the diffusion processes to be enhanced. Under high-pressure, gas-liquid reactions are improved due to the increased dissolution of gas into the liquid phase. In addition, highly exothermic reactions can be easily performed since the heat diffusion through the microreactor walls is faster<sup>5</sup>. In the work of Verboom (2009), a review on reactions performed in high-pressure microreactors indicates the benefits of such systems, including improved efficiencies in Diels-Alder reactions and better yields obtained with the use of supercritical carbon dioxide. In the work of Quitain et al. (2018), supercritical carbon dioxide is used as a solvent in the esterification of oleic acid with methanol in the presence of catalyst ( $H_2SO_4$ ) in a microreactor at a pressure of 10 MPa and temperatures between 333 K and 393 K. The microreactor employed is presented in Figure 1.12. The reaction has been shown to proceed in less than one minute of residence time with a yield increased up to 90%. In addition, the reaction occurred successfully even without the use of catalyst due to the fast diffusion process in the microreactor.

<sup>5</sup>It is therefore easier to maintain a constant temperature in microreactors compared with macro-scale apparatus.



**Figure 1.12** – Micro reactor employed for esterification of oleic acid with methanol where supercritical carbon dioxide acts as a solvent at a pressure of 10 MPa and temperatures between 333 K and 393 K. Taken from Quitain et al. (2018).

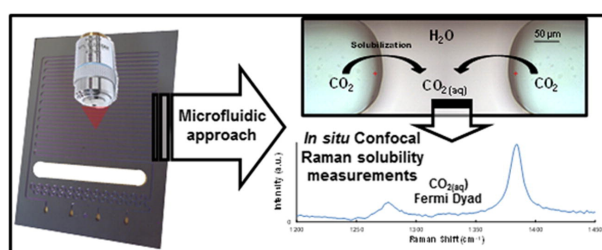
- Nanomaterial generation:** Section 1.1.2 presented the use of supercritical fluids for the generation of small particles in processes such as RESS, PGSS and SAS. In the work of Arora et al. (2020), drug particles of griseofulvin are precipitated from a dimethylformamide solution with supercritical carbon dioxide, which is used as the antisolvent (like in the SAS process) in a microreactor presented in Figure 1.13. In this study, the pressure variation from 1 MPa to 2 MPa during the formation process is linked to the particle diameter (from 0.5  $\mu\text{m}$  to 500  $\mu\text{m}$ ) in order to generate size controlled particles. In the work of Couto et al. (2014) and Jaouhari et al. (2020), the SAS process is performed in microreactors ( $\mu\text{SAS}$ ) for the generation of ultra-small organic nanoparticles of poly(3-hexylthiophene) and tetraphenylethylene respectively.



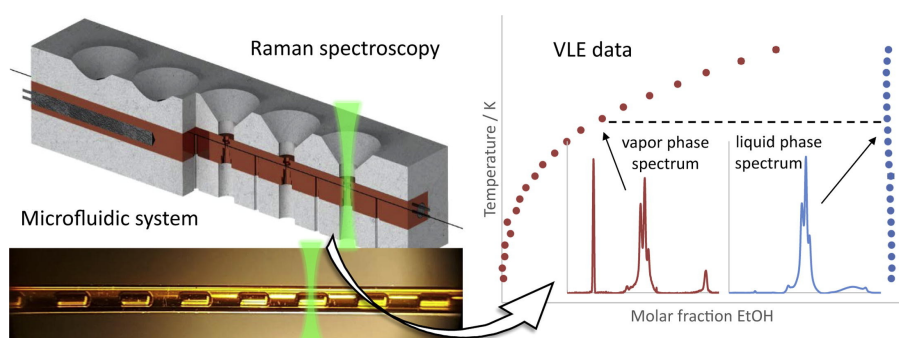
**Figure 1.13** – Micro reactor employed in the griseofulvin particle generation from a solution of griseofulvin and dimethylformamide with carbon dioxide as antisolvent. Taken from Arora et al. (2020).

- Thermodynamic data acquisition:** As mentioned before, the acquisition of solubility data under ambient conditions and also at high-pressure is commonly performed in macro-scale apparatus. These macro-scale apparatus are pressure-volume-temperature variable cells (PVT). In the case of a binary system, the two compounds are inserted in the cell with a certain molar ratio. The P, V, T parameters can be modified in order to

obtain the entire liquid-vapor equilibrium curve by sampling the liquid and the vapor phases or with spectroscopic techniques if the cell has optical access. The disadvantage of such cells are the long experimental times required to reach the thermodynamic equilibrium<sup>6</sup>, which can last several hours. However, in microreactors, due to the high surface to volume ratios and therefore the fast heat and mass transfer rates, thermodynamic equilibrium can be reached in several seconds. In the work of N. Liu et al. (2012),  $H_2O$ , brine and  $CO_2$  are mixed in a high-pressure microreactor, presented in Figure 1.14 where a Raman spectroscopy technique is employed for the determination of the  $CO_2$  solubility in  $H_2O$  and brine. In the work of Klima et al. (2019), entire vapor-liquid equilibria diagrams are obtained with a Raman spectroscopy technique, for fuel-nitrogen systems at engine-like conditions (pressures between 3 MPa and 8 MPa, temperature up to 593 K) in a microcapillary presented in Figure 1.15. These techniques combine microfluidics and optical techniques that allow the fast acquisition of thermodynamic data. In the work of Gavaille et al. (2019), recent approaches to determine viscosity, density and phase equilibria at high-pressure and high-temperature in microreactors are reviewed.

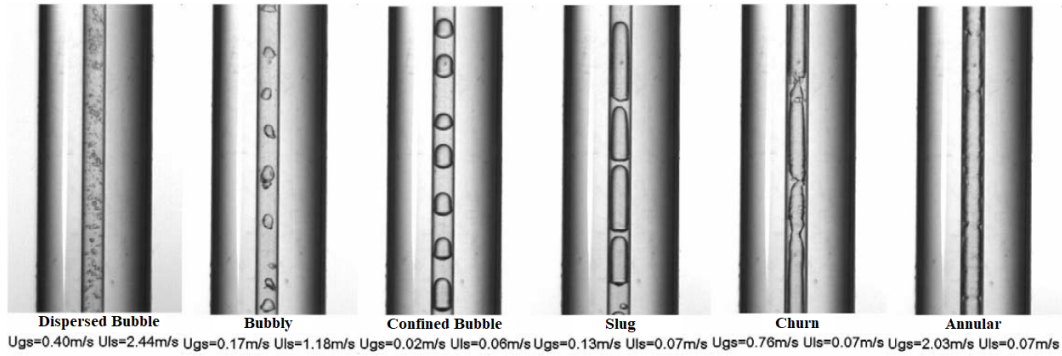


**Figure 1.14** – Microfluidic approach for the determination of  $CO_2$  solubility into a  $H_2O$  and brine liquid solution at high pressure. Taken from N. Liu et al. (2012).



**Figure 1.15** – Determination of the vapor-liquid equilibria for fuel-nitrogen systems at pressures between 3 MPa and 8 MPa, temperature up to 593 K, in a microcapillary where a Raman spectroscopy technique is employed. Taken from Klima et al. (2019).

<sup>6</sup>When one out of the three parameters is changed, the equilibrium is supposed to be reached when the two others parameters are stable



**Figure 1.16** – Flow patterns obtained at 1 MPa with a 1.10 mm internal diameter tube. Taken from L. Chen et al. (2006) where  $U_{gs}$  and  $U_{ls}$  are the gas and liquid superficial velocities respectively.

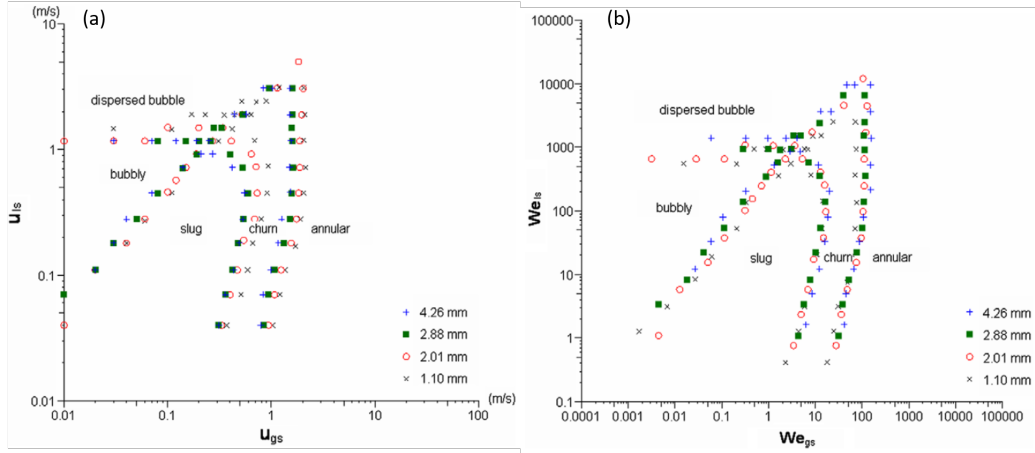
### 1.3 Gas-liquid two phase flow in microsystems

Initially, studies of gas-liquid flows in microchannels consisted in characterizing the different flow regimes generated as a function of operating conditions (Triplett et al. (1999), Akbar et al. (2002), Waelchli et al. (2006), L. Chen et al. (2006)). Typical observable flow types are numerous such as dispersed, bubbly, confined bubble, slug, churn and annular flows. These different flow types are presented in Figure 1.16 and described as follows:

- Dispersed flow: a large amount of very small bubbles dispersed in a continuous liquid phase.
- Bubbly flow: a distribution of irregular bubbles with comparable diameters but not as large as the microchannel diameter.
- Confined bubble: a train of almost spherical bubbles with a diameter as large as the microchannel diameter, with spherical caps.
- Slug flow: a train of bubbles composed of a cylindrical part and caps that can be spherical, also called Taylor or segmented flow.
- Annular flow: the gas phase forms a continuous core and is separated from the channel wall by a liquid film.
- Churn flow: an unstable annular flow where small bubbles are ripped off the gas core.

These different kinds of flows are obtained by modifying the gas and liquid superficial velocities ( $U_G$ ,  $U_L$ ), which corresponds to the phase volumetric flow-rate divided by the cross section of the microchannel as presented in Equation 1.1. However, the superficial velocities can also be modified by temperature (T) and pressure (P).

$$U_L = \frac{\dot{V}_L}{A} \quad U_G = \frac{\dot{V}_G}{A} \quad (1.1)$$



**Figure 1.17** – Flow pattern maps obtained by L. Chen et al. (2006), plotted as function of the gas and liquid superficial velocities (a) and as a function of the Weber number of each phase (b) for channel diameters of 4.26 mm, 2.88 mm, 2.01 mm and 1.10 mm.

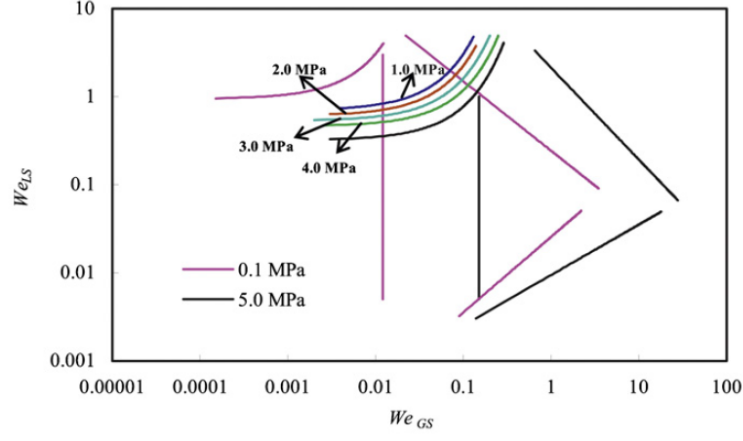
Differences between the flow types depends on the balance of viscous, inertial and interfacial tension forces. These forces can be compared using dimensionless numbers which are presented in Table 1.4. The dominant forces controlling flows in microchannels are different than in macro-scale devices due to the significant difference in characteristic length scale, i.e. hydraulic diameter  $d_h$ . In macro-scale equipment, the hydraulic diameter is typically in the range  $10^{-1}$ – $1$  m, whereas in microchannels the hydraulic diameter is in the range  $10^{-4}$  –  $10^{-3}$  m. This difference leads to a reduction of  $Re$  and  $We$  numbers by a factor 1000 and of the  $Bo$  number by a factor 1000000. This means that the inertial and gravitational forces are completely negligible compared with the interfacial tension and viscous forces in microchannels.

**Table 1.4** – Dimensionless numbers employed in gas-liquid microfluidic studies. The subscript  $\Phi$  corresponds to the investigated phase, gas or liquid.

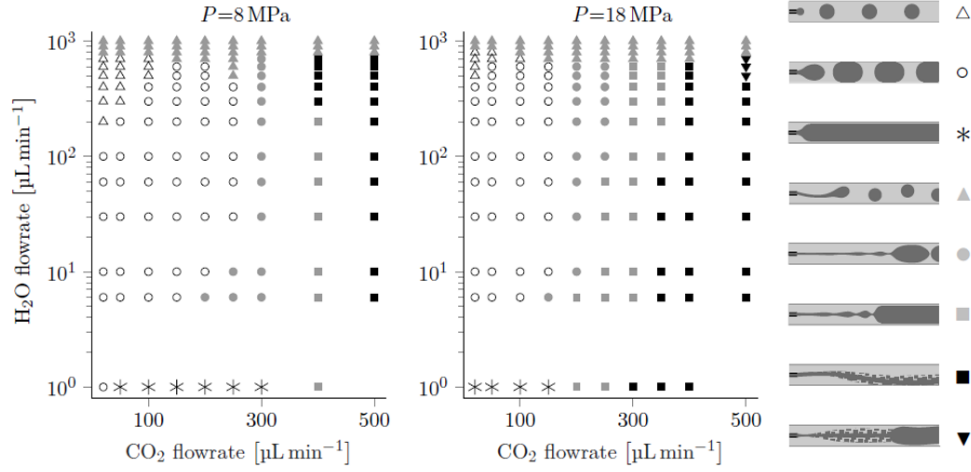
Dimensionless number	Formula	Involved forces
Reynolds	$Re_\Phi = \frac{\rho_\Phi U_\Phi d_h}{\mu_\Phi}$	$\frac{\text{inertial forces}}{\text{viscous forces}}$
Capillary	$Ca_\Phi = \frac{U_\Phi \mu_\Phi}{\sigma}$	$\frac{\text{viscous forces}}{\text{interfacial tension forces}}$
Bond	$Bo = \frac{g d_h^2 \Delta \rho_\Phi}{\sigma}$	$\frac{\text{gravitational forces}}{\text{interfacial tension forces}}$
Weber	$We_\Phi = \frac{\rho_\Phi U_\Phi^2 d_h}{\sigma}$	$\frac{\text{inertial forces}}{\text{interfacial tension forces}}$

### 1.3.1 Flow regime map

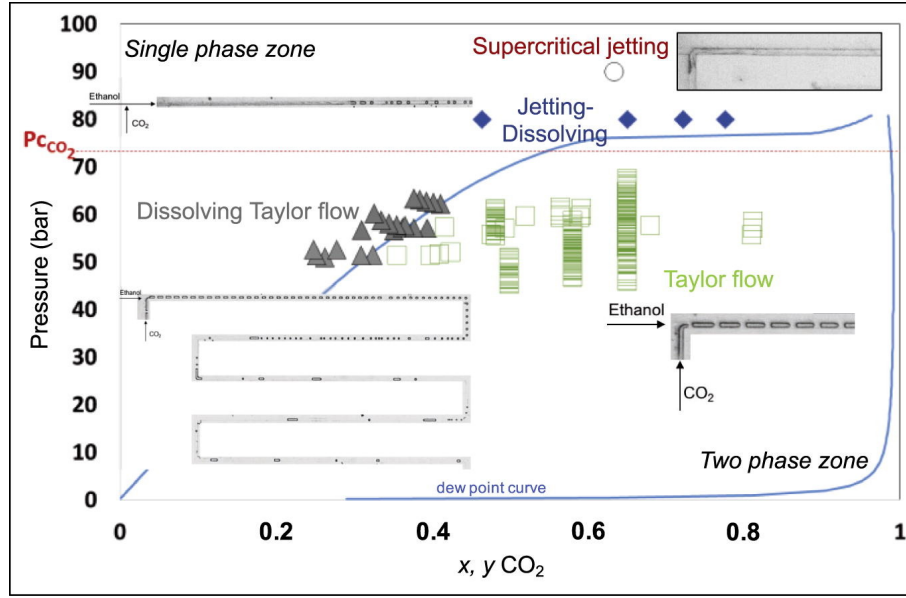
Transitions between the different flow regimes have been investigated, amongst others, by Triplett et al. (1999), Akbar et al. (2002), L. Chen et al. (2006), Menech et al. (2008) at



**Figure 1.18** –  $N_2$ - $H_2O$  flow pattern map obtained in a T-junction microchannel for pressures between 0.1 MPa and 5 MPa taken from Y. Zhao et al. (2013).



**Figure 1.19** – Dynamic phase diagrams of a  $CO_2$ -liquid water system obtained at two different pressure, 8 MPa on the left and 18 MPa on the right, all other parameters being kept constant ( $d_h = 75 \mu m$ ,  $T = 323 K$ ) taken from Marre et al. (2009).

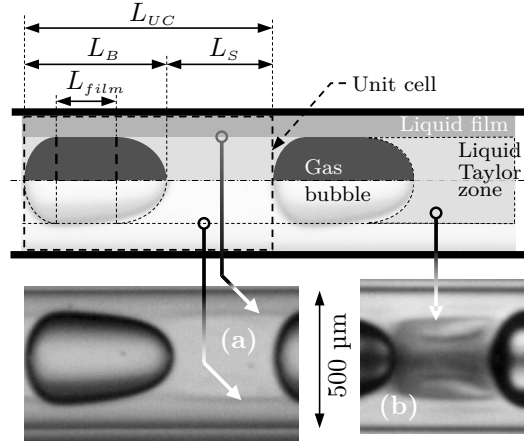


**Figure 1.20** – Phase diagram for  $CO_2$ - $EtOH$  at 313 K and flow regime map. Superficial velocity ranges:  $0.13 \text{ m s}^{-1} < U_G < 0.30 \text{ m s}^{-1}$ ,  $0.01 \text{ m s}^{-1} < U_L < 0.05 \text{ m s}^{-1}$  taken from Martin et al. (2018).

atmospheric pressure and then by (Y. Zhao et al. (2013) and Marre et al. (2009)) at elevated pressure (up to 18 MPa). Flow regime maps are typically plotted as a function of the superficial gas and liquid velocities ( $U_G$  and  $U_L$ ) as presented in Figure 1.17 (a). In these flow regime maps, the transition lines between flow regimes depend on the geometry (e.g. hydraulic diameter, contacting design, channel cross section) of the micro system and the physical properties of the fluids employed. Akbar et al. (2002) proposed an universal flow regime map as a function of the Weber numbers of each phases in order to take into account the differences in hydraulic diameter, fluid density and interfacial tension. Figure 1.17 (b) is an example of this approach and shows the Weber number flow regime map that allows the different transition lines to collapse.

At moderate pressure (5 MPa), Y. Zhao et al. (2013) investigated  $N_2$ - $H_2O$  flow patterns as a function of the Weber number ( $We_L$ ,  $We_G$ ) as presented in Figure 1.18. They observed that the flow patterns are the same as those obtained at atmospheric pressure. Nevertheless, the transition lines shift to higher values of  $We_G$  due to the density change of the gas at higher pressure. The transition lines are however almost unchanged in terms of  $We_L$ .

The Weber flow regime map is therefore not suitable to classify high-pressure gas-liquid flows since the gas density variations can be important at high-pressure. Marre et al. (2009) proposed a dynamic phase diagram of  $CO_2$ - $H_2O$  system at 80 bar and 180 bar that is presented in Figure 1.19. They showed that by increasing the pressure (keeping the volumetric flow-rates constant), the transition lines shift to lower  $CO_2$  flow rate values. They showed that the process is reversible and that a decrease in pressure brings the system back to the initial flow regime. Blanch-Ojea et al. (2012) and Martin et al. (2018) proposed a new type of



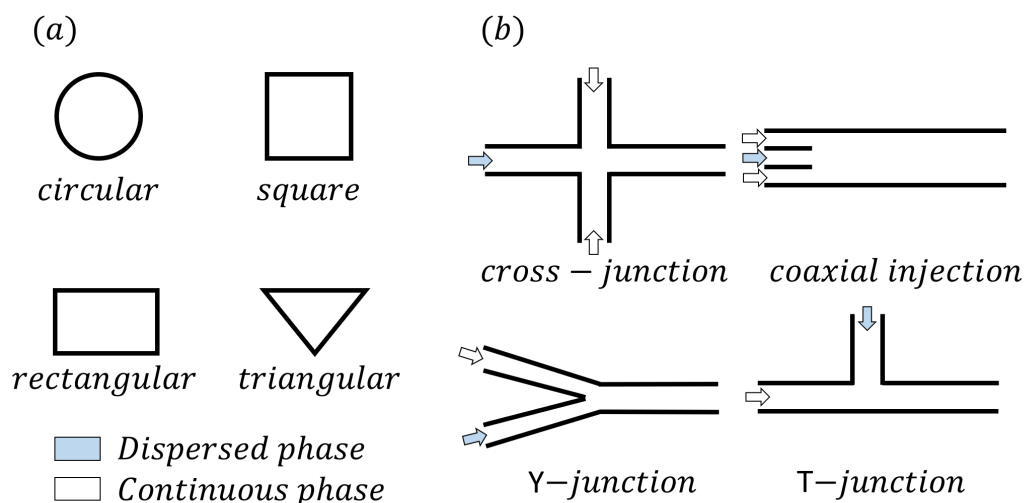
**Figure 1.21** – (a) In this microcapillary device [scCO<sub>2</sub>-BMImPF<sub>6</sub> 11.5 MPa 318 K] the boundary of this peculiarly thick film is made visible due to the impact of the high gradient of dissolved CO<sub>2</sub> on the refraction coefficient in the bubble wake border; (b) With the same system and other operating conditions, a modification in the lighting allows the torroidal recirculation in the Taylor zone to be clearly seen (*unpublished J.-J. Letourneau (2014)*).

flow pattern map that take into account the changes in physical properties at high-pressure. They respectively investigated CO<sub>2</sub>-methanol and CO<sub>2</sub>-ethanol systems at different pressure and temperature and plotted the flow regimes in the vapor liquid pressure composition (P,x) diagram. The CO<sub>2</sub>-ethanol (P,x) diagram from the work of Martin et al. (2018) is presented in Figure 1.20. The mass ratio between the gas and the liquid is constant for each experiments. However, this is not the case in conventional studies when the volumetric flow-rates are constant. Several types of flow are obtained in the (P,x) diagram: the classical two-phase flow patterns (e.g. churn, slug, slug-annular and annular flows) but also single phase flow due to the complete miscibility of compounds at certain conditions. This study allows the potential mutual solubility of the binary system to be evaluated by taking into account the thermodynamics properties of the system.

### 1.3.2 Hydrodynamics of Taylor flow

Segmented flow, also called Taylor flow, is characterized by regular elongated bubbles with a length that is typically greater than the channel diameter, separated by liquid slugs. The bubbles adopt a characteristic capsular shape (depending on Re and Ca) and can either completely or nearly completely fill the channel cross-section where a thin liquid film separates them from the channel wall. In particular, segmented flow has shown to be effective in different applications such as extraction, absorption (Li et al. (2014), Zhu et al. (2014)) and multiphase reactions (Kreutzer et al. (2005)). Indeed such flows provide high interfacial area, as well as fast mixing in the liquid slugs. In addition, the residence time, which is an important parameter in reactive processes, is linked to the bubble velocity which can be adjusted by changing the superficial velocities of both phases. In general, the bubble velocity  $U_B$  is slightly higher than the two-phase velocity  $U_{TP} = U_L + U_G$  but





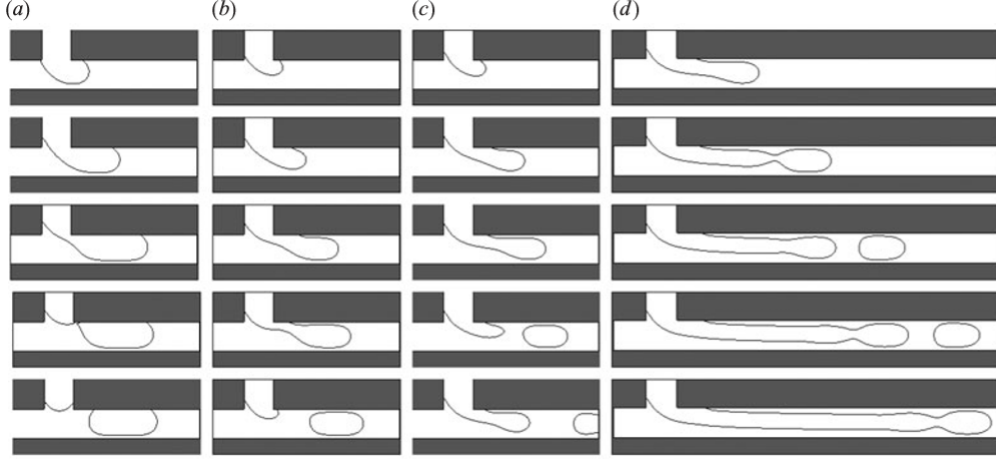
**Figure 1.22** – Various microchannel geometry employed in the Microfluidics litterature: (a) cross-sections (b) inlet geometries.

lower than the velocity at the center of the cross section. This phenomenon is due to the liquid film at the wall that flows in a backward direction and leads to recirculation in the liquid slug. In the stationary frame of reference, the velocity of liquid recirculation at the center of channel is twice the bubble velocity. This recirculation promotes mixing in the liquid slug and allows the gas-liquid interface to be renewed continuously. Both of which enhance mass transfer and reaction. Figure 1.21 shows the specific behaviour of this flow in the case of a two-phase flow of  $CO_2$  and ionic liquid ( $BMimPF_6$ ). A train of bubbles is separated by liquid slugs. In Figure 1.21 (b) the recirculation present in the liquid slug helps the mixing of the liquid phase and also promotes a mixing between the slug and the liquid film.

The hydrodynamics of Taylor flow has been widely investigated in the literature, especially in terms of the phenomena governing the bubble generation process, the liquid film thickness surrounding the bubble, as well as the mixing in the liquid slug. These aspects are detailed in the following sections.

## Bubble generation

The bubble formation mechanism in gas-liquid Taylor flow has been extensively studied under ambient conditions in the literature (Yun et al. (2010), Shao et al. (2008), D. Liu et al. (2008), Dang et al., 2013, Garstecki et al. (2006), Leclerc et al. (2010)). Indeed, the bubble size and velocities in the channel are directly linked to the flow properties at the inlet of the microchannel. Variations in reactor cross-section (e.g. rectangular, circular, square), the inlet geometries (T-junction, Y-junction, coaxial, cross-junction), the wall wettability and liquid film thickness (Fouilland et al. (2010), Choi et al. (2011) and Han et al. (2009)) are factors that influence the bubble generation process. Different microchannel geometries are presented in Figure 1.22. The forces involved in the bubble formation mechanism are the interfacial



**Figure 1.23** – Squeezing to shearing regime from Menech et al. (2008) in a T-junction square microchannel: (a)  $Ca_L = 0.004$ ; (b,c)  $Ca_L = 0.035$ ; (d)  $Ca_L = 0.05$ .

tension forces between gas and liquid, the shear stress at the interface and the resistance force or pressure drop. The dimensionless numbers used to study the bubble generation process are typically the liquid phase, bubble and two phase capillary numbers ( $Ca_L$ ,  $Ca_B$  and  $Ca_{TP}$ ) which compare the effects of inertial forces versus interfacial tension forces. When  $Ca_L < 0.01$ , the bubble formation regime is called squeezing regime. The bubble formation is governed by the interfacial tension forces and the resistance forces as presented in Figure 1.23(a). Indeed, the bubble section is almost equal to the channel cross-section and the rupture is driven by the pressure build-up across the bubble. In a T-junction channel, the break up point is located at the T-junction. In the work of Garstecki et al. (2006), a model for the bubble length  $L_B$  in non-inertial flows and in the squeezing regime was proposed based on characteristic times (filling and squeezing times). It was shown that bubble size is independent of fluid properties under these conditions. The bubble length formulation is presented in Equation 1.2, valid for microchannels with a square cross section. The ratio of the bubble length over the square cross section side  $w$  is proportional to the ratio of the superficial velocities  $U_G/U_L$ , where  $\lambda_1$  and  $\lambda_2$  are constants.

$$\frac{L_B}{w} = \lambda_1 + \lambda_2 \frac{U_G}{U_L} \quad (1.2)$$

Steijn et al. (2007) improved this correlation by taking into account the liquid leakage in the corner of the microchannel cross section. This correlation is presented in Equation 1.3 where  $w_{in}$  is the side of the gas inlet square cross section in the T-junction.

$$\frac{L_B}{w} = \lambda_1 + \frac{w_{in}}{w} \frac{U_G}{U_L} \quad (1.3)$$

Völkel (2009) suggested a correlation for the liquid slug length  $L_S$  based on the work of Steijn et al. (2007), as presented in Equation 1.4.

$$\frac{L_S}{w} = \lambda_2 + \lambda_1 \frac{U_L}{U_G} \quad (1.4)$$

Abadie (2013) then showed that for inertial flows, these constants are dependent on operating conditions and of the fluid properties. He proposed the equation (1.5) where the bubble length relative to the unit cell is described with  $\alpha$ , a constant independent of operating conditions, fluid properties and microchannel geometry.

$$\frac{L_B}{L_B + L_S} = \frac{\frac{U_G}{U_L}}{\alpha + \frac{U_G}{U_L}} \quad (1.5)$$

In the work of Martin et al. (2018) where a segmented flow of  $CO_2$  and  $EtOH$  is investigated at high-pressure, the correlation of Abadie (2013) is applied and shows a good agreement in the same  $Ca_L$  range ( $Ca < 0.01$ ).

When the shear stress cannot be neglected ( $Ca > 0.01$ ), the bubble generation mechanism is called "shearing", which is depicted in Figure 1.23 (d). In this regime, the break-up point is located after the T-junction, and gas bubbles do not block the channel. The shear stress is predominant inducing the bubble break-up with the inertial effects. At high-pressure, in the work of Yao et al. (2014c), it is shown that the shear stress is less important as pressure increases. The break-up point is located nearer the T-junction (like in the squeezing regime) even for liquid capillary numbers greater than 0.01. Due to the interfacial tension between the gas and the liquid, the gas cannot span the complete cross-section of the microchannel and leakage flow of liquid is observable around the bubble. Yao et al. (2014c) showed that this leakage flow is more significant with pressure increase and has an impact on the bubble size. They made the hypothesis that this difference, compared with experiments at ambient conditions, comes from a greater force balance between the dense gas and the liquid. It was also shown that an increase in leakage flow with pressure has an impact on the bubble formation frequency and on the slug length, which is lower than at atmosphere pressure at same velocities conditions. The classification of shearing and squeezing regime of bubble formation as a function of the capillary number still needs further work at high pressure due to the current lack of experimental data. Indeed, as the physical properties of gases (like  $CO_2$ ) can be significantly different at high pressure, the critical capillary number (i.e. the capillary number where the bubble formation regime passes from squeezing to shearing) depends on the pressure and the nature of the binary system studied. In the work of Yao et al. (2014c), the capillary number is almost constant between the different experiments since the binary used is  $N_2-H_2O$ . Indeed, the viscosity of  $N_2$  and its interfacial tension with  $H_2O$  are almost constant with pressure. However, for a segmented flow of  $CO_2$  and  $H_2O$ , for constant volumetric flow rates, an increase in pressure leads to an increase in capillary number (due to the lower interfacial tension and higher viscosity) and therefore the shift

---

between squeezing and shearing, which is characterized by a critical capillary number, is expected to change.

## Liquid film

After the bubble generation process, the bubbles and slugs form a periodic flow in the microchannel. This periodic flow is characterized by a succession of unit-cells. A unit-cell is composed of one bubble, one liquid slug and a liquid film surrounding the bubble. The liquid film thickness  $\delta$  has been investigated vastly in circular cross-sectional tubes (Taylor (1961), Bretherton (1961), J.-D. Chen (1986), Aussillous et al. (2000)) and square cross sections (Kolb et al. (1991), Wong et al. (1995), Fries et al. (2008b)). The dimensionless liquid film thickness  $\frac{\delta}{R}$  in a tube (with  $R$  the bubble radius) is typically expressed as a function of the capillary number  $Ca_B$ . This capillary number is expressed in Equation 1.6 where  $U_B$  is the bubble velocity,  $\mu_L$  the viscosity of the liquid phase and  $\sigma$  the interfacial tension between the dispersed and the continuous phase.

$$Ca_B = \frac{U_B \mu_L}{\sigma} \quad (1.6)$$

Bretherton (1961) proposed the correlation presented in Equation 1.7. This equation is based on the lubrication theory, which is valid for negligible liquid thickness with respect to the bubble diameter and therefore low capillary numbers. The correlation of Bretherton (1961) is not valid for  $Ca_B$  greater than 0.005.

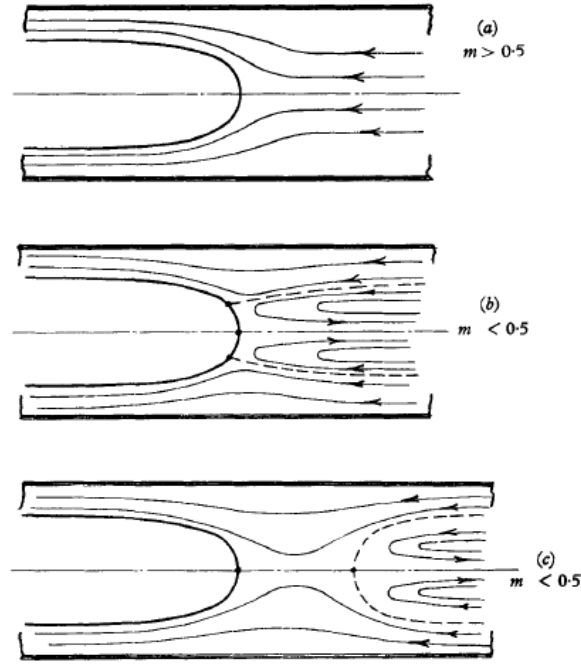
$$\frac{\delta}{R} = 1.34 Ca_B^{2/3} \quad Ca_B < 0.005 \quad (1.7)$$

Aussillous et al. (2000) further extended range of the correlation such that it can be used for capillary number values ( $10^{-4} < Ca_B < 1$ ). This correlation is presented in 1.8 where the constant 2.5 was obtained experimentally.

$$\frac{\delta}{R} = \frac{1.34 Ca_B^{2/3}}{1 + 2.5 \times 1.34 Ca_B^{2/3}} \quad 10^{-4} < Ca_B < 1 \quad (1.8)$$

Abadie (2013) proposed to rewrite these correlations as a function of the capillary number written with the two-phase velocity  $U_{TP}$ ,  $Ca_{TP} = \frac{U_{TP} \mu_L}{\sigma}$  so that film thickness can be determined from the operating parameters only, rather than the bubble velocity  $U_B$  which must be measured. Furthermore, he improved the correlations in order to extend the capillary number validity range to  $10^2$ , as presented in Equation 1.9. He also proposed a correlation to compute the ratio between the bubble velocity  $U_B$  and the two-phase velocity  $U_{TP}$  as presented in Equation 1.10.

$$\frac{\delta}{R} = \frac{1.34 Ca_{TP}^{2/3} \left(1 + \frac{4}{3} \times 1.34 Ca_{TP}^{2/3}\right)}{1 + 1.34 Ca_{TP}^{2/3} \left(1.2 + \frac{4}{3} \times 1.34 Ca_{TP}^{2/3}\right)} \quad 10^{-4} < Ca_{TP} < 10^2 \quad (1.9)$$



**Figure 1.24** – Rough sketch of possible streamlines. Taken from Taylor (1961) where  $m$  is the dimensionless number  $(U_B - U_{TP})/U_B$ .

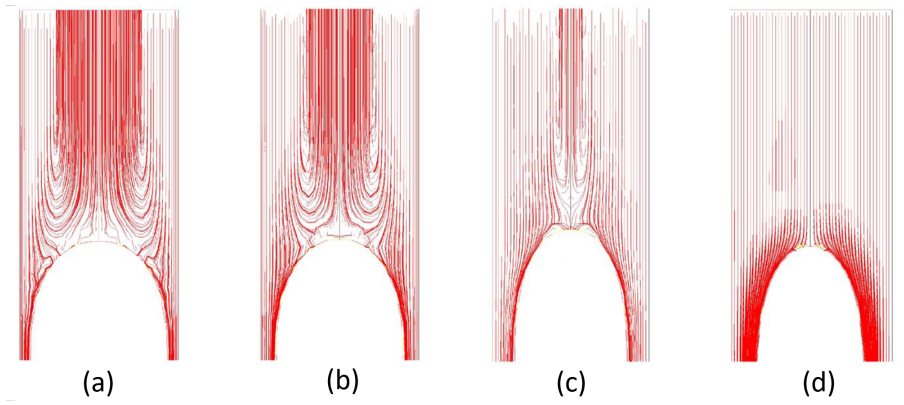
$$\frac{U_B}{U_{TP}} = \left[ 1 - \left( \frac{1.34Ca_{TP}^{2/3} \left( 1 + \frac{4}{3} \times 1.34Ca_{TP}^{2/3} \right)}{1 + 1.34Ca_{TP}^{2/3} \left( 1.2 + \frac{4}{3} \times 1.34Ca_{TP}^{2/3} \right)} \right)^2 \right]^{-1} \quad 10^{-4} < Ca_{TP} < 10^2 \quad (1.10)$$

The relationship between Equations 1.9 and 1.10 is based on the following analysis. Under ambient pressure, the pressure in the bubble is uniform due to its low viscosity. In addition, assuming a constant thickness of the liquid film along the microchannel, the pressure in the liquid film is uniform and the velocity is zero. With these hypotheses, the volume balance leads to Equation 1.11.

$$\frac{U_B}{U_{TP}} = \frac{1}{\left( 1 - \left( \frac{\delta}{R} \right)^2 \right)} \quad (1.11)$$

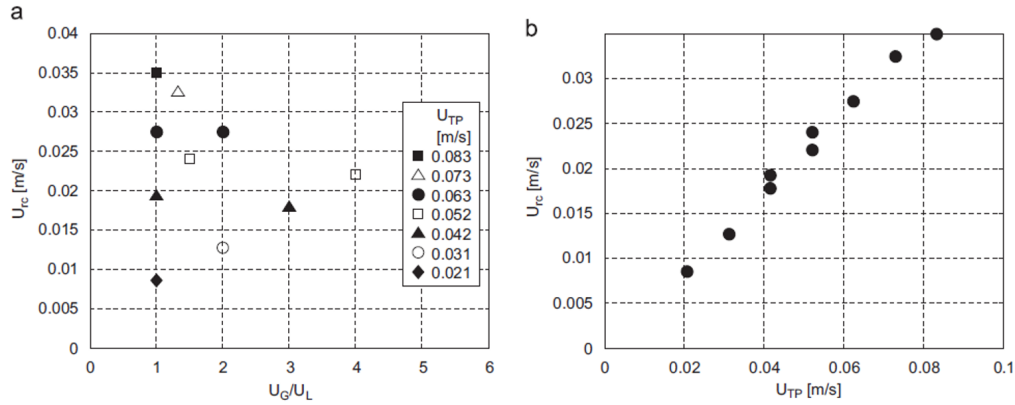
### Recirculation in the liquid slug

The relative difference between the bubble velocity and the two-phase superficial velocity results in a recirculation flow pattern in the liquid slug. This recirculation flow was first experimentally investigated by Taylor (1961) and Thulasidas et al. (1997). The results are presented in Figure 1.24. The difference in streamlines is discussed according to the relative velocity difference,  $m = (U_B - U_{TP})/U_B$ . A complete bypass flow pattern was observed for  $m > 0.5$ . For  $m < 0.5$ , however, two flow patterns are observed: one where a stagnation point is on the bubble cap as shown in Figure 1.24 (b), and the other where



**Figure 1.25** – Liquid slug streamlines obtained by CFD simulations at different capillary numbers ( $Ca_B$ ) in the work of Taha et al. (2004). (a)  $Ca_B = 0.03$  (b)  $Ca_B = 0.10$  (c)  $Ca_B = 0.3$  (d)  $Ca_B = 1.34$ .

two stagnations points are present, one on the bubble cap and one inside the liquid slug as presented in Figure 1.24 (c). Thulasidas et al. (1997) worked on segmented flows with long liquid slugs and fully developed laminar velocity profiles (Poiseuille) and in short liquid slugs. They observed recirculation flow in the latter only and showed that the recirculation time increases with the bubble capillary number  $Ca_B$ . Günther et al. (2004), Trachsel et al. (2005), Zaloha et al. (2012) and Taha et al. (2004) investigated the liquid slug recirculation with modern techniques. Taha et al. (2004) obtained the streamlines in the liquid slug with a Computational Fluid Dynamics study and an example of results are presented in Figure 1.25. It can be seen that the radial position of the centre of the recirculation loop is displaced toward the capillary wall when  $Ca_B$  is decreased and the liquid film thickness decreases. When the bubble velocity is increased (thereby increasing  $Ca_B$ ), the recirculation in the liquid slug is less intense and eventually bypass flow is obtained. In bypass flow, the bubble velocity is equal to the velocity at the center of the fully developed Poiseuille flow, which is twice the two-phase velocity  $U_{TP}$ . It is also observable that regardless of the capillary number, there is no recirculation near the capillary wall due to the presence of liquid film. Micro particle image velocimetry ( $\mu$ PIV) and fluorescence microscopy techniques were used to characterize micro-scale segmented gas-liquid flows at low superficial velocities in the work of Günther et al. (2004), Trachsel et al. (2005) and Zaloha et al. (2012). In the work of Zaloha et al. (2012), the recirculation in the liquid slug was investigated for low superficial velocities,  $U_G$  and  $U_L$ , between  $0.010$  and  $0.042 \text{ m s}^{-1}$ . These superficial velocities corresponds to a range of  $Ca_{TP}$  between  $1.1 \times 10^{-3}$  and  $4.5 \times 10^{-3}$ . It was demonstrated that in this range, the recirculation velocity,  $U_{rc}$  increases linearly with  $U_{TP}$  and is independent of the ratio  $\frac{U_G}{U_L}$  as presented in Figure 1.26. It was also shown that the recirculation time is proportional to the ratio  $\frac{L_S}{U_{TP}}$  where  $L_S$  is the liquid slug length. Furthermore, the number of fluid revolutions in the liquid slug  $L_S$  was found to be independent of  $U_{TP}$  for a fixed residence time in the microchannel. This last observation suggests that the recirculation performance is mainly due to the liquid slug length rather than the two phase velocity  $U_{TP}$ . The investigation of the recirculation and especially a decrease in the recirculation time allows the interface



**Figure 1.26** – (a) Recirculation velocity  $U_{rc}$  as a function of the superficial velocity ratio  $\frac{U_G}{U_L}$ . (b) Recirculation velocity as a function of the two-phase superficial velocity,  $U_{TP}$ . Taken from Zaloha et al. (2012).

renewal near the bubble caps and mixing performance in the liquid slug to be increased, thereby improving the efficiency of mass transfer in gas-liquid segmented flow.

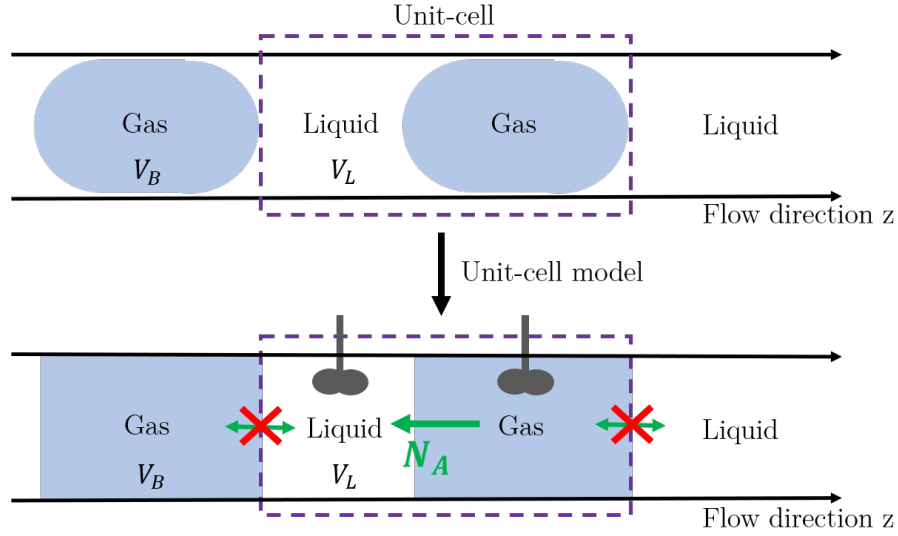
## 1.4 Mass Transfer in Taylor flow

Mass transfer in two-phase segmented flow in microchannels has been widely investigated in the literature under ambient conditions (Irandoost et al. (1992), Baten et al. (2004), Vandu et al. (2005), Garstecki et al. (2006), Sobieszuk et al. (2012), Yao et al. (2015)). The knowledge of the mass transfer behaviour in such systems is interesting for at least two reasons: microsystems can be used as data acquisition tools and as reactors for chemical synthesis.

- Two-phase flow in microchannels can be used for the determination of physical properties that are not scale dependent, e.g. diffusion coefficients, and physical mixture properties when thermodynamic equilibrium is not reached (such as density, viscosity and surface tension)<sup>7</sup>. If these properties are obtained in microsystems, this opens the possibility for extensive data acquisition in short experimental campaigns, for different systems and without high investment cost.
- Microstructured reactors, composed of many microchannels, are developed with the aim to reach reaction or absorption efficiencies that are not possible in macro-scale apparatus. The sizing of these microstructured reactors requires the knowledge of the mass transfer behaviour in single microchannels by the determination of mass transfer coefficients.

It comes from that the need of parameters investigation which can influence the mass transfer in microreactors (Sattari-Najafabadi et al. (2018), Kashid et al. (2011), Haase et al. (2016),

<sup>7</sup>Microsystems are also used to determine thermodynamic solubility data but mass transfer is typically not investigated in such experiments.



**Figure 1.27** – Presentation of the plug flow unit-cell model.

Sobieszuk et al. (2012)).

In this section the plug flow unit-cell model which is widely used in the literature for the determination of mass transfer coefficient in two-phase segmented micro-flow under ambient conditions is presented. After an overview of this model, the correlations of volumetric liquid mass transfer coefficient  $k_L a_L$  based on this model are presented. Furthermore, the high-pressure or moderate pressure studies available in the literature are also described.

### 1.4.1 Plug flow unit-cell model

The plug flow unit-cell model consists in a Lagrangian approach to model segmented flow in a microchannel. A unit-cell is composed of a bubble, a liquid slug and the liquid film surrounding the bubble. In this model, it is supposed that the mass transfer occurs from the gas phase to the liquid phase only. The gas phase is considered as pure and composed of  $A$  molecules. A graphical description of the unit-cell model is presented in Figure 1.27. The unit-cell is considered as moving inside the microchannel at the two-phase velocity  $U_{TP}$  and the hypotheses of ideal plug flow are made as follows:

- pressure and temperature are constant along the microchannel.
- the liquid slug volume  $V_L$  is constant along the microchannel.
- the phases are perfectly mixed (i.e. uniform concentrations in the volumes  $V_L$  and  $V_B$ ).
- there is no mass transfer between two consecutive unit-cells.

Considering these hypotheses, the decrease of the bubble volume  $V_B$  is only due to  $A$  molecules transferring from the pure gas bubble to the liquid slug through the bubble interface. The combined flux (diffusion and convection)  $N_A$  ( $\text{mol.m}^{-2}.\text{s}^{-1}$ ) can be written with the local



mass transfer coefficient  $k_L$  ( $m.s^{-1}$ ) and the mass transfer potential ( $C_A^{L,*} - C_A$ ) where  $C_A^L$  is the A concentration in the liquid phase and  $C_A^{L,*}$  the A concentration in the liquid phase when thermodynamic equilibrium is reached ( $mol.m^{-3}$ ):

$$N_A = k_L(C_A^{L,*} - C_A^L) \quad (1.12)$$

The partial mass balance of A in the liquid volume  $V_L$  gives Equation 1.13, where  $a_L$  is the specific surface equals to the ratio of the bubble surface  $S_B$  over the liquid slug volume  $V_L$ :

$$\frac{dC_A^L}{dt} = k_L a_L (C_A^{L,*} - C_A^L) \quad (1.13)$$

Since the unit-cell is moving at  $U_{TP}$ , Equation 1.13 can be written as a function of  $z$ , the axis-location where  $U_{TP} = dz/dt$ :

$$\frac{dC_A^L}{dz} = \frac{k_L a_L}{U_{TP}} (C_A^{L,*} - C_A^L) \quad (1.14)$$

Equation 1.14 is integrated along the microchannel with length  $L$ . Typically, the product  $k_L a_L$  is assumed to be constant and represents an average of the mass transfer rate between  $z = 0$  and  $z = L$ . The result is presented in Equation 1.15:

$$k_L a_L = \frac{U_{TP}}{L} \ln \left( \frac{C_A^{L,*} - C_A^L(z=0)}{C_A^{L,*} - C_A^L(z=L)} \right) \quad (1.15)$$

### 1.4.2 Volumetric mass transfer coefficient ( $k_L a_L$ ).

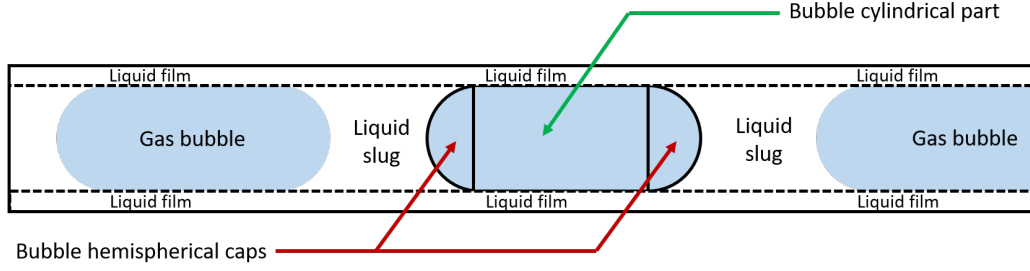
The studies presented in the literature for the determination of mass transfer coefficients in microchannels under ambient conditions are based on the plug flow unit-cell model presented below. The volumetric mass transfer coefficients  $k_L a_L$  are computed with Equation 1.15. The  $k_L a_L$  values are then often correlated as function of dimensionless numbers such as  $Re_L$ ,  $Re_G$ ,  $Ca_L$ ,  $Ca_G$ ,  $Sh_L$  and  $Sc_L$  with the form presented in Equation 1.16.

$$Sh_L a_L d_h = a_1 Re_G^{a_2} Re_L^{a_3} Ca_G^{a_4} Ca_L^{a_5} Sc_L^{a_6} \quad (1.16)$$

$Sh_L = k_L d_h / \mathcal{D}$  is the Sherwood number,  $Sc_L = \mu_L / (\rho_L \mathcal{D})$  is the Schmidt number,  $\mathcal{D}$  is the diffusion coefficient,  $d_h$  is the hydraulic diameter and  $(a_i)_{i=1..6}$  are empirical constants. The volumetric mass transfer coefficient correlations under ambient conditions are numerous; some have been selected and are presented in Table 1.5 and 1.6 at the end of this section<sup>8</sup>. The remainder of this paragraph presents the works which have founded different methods for the determination of the volumetric mass transfer coefficient. The studies are presented in chronological order since the knowledge on the determination of volumetric mass transfer coefficient was developed step by step.

---

<sup>8</sup>Note that studies on two-phase segmented flow where a chemical reaction is investigated are not presented in this thesis work.



**Figure 1.28** – Bubble decomposition in one cylindrical part and two hemispherical caps in a two-phase segmented flow.

The methods used to determine volumetric mass transfer coefficients can be classified into three classes:

- Inlet-outlet methods: The liquid phase is sampled at the outlet of the system and an average volumetric mass transfer coefficient  $k_L a_L$  is calculated with Equation 1.15 from the unit-cell model.
- Online methods: The gas dissolution in the liquid phase is followed by laser induced fluorescence (LIF), colorimetric or shadowgraphy techniques and the volumetric mass transfer coefficient  $k_L a_L$  is also obtained with Equation 1.15. These techniques allow quantification of mass transfer that occurs at different locations in the microchannel, including during the bubble generation process.
- Modelling work: The volumetric mass transfer coefficient is calculated using CFD to solve the Navier-Stokes equations and the convection-diffusion equation with the knowledge of diffusion coefficient<sup>9</sup>.

The first work on the determination of mass transfer coefficients in gas-liquid slug conditions in small tubes started in 1963 with the work of Heuven et al. (1963) where  $\text{CO}_2$  absorption in Taylor flow inside a gas lift was investigated. The mass transfer resistance in the aqueous phase for a unique bubble was studied. The following major study in the domain was oxygen absorption into water-ethanol-ethylene glycol mixtures in Taylor flow through a capillary (Irandoost et al. (1992)). The authors developed a semi-theoretical convection-diffusion model correlating mass transfer coefficients with liquid concentrations at the inlet and the outlet of the microreactor. In this study, the plug flow unit-cell model was used. A few years later, Bercic et al. (1997) proposed a correlation for the volumetric mass transfer coefficient in the liquid phase  $k_L a_L$  in the context of absorption of methane into water as a function of the two-phase velocity  $U_{TP}$ , the bubble and slug lengths  $L_B$ ,  $L_S$  and the gas void fraction  $\epsilon_G$ . This correlation is presented in Equation 1.17. The bubble is decomposed into a cylindrical part, which is in contact with the liquid film surrounding the bubble, and two hemispherical caps, which are in contact with the liquid slug, as presented in Figure 1.28. The authors

<sup>9</sup>Note that this is typically a poor method because accurate simulation of concentration gradients requires extremely fine computational grids which is computationally very expensive. The results in a majority of the papers in the literature are poor as they are not mesh independent.

supposed that the liquid film was rapidly saturated with methane. Hence, the mass transfer at the cylindrical part was considered negligible compared with the mass transfer at the bubble caps. The correlation presents two drawbacks: the hydraulic diameter  $d_h$  is not taken into account (which is considered incorrect in later studies) and the diffusion coefficient does not appear in the correlation. This correlation is therefore valid for methane-water system only.

$$k_L a_L = \frac{0.133 U_{TP}^{1.2}}{((1 - \epsilon_G)(L_B + L_S))^{0.57}} \quad (1.17)$$

Later, Heiszwolf et al. (2001) proposed a correction to the previous correlation. A non-linear regression with air-water systems was proposed and the influence of the diffusion coefficient between air and water was taken into account. The corrected correlation is presented in Equation 1.18.

$$k_L a_L = \frac{0.133 U_{TP}^{1.2}}{\sqrt{L_S}} \left( \frac{\mathcal{D}_{O_2}}{\mathcal{D}_{CH_4}} \right)^\alpha \quad 0.5 < \alpha < 1 \quad (1.18)$$

Later, Baten et al. (2004) proposed a CFD semi-empirical model for air-water systems based on the Higbie's penetration theory for mass transfer through bubble caps and a laminar falling film expression for mass transfer through the cylindrical part of the bubble in contact with the liquid film. They showed that the contribution of mass transfer through the cylindrical part is non-negligible and can dominate that at the caps. This model takes into account the diffusivity and the hydraulic diameter. They proposed different correlations depending on the contact time between the liquid film and the bubbles in the microchannel as presented in Table 1.5 at the end of this section. The greater the ratio between the bubble length and the unit-cell length ( $L_B/(L_B + L_S)$ ), the longer the contact time between the liquid film and the bubble. The Fourier number  $Fo = \mathcal{D} t_{film} / \delta_{film}^2$  was also employed to quantify this; if  $Fo \ll 1$ , the liquid film is rapidly saturated and mass transfer through the cylindrical part of the bubble is negligible. This statement confirms the experimental results of Bercic et al. (1997) where the mass transfer through the liquid film was neglected since the experiments were performed with long bubbles and shorter liquid slugs. The main drawback of this model is the correlation used for the liquid film thickness and the hemi-spherical form of the bubble caps, both of which lead to an overestimation of the mass transfer coefficient. Indeed, in square or rectangular microchannels, the thickness of the liquid film is not uniform over the cross-section of the channel and is, not easily measured or easy to predict. In addition, the shape of the bubble caps can differ depending on the system studied and the operating conditions; very often they are significantly different from the ideal hemi-spherical shape.

Baten et al. (2004) concluded that mass transfer through the liquid film cannot be always neglected and this was confirmed by the work of Vandu et al. (2005) using air-water experiments. It was found that the contact time between the liquid film and the bubble is short enough to obtain a predominant mass transfer through cylindrical part of the bubble. This agreed with the CFD model of Baten et al. (2004). Vandu et al. (2005) also showed that in the experimental setup of Bercic et al. (1997), the liquid film was also saturated by reproducing the experiments at the same conditions.

---

Yue et al. (2007) proposed a correlation between the mass transfer coefficient and the pressure drop along a two-phase segmented flow of  $H_2O$  and  $CO_2$  as shown in Equation 1.19. The pressure drop is calculated using the Lockhart-Martinelli equation (Kawahara et al. (2002), Fries et al. (2008a)) which takes the contributions of both phases into account. When mass transfer from the  $CO_2$  bubbles to the  $H_2O$ -rich phase is significant, the bubble size decreases as well as the gas holdup in the microchannel. A lower gas fraction leads to higher pressure drop. Thus, the higher the pressure drop, the greater the volumetric mass transfer coefficient. The plug flow unit-cell model was also employed and a dimensionless empirical correlation was proposed as presented in Equation 1.20. Two years later, the same authors proposed an alternate correlation of  $k_L a_L$  as function of  $d_h$ ,  $L_B$ ,  $L_S$ ,  $\mathcal{D}$  and  $U_B$  for a segmented flow of air and  $H_2O$  (Yue et al. (2009)). However, this type of correlation is less useful since  $k_L a_L$  is a function of  $U_B$ ,  $L_B$  and  $L_S$ , all of which must be measured experimentally.

$$k_L a_L = 0.0863 \left( \frac{\Delta P_F}{L} \right)^{0.881} \quad (1.19)$$

$$Sh_L a_L d_h = 0.084 Re_G^{0.213} Re_L^{0.937} Sc_L^{0.5} \quad (1.20)$$

D. Liu et al. (2011) employed the model of Baten et al. (2004) and prompted to a dimensionless regression of  $k_L a_L$ . The results show that  $k_L a_L$  increases with the increase of the film length  $L_{film}$ ,  $\mathcal{D}$  and  $U_B$  whilst it decreases with increasing  $L_S$ ,  $d_h$  and  $\delta_{film}$ . They showed that when the liquid slug is short enough, recirculation rate inside the liquid phase increases, as does mass transfer. On the other hand, if the liquid slug is too short, the liquid is rapidly saturated. As presented in Section 1.3.2, the characterization of "short enough" for the recirculation process in the liquid slug depends on the system studied. The criterion that characterizes the liquid recirculation rate is the dimensionless capillary number.

Numerous studies investigated the change in bubble size due to mass transfer of a two-phase segmented flow in microreactors (Heiszwolf et al. (2001), Musterd et al. (2015), Jia et al. (2016), Kreutzer et al. (2005), R. Sun et al. (2011), Molla et al. (2013) and Tan et al. (2012)). Tan et al. (2012) proposed to link the mass transfer coefficient with the decrease in bubble size for a  $CO_2/N_2$  - NaOH aqueous solution system using the unit cell model and the ideal gas law. They found that the mass transfer in the bubble formation stage is about 30-40% of the global mass transfer. Kuhn et al. (2012) proposed an online pH-sensitive laser induced fluorescence (LIF) technique in order to evaluate the change in  $CO_2$  concentration in alkaline solutions along the length of the microreactor. They used the unit cell model to calculate  $k_L a_L$  and compared their values for several slug lengths ( $L_S$ ) with values in the literature (Bercic et al. (1997), Vandu et al. (2005), Yue et al. (2007) and Baten et al. (2004)). The predictions of these correlations were not in good agreement for low gas void fractions  $\epsilon_G$  but acceptable for  $\epsilon_G > 0.6$ .

Lefortier et al. (2012) also evaluated  $k_L a_L$  by linking the decrease of bubble size in various solvents with  $CO_2$  gas dissolution. They obtained diffusion coefficients using a model based on Baten et al. (2004) work that was calibrated with a binary system where the diffusion coefficient was already known. In addition, the variation of the gas density due to the pressure drop along the microchannel was taken into account. Eskin et al. (2012) performed CFD simulations with a model that was also based on the work of Baten et al. (2004). However, mass transfer through the liquid film was calculated by solving the convection-diffusion equation instead of using the falling film theory. In addition, the pressure drop along the reactor was taken into account as a linear law in the same way as Lefortier et al. (2012) and Henry's law was used to calculate the saturation concentration of gases (methane and decane) in water.

Dietrich et al. (2013) proposed an online colorimetric method to study oxygen absorption with the model of Baten et al. (2004). The experimental values of  $k_L a_L$  differ from the model but according to the authors, this discrepancy is due to mass transfer during the bubble formation step that is not depicted by the model of Baten et al. (2004). This experimental results show that mass transfer during bubble formation is approximately 30-40% of the whole mass transfer process, which is a similar result to that of Tan et al. (2012). Yao et al. (2014a) obtained  $k_L a_L$  by analysing the decrease in bubble size using a high-speed camera. Their results show however that the contribution of the bubble generation process to the entire mass transfer process is only about 2-10%. This difference can be explained by the duration of the bubble formation stage, which is only several milliseconds compared with 0.3 s in the work of Tan et al. (2012). Furthermore, in the work of Ganapathy et al. (2014) and Abolhasani et al. (2015) who carried out experiments in the same conditions as Yao et al. (2014a), the same order of magnitude for the formation stage contribution to the mass transfer (2-10%) has been found. These studies show that the inlet geometry and the bubble formation regime (squeezing or shearing) significantly influence the mass transfer process. Indeed, in order to design for process intensification, these parameters should be investigated.

Zhu et al. (2014) and Yao et al. (2015) proposed to use the plug flow unit-cell model and the ideal gas law ( $PV = nRT$ ) to express the bubble length along the reactor as a function of the axial location  $z$  and the volumetric mass transfer coefficient  $k_L a_L$ . In addition, the bubble is considered as a cylinder of volume  $V_B = L_B A$  where  $A$  is the cross section of the microchannel. The bubble length  $L_B$  is expressed by Equation 1.21, where  $A_1$  is the final length,  $A_1 + A_2$  is the initial length of the bubble right after the bubble generation process and  $A_3 = -k_L a_L z / U_{TP}$ .

$$L_B = A_1 + A_2 \exp(-A_3 z) \quad (1.21)$$

Using this equation, Zhu et al. (2014) and Yao et al. (2015) determined the volumetric mass transfer coefficient via the regression of the bubble length that was measured along the microchannel.

**Table 1.5** – Theoretical model, empirical model and dimensionless regression of the liquid mass transfer coefficient in a gas-liquid Taylor flow in microchannel (*order of publication date*).

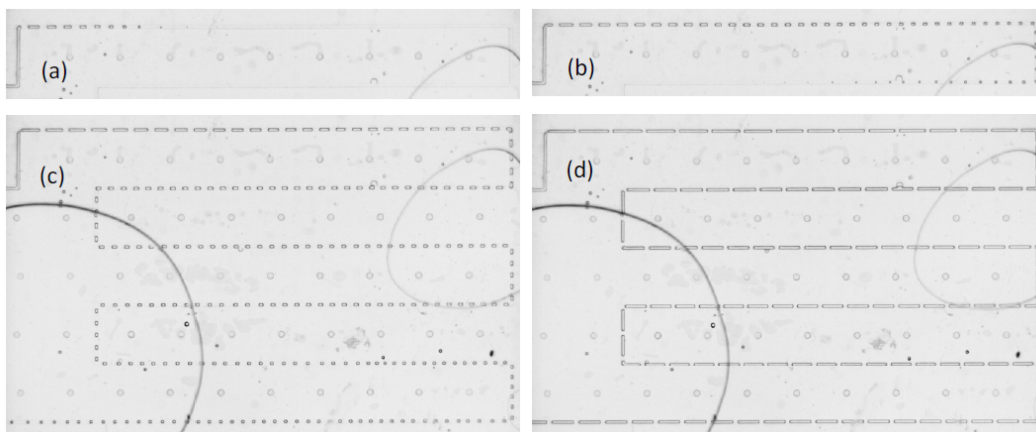
Authors & Year	BST <sup>a</sup> Cases	List of the system substances	Operating conditions	Microdevice specifications	
				Main equations of the mass transfer model	Short note and $k_L a_L$ values.
Irandoust et al. 1992	V	O <sub>2</sub> - H <sub>2</sub> O - Ethanol - Ethylene	Ambient	Capillary 1.5 and 2.0 mm ID	Convection diffusion semi-empirical model with inlet/outlet concentration data. $k_L a_L \in [0.02, 0.32](s^{-1})$ .
Bercic and Pintar 1997	V	CH <sub>4</sub> - H <sub>2</sub> O	Ambient	Capillary 1.5, 2.5 and 3.1 mm ID	Non linear regression based on the unit cell model with inlet/outlet concentration data. $k_L a_L \in [0.005, 0.26](s^{-1})$ .
Heiszwolf et al. 2001	V	O <sub>2</sub> - H <sub>2</sub> O	Ambient	Square channel 1.5 mm	Non linear regression based on the unit cell model with inlet/outlet concentration data. $k_L a_L \in [0.4, 1](s^{-1})$ .
van Baten and Krishna 2004	V	CH <sub>4</sub> - H <sub>2</sub> O	Ambient	Capillary 1.5, 2.5 and 3.1 mm ID	CFD semi-empirical model based on penetration theory and laminar falling film model. $k_L a_L \in [0.04, 0.25](s^{-1})$ .
Vandu et al. 2005	V	Air - H <sub>2</sub> O	Ambient	Capillary 1, 2 and 3 mm ID, Square channel 1 and 3 mm	Unit cell model with inlet/outlet concentration data and van Baten and Krishna film model. $k_L a_L \in [0.01, 0.8](s^{-1})$ .
Yue et al. 2007	V	CO <sub>2</sub> - H <sub>2</sub> O	Ambient	Channel 1 mm × 0.5 mm	Unit cell model with inlet/outlet concentration data, dimensionless empirical correlation and link with pressure drop. $k_L a_L \in [0.6, 21](s^{-1})$ .
Yue et al. 2009	V	Air - H <sub>2</sub> O	Ambient	Square Channel 200 μm and 400 μm	Unit cell model with inlet/outlet concentration data and non linear regression. $k_L a_L \in [3, 9](s^{-1})$ .
Liu and Wang 2011	V	CH <sub>4</sub> - H <sub>2</sub> O	Ambient	Capillary 1.5, 2, 2.5 and 3 mm ID	CFD studies with Baten et al. 2004 model and dimensionless empirical correlation. $k_L a_L \in [0.1, 2.2](s^{-1})$ .
Kuhn and Jensen 2012	V	CO <sub>2</sub> - alkaline solution	Ambient	Square channel 400 μm	Online pH-sensitive LIF technique, Unit cell model. $k_L a_L \in [0.05, 0.85](s^{-1})$ .

<sup>a</sup> The Bubble Size Trend Cases corresponds to the binary system classification presented in Chapter 2.

**Table 1.6** – Theoretical model, empirical model and dimensionless regression of the liquid mass transfer coefficient in a gas-liquid Taylor flow in microchannel (*order of publication date*).

<i>Ren et al.</i> 2012	V	O <sub>3</sub> - H <sub>2</sub> O - PCP	Ambient	Channel 400 μm × 500 μm
		$Sh_L a_L d_h = 0.02469 Re_G^{0.3245} Re_L^{0.7764} Sc_L^{0.5}$		Unit cell model with inlet/outlet concentration data and dimensionless empirical correlation. $k_L a_L \in [0.3, 7.5](s^{-1})$ .
<i>Lefortier et al.</i> 2012	IV	CO <sub>2</sub> - various solvents	Ambient	Hemicylindrical channel 91 μm ID
		$k_L a_L = 1.19 \sqrt{\frac{\mathcal{D} U_B}{d_h L_S^2}} + 0.65 \frac{L_B}{L_S} \sqrt{\frac{\mathcal{D} U_B}{d_h^2 L_B}}$		Bubble Shrinkage linked with the mass transfer, unit cell model. no $k_L a_L$ value.
<i>Eskin and Mostowfi</i> 2012	IV	CH <sub>4</sub> - H <sub>2</sub> O, C <sub>10</sub> H <sub>22</sub> - H <sub>2</sub> O	3 MPa	Capillary 25 to 200 μm
		$k_L a_L = \frac{2\pi \left(R_c - \frac{\delta_{film}}{2}\right) U_B (C_0 - C_m) \delta}{(C_0 - C^*) (V_L + V_B)} + \frac{4\pi R_B^2 k_{Lcap}}{(C_0 - C^*)}$ with $k_{Lcap}$ from Baten et al. 2004		CFD semi-empirical model based on penetration theory and convection-diffusion equation. $k_L a_L \in [19, 180](s^{-1})$ .
<i>Dietrich et al.</i> 2013	V	O <sub>2</sub> - H <sub>2</sub> O + resazurin	Ambient	Square channel 2 mm
		$k_{Lcap} a_{Lcap} = \frac{8}{L_{UC}} \sqrt{2 \frac{\mathcal{D} U_B}{\pi^2 d_h}}$ $k_{Lfilm} a_{Lfilm} = \frac{2}{L_{UC} d_h} \sqrt{\frac{2 \mathcal{D} U_B (L_B - d_h)}{\pi^2}}$		Online colorimetric method, concentrations fields. $k_L \in [1.55, 5.49](\times 10^{-4} ms^{-1})$ .
<i>Yao et al.</i> 2014	V	CO <sub>2</sub> - H <sub>2</sub> O - Ethanol	Ambient	Channel 300 μm × 150 μm
		$Sh_L a_L d_h = 1.367 Re_G^{0.421} Re_L^{0.717} Sc_L^{0.640} Ca_{TP}^{0.5}$		Bubble Shrinkage linked with the mass transfer, unit cell model. $k_L a_L \in [1, 6](s^{-1})$ .
<i>Yao et al.</i> 2015	V	CO <sub>2</sub> - H <sub>2</sub> O	3 MPa	Square channel 300 μm
		$Sh_L a_L d_h = 0.094 Re_G^{0.0656} Re_L^{0.654} Sc_L^{1.449} Ca_{TP}^{0.839}$		Bubble Shrinkage linked with the mass transfer, unit cell model. $k_L a_L \in [1, 6](s^{-1})$ .
<i>Yao et al.</i> 2017	IV	CO <sub>2</sub> - H <sub>2</sub> O	4 MPa	Square channel 300 μm
		$k_L a_L = 0.239 \left(\frac{\varepsilon_L}{\Delta P_L}\right)^{0.352} \left(\frac{\varepsilon_G}{\Delta P_G}\right)^{0.648} Re_L^{-0.146} Re_G^{-0.129}$ (without reaction) $k_L a_L = 67 \sqrt{\frac{\eta_{DEA}}{\eta_{CO_2}}} \left(\frac{\varepsilon_L}{\Delta P_L}\right)^{0.824} \left(\frac{\varepsilon_G}{\Delta P_G}\right)^{0.176} Re_L^{0.355} Re_G^{-0.638}$ (with reaction)		Pressure loss model and dimensionless correlation. $k_L a_L \in [0.5, 3.8](s^{-1})$ .

<sup>a</sup> The Bubble Size Trend Cases corresponds to the binary system classification presented in Chapter 2.



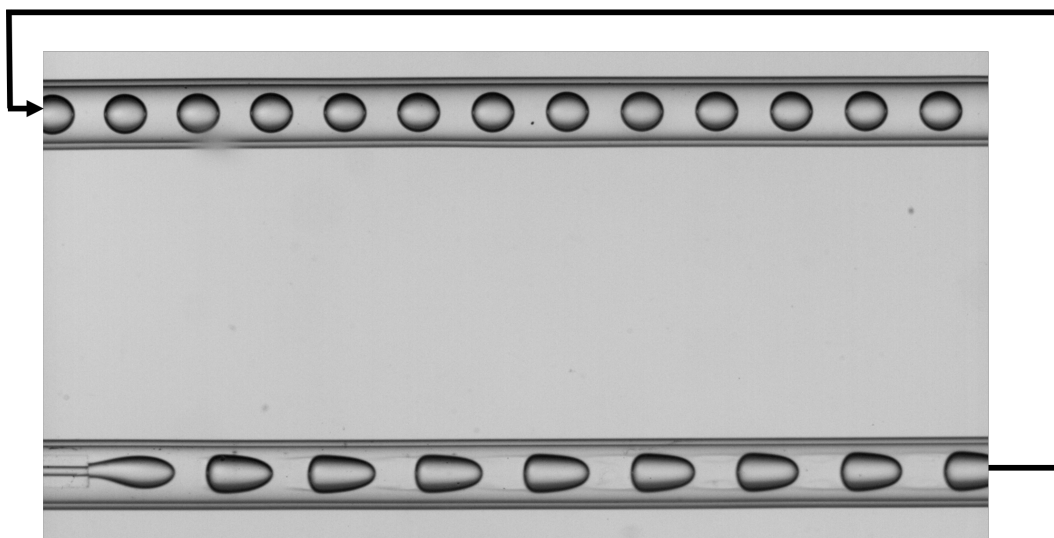
**Figure 1.29** –  $CO_2$ - $EtOH$  segmented flows at 4.3 MPa, 313 K. (a,b) the single-phase zone is reached (c) flow near the bubble point (d) flow stabilized in the gas-liquid zone, taken from Martin et al. (2018).

### 1.4.3 High-pressure mass transfer studies in two-phase segmented micro-flows

The hydrodynamics and mass transfer behaviour of gas-liquid segmented micro-flow at high pressure may be noticeably different than that at atmospheric conditions. The first difference concerns the solubility of the gas in the liquid which can be significantly greater at high pressure than at atmospheric pressure. This difference can lead to a faster decrease in bubble length along the microchannel and can even result in total bubble dissolution. The ambient pressure mass transfer models do not take into account the impact of pressure on solubility. In the work of Martin et al. (2018), segmented flows of  $CO_2$  and  $EtOH$  were investigated at 4.3 MPa and 313 K in a square microchannel ( $200\text{ }\mu\text{m} \times 200\text{ }\mu\text{m}$ ) with a total length of 12.5 cm, which is presented in Figure 1.29. Depending on the flow rates, different flow types were obtained including Taylor flow, dissolving Taylor flow, and also total bubble dissolution after a certain length of microchannel. In this binary fluid system, the  $CO_2$  dissolves in the  $EtOH$ -rich phase and the  $EtOH$  dissolves in the  $CO_2$ -rich phase. It is therefore not possible to evaluate the amount of gaseous  $CO_2$  that dissolves in the liquid phase by observing the decrease in bubble size.

The nitrogen-water binary has been investigated by Yao et al. (2014c) and Y. Zhao et al. (2013) at high-pressure (3 MPa and 5 MPa respectively). Nitrogen obeys the ideal gas law at these pressures and water is not soluble in nitrogen phase. Hence, the models of Zhu et al. (2014) and Yao et al. (2015), that were previously presented, can be applied in this case. Another binary system studied at high pressure is  $CO_2$ -water due to its interest in fields such as geology and green chemistry (Marre et al. (2009), Ogden et al. (2014)). At pressure above the critical point of  $CO_2$ ,  $CO_2$  does not follow the ideal gas law and therefore a specific thermodynamic model is required to relate the decrease in bubble volume shrinkage to  $CO_2$  dissolution in the  $H_2O$ -rich phase (Diamond et al. (2003), Aasen et al. (2017)).





**Figure 1.30** –  $CO_2$ - $BMimPF_6$  segmented flow at 11.4 MPa, 313 K,  $\dot{V}_{BMimPF_6} = 90 \mu\text{L min}^{-1}$ ,  $\dot{V}_{CO_2} = 111 \mu\text{L min}^{-1}$  taken from Macedo Portela da Silva et al. (2014).

The other major change associated with two-phase flows at high-pressure is the modification of the physical properties of the liquid and gas phases. Indeed, since gases are more soluble in liquids at high pressure than at atmospheric pressure, a larger amount of dissolved gas is present in the liquid phase at the thermodynamic equilibrium. This can lead to significant modifications of the liquid density and viscosity compared with those of the pure liquid. Hence, between the contacting zone at the inlet of the microchannel and the microchannel zone where the equilibrium is reached, non-negligible density and viscosity differences can be observed.

In the work of Macedo Portela da Silva et al. (2014), where a segmented flow of  $CO_2$  and an ionic liquid ( $BMimPF_6$ ) is studied, the liquid density increases 1.7 times and viscosity decreases by a factor 12 between the contacting zone and the equilibrium zone. Figure 1.30 shows the two phase segmented flow of  $CO_2$  and  $BMimPF_6$  at high pressure in a microcapillary. It can be seen that the bubble shape is different to the well-known cylindrical bubble with two hemispherical caps. In addition, the liquid film around the bubble is relatively thick and is not constant along the capillary. The recirculation in the bulk of the liquid slug can easily be seen due to the viscosity gradient between the zones that are highly concentrated in  $CO_2$  and those that have low concentration. The two-phase segmented flow studies at high-pressure showed that the characteristics of the flow due to high pressure (i.e. different bubble shapes, high mutual solubility, physical properties change along the microchannel, non ideal gas phase<sup>10</sup>..) make the plug flow unit-cell model inappropriate for the determination of volumetric mass transfer coefficient. Furthermore, the volumetric mass transfer coefficient at ambient pressure is often averaged between the inlet and the outlet of the microchannel. However, according to the literature, the mass transfer rate seems to be more significant in the bubble generation process. The development of a mass transfer model

<sup>10</sup>Except for the studies involving the use of nitrogen since the ideal gas law is still valid at higher pressures.

---

that takes the bubble generation zone into account therefore seems to be more appropriate (i.e. when the volumetric mass transfer coefficient  $k_L a_L$  is obtained at different axis location of the microchannel).

## Conclusion

Processes using supercritical fluids are increasingly investigated in the chemical engineering field and new designs and fluids are explored with an aim of process intensification. The improvement of such processes is directly linked to the understanding of the phenomena involved and how they are modelled. In particular, the contact between a liquid phase and a supercritical fluid that takes place in the PGSS, RESS and SAS processes has to be modelled. The modelling of such process steps requires detailed knowledge of the fluid properties at saturation (e.g. mutual solubility, density, viscosity, surface tension) but also during unsteady state (e.g. diffusion coefficient). However, the knowledge of such two-phase properties is costly due to the high-pressure work conditions of conventional measurement apparatus.

Microfluidics, which is the study of micro-scale flow behavior, provides a means to determine thermodynamic properties rapidly. Under ambient conditions, microfluidic systems have shown to be effective for the measurement of saturation and unsteady state properties, such as mutual solubility and diffusion coefficients in two-phase systems. However, the investigation of such systems at high pressure is scarce in the literature. Studies concerning the measurements of properties at saturation are available, however, few works have dealt with the behavior of unsteady states. Two-phase segmented flow seems to be the most adapted flow regime for mass transfer investigations in microchannel due to its regular hydrodynamics. The volumetric mass transfer coefficient, which is an indicator of the mass transfer rate, has been widely studied under ambient conditions with the plug flow unit-cell model. However, this model has to be adapted to the behavior of high-pressure two-phase flows. This means that mass transfer models must be adapted for use with two-phase segmented flow at high pressure such that the impact of pressure on the physical properties of the fluids is accounted for.

The main objective of this thesis work is therefore to provide a model and experimental methods for the determination of the volumetric mass transfer coefficient in two-phase micro-flows at high pressure. The model has to take into account the effects of high pressure on the physical properties of the fluids and their evolution during the mass transfer process.

# Thermodynamics and mass transfer in high-pressure microchannel flows

Introduction . . . . .	61
2.1 Changes in bubble volume in high-pressure flows . . . . .	62
2.2 Thermodynamic study of $CO_2$ - $H_2O$ , $CO_2$ - $EtOH$ and $CO_2$ - $BMimPF_6$ systems . . . . .	65
2.2.1 Mutual solubility of $CO_2$ - $H_2O$ , $CO_2$ - $EtOH$ and $CO_2$ - $BMimPF_6$ systems . . . . .	66
2.2.2 Physical properties of pure water, carbon dioxide, $EtOH$ and $BMimPF_6$ at high-pressure . . . . .	71
2.2.3 Physical properties of $CO_2$ - $H_2O$ , $CO_2$ - $EtOH$ and $CO_2$ - $BMimPF_6$ mixtures . . . . .	75
2.2.4 Impact of evolving physical properties along the microchannel . . . . .	82
2.3 Mass transport modelling . . . . .	82
2.3.1 Two-phase mass transport . . . . .	83
2.3.2 Mass transfer model for high-pressure two-phase segmented micro-flow . . . . .	86
2.4 Conclusion . . . . .	91

## Introduction

This chapter presents a mass transfer model for the determination of local mass transfer coefficients in high pressure two-phase segmented flow in microchannels. The bases of such a model and the hypotheses made are highly dependent on the properties of the fluids, i.e. the binary system, studied. As an example, a binary system in which the fluids are highly soluble in one another requires different hypotheses and terms in the model than for a system where the compounds are weakly soluble in one another. The model presented in this chapter describes mass transfer in a high pressure two-phase segmented flow of  $CO_2$  and  $H_2O$ , where  $CO_2$  is soluble in  $H_2O$  but  $H_2O$  very weakly soluble in  $CO_2$ . However, the model will also be discussed for two additional binary systems,  $CO_2$ - $EtOH$  and  $CO_2$ - $BmimPF_6$ , which have

---

different solubility behaviour. The idea is to demonstrate how the model can be adapted for the determination of the volumetric mass transfer coefficient at high pressure of different binary systems based on their thermodynamic properties. This demonstration is given in three steps:

- Firstly, a qualitative analysis of the change in bubble volume in a two-phase segmented flow in a microchannel is carried out. Depending on the mutual solubility of the compounds employed and on pressure drop along, the bubble may shrink or expand, or a combination of both. In order to understand this change in bubble volume, impact of mass transfer and pressure drop have to be analysed separately.
- Secondly, the thermodynamics of the binary system is investigated. This includes the quantification of the mutual solubility of the fluids, as well as the change in physical properties as solubility occurs and when equilibrium is reached. The physical properties of interest are the fluid<sup>1</sup> and liquid pure properties (density, viscosity), the mixture properties of the liquid phase (liquid mixture density and viscosity) and the interfacial tension between the phases.
- Finally, a "unit-cell"-type mass transfer model is developed that considers the high-pressure specificities of a binary system composed of  $CO_2$  and  $H_2O$  for the determination of liquid volumetric mass transfer coefficient. The hypotheses of this model are discussed for the other two binary systems  $CO_2$  and  $EtOH$ , and  $CO_2$  and an ionic liquid,  $BMimPF_6$ .

The discussion of the additional binary systems, which are not investigated experimentally in this thesis work, enables the adequacy of the hypotheses in the mass transfer model to be evaluated and identification of when and how they need to be adapted.

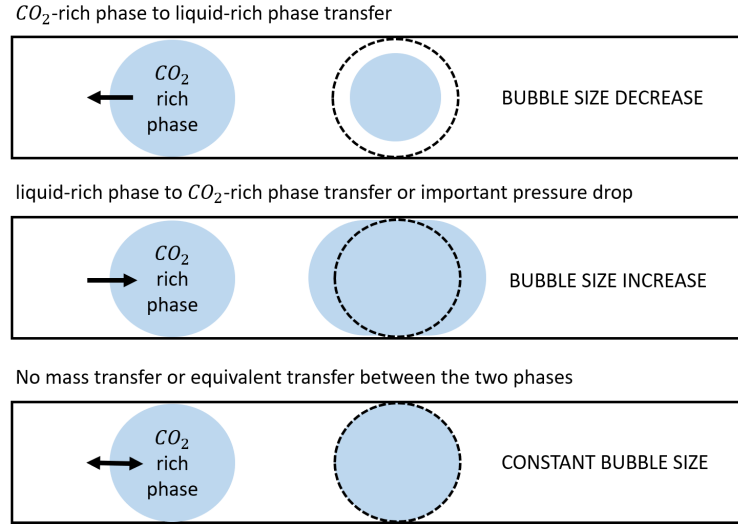
## 2.1 Changes in bubble volume in high-pressure flows

For the sake of simplicity, from here on the term "bubble" designates both bubbles and drops since the dispersed phase can be in either the liquid or gas state, depending on the temperature and pressure. In the following, a high-pressure two-phase segmented flow in a microchannel is considered. The flow is composed of regular sized bubbles, which are separated by liquid slugs and surrounded by a liquid film. In such flows, several phenomena can impact the bubble and the liquid slug sizes. In the case of a binary system composed of  $CO_2$  and a liquid, several scenarios for a change in bubble size are presented in Figure 2.1:

- The bubble size may decrease if the  $CO_2$  is soluble in the continuous liquid rich-phase and the liquid is not soluble in the  $CO_2$ -rich phase.

---

<sup>1</sup>The term fluid corresponds to the carbon dioxide since in the range of pressure and temperature studied, the carbon dioxide can be either liquid, gas or in a supercritical state.



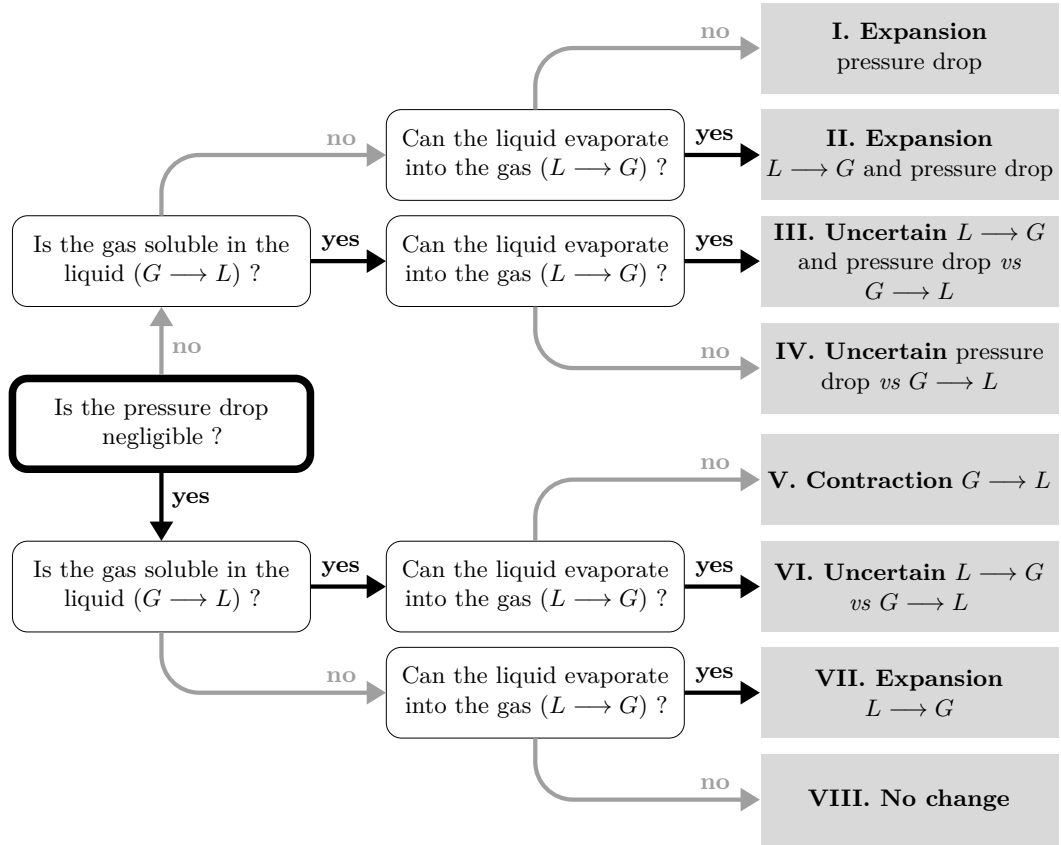
**Figure 2.1** – Mass transfer phenomena and pressure drop affecting the bubble size in a two-phase segmented micro-flow.

- The bubble size may increase if the liquid is soluble in the  $CO_2$ -rich phase and the  $CO_2$  is insoluble in the liquid phase and/or if there is a significant pressure drop along the channel<sup>2</sup>.
- The bubble may remain constant in size if there is no mass transfer between the phases, if the mass transfer from the  $CO_2$ -rich phase to the liquid and vice versa are strictly equivalent in terms of volume, or if the decrease in bubble size due to mass transfer from the  $CO_2$ -rich phase to the liquid is balanced by an increase in bubble size due to pressure drop.

For the first two cases presented above, the changes in bubble size can be observed and quantified to determine the mass transfer rate between the two phases, and therefore for the determination of volumetric mass transfer coefficient. However, when two opposing phenomena occur, e.g. transfer of the  $CO_2$ -rich phase to the liquid-rich phase at the same time as the transfer of the liquid phase to the  $CO_2$ -rich phase, it is not possible to easily predict the change in bubble size along the microchannel nor link it to mass transfer. Figure 2.2 presents a flow chart for the change in bubble size as a function of the mutual solubility of the binary systems and as a function of the potential pressure drop along the microsystem.

- In the case of the  $CO_2$ - $H_2O$  system and considering that pressure drop is negligible, the  $CO_2$  is soluble in the  $H_2O$ -rich phase and the  $H_2O$  is only weakly soluble in the  $CO_2$ -rich phase, which corresponds to the case V. It is predictable that the  $CO_2$  bubble size will decrease along the microsystem. When the pressure drop is non-negligible, case IV occurs: the change in bubble size is not predictable. If pressure drop is significant, the increase in bubble size due to the pressure drop counteracts the decrease in size due to mass transfer from the gas to the liquid phase.

<sup>2</sup>The pressure decrease reduces the gas density. This reduction for a constant mass in the gas bubble leads to an increase in volume.



**Figure 2.2** – Expected outcome (grey boxes) of the change in bubble size in a two-phase segmented micro-flow depending on the thermodynamics of the binary system and the pressure drop.

- In the case of the  $CO_2$ - $EtOH$  system, both fluids are mutually soluble in one another. This change in bubble size for such a system corresponds to cases III and VI with and without pressure drop respectively. In both cases, the expected change of bubble size is uncertain without investigation of the solubilities.
- For the  $CO_2$ - $BMimPF_6$  system,  $CO_2$  is soluble in the  $BMimPF_6$ -rich phase whereas the  $BMimPF_6$  is not soluble in the  $CO_2$ -rich phase. Therefore if pressure drop is negligible, the bubble size is expected to decrease (case V), whilst if the pressure drop is non-negligible, there is a competition between gas expansion due to pressure drop and bubble shrinkage due to mass transfer from the gas to the liquid. As a result the change in bubble size is uncertain (IV).

The Figure 2.2 shows that in many cases, there is competition between bubble expansion and shrinkage due to different phenomena. Therefore knowledge of the how the bubble size changes along the microchannel does not necessarily enable the mass transfer rate between the two-phases of a segmented flow to be quantified and is therefore not sufficient for the determination of mass transfer coefficient in many cases.

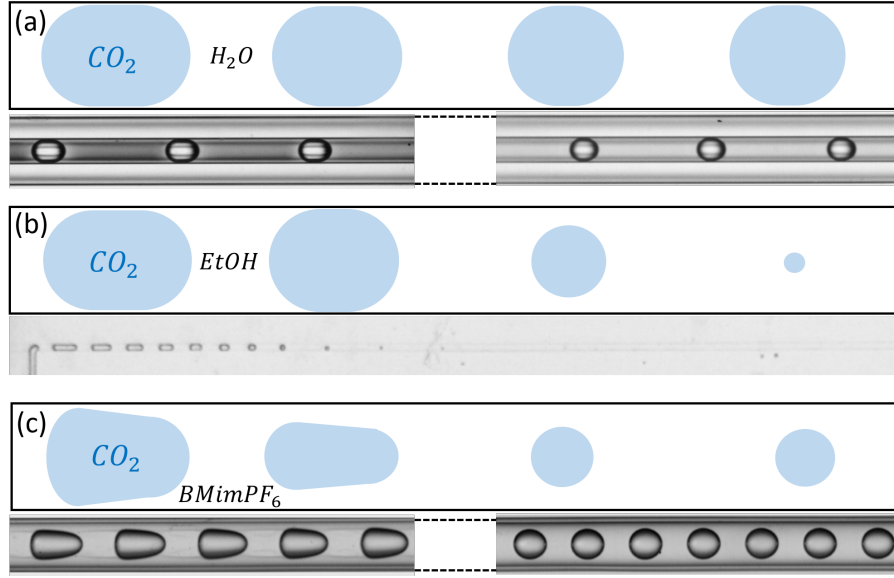
This is even more so when the experiments are performed at high pressure. Indeed, the models based on the bubble shrinkage link the bubble volume to a number of moles via the density of the gas mixture<sup>3</sup>. At high pressure, the mixture density can significantly change in both phases along the micro-channel due to the increased solubility of gas into liquids. Therefore knowledge of rate of decrease of the bubble volume is not sufficient for the determination of mass transfer coefficients. Indeed, it is necessary that the change in properties of the two phases are taken into account in the global modelling of mass transfer. Figure 2.3 depicts the change in bubble size for the three binary systems,  $CO_2$ - $H_2O$ ,  $CO_2$ - $EtOH$  and  $CO_2$ - $BMimPF_6$ . Figure 2.3 (a) shows the  $CO_2$ - $H_2O$  system flowing in a silica microcapillary at 10 MPa and 303 K. It can be seen that the bubble shrinks only slightly due to the low solubility of  $CO_2$  in the  $H_2O$ -rich phase. On the other hand, a significant change in size and shape of  $CO_2$  bubbles is observed for the  $CO_2$ - $EtOH$  system at 4.3 MPa and 313 K due to high solubility of  $CO_2$  inside the  $EtOH$ -rich phase. For the  $CO_2$ - $BMimPF_6$  system at 11.4 MPa and 313 K, the high solubility of  $CO_2$  in the  $BMimPF_6$ -rich phase leads to a significant decrease in bubble size. In addition, the bubble changes from a bullet shape to a sphere. This change is due to the strong decrease in the viscosity of the continuous  $BMimPF_6$ -rich phase when the  $CO_2$  dissolves into it and the decrease in volume of the gas phase.

In order to integrate the different specificities of high-pressure two-phase flows (physical properties change, higher gas solubility into liquids..), it is necessary that different modelling approaches are developed. These specificities render the investigation of mass transfer from the visualization of the bubble shrinkage only impossible, and additional information (such as the molar ratio in one of the two phases or concentrations of compounds into one of the two phases) have to be measured experimentally. The specificities at high-pressure two-phase flows depends on the binary system itself and therefore knowledge of the thermodynamics is required.

## 2.2 Thermodynamic study of $CO_2$ - $H_2O$ , $CO_2$ - $EtOH$ and $CO_2$ - $BMimPF_6$ systems

This section presents a study of thermodynamics of the three binary systems,  $CO_2$ - $H_2O$ ,  $CO_2$ - $EtOH$  and  $CO_2$ - $BMimPF_6$  considered in this work. These binary systems have different thermodynamic properties, which impact the terms included in the transfer model for the determination of volumetric mass transfer coefficient in a two-phase segmented micro-flow at high pressure. In this section, the mutual solubility of the binary systems are presented. The physical properties of each pure compound are presented in order to understand the potentials difference that occurs between experiments when pressure or temperature are changed. In addition, the liquid mixture properties are investigated with the aim of showing the effect of  $CO_2$  dissolution in  $H_2O$ ,  $EtOH$  and  $BMimPF_6$ -rich phases along the microchannel. The

<sup>3</sup>In the literature, and for ambient conditions studies, the gas mixture density is assumed to be constant and is calculated using an ideal gas law



**Figure 2.3** –  $CO_2$  dissolution behaviour of the three types of binary systems. (a)  $CO_2$ - $H_2O$  and Bromophenol blue at 10 MPa, 303 K,  $\dot{V}_{H_2O} = 150 \mu\text{L min}^{-1}$ ,  $\dot{V}_{CO_2} = 50 \mu\text{L min}^{-1}$ . (b)  $CO_2$ - $EtOH$  at 4.3 MPa, 313 K,  $\dot{M}_{EtOH} = 2.32 \text{ g h}^{-1}$ ,  $\dot{M}_{CO_2} = 2.0 \text{ g h}^{-1}$  from Martin (2016). (c)  $CO_2$ - $BMimPF_6$  at 11.4 MPa, 313 K,  $\dot{V}_{BMimPF_6} = 90 \mu\text{L min}^{-1}$ ,  $\dot{V}_{CO_2} = 111 \mu\text{L min}^{-1}$  from Silva (2014).

thermodynamic models for the  $CO_2$ - $H_2O$  system are presented in detail since this binary system is the focus of the experimental studies in remainder of this thesis work. In addition, for each binary system, the influence of each thermodynamic property on the two-phase segmented flow is discussed.

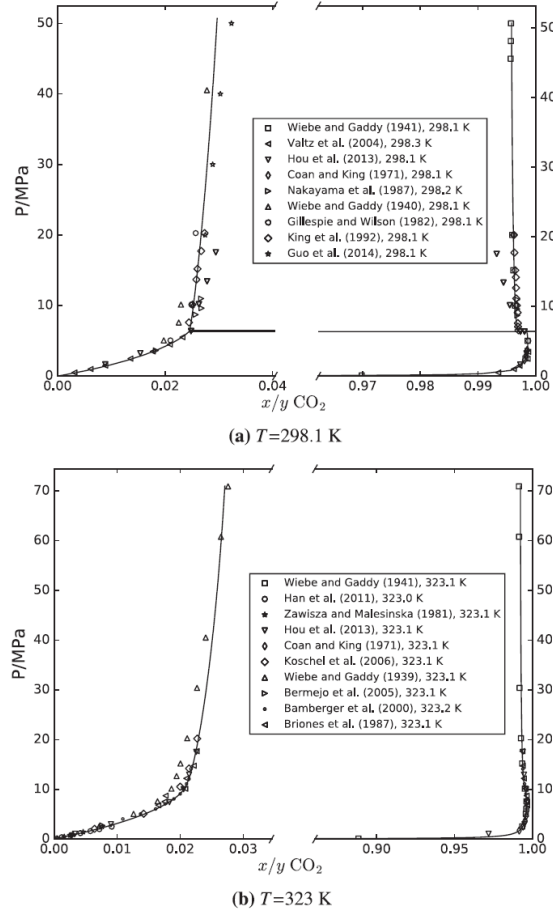
### 2.2.1 Mutual solubility of $CO_2$ - $H_2O$ , $CO_2$ - $EtOH$ and $CO_2$ - $BMimPF_6$ systems

The mutual solubility of the binary system studied provides information about the bubble shrinkage and answers to the questions presented in Figure 2.2, which evaluates the bubble size evolution.

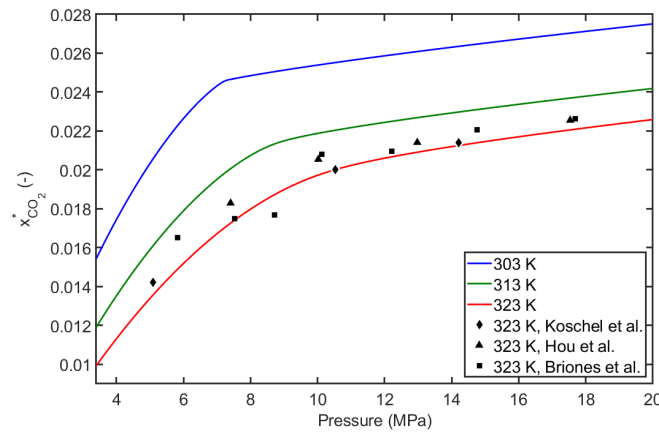
#### Solubility of $CO_2$ and $H_2O$

The mutual solubility of  $CO_2$ - $H_2O$  mixtures at high pressure is widely studied due to the investigation of  $CO_2$  sequestration in deep saline aquifers. The pressure-composition diagram of the binary system is presented in Figure 2.4 and has been taken from the work of Aasen et al. (2017) at 298.1 K and 323 K for pressures between 0.1 MPa and 70 MPa. Figure 2.4 shows that the molar fraction of  $CO_2$  in the  $H_2O$ -rich phase is around 0.02 at 10 MPa for each temperature. It also shows that the  $H_2O$  molar fraction in the  $CO_2$ -rich phase is less than 0.005 at 10 MPa. Hence it can be concluded that  $CO_2$  is slightly soluble in the  $H_2O$ -rich phase, whilst  $H_2O$  is almost insoluble in the  $CO_2$ -rich phase.





**Figure 2.4** – Pressure-composition diagram of the binary system  $CO_2$ - $H_2O$  at 298.1 K and 323 K for pressures between 0.1 MPa and 70 MPa. The figures have been taken from the work of Aasen et al. (2017) where a thermodynamic model is compared with experimental data from the literature.



**Figure 2.5** – Equilibrium molar fraction of  $CO_2$  ( $x_{CO_2}^*$ ) in a  $H_2O$ -rich phase at 303 K, 313 K and 323 K for pressures between 0.1 MPa and 20 MPa calculated with the model of Enick et al. (1990). The model is compared with experimental data from Briones et al. (1987), Koschel et al. (2006) and Hou et al. (2013).

---

Following this, the presence of  $H_2O$  in the  $CO_2$ -rich phase is therefore neglected in this thesis work and the equilibrium fraction of  $CO_2$  in the  $H_2O$ -rich phase,  $x_{CO_2}^*$ , is calculated using the work of Enick et al. (1990) as presented in Figure 2.5. The work of Enick et al. (1990) is based on a Henry's law analysis that has been adapted with a Poynting correction<sup>4</sup>, presented in Equation 2.1. The  $CO_2$  fugacities  $f_{CO_2}$  are calculated with the Span et al. (1996) equation of state.

$$\frac{f_{CO_2}}{x_{CO_2}^*} = H_{CO_2}^* \exp\left(\frac{v_{CO_2}^\infty P}{RT}\right) \quad (2.1)$$

The reference Henry's law constant  $H_{CO_2}^*$  and the partial molar volume of  $CO_2$  at infinite dilution,  $v_{CO_2}^\infty$  are fitted with 110 solubility data points for temperatures between 298 K and 523 K and for pressures between from 3.4 MPa to 72.41 MPa. An empirical correlation for each of the parameters is given by Equation 2.2 and Equation 2.3, where T is temperature in Kelvin.

$$H_{CO_2}^* = -5032.99 + 30.74113 T - 0.052667 T^2 + 2.630218 \cdot 10^{-5} T^3 \quad (2.2)$$

$$v_{CO_2}^\infty = 1799.36 - 17.8218 T + 0.0659297 T^2 - 1.05786 \cdot 10^{-4} T^3 + 6.200275 \cdot 10^{-8} T^4 \quad (2.3)$$

The  $CO_2$  molar fractions in the  $H_2O$ -rich phase at equilibrium calculated with Equation 2.1 are presented in Figure 2.5. First of all, the figure shows that the model is in agreement with the experimental data from the literature at 323 K. Moreover, the  $CO_2$  solubility in the  $H_2O$ -rich phase increases with pressure and decreases with temperature.

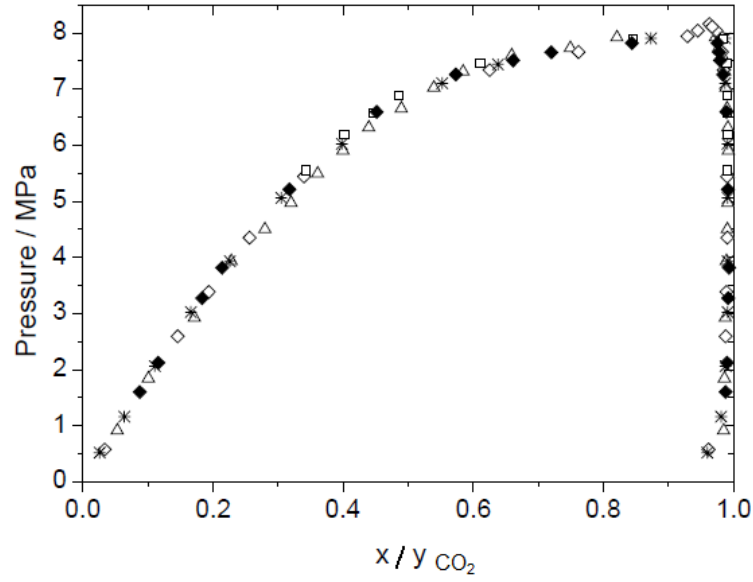
In a two-phase segmented flow, the low solubility of  $CO_2$  in the  $H_2O$ -rich phase is characterised by a small variation of the  $CO_2$  bubble size along the micro-channel and equilibrium is reached quickly (i.e. in a short distance). The solubility of  $H_2O$  in the  $CO_2$ -rich phase is negligible compared with the solubility of  $CO_2$  in the  $H_2O$ -rich phase. Consequently, the density and the viscosity of the  $CO_2$ -rich phase remain almost unchanged along the micro-channel. As a result, the mass balance written in the  $CO_2$ -rich phase is simplified since only  $CO_2$  is transferred from this phase and no  $H_2O$  is transferred to this phase.

## Mutual solubility of $CO_2$ and $EtOH$

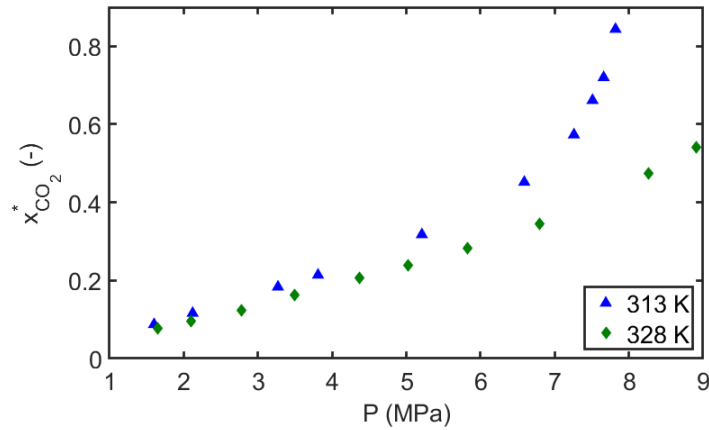
Figure 2.6 presents the pressure-composition liquid-vapor equilibrium of  $CO_2$  and  $EtOH$  at 313 K and for pressures from 0.1 MPa up to the critical pressure of the mixture, which is around 8 MPa. It can be seen that the  $CO_2$  is highly soluble in the  $EtOH$ -rich phase and the  $EtOH$  is only slightly soluble in the  $CO_2$ -rich phase. Figure 2.7 presents the solubility

---

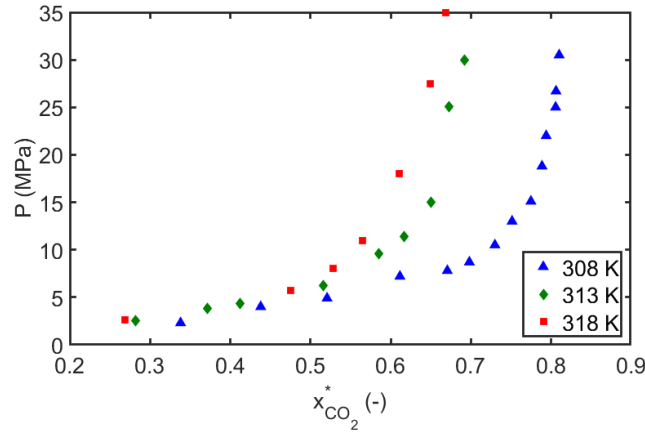
<sup>4</sup>The Poynting correction allows to take into account the pressure influence on the carbon dioxide solubility in the water-rich phase.



**Figure 2.6** – Comparison of experimental vapor-liquid equilibrium data for  $CO_2$  (1)- $EtOH$  (2): (♦) Tsivintzelis et al. (2004) (313.2 K); (□) Jennings et al. (1991) (314.5 K); (\*) Suzuki et al. (1990) (313.4 K); (◇) Joung et al. (2001) (313.4 K); (△) Chang et al. (1997) (313.15 K). Figure taken from Tsivintzelis et al. (2004).



**Figure 2.7** – Equilibrium molar fraction of  $CO_2$  ( $x_{CO_2}^*$ ) in a  $EtOH$ -rich phase at 313 K and 328 K for pressures between 1.6 MPa and 9.42 MPa from the work of Tsivintzelis et al. (2004).



**Figure 2.8** – Equilibrium molar fraction of  $CO_2$  ( $x_{CO_2}^*$ ) in a  $BMimPF_6$ -rich phase at 308 K, 313 K and 318 K for pressures between 2.3 MPa and 35 MPa from the work of Adamou et al. (2006).

of  $CO_2$  in a  $EtOH$ -rich phase at 313 K and 328 K for pressures between 1.6 MPa and 9.42 MPa. Tsivintzelis et al. (2004) used a recirculation-type apparatus equipped with an equilibrium cell, two densitometers for the measurement of saturated densities and a gas chromatograph for the determination of phase compositions. The results show that the  $CO_2$  is more soluble in the  $EtOH$ -rich phase when the temperature is decreased. The mutual solubility is not given in detail in this thesis work since the  $CO_2$ - $EtOH$  binary will not be experimentally investigated. However, it is possible to model the mutual solubility of this binary system using a Soave-Redlich-Kwong equation of state. The mutual solubility is computed at 293.15 K, 303.15 K and 313.5 K for pressures between 0.1 MPa and 8 MPa in the work of Martin (2016) with this type of equation of state.

The high solubility of  $CO_2$  in the  $EtOH$ -rich phase in a two-phase segmented flow results in a significant decrease in the size of the  $CO_2$  bubbles, as previously depicted in Figure 2.3. Depending on temperature and pressure, this decrease can also lead to full dissolution of  $CO_2$  and the disappearance of bubbles. Compared with the  $CO_2$ - $H_2O$  system,  $EtOH$  is more soluble in  $CO_2$  than  $H_2O$ . The dissolution of  $EtOH$  in the  $CO_2$ -rich phase can affect the gas mixture density. Due to this particularity, mass transfer modelling of a two-phase segmented flow of  $CO_2$  and  $EtOH$  at high-pressure cannot be obtained experimentally by measuring bubble shrinkage only. It is necessary to also include information on the molar composition in at least one of the two phases.

### Solubility of $CO_2$ - $BMimPF_6$

The particularity of the  $CO_2$ - $BMimPF_6$  system is that  $CO_2$  is highly soluble in the  $BMimPF_6$ -rich phase as shown in Figure 2.8 where the equilibrium molar fractions of  $CO_2$  are presented at 308 K, 313 K and 318 K for pressures between 2.3 MPa and 35 MPa. These experimental results from the work of Adamou et al. (2006) are obtained by mixing

known volumes of  $CO_2$  and  $BMimPF_6$  in a high pressure cell, waiting for the thermodynamic equilibrium, sampling the liquid phase, quantifying the volume of  $CO_2$  released from it under ambient conditions and calculating the fraction of  $CO_2$  previously dissolved in the liquid phase at pressure and temperature of the apparatus. At 308 K and 30.5 MPa, the  $CO_2$  equilibrium molar fraction is equal to 0.8 in the liquid  $BMimPF_6$ -rich phase. Adamou et al. (2006) also demonstrated that  $BMimPF_6$  is not at all soluble in  $CO_2$ . The mutual solubility modelling of the  $CO_2$ - $BMimPF_6$  system is not straight forward since  $BMimPF_6$  is an electrolytic compound that is highly polar and requires an electrolytic thermodynamic approach, which differs from conventional equation of state approaches.

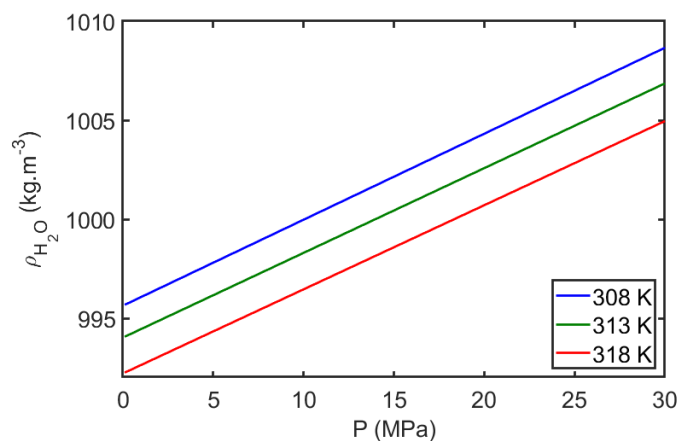
The high solubility of  $CO_2$  in the  $BMimPF_6$ -rich phase is characterized by a significant decrease in the size of  $CO_2$  bubbles along the microchannel. The ionic liquid  $BMimPF_6$  is not soluble in the  $CO_2$  phase so one would expect this simplify the mass transfer modelling as for the  $CO_2$ - $H_2O$  system. However, it will be demonstrated later that the dissolution of  $CO_2$  in the  $BMimPF_6$ -rich phase cause the liquid mixture density and viscosity to change significantly. This in turn affects the hydrodynamics of the flow and therefore the mass transfer rate between the two phases.

### 2.2.2 Physical properties of pure water, carbon dioxide, $EtOH$ and $BMimPF_6$ at high-pressure

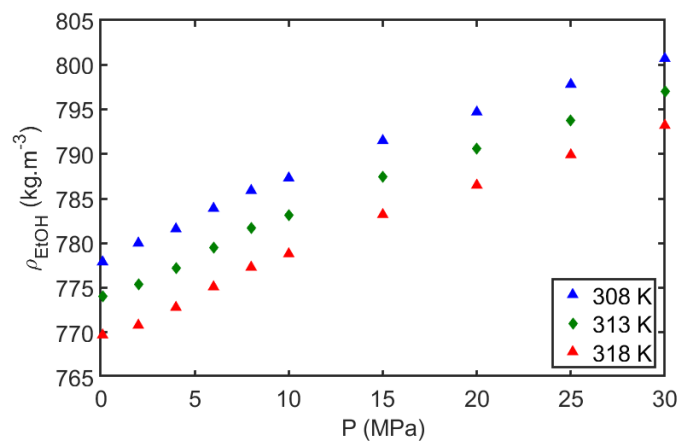
Knowledge of the physical properties of pure compounds involved in a two-phase segmented flow enables the dimensionless numbers such as Reynolds (Re), capillary (Ca), Weber (We) and Schmidt (Sc) numbers to be computed, hence allowing an understanding of the dominant forces in the flow. The common volumetric mass transfer coefficient correlations at ambient pressure are typically written as a function of these numbers as presented in Section 1.4.2 of the first chapter. However, at high pressure, the knowledge of the mixture properties is also essential.

#### Density

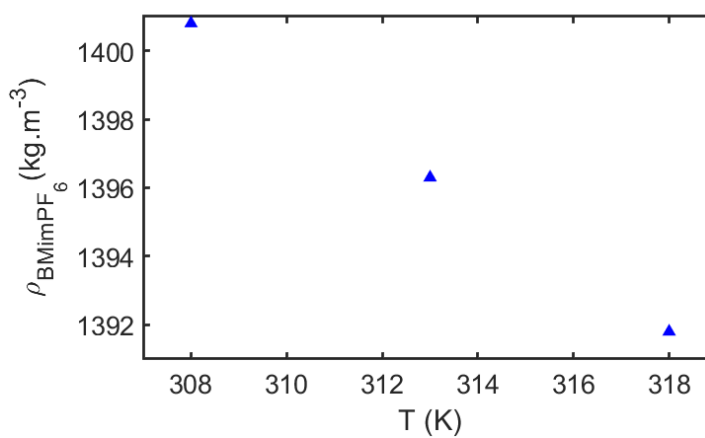
The experimental or computed densities of pure  $H_2O$ ,  $EtOH$ ,  $BMimPF_6$  and  $CO_2$  are presented in Figures 2.9, 2.10, 2.11 and 2.12 respectively. The densities of pure  $H_2O$ ,  $EtOH$  and  $BMimPF_6$  do not change significantly with temperature and pressure. In general, density increases slightly with increasing pressure, and decreases slightly with increasing temperature due to the incompressible and non-expandable properties of liquids. However, the case of  $CO_2$  is completely different and explains that the dissolution of  $CO_2$  in a liquid phase of a two-segmented flow can affect its density at high pressure (see next section). For pressures under the critical pressure (7.3 MPa), the density of  $CO_2$  does not increase significantly with increasing pressure nor does not decrease significantly with increasing temperature. On the other hand, when the pressure is above its critical pressure, the  $CO_2$  density increases towards a like density and the effect of temperature is no longer negligible.



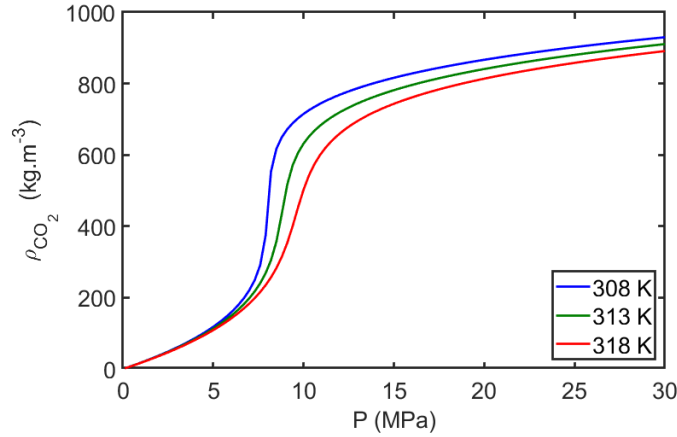
**Figure 2.9** – Density values of pure  $H_2O$  at 308 K, 313 K and 318 K for pressures between 0.1 MPa and 30 MPa based on the work of Wagner et al. (2002).



**Figure 2.10** – Density values of pure  $EtOH$  at 308 K, 313 K and 318 K for pressures between 0.1 MPa and 30 MPa based on the work of Gonçalves et al. (2010).



**Figure 2.11** – Density values of pure  $BMimPF_6$  at 0.1 MPa and for temperatures between 308 K and 318 K from the work of Adamou et al. (2006).



**Figure 2.12** – Density values of pure  $CO_2$  at 308 K, 313 K and 318 K for pressures between 0.1 MPa and 30 MPa calculated with the Span et al. (1996) equation of state.

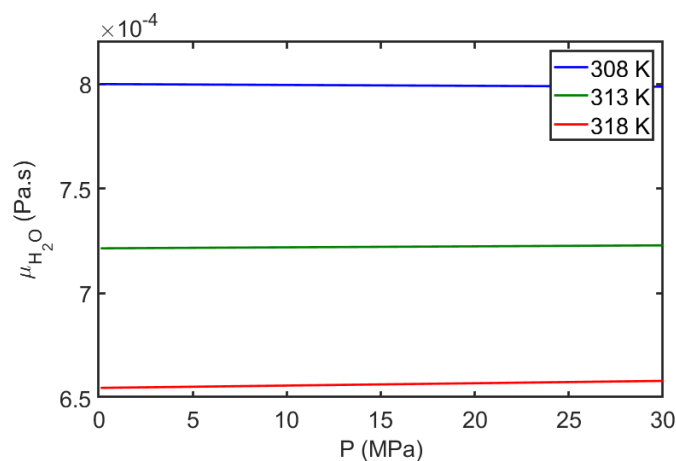
This behavior of  $CO_2$  has several consequences on the determination of the volumetric mass transfer coefficient in a two-phase segmented flow at high-pressure. Experimentally, when the pressure or the temperature in the system is modified, the flow regime is modified. As an example, it is possible to alternatively change between a segmented flow and an annular flow only by modifying the pressure (Marre et al. (2009)). The second aspect is that when the microchannel is fed with a volumetric high-pressure pump that is typically cooled in order to pump liquid  $CO_2$ , the volumetric flow rate in the microchannel may be more than twice as high as the fixed volumetric flow rate in the pump cylinder. Furthermore, when the amount of  $CO_2$  dissolved in the liquid phase is tracked with images of the bubble shrinkage at pressures near the critical point, the knowledge of the exact pressure along the micro-channel is needed in order to convert the bubble volume into a mass of  $CO_2$  dissolved<sup>5</sup> in the liquid phase, since a small change in pressure leads to a significant change in density.

## Viscosity

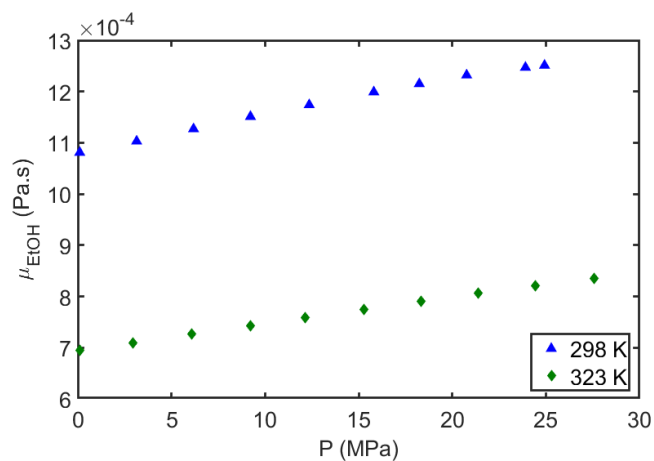
Experimental or computed viscosities of pure  $H_2O$ ,  $EtOH$  and  $BMimPF_6$  presented in Figures 2.13, 2.14 and 2.15 show that pressure has a small impact on the viscosity of a liquid, whereas an increase in temperature leads to a decrease in viscosity. The viscosities of  $H_2O$  and  $EtOH$  are very low compared with the viscosity of  $BMimPF_6$  and the viscosity of  $CO_2$  at high pressure follows the same trends as the density. The viscosity of  $CO_2$  at pressures under the critical pressure is almost independent of temperature and pressure, whereas above the critical pressure, the viscosity of  $CO_2$  increases significantly with an increase in pressure and increases with a decrease in temperature.

The main conclusion on the impact of pressure on the physical properties of pure components is that the properties of  $CO_2$  are significantly different at ambient conditions and at high-

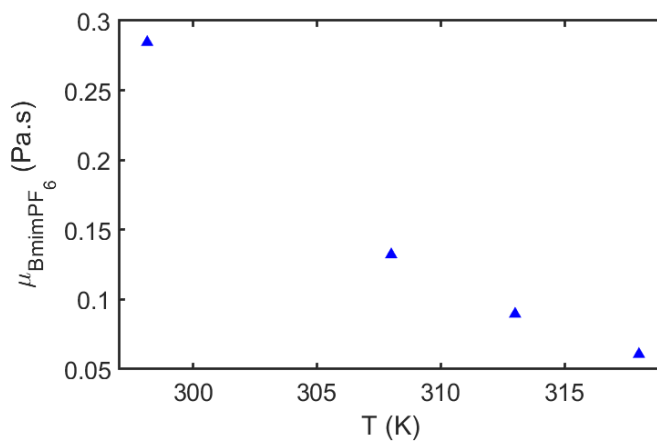
<sup>5</sup>The knowledge of density with pressure allows to convert the bubble volume change into a carbon dioxide mass dissolution in the liquid phase



**Figure 2.13** – Viscosity of  $H_2O$  at 308 K, 313 K and 318 K for pressures between 0.1 MPa and 30 MPa based on the work of Wagner et al. (2002).

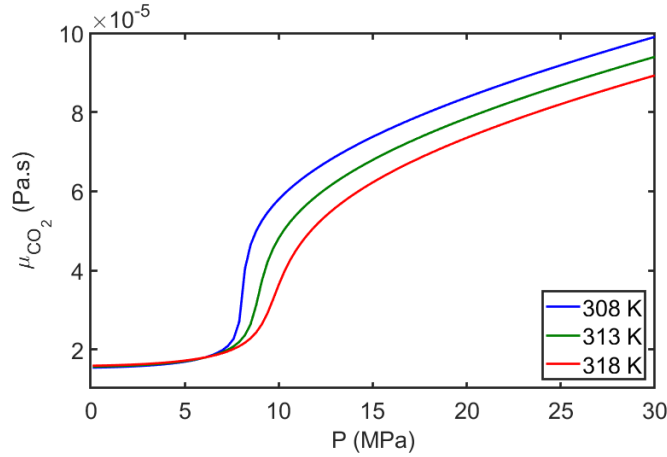


**Figure 2.14** – Viscosity of  $EtOH$  at 298 K and 323 K for pressures between 0.1 MPa and 27.56 MPa from the work of Assael et al. (1994).



**Figure 2.15** – Viscosity of  $BMimPF_6$  at 0.1 MPa and for temperatures between 298 K and 323 K from the work of Adamou et al. (2006).





**Figure 2.16** – Viscosity of  $CO_2$  at 308 K, 313 K and 318 K for pressures between 0.1 MPa and 30 MPa based on the work of Fenghour et al. (1998).

pressure. The  $CO_2$  properties affect the hydrodynamics of the segmented flow and the thermodynamic properties, both of which influence mass transfer.

### 2.2.3 Physical properties of $CO_2$ - $H_2O$ , $CO_2$ - $EtOH$ and $CO_2$ - $BMimPF_6$ mixtures

Due to the specificities of  $CO_2$  at high pressure, the dissolution of  $CO_2$  in the liquid slug can affect both its viscosity and density, whereas this effect is negligible under ambient conditions. It is thus necessary to investigate the properties (i.e. interfacial tension, density and viscosity) of the liquid-phase mixtures containing dissolved  $CO_2$ .

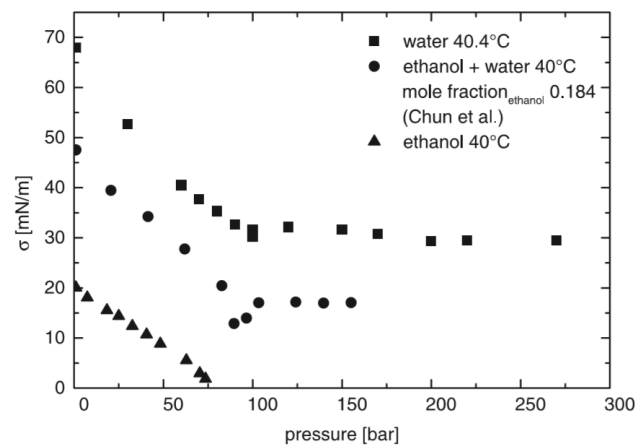
#### Interfacial tension

Figures 2.17 and 2.18 present experimental values of the interfacial tension of  $CO_2$ - $H_2O$ ,  $CO_2$ - $EtOH$  and  $CO_2$ - $BMimPF_6$  systems as a function of pressure. It can be observed that an increase in pressure decreases the interfacial tension between the compounds down to a certain value. This modification affects the stability of the gas-liquid interface and therefore affects the size of the  $CO_2$  bubble formed at high pressure. It can also be seen that the interfacial tension increases with decreasing ethanol concentration. This could lead to Marangoni convection effects<sup>6</sup> and therefore a non-homogeneous molar distribution at the interface of the bubbles. This may then impact local mass transfer at the interface, especially during the bubble generation process. However, it is reasonable to neglect such effects far from the bubble generation zone.

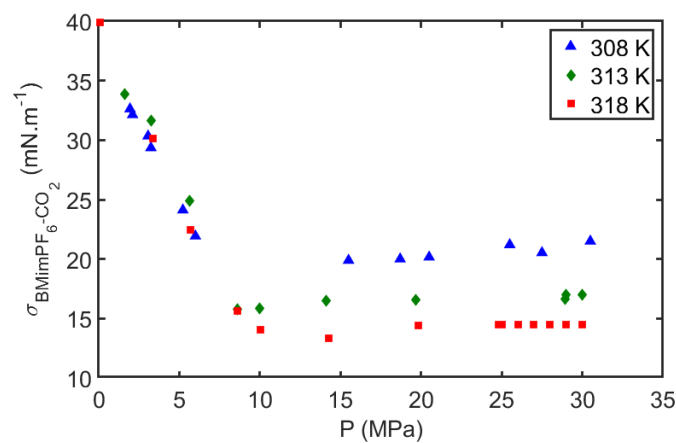
#### Mixture density

The mixture densities of  $CO_2$  and  $H_2O$  mixtures are computed following the methodology of Bachu et al. (2003). In the case of non-ideal solutions such as  $CO_2$  and  $H_2O$  mixtures, it is

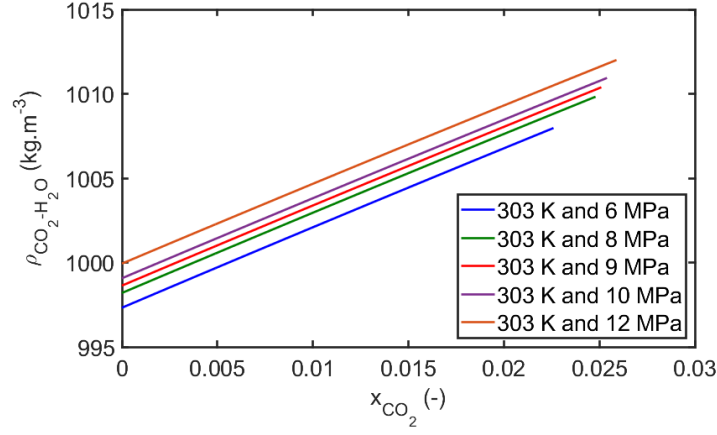
<sup>6</sup>The Marangoni effect is the mass transfer that occurs at the interface between two fluids due to a gradient of interfacial tension along the interface.



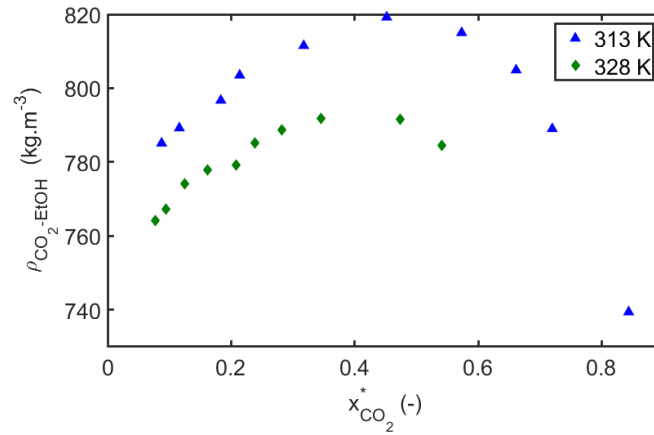
**Figure 2.17** – Interfacial tension of  $H_2O$ ,  $H_2O + EtOH$  and  $EtOH$  saturated with  $CO_2$  at 313 K for pressures between 0.1 MPa and 27 MPa taken from Dittmar et al. (2002).



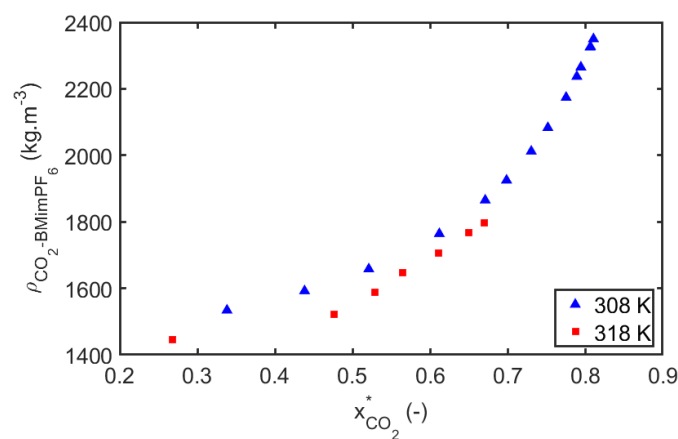
**Figure 2.18** – Interfacial tension of  $BMimPF_6$  saturated with  $CO_2$  at 308 K, 313 K and 318 K for pressures between 0.1 MPa and 30.5 MPa based on the work of Adamou et al. (2006).



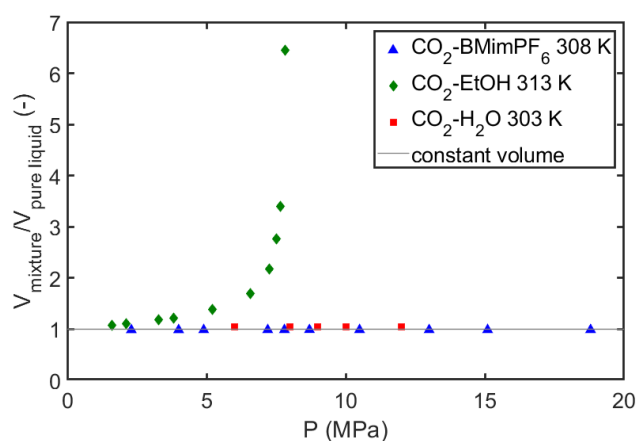
**Figure 2.19** –  $H_2O$ - $CO_2$  liquid mixture density versus the molar fraction of  $CO_2$  at 303 K for pressures between 6 MPa and 12 MPa based on the work of Bachu et al. (2003) and Garcia (2001). For each pressure, the mixture density is calculated from pure  $H_2O$  up to the density of the mixture when thermodynamic equilibrium is reached.



**Figure 2.20** –  $EtOH$ - $CO_2$  liquid mixture density versus the equilibrium molar fraction of  $CO_2$  at 313 K and 328 K from the work of Tsivintzelis et al. (2004).



**Figure 2.21** –  $\text{CO}_2\text{-BMimPF}_6$  mixture density versus the equilibrium molar fraction of  $\text{CO}_2$  at 308 K and 318 K from the work of Adamou et al. (2006).



**Figure 2.22** – Ratio of liquid mixture volume saturated with  $\text{CO}_2$  over the volume of the pure liquid as a function of pressure, where the liquid is  $\text{H}_2\text{O}$ ,  $\text{EtOH}$  and  $\text{BMimPF}_6$ .

assumed that the volume of the liquid mixture is the sum of two contributions: the volume occupied by the solvent in its pure state (i.e. pure  $H_2O$ ) and the apparent volume occupied by the solute (i.e.  $CO_2$ ). The total volume of the solution is written using the partial molar volume of each components as shown in Equation 2.4.

$$\begin{aligned} V_L &= n_{H_2O} \left( \frac{\partial V}{\partial n_{H_2O}} \right)_{T,P,n_{CO_2}} + n_{CO_2} \left( \frac{\partial V}{\partial n_{CO_2}} \right)_{T,P,n_{H_2O}} \\ &= n_{H_2O} v_{H_2O} + n_{CO_2} v_{CO_2} \end{aligned} \quad (2.4)$$

The apparent molar volume of  $CO_2$ ,  $v_{CO_2}^a$ , defined in Equation 2.5 is the difference between the total volume and the molar volume of pure  $H_2O$ ,  $v_{H_2O}^o$ , multiplied by the number of moles of  $H_2O$  and divided by the number of mole of  $CO_2$ . The apparent molar volume is different to the partial molar volume,  $v_{CO_2}$  as shown in Equation 2.6

$$v_{CO_2}^a = \frac{V_L - n_{H_2O} v_{H_2O}^o}{n_{CO_2}} \quad (2.5)$$

$$V_L = n_{CO_2} v_{CO_2} + n_{H_2O} v_{H_2O} = n_{CO_2} v_{CO_2}^a + n_{H_2O} v_{H_2O}^o \quad (2.6)$$

For  $CO_2$  and  $H_2O$  mixtures, numerous correlations for  $v_{CO_2}^a$  can be found in the literature due to their use in geology (Andersen et al. (1992), Enick et al. (1990)). In this work, the correlation from Garcia (2001) given by Equation 2.7 is employed. It is based on 54 data points obtained for temperature and pressure ranges of 278 K to 573 K and 0.2 MPa to 35 MPa respectively.

$$v_{CO_2}^a = 37.51 - 9.585 \cdot 10^{-2} \theta + 8.740 \cdot 10^{-4} \theta^2 - 5.044 \cdot 10^{-7} \theta^3 \quad (2.7)$$

where  $\theta$  is temperature in Celsius and  $v_{CO_2}^a$  in  $cm^3.mol^{-1}$ . Garcia (2001) demonstrated that the influence of pressure is negligible when the temperature is lower than 573 K, which is the case in the current work. Equation 2.8 gives the liquid density of the  $H_2O$  and  $CO_2$  mixture,  $\rho_L(T, P, x_{CO_2})$  derived from Equation 2.6:

$$\rho_L(T, P, x_{CO_2}) = \frac{\rho_{H_2O}^o(T, P)}{1 - w_{CO_2} \left( 1 - \frac{v_{CO_2}^a(T) \rho_{H_2O}^o(T, P)}{M_{CO_2}} \right)} \quad (2.8)$$

where  $w_{CO_2}$  is the mass fraction of  $CO_2$  and  $\rho_{H_2O}^o(T, P)$  is the density of pure  $H_2O$  which is determined using the correlation of Batzle et al. (1992) given by Equation 2.9

$$\begin{aligned} \rho_{H_2O}^o(T, P) &= 1 + 10^{-6}(-80\theta - 3.3\theta^2 + 0.00175\theta^3 + 489P \\ &\quad + 0.016\theta^2 P - 1.3 \cdot 10^{-5}\theta^3 P - 0.333P^2 - 0.002\theta P^2) \end{aligned} \quad (2.9)$$

where  $P$  is pressure in  $MPa$ ,  $\theta$  is temperature in Celsius and  $\rho_{H_2O}^o(T, P)$  is in  $g.cm^{-3}$ .

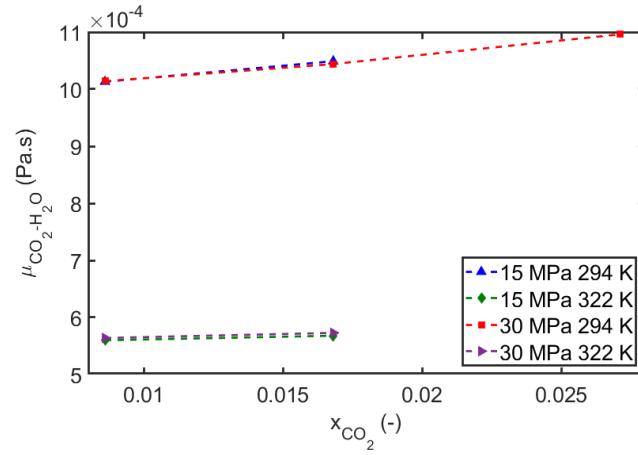
---

Under ambient conditions, the liquid mixture density is commonly supposed constant along a two-phase segmented flow since its variations are negligible. However, the mixture density has a significant influence on a two-phase segmented flow at high pressure when the  $CO_2$  is one of the two phases. Figures 2.19, 2.20 and 2.21 present the variations of liquid mixture density of  $H_2O$ ,  $EtOH$  and  $BMimPF_6$  in contact with  $CO_2$  at high pressure. The evolution of the  $H_2O$ -rich phase mixture density presented in Figure 2.19 shows that the dissolution of  $CO_2$  in a  $H_2O$ -rich phase is almost negligible (1% difference between pure  $H_2O$  and  $H_2O$  saturated with  $CO_2$ ). The case of  $CO_2$ - $EtOH$  in Figure 2.20 presents a different trends, the liquid mixture density increases with  $CO_2$  dissolution up to an equilibrium molar fraction,  $x_{CO_2}^*$  of 0.4 (which corresponds to a pressure of 6.6 MPa in this case) and decreases for higher equilibrium molar fraction of  $CO_2$ . The mixture density of the  $BMimPF_6$ -rich phase presented in Figure 2.21 can be seen to increase (by up to almost two times the density of the pure  $BMimPF_6$ ) with an increase in the equilibrium molar fraction of  $CO_2$ .

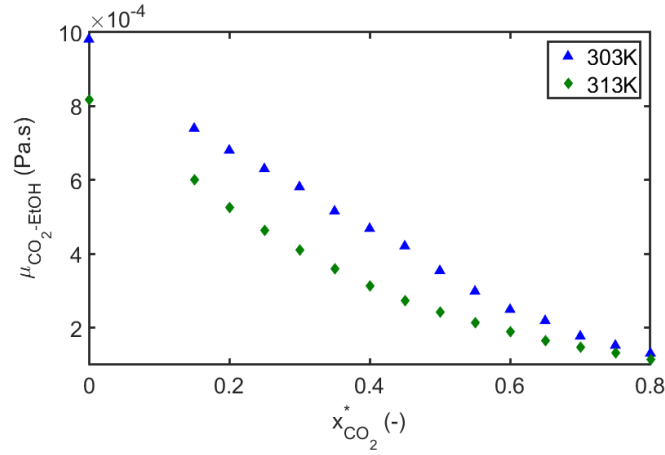
However, an increase in liquid mixture density must be differentiated from an increase in liquid volume. Figure 2.22 presents the ratio between the liquid mixture volume (i.e. saturated with  $CO_2$ ) over the pure liquid volume versus the pressure (and therefore amount of  $CO_2$  dissolved). It can be seen that the volume of the  $H_2O$ -rich phase saturated with  $CO_2$  is slightly larger than the volume of pure  $H_2O$ . For the  $CO_2$ - $BMimPF_6$  system, even if the liquid mixture density is two times greater than that of pure  $BMimPF_6$ , the volume of the  $BMimPF_6$ -rich phase saturated with  $CO_2$  is equal to the volume of  $BMimPF_6$  in its pure state. On the other hand, the  $EtOH$ -rich phase saturated with  $CO_2$  has a volume of up to 6.5 times the volume of pure  $EtOH$  and this volume expansion has a strong impact on the flow behaviour of a two-segmented flow of  $EtOH$  and  $CO_2$ . It appears therefore important to take the variation of the liquid phase volume into account in the mass transfer model.

## Mixture viscosity

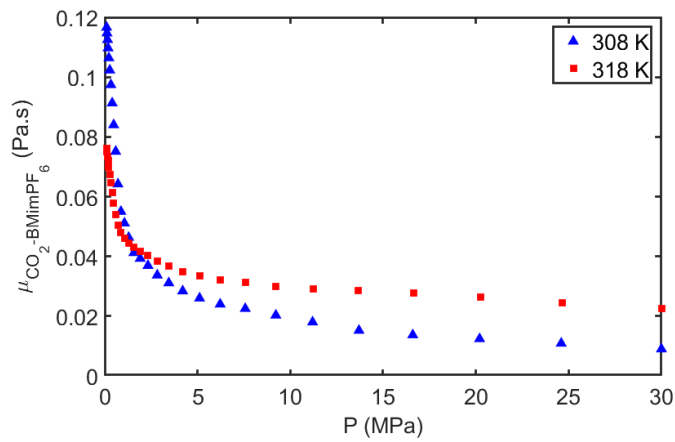
Figures 2.23, 2.24 and 2.25 present the variations of liquid mixture viscosity of  $H_2O$ ,  $EtOH$  and  $BMimPF_6$  in contact with  $CO_2$  at high pressure. The dissolution of  $CO_2$  in the  $H_2O$ -rich phase at high pressure does not strongly influence the mixture viscosity, whereas it has an important impact on the  $EtOH$ -rich phase and the  $BMimPF_6$ -rich phase. Indeed, for a  $CO_2$ - $EtOH$  liquid mixture with a  $CO_2$  molar fraction of 0.8, the liquid mixture viscosity is ten times smaller than for pure  $EtOH$ . For a  $CO_2$ - $BMimPF_6$  mixture with a  $CO_2$  molar fraction of 0.8 (which corresponds to a pressure of 20 MPa at 308 K), the mixture viscosity is twelve times smaller than for pure  $BMimPF_6$ . Again, this important difference in the mixture viscosity with respect to the pure component has a significant impact on the two-phase flow behavior, from the generation process of segmented flow to when thermodynamic equilibrium is reached.



**Figure 2.23** –  $\text{CO}_2\text{-H}_2\text{O}$  non-saturated mixture viscosity versus the molar fraction of  $\text{CO}_2$  at 294 K and 322 K with pressures of 15 MPa and 30 MPa based on the work of McBride-Wright et al. (2015).



**Figure 2.24** –  $\text{CO}_2\text{-EtOH}$  mixture viscosity versus the equilibrium molar fraction of  $\text{CO}_2$  at 303 K and 313 K from the work of Sih et al. (2008).



**Figure 2.25** –  $\text{CO}_2\text{-BMimPF}_6$  mixture viscosity at 308 K and 318 K for pressures between 0.1 MPa and 30 MPa from the work of Adamou et al. (2006).

### 2.2.4 Impact of evolving physical properties along the microchannel

The use of a thermodynamic model for the calculation of mixture viscosity and mixture density is not sufficient alone for the prediction of two-phase segmented flow regimes at high pressure. The example of the liquid volumes computed in Figure 2.22 emphasizes this challenge. However, knowledge of such properties enables dimensionless numbers such as Reynolds ( $Re$ ) and Capillary ( $Ca$ ) to be computed and these indicate the dominant forces (inertial, viscous and interfacial tension) in the segmented flow. Correlations of volumetric mass transfer coefficients at ambient conditions are a function of these dimensionless numbers. However, as presented in Table 2.1, the values of these dimensionless numbers can change significantly along the microchannel at high-pressure. The table presents the ratio between the dimensionless numbers of the liquid phase at the inlet of the microchannel divided by the value at equilibrium. For the  $CO_2$ - $H_2O$  system, the ratios are approximately one, so there is no significant change in dominating forces along the microchannel. On the other hand, the Reynolds number at equilibrium for  $CO_2$ - $EtOH$  and  $CO_2$ - $BMimPF_6$  are four and eight times higher, respectively, than at the microchannel inlet. The capillary number at equilibrium is five times lower than the capillary number at the inlet.

These changes along the microchannel may question the adaptability of the existing mass transfer coefficient correlations on high-pressure systems. Indeed, under ambient conditions, these correlations are based on the hypothesis that the volumetric mass transfer coefficient is constant along the microchannel. Alternate correlation for the mass transfer coefficient with the dimensionless numbers of the system has to be considered at high-pressure.

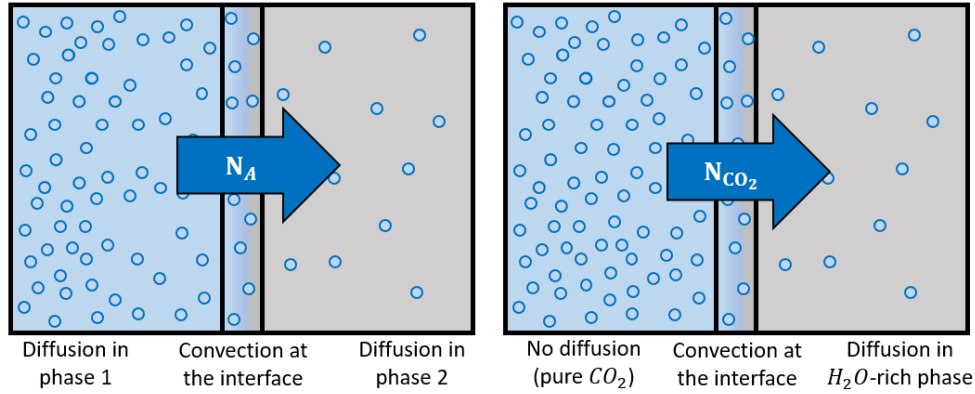
**Table 2.1** – Comparison of dimensionless numbers in the liquid phase along the microchannel. As an example,  $Re^*$  is calculated with the liquid mixture properties when thermodynamic equilibrium is reached, and  $Re$  with the pure liquid properties at the inlet. The superficial velocities and the interfacial tensions are supposed constant.

-	T (K)	P(MPa)	$Re^*/Re$	$Ca^*/Ca$	$Bo^*/Bo, We^*/We$
$CO_2$ - $H_2O$	303	10	0.91	1.11	1.01
$CO_2$ - $EtOH$	313	7	4.29	0.24	1.05
$CO_2$ - $BMimPF_6$	308	10	8.16	0.17	1.36

## 2.3 Mass transport modelling

This section presents the mass transfer modelling in an isothermal system composed of two phases. The classical approach used in chemical engineering is firstly presented and applied to segmented two-phase micro-flow at high pressure. The model is then adapted to the





**Figure 2.26** – [Left] Three contributions of the two-phase mass transfer of a component A: diffusion in phase 1, convection at the interface and diffusion in phase 2.  $N_A$  corresponds to the combined molar flux (diffusion + convection). [Right] Two phase mass transfer of  $CO_2$  from a  $CO_2$  pure phase to a  $H_2O$ -rich phase. No diffusion in the  $CO_2$  pure phase.

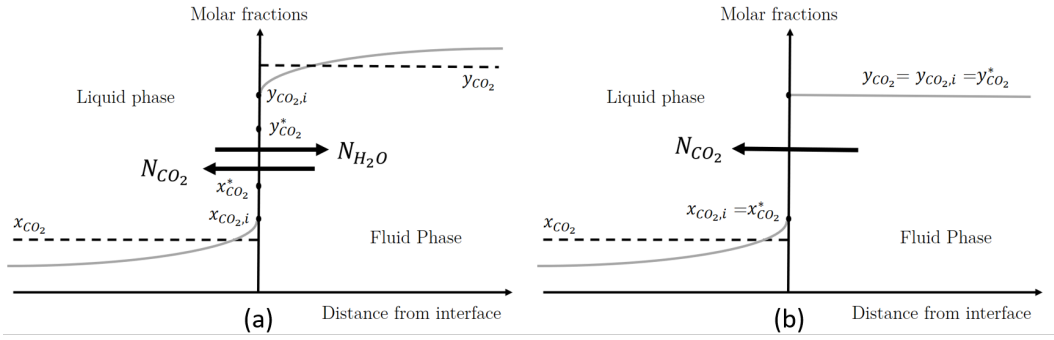
$CO_2$ - $H_2O$  system, which is investigated experimentally in Chapters 4 and 5 using different measurement techniques. The hypotheses of the model are discussed for the two other binary systems,  $CO_2$ - $EtOH$  and  $CO_2$ - $BMimPF_6$ .

### 2.3.1 Two-phase mass transport

Mass transfer is characterized by the spatial movement of matter. In a multicomponent system, mass transfer is due to diffusion and convection. Diffusion is mass transfer from a zone of high concentration to a zone of low concentration. The driving force of diffusion is this difference of chemical potentials. Convective mass transport can be natural or forced. The driving force for natural convection is a difference of density, whereas the driving force for forced convection is an artificial motion of the fluid (generated with a pump for example). The mass transfer behaviour of a component A from one phase to another phase depends on the concentration gradient of A between the phases, as well as the physico-chemical properties of the fluids and the hydrodynamics of the flow. It is common to separate the mass transfer of a component A from phase 1 to a phase 2 into three steps, as depicted in the left part of Figure 2.26. The first step is mass transfer due to diffusion in phase 1. Note that if phase 1 contains only A, the concentration of A is uniform in this phase, the concentration gradient of A is null and then there is no diffusion process in this phase like presented in the right hand side part of the figure. The second step is mass transfer due to convection at the interface between the two phases and the third step is the diffusion of component A in phase 2. A common simplification is that the volume of the interface is considered as a simple surface. Interface theory is not investigated in this thesis work and the hypothesis made is that the components of both phases have uniform concentration at the interface. In order to write the diffusive and convective fluxes, Table 2.2 presents the basic definitions for the determination of the combined molar flux of component i within a multicomponent system containing N components.

**Table 2.2** – Basic notations for the investigation of molar transport in a multicomponent system, adapted from Bird (2002). The introduction of the local molar average velocity  $\mathbf{v}^*$  enables the molar fluxes to be written with respect to stationary axes and an average molar velocity. This simplification makes it easier to switch between Euler and Lagrangian modelling approaches.

Formula	Definition	Units
$C_i$	molar concentration of the component i in the bulk phase	$\text{mol.m}^{-3}$
$C = \sum_{i=1}^N C_i$	molar density of the phase	$\text{mol.m}^{-3}$
$x_i = C_i/C$	mole fraction of component i	-
$\mathbf{v}_i$	average velocity of i molecules in a small volume	$\text{m.s}^{-1}$
$\mathbf{v}^* = \sum_{i=1}^N x_i \mathbf{v}_i$	local molar average velocity	$\text{m.s}^{-1}$



**Figure 2.27** – Two-film model with mass transfer in both directions (a) and fluid to liquid only (b) where  $y_{CO_2}$  is the molar fraction of  $CO_2$  in the bulk of  $CO_2$ -rich phase,  $y_{CO_2,i}$  is the molar fraction of  $CO_2$  at the interface in equilibrium with  $x_{CO_2,i}$  and  $y_{CO_2}^*$  is the molar fraction of  $CO_2$  in the  $CO_2$ -rich phase in equilibrium with the liquid phase with the molar fraction of  $CO_2$  in the bulk,  $x_{CO_2}$ . Adapted from Bird (2002).

In a two component system of A and B, the molar flux of A (defined by the number of moles of A flowing through a unit area per unit time) is written by Equation 2.10 with respect to the diffusion velocity  $\mathbf{v}_A - \mathbf{v}^*$  and Fick's first law of diffusion, where  $\mathcal{D}_{AB}$  is the binary diffusion coefficient:

$$\mathbf{J}_A^* = C_A (\mathbf{v}_A - \mathbf{v}^*) = -C \mathcal{D}_{AB} \nabla x_A \quad (2.10)$$

Component A can also be transported by the motion of the fluid (i.e. by convection). In order to determine the convective molar flux across a unit surface that has a normal unit vector  $\mathbf{n}$ , the scalar product  $\mathbf{n} \cdot C_A \mathbf{v}^*$  has to be computed. The combined molar flux of diffusion and convection is then expressed as in Equation 2.11:

$$\mathbf{N}_A = \mathbf{J}_A^* + C_A \mathbf{v}^* = C_A (\mathbf{v}_A - \mathbf{v}^*) = -C \mathcal{D}_{AB} \nabla x_A + C_A \mathbf{v}^* \quad (2.11)$$

In a two-phase mass transfer process, the transfer potential in each phase can be written as the difference between the mean molar concentration of A at the interface,  $C_{A,i}$ , and the mean mass concentration of A in the bulk,  $C_A$ . In the two-film theory, the combined molar flux are proportional to the transfer potential. Figure 2.27 presents mass transfer between a  $CO_2$ -rich phase also called the "fluid phase"<sup>7</sup> and a  $H_2O$ -rich phase called the liquid phase. Part (a) of the figure depicts the case where both  $CO_2$  and  $H_2O$  transfer from one phase to another. The combined molar fluxes  $N_{CO_2}$  and  $N_{H_2O}$  are given. Part (b) depicts the case where only  $CO_2$  transfers from the  $CO_2$ -phase to the  $H_2O$ -rich phase. In both cases, the combined molar flux  $N_{CO_2}$  can be written with a local approach or an overall approach in each of the phases, as presented in Table 2.3. The proportional coefficients  $k_L$  and  $k_F$  are the local mass transfer coefficients of liquid and fluid phases, respectively, and  $K_L$  and  $K_F$  are the overall mass transfer coefficients of liquid and fluid phases, respectively.

**Table 2.3** – Combined molar  $CO_2$  flux expressions,  $N_{CO_2}$ , where  $C_{CO_2,i}^L$ ,  $C_{CO_2,i}^F$  are the  $CO_2$  molar concentrations at the interface in the liquid and fluid sides, respectively, and  $C_{CO_2}^{L,*}$ ,  $C_{CO_2}^{F,*}$  are the  $CO_2$  molar concentration at thermodynamic equilibrium in the liquid and fluid phases, respectively. The units of the mass transfer coefficients are  $m.s^{-1}$

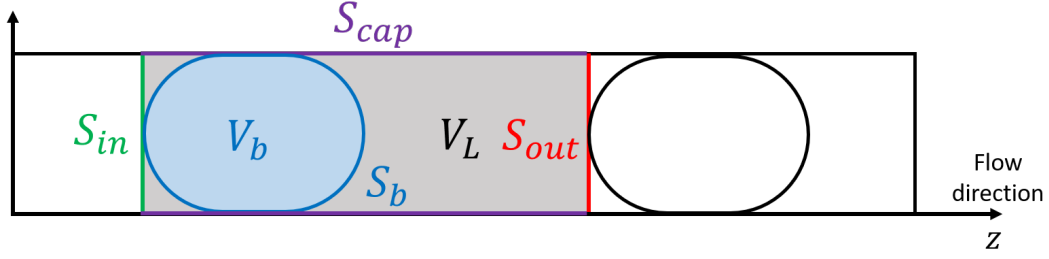
-	Local approach	Overall approach
Liquid phase	$k_L(C_{CO_2,i}^L - C_{CO_2}^L)$	$K_L(C_{CO_2}^{L,*} - C_{CO_2}^L)$
Fluid phase	$k_F(C_{CO_2}^F - C_{CO_2,i}^F)$	$K_F(C_{CO_2}^F - C_{CO_2}^{F,*})$

The continuity of molar flux at the interface ensures the equality of these  $N_{CO_2}$  expressions and since  $H_2O$  is considered insoluble in the  $CO_2$  phase, the overall mass transfer coefficient of the liquid phase  $K_L$  is equal to the local mass transfer coefficient of the liquid phase  $k_L$ . The concentration of  $CO_2$  at the interface in the liquid phase  $C_{CO_2,i}^L$  is then equal to the concentration at equilibrium in the liquid bulk  $C_{CO_2}^{L,*}$ . The combined molar  $CO_2$  flux can then be written by Equation 2.12.

$$N_{CO_2} = k_L(C_{CO_2}^{L,*} - C_{CO_2}^L) \quad (2.12)$$

In the general case of a two-components system where both components transfer to each of the phases (such as for  $CO_2$ - $EtOH$ ), the overall and local mass transfer coefficients are not equal. The continuity of flux at the interface must then be written for each components. Experimentally, the overall mass transfer coefficients of each phase and for each components ( $K_F^{CO_2}$ ,  $K_F^{EtOH}$ ,  $K_L^{CO_2}$ ,  $K_L^{EtOH}$ ) are obtained using a unit-cell model and an experimental method that enables measurement of the molar fraction of  $CO_2$  and  $EtOH$  in each phases. With the addition of a thermodynamic model, which provides the link between the molar

<sup>7</sup>In this study the  $CO_2$  can be either liquid or gas



**Figure 2.28** – Presentation of the unit-cell model, which is composed of one  $CO_2$  segment with volume  $V_b$  and delimited by the surface  $S_b$ , and one  $H_2O$ -rich liquid segment of volume  $V_L$ , which is delimited by its surface  $S_L$  composed of  $S_{cap}$ ,  $S_{in}$  and  $S_{out}$ .

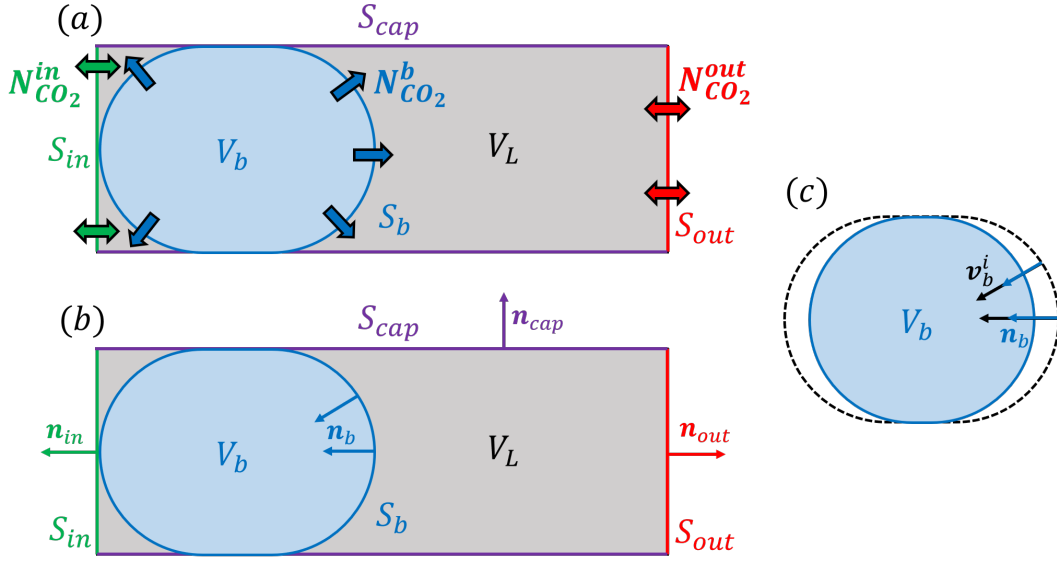
fraction of  $CO_2$  and  $EtOH$  at equilibrium in each phase, the local mass transfer coefficients ( $k_F^{CO_2}$ ,  $k_F^{EtOH}$ ,  $k_L^{CO_2}$ ,  $k_L^{EtOH}$ ) can be deduced. In this thesis work, this model is elaborated for the case of  $CO_2$ - $H_2O$ , where the transfer occurs from the  $CO_2$  phase to the  $H_2O$ -rich phase only.

### 2.3.2 Mass transfer model for high-pressure two-phase segmented micro-flow

The model presented below allows the determination of mass transfer coefficient in a two-phase segmented flow of  $CO_2$  and  $H_2O$  at high-pressure in a micro-capillary. It is based on a Lagrangian approach whereby the ensemble of one  $CO_2$  segment and one  $H_2O$ -rich segment, called a unit-cell, is considered. The unit-cell is presented in Figure 2.28. The  $CO_2$  segment is modelled as a cylinder with two hemispherical caps with a diameter equal to the diameter of the capillary tube. This configuration corresponds to the  $CO_2$ - $H_2O$  segmented flow presented in Figure 2.3.

Modelling the  $CO_2$ - $EtOH$  and  $CO_2$ - $BMimPF_6$  segmented flows is different than for the case of  $CO_2$ - $H_2O$  segmented flow. The  $CO_2$ - $EtOH$  system requires two different physical descriptions of the bubble size in the capillary: one where the  $CO_2$  bubble cross section is equal to the capillary cross section (like for the  $CO_2$ - $H_2O$  description) and one where the  $CO_2$  bubble is a sphere with a diameter smaller than that of the capillary tube. The  $CO_2$ - $BMimPF_6$  system is even more complicated. The unit-cell is composed of the bubble, a liquid film surrounding the bubble and a liquid slug. In addition, a viscosity gradient exists between the liquid film and the bulk of the liquid slug along the length of the microchannel due to the dissolution of  $CO_2$ . This viscosity gradient impacts the velocity profile in the liquid film and in the liquid bulk and therefore, the two different zones of the liquid segment must be treated differently. This approach is presented in the work of Silva (2014).

The liquid film of the  $CO_2$ - $H_2O$  system is neglected here due to the low values of bubble capillary number considered in this work ( $Ca_B < 10^{-3}$ ). Indeed, the film thickness can be



**Figure 2.29** – (a) Unit-cell and combined molar flux of  $CO_2$  transferring through the  $H_2O$ -rich liquid slug surface. (b) Unit-cell and normal vectors of each  $H_2O$ -rich liquid slug surfaces. (c)  $CO_2$ -rich bubble shrinkage where  $v_b^i$  is the bubble interface velocity vector.

approximated by the correlation given by Bretherton (1961):  $\frac{\delta}{R} = 1.34Ca_B^{2/3}$  where  $R$  is the  $CO_2$  bubble cross section radius and  $\delta$  the film thickness. This correlation estimates a film thickness that is less than 1.3% of the capillary tube radius, i.e. less than 2 microns thick. Considering a finite volume of the  $H_2O$ -rich slug, the partial molar balance of  $CO_2$  can be written as Equation 2.13 where  $C_{CO_2}$  is the concentration of  $CO_2$  in the liquid volume in  $mol.m^{-3}$  and  $N_{CO_2}$  the combined molar flux (convective and diffusive) of  $CO_2$  passing through the surface of this volume in  $mol.m^{-2}.s^{-1}$ .

$$\frac{\partial C_{CO_2}}{\partial t} = -\nabla \cdot N_{CO_2} \quad (2.13)$$

The equation of continuity is integrated in the entire volume of the  $H_2O$ -rich slug,  $V_L$ . The result is presented in Equation 2.14 which includes two terms, A and B:

$$\underbrace{\iiint_{V_L} \frac{\partial C_{CO_2}}{\partial t} dV}_A = - \underbrace{\iiint_{V_L} \nabla \cdot N_{CO_2} dV}_B \quad (2.14)$$

Using the Green-Ostrogradski theorem, term B can be written as a flux passing through the boundary of the volume  $V_L$ , i.e. the surface  $S_L$ :

$$- \iiint_V \nabla \cdot N_{CO_2} dV = - \iint_{S_L} N_{CO_2} \cdot n dS \quad (2.15)$$

---

The liquid surface  $S_L$  can be separated into four contributions (see Figure 2.29) as follows:

$$\begin{aligned}
-\iint_{S_L} \mathbf{N}_{CO_2} \cdot \mathbf{n} \, dS = & -\iint_{S_b} \mathbf{N}_{CO_2}^b \cdot \mathbf{n}_b \, dS - \iint_{S_{in}} \mathbf{N}_{CO_2}^{in} \cdot \mathbf{n}_{in} \, dS \\
& - \iint_{S_{out}} \mathbf{N}_{CO_2}^{out} \cdot \mathbf{n}_{out} \, dS - \iint_{S_{cap}} \mathbf{N}_{CO_2}^{cap} \cdot \mathbf{n}_{cap} \, dS
\end{aligned} \tag{2.16}$$

The integral on  $S_{cap}$  is zero since there is no transfer through the capillary tube wall. The integrals on  $S_{in}$  and  $S_{out}$  can be treated with the following argument. Considering a random cross sectional surface  $S$  in the liquid slug that is, moving with the mean flow velocity (Lagrangian approach), the total flux through this surface is written by Equation 2.17:

$$\iint_S \mathbf{N}_{CO_2} \cdot \mathbf{n} \, dS \tag{2.17}$$

Is this total flux null in a Lagrangian approach? No. Even if the density and the viscosity of the liquid slug are constant along the entire capillary (which is not the case here), since the concentration of  $CO_2$  in the liquid phase at the end of the capillary is higher than the concentration at the beginning, the total flux cannot be zero. Considering the surfaces before and after this random surface  $S$ , spaced up to one unit-cell (like  $S_{in}$  and  $S_{out}$ ), it is reasonable to say that if the surfaces are far enough from the bubble generation zone, the total flux through these surfaces are almost equal. Applying this argument to the surfaces  $S_{in}$  and  $S_{out}$  of the unit-cell (spaced up to one unit-cell), gives Equation 2.18:

$$\iint_{S_{in}} \mathbf{N}_{CO_2}^{in} \cdot \mathbf{n}_{in} \, dS \approx - \iint_{S_{out}} \mathbf{N}_{CO_2}^{out} \cdot \mathbf{n}_{out} \, dS \tag{2.18}$$

Therefore, the difference of these integrals in the B term are negligible compared with the integral of  $S_b$ :

$$\iint_{S_{in}} \mathbf{N}_{CO_2}^{in} \cdot \mathbf{n}_{in} \, dS + \iint_{S_{out}} \mathbf{N}_{CO_2}^{out} \cdot \mathbf{n}_{out} \, dS << \iint_{S_b} \mathbf{N}_{CO_2}^b \cdot \mathbf{n}_b \, dS \tag{2.19}$$

The validity of the hypothesis depicted by Equation 2.18 can be altered by several phenomena:

- The liquid mixture density variation along the capillary due to the  $CO_2$  dissolution in the liquid phase, which modifies the convective term of the total flux.
- Segmented flows where the length of the liquid slug is significantly greater than the length of the gas bubble (at least one order of magnitude higher).

For example, the case of the binary system  $CO_2$ - $BMimPF_6$  involves a significant increase in liquid density and a significant decrease in liquid viscosity, both of which greatly increase the magnitude of the convective term. The total flux on  $S_{out}$  could be different from the one on  $S_{in}$ .

For the  $CO_2$ - $H_2O$  flow, this hypothesis is valid and the B term is equal to the total flux through the bubble surface  $S_b$ :

$$-\iint_{S_L} N_{CO_2} \cdot \mathbf{n} \, dS = -\iint_{S_b} N_{CO_2}^b \cdot \mathbf{n}_b \, dS \quad (2.20)$$

The total flux can be written with the liquid overall mass transfer coefficient  $K_L$  as presented in Section 2.3.1. Furthermore, since  $H_2O$  is almost insoluble in the  $CO_2$ -rich phase, the overall liquid-side mass transfer coefficient is equal to the local mass transfer coefficient  $k_L$ . The B term is therefore a function of  $k_L$ , the bubble surface  $S_b$ , the equilibrium concentration of  $CO_2$  in the  $H_2O$ -rich phase  $C_{CO_2}^*$  and the concentration of  $CO_2$  of the  $H_2O$ -rich phase  $C_{CO_2}$ :

$$-\iint_{S_b} N_{CO_2}^b \cdot \mathbf{n}_b \, dS = -\iint_{S_b} N_{CO_2}^b (-\mathbf{n}_b) \cdot \mathbf{n}_b \, dS = k_L (C_{CO_2}^* - C_{CO_2}) S_b \quad (2.21)$$

The A term has two contributions, given by the Leibnitz theorem and written in Equation 2.22. The first term corresponds to the variation of  $C_{CO_2}$  in the liquid slug when the volume  $V_L$  does not change. The second term is added when the boundaries of the liquid volume  $V_L$  are moving along the capillary, where  $\mathbf{v}_S$  is the velocity vector of the moving surface.

$$\iiint_{V_L} \frac{\partial C_{CO_2}}{\partial t} \, dV = \frac{d}{dt} \iiint_{V_L} C_{CO_2} \, dV - \iint_{S_L} C_{CO_2} \mathbf{v}_S \cdot \mathbf{n} \, dS \quad (2.22)$$

The first term is decomposed in Equation 2.23, where  $\langle C_{CO_2} \rangle$  is the mean concentration in the liquid slug volume  $V_L$ :

$$\frac{d}{dt} \iiint_{V_L} C_{CO_2} \, dV = \langle C_{CO_2} \rangle \frac{dV_L}{dt} + V_L \frac{d\langle C_{CO_2} \rangle}{dt} \quad (2.23)$$

The second term is separated with the four contributions of  $S_L$  in Equation 2.24:

$$\begin{aligned} -\iint_{S_L} C_{CO_2} \mathbf{v}_S \cdot \mathbf{n} \, dS &= -\iint_{S_{in}} C_{CO_2} \mathbf{v}_{in} \cdot \mathbf{n}_{in} \, dS - \iint_{S_b} C_{CO_2}^L \mathbf{v}_b^i \cdot \mathbf{n}_b \, dS \\ &\quad - \iint_{S_{out}} C_{CO_2} \mathbf{v}_{out} \cdot \mathbf{n}_{out} \, dS - \iint_{S_{cap}} C_{CO_2} \mathbf{v}_{cap} \cdot \mathbf{n}_{cap} \, dS \end{aligned} \quad (2.24)$$

The term on  $S_{cap}$  is zero since the velocity of the surface  $\mathbf{v}_{cap}$  is zero. The terms on the surfaces  $S_{in}$  and  $S_{out}$  are calculated in Equation 2.25 by assuming that the mean concentration on both surfaces is equal to the mean concentration in the entire liquid slug  $V_L$ . The validity

of this assumption can be altered when the liquid slugs are long and when the unit-cell is near the bubble generation zone. The term  $V_{UC}$  is the volume of the entire unit-cell,  $V_L + V_b$ .

$$\begin{aligned}
& - \iint_{S_{in}} C_{CO_2} \mathbf{v}_{in} \cdot \mathbf{n}_{in} dS - \iint_{S_{out}} C_{CO_2} \mathbf{v}_{out} \cdot \mathbf{n}_{out} dS \\
& = - \iint_{S_{in}} C_{CO_2} v_{in} \mathbf{e}_z \cdot (-\mathbf{e}_z) dS - \iint_{S_{out}} C_{CO_2} v_{out} \mathbf{e}_z \cdot \mathbf{e}_z dS \\
& = - \langle C_{CO_2} \rangle \left( \iint_{S_{out}} v_{out} dS - \iint_{S_{in}} v_{in} dS \right) \\
& = - \langle C_{CO_2} \rangle \frac{dV_{UC}}{dt}
\end{aligned} \tag{2.25}$$

The term on  $S_b$  is calculated by assuming that the concentration at the interface  $C_{CO_2,i}^L$  is uniform over the entire bubble surface and by assuming that the velocity vector  $\mathbf{v}_b^i$  is collinear to the bubble normal vector  $\mathbf{n}_b$ . The validity of these assumptions can be altered when the bubble has a non-spherical shape, like that obtained in the  $CO_2$ - $BMimPF_6$  system, and when the surface tension is not constant over the entire surface (this is the case for Marangoni effect), as for the  $CO_2$ - $EtOH$  system.

$$- \iint_{S_b} C_{CO_2,i}^L \mathbf{v}_b^i \cdot \mathbf{n}_b dS = - C_{CO_2,i}^L \iint_{S_b} v_b^i dS = C_{CO_2,i}^L \frac{dV_b}{dt} \tag{2.26}$$

Equations 2.23, 2.25 and 2.26 are substituted into Equation 2.22 and the result is given in Equation 2.27.

$$\begin{aligned}
\iiint_{V_L} \frac{\partial C_{CO_2}}{\partial t} dV & = \langle C_{CO_2} \rangle \frac{dV_L}{dt} + V_L \frac{d\langle C_{CO_2} \rangle}{dt} - \langle C_{CO_2} \rangle \frac{dV_{UC}}{dt} + C_{CO_2,i}^L \frac{dV_b}{dt} \\
& = V_L \frac{d\langle C_{CO_2} \rangle}{dt} + (C_{CO_2,i}^L - \langle C_{CO_2} \rangle) \frac{dV_b}{dt}
\end{aligned} \tag{2.27}$$

The terms A and B from Equation 2.14 are therefore simplified and it becomes:

$$V_L \frac{d\langle C_{CO_2} \rangle}{dt} + (C_{CO_2,i}^L - \langle C_{CO_2} \rangle) \frac{dV_b}{dt} = k_L (C_{CO_2}^* - \langle C_{CO_2} \rangle) S_b \tag{2.28}$$

For systems where the variation of the bubble size is not significant (such as segmented flow of  $CO_2$  and  $H_2O$ ), the term  $(C_{CO_2,i}^L - \langle C_{CO_2} \rangle) \frac{dV_b}{dt}$  is negligible compared with  $V_L \frac{d\langle C_{CO_2} \rangle}{dt}$  and the Equation 2.29 is then obtained, where  $a_L = S_b/V_L$  is the liquid specific surface.

$$\frac{d\langle C_{CO_2} \rangle}{dt} = k_L a_L (C_{CO_2}^* - \langle C_{CO_2} \rangle) \tag{2.29}$$



The Lagrangian approach enables the time derivative to be converted into a spatial derivative by assuming that the unit-cell is moving in the micro-channel at the mean velocity  $U_{TP}$  as given by Equation 2.30, where  $\dot{V}_{CO_2}$  and  $\dot{V}_{H_2O}$  are the volumetric flow rates of  $CO_2$  and  $H_2O$  at the inlet of the capillary and  $S$  the capillary cross section. The conversion of Equation 2.29 is presented in Equation 2.31.

$$U_{TP} = \frac{dz}{dt} = \frac{\dot{V}_{CO_2} + \dot{V}_{H_2O}}{S} \quad (2.30)$$

$$\frac{d\langle C_{CO_2} \rangle}{dz} = \frac{k_L a_L}{U_{TP}} (C_{CO_2}^* - \langle C_{CO_2} \rangle) \quad (2.31)$$

The determination of mass transfer coefficients under ambient conditions is based on the integration of Equation 2.31 along the micro-channel by assuming that  $k_L a_L$  is constant. However, it will be demonstrated in this thesis work that that this assumption is not valid at high pressure. The volumetric mass transfer coefficient  $k_L a_L$  is therefore determined with Equation 2.32 at different z-axis locations for an isothermal and isobaric system.

$$k_L a_L = \frac{U_{TP}}{C_{CO_2}^*(T, P) - \langle C_{CO_2} \rangle(z)} \frac{d\langle C_{CO_2} \rangle}{dz} \quad (2.32)$$

## 2.4 Conclusion

This chapter has presented a new way to approach the determination of mass transfer coefficient in a high-pressure two-phase segmented micro-flow. It has been demonstrated that the choice of the binary system has non-negligible impact on the modelling hypotheses. Indeed, the thermodynamic mixture properties of one binary system can be very different than those of another binary system and as a result, some hypotheses may no longer be valid. The mixture properties of  $H_2O$ ,  $EtOH$  and  $BMimPF_6$  saturated with  $CO_2$  have been investigated and the properties that can affect the behaviour of a two phase segmented flow have been highlighted and discussed. Finally, a unit-cell type mass transfer model has been developed for the  $CO_2$ - $H_2O$  system. Each hypothesis has been discussed for the other two exemplary binary systems and the differences with the model hypotheses at ambient conditions have been emphasized. The last part of this chapter presents the equations for the determination of the liquid volumetric mass transfer coefficient of a two-phase segmented flow of  $CO_2$ - $H_2O$ , which are used in the experimental chapters of this thesis work. Using this approach, the volumetric mass transfer coefficient can be calculated at different locations along a microchannel and it is therefore possible to observe the spatial evolution of the mass transfer rate.



# Microreactor design and manufacturing process

Introduction . . . . .	93
3.1 Microreactor elements and manufacturing tools . . . . .	96
3.2 Frame manufacturing . . . . .	99
3.3 Assembly and integration of capillary tubes in the frame . . . . .	100
3.4 Casting of the resin . . . . .	102
3.5 Manufacturing time . . . . .	102
3.6 Manufacture of the temperature-controlled chamber . . . . .	104
3.7 Pressure and temperature resistance tests . . . . .	106
Conclusion . . . . .	107

## Introduction

Over the last twenty years , microreactors have shown to be efficient tools to investigate heat and mass transport, as well as chemical process intensification (Kockmann (2007), Santana et al. (2018)). Due to the decrease in the characteristic length of the system and consequently the massive increase of the surface to volume ratio (about a thousand times higher compared with conventional macro-scale vessels), the characteristic times of different phenomena (e.g. heat and mass transfer) are drastically reduced. This reduction in characteristic times leads to shorter experimental times, thereby allowing high data acquisition rates and the potential explore of operating conditions wide ranges (such as temperature, pressure and flow rates) very quickly. Due to the intensified transport processes, microreactors have also shown to be of interest for applications in the field of supercritical fluids (Marre et al. (2010), Luther et al. (2012), Andersson et al. (2018)). Microreactors used for such applications require high pressure resistance in order to reach the supercritical region of the fluid employed (e.g. 7.3 MPa for the carbon dioxide) and various kinds of pressure resistant microreactors have been developed as presented in Section 1.2.3 of Chapter 1. For the fundamental study and understanding of transport phenomena in supercritical fluids in microreactors, optical access

---

to the flow is often desired. Whilst some pressure-resistant microreactors are commercially available, they do not always provide the desired characteristics for the intended measurement techniques and process conditions.

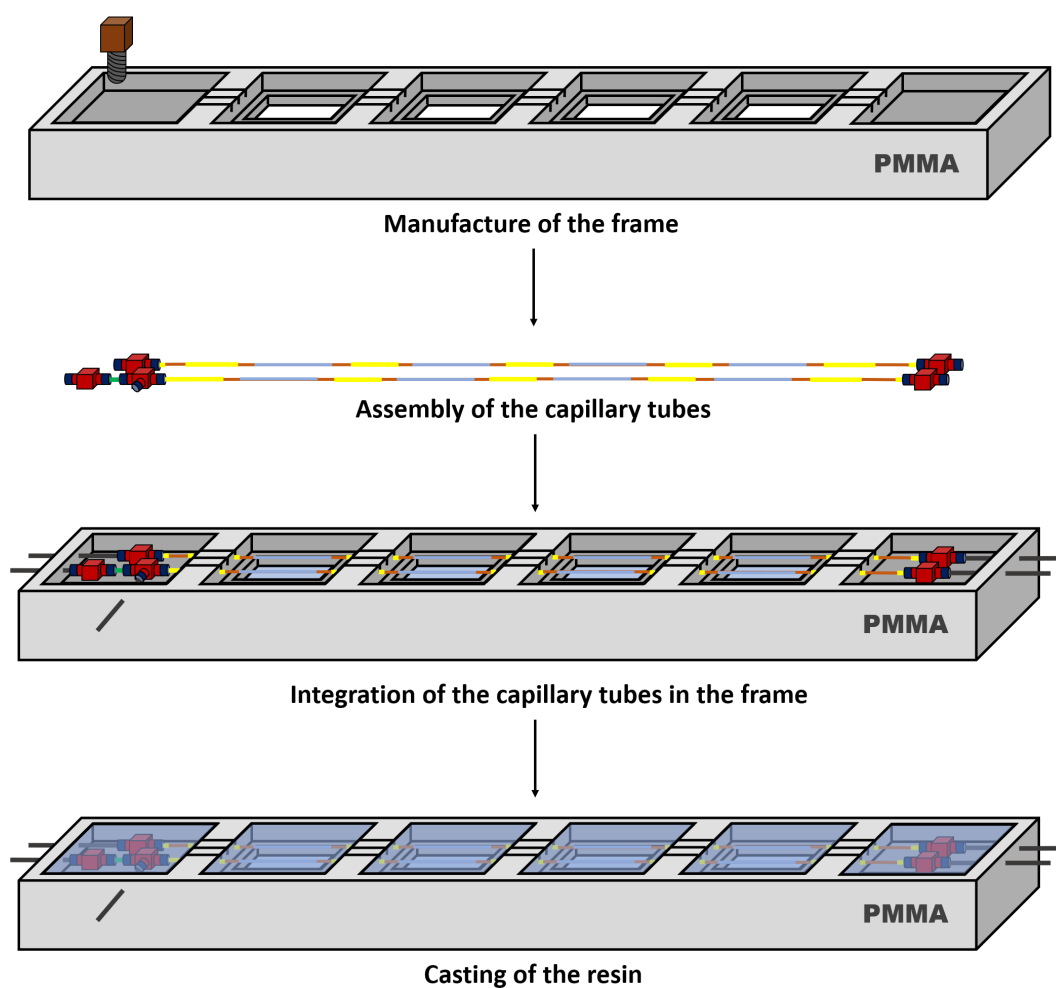
The objectives of the work detailed in this chapter are therefore to develop a microreactor for the study of flow and mass transfer in high-pressure two-phase flow that allows:

- fast screening and data acquisition
- on-line characterization of transport phenomena and reactions
- reliable control of temperature and pressure
- repeatability of measurements

This chapter presents the manufacturing process of a temperature-controlled and pressure-resistant microreactor based on the previous work of Macedo Portela da Silva et al. (2014). The device is composed of two parts: (i) the microreactor made with silica micro-capillary tubes embedded in resin (ii) a temperature-controlled chamber in order to maintain a constant temperature in the microreactor. The specifications of the entire device are as follows:

- Suitable in particular for supercritical carbon dioxide investigations and all other fluids that are compatible with stainless steel and fused silica.
- Resistant to pressures tested up to 25 MPa and temperatures tested up to 333 K.
- Excellent optical access provided (from the top and the bottom reactor).
- Optical access over a length of 0.16 m.
- Inexpensive to make (less than 200 euros of materials per reactor).

The main advantage of such an experimental device for investigating and characterizing transport phenomena is that experiments can be performed quickly, giving access to a large quantity of data in a short time. For example, in a segmented two-phase flow, up to a thousand data points can be obtained in just one second. This chapter presents each step of the manufacturing process, which is summarized in Figure 3.1. The first step consists in the manufacture of the reactor frame by drilling a Polymethyl methacrylate (PMMA) block. The second step is the assembly of the micro-capillary tubes. In the third step, these micro-capillaries are inserted in the PMMA frame. Finally, an epoxy resin is cast in the frame. Following this, the manufacture of the temperature-controlled chamber is presented. Lastly, the pressure, temperature and hydrodynamics tests of the microreactor are presented.



**Figure 3.1** – Fabrication steps of the microreactor made of fused silica capillary tubes able to resist high pressure.

---

## 3.1 Microreactor elements and manufacturing tools






Tables 3.1 to 3.4 present the different elements and tools used to manufacture the microreactor. Each element has an associated code and symbol, which facilitate the reading of other figures. The specifications and the supplier of the different elements and tools are also provided. The manufacturing process requires the use of different kinds of tubes listed in Table 3.1. These include silica capillary tubes (TU-01 and TU-02, later called outer capillary and inner capillary, respectively), cylindrical plastic tubes or sleeves (TU-02 and TU-03), which allow to the silica capillary tubes to be connected to 1/16'' tubes and fittings, and 1/16'' stainless steel tubes (TU-05), which enable connection with the feeding system (pumps).

The pressure-resistant fittings used are listed in Table 3.2. The T-junctions and U-junctions (CO-01 and CO-02) allow the capillary tubes (TU-01 and TU-02) in the reactor to be connected with the rest of the setup (e.g. pumps) via stainless steel tubes (TU-05). The fitting CO-03 is a bulkhead that penetrates the temperature-controlled chamber of the reactor. All the previously cited fittings use a combination of nuts (CO-04) and ferrules (CO-05) in order to maintain the seal under high-pressure.

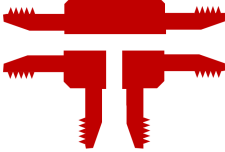




The manufacturing process requires the use of diverse raw materials, glues and fluids, which are presented in Table 3.3. The PMMA block (RM-01) is the basis for the reactor frame and the glass windows (RM-02) provide optical access to the flow in the tube. The epoxy glue (FL-01) is used to stick the capillaries to the frame before casting epoxy resin inside (FL-02). During the fabrication of the reactor, cleaning steps are performed using ethanol (FL-03) and acetone (FL-04) in order to remove impurities that could lead to poor quality images and measurements of the flow. The solvents are almost pure in order to avoid the addition of undesired dust on the cleaned surfaces. Lastly, silicone seals (FL-05) are used to handle the thermal dilatation difference between the glass slides, the PMMA frame and the resin.

The tools employed in the fabrication steps are listed in Table 3.4. They include a CharlyRobot digital milling machine (TL-01), a small electric drill (TL-02) and tube cutters (TL-03 and TL-04), which are used to cut the capillary tubes (TU-01 and TU-02) and the stainless steel tubes (TU-05) respectively.

**Table 3.1** – Types of capillary tubes required for the microreactor and suppliers. ID (inner diameter). OD (outer diameter).

Code	Name	Specifications	Supplier	Symbol/Picture
TU-01	Silica capillary	$ID = 250\ \mu\text{m}$ $OD = 660\ \mu\text{m}$	Molex Polymicro Technologies	
TU-02	Silica capillary	$ID = 75\ \mu\text{m}$ $OD = 150\ \mu\text{m}$	Molex Polymicro Technologies	
TU-03	Sleeve	$ID = 675\ \mu\text{m}$ $OD = 1/16''$	Molex Polymicro Technologies	
TU-04	Sleeve	$ID = 175\ \mu\text{m}$ $OD = 1/16''$	Molex Polymicro Technologies	
TU-05	Stainless steel tube	$ID = 600\ \mu\text{m}$ $OD = 1/16''$	Upchurch Scientific	




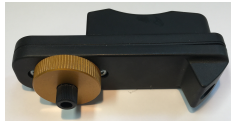
**Table 3.2** – Listing of the 1/16'' fittings employed to manufacture the microreactor.

Code	Name	Specifications	Supplier	Symbol/Picture
CO-01	T-junction	U-402	Upchurch Scientific	
CO-02	Union	U-428	Upchurch Scientific	
CO-03	Bulkhead	1BU316	Gyroloc	
CO-04	Nut	1/16''	Upchurch Scientific	
CO-05	Ferrule	1/16''	Upchurch Scientific	

**Table 3.3** – Glue, fluids and raw materials employed in the fabrication steps.

Code	Name	Specifications	Supplier
RM-01	PMMA block	270×140×20 mm <sup>3</sup>	Abaqueplast
RM-02	Glass slides	71×32×2 mm <sup>3</sup>	Miroiterie Ets Malzac (Albi)
FL-01	Epoxy glue	159-3957	RS components
FL-02	Epoxy resin	EP 601-LV	Polytec
FL-03	Ethanol	Purity 99% molar	Sigma-Aldrich
FL-04	Acetone	Purity 99% molar	Sigma-Aldrich
FL-05	Silicone seal	494-102	RS components

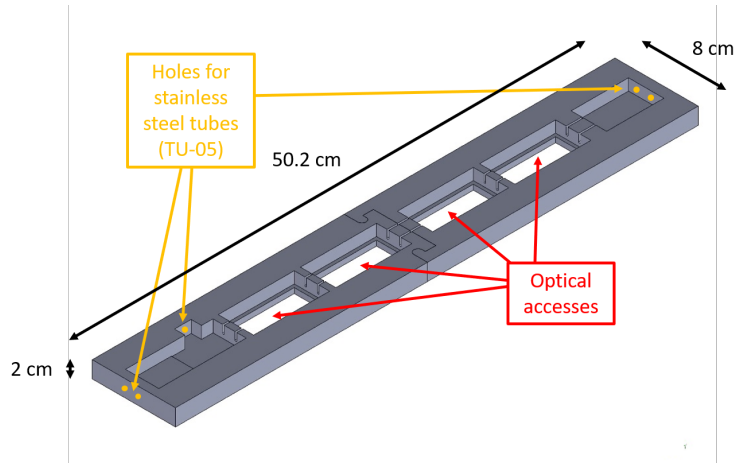
**Table 3.4** – Tools used for the different fabrication steps.

Code	Name	Supplier	Photo
TL-01	Milling machine	Mécanuméric, France	
TL-02	Electric drill	Dremel, EU	
TL-03	Tube cutter 1	Scientific Glass Technology	
TL-04	Tube cutter 2	RS components, UK	



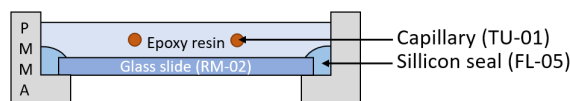
## 3.2 Frame manufacturing

The manufacturing step of the frame is the first part of the microreactor fabrication process. The frame of the microreactor is the support in which the micro capillary tubes are placed so that they are held in place in a perfectly horizontal manner. The frames are created by milling a polymethyl methacrylate (PMMA) block ( $270 \times 140 \times 20 \text{ mm}^3$ ) using a digital milling machine, CharlyRobot-4U from MECAnumeric. The reactor frame is presented in Figure 3.2. Milling is performed using four different drills. Table A.1 in Appendix A provides values of the drill diameter, angular speed, advance speed and plunge speed. The drill speeds are key parameters for milling since the milling time is function of these speeds. However, if the drilling speeds are too fast, the PMMA block can be damaged. Several tests have been performed in order to choose the optimal parameters for milling.



**Figure 3.2** – 3D view and dimensions of the microreactor frame.

The frame of the microreactor is divided into two parts called part 1 and part 2. The dimensions of both parts are presented in Figure A.2 in Appendix A as well as the drilling depth for each drill (Figure A.3 in Appendix A). After the milling step, glass slides (RM-02) are glued with an epoxy glue (FL-01) inside the PMMA frame of the reactor. The glass slides provide optical access as shown in Figure 3.2. Both parts of the reactor are then carefully glued together. Preliminary compatibility tests between PMMA and glues such as epoxy, araldite and cyanoacrylate have been carried out. It was found that cyanoacrylate glues are not compatible with PMMA (and epoxy resin) since they diffuse within-it. Araldite and epoxy glues are compatible with PMMA but since the resin cast in the next step is an epoxy type, the final choice was the epoxy glue. After a drying period of at least two hours at ambient temperature, a silicone seal (FL-05) is fitted to the edges of the glass slides as can be seen in Figure 3.3.

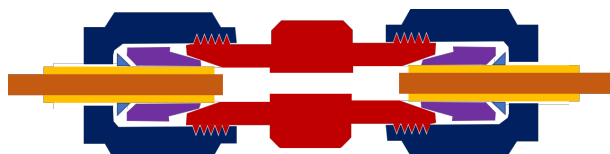


**Figure 3.3** – Cross-section of the optical access window in the microreactor.

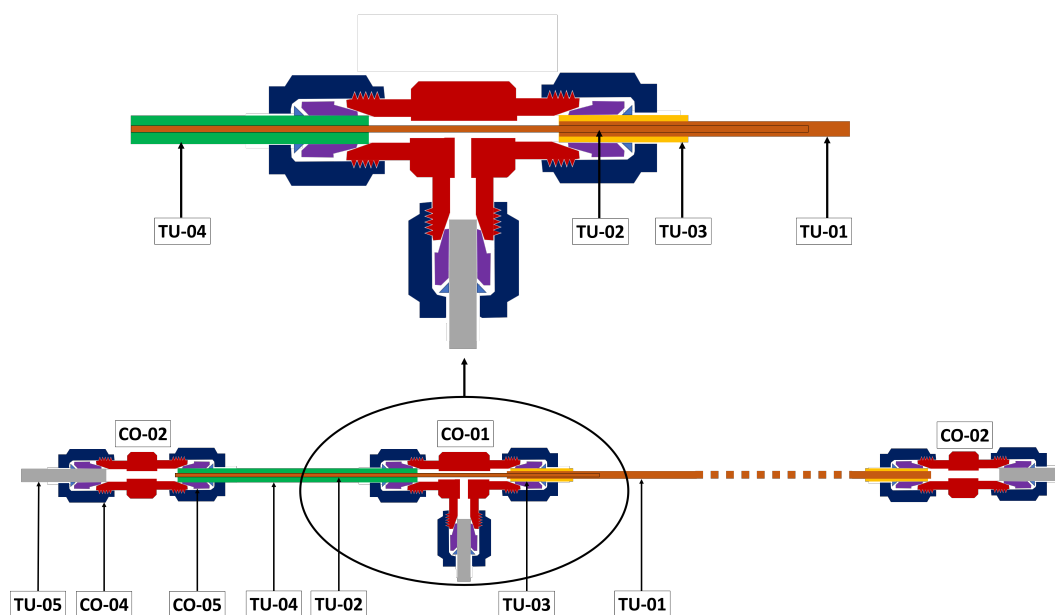
It is important to point out that when the reactor temperature is greater than 303 K and no silicone seals are used, the glass slides inside the reactor break due to a difference in thermal dilatation of the different materials (PMMA, glass and the epoxy resin). After a second drying step of one hour at room temperature, five holes with a diameter of 1/16" are drilled with an electrical drill (TL-02) in order to insert the 1/16" stainless steel tubes through the PMMA frame (see Figure 3.2).

### 3.3 Assembly and integration of capillary tubes in the frame

The fittings employed in the microreactor are based on assembling ferrules, sleeves and nuts as presented in Figure 3.4. This type of assembly enables pressure-resistant connection between micro capillary tubes and any kind of 1/16" tubes (including sleeves). This type of connection is also used in order to create a coaxial injection of two fluids at the inlet of the microreactor. Figure 3.5 shows the coaxial injection setup, which is made with a T-junction (CO-01), two different sizes of silica capillaries (TU-01 and TU-02) and adapted sleeves to increase their diameter to 1/16" (TU-03 and TU-04). The "inner capillary" (TU-02) is inserted inside the T-junction (CO-01) and then in the "outer capillary" (TU-01).

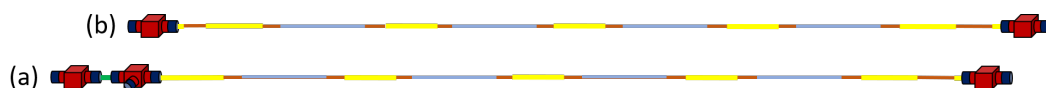


**Figure 3.4** – Ferrule-sleeve-nut assembling.



**Figure 3.5** – Coaxial injection inside the microreactor.

The silica capillary (TU-01) is cut with the tube cutter (TL-03) into two 38.2 cm pieces and the silica capillary (TU-02) into one 8 cm piece. The stainless steel tube (TU-05) is cut with the tube cutter (TL-04) into five 12 cm pieces. Appropriate sleeves are placed around the capillaries in order to make a support on the frame and to align it horizontally. The five stainless steel tubes are placed inside the five holes drilled during the frame fabrication step. The coating of the two pieces of "outer capillary" (TU-01) is removed with a flame in order to obtain an optical access. The coating layer is removed over a length of 2 cm at eight different spots (two for each optical glass window). After the coating layer is removed, the capillary is carefully cleaned with cotton buds impregnated with ethanol (FL-03). The capillary is checked with a microscope to ensure that no combustion residues from the removal of the coating are present. Four unions (CO-02) and one T-junction (CO-01) are used to connect the inner capillary and the outer capillary as presented in the Figure 3.6. Two channels are made in the reactor: one where two fluids can be mixed ((a) on Figure 3.6), and one where only one fluid can flow ((b) on Figure 3.6). The two assemblies of capillary tubes are then placed inside the frame and the five previous stainless-steel tubes are connected. The capillary assemblies are glued to the frame with epoxy glue (FL-01). The microreactor is connected to an ISCO pump filled with water in order to verify that the microreactor is not clogged (water flow rate of  $500 \mu\text{L min}^{-1}$ ).

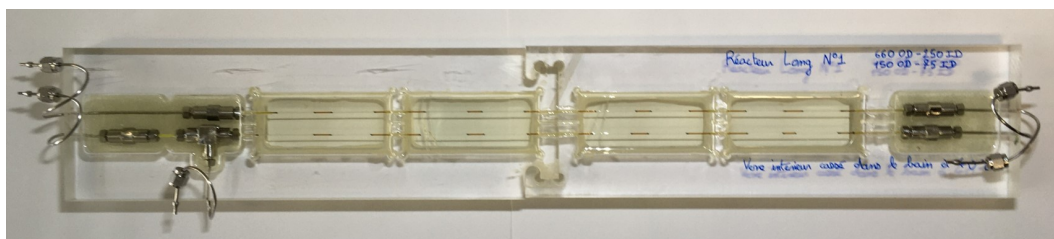


**Figure 3.6** – Assembly of the capillary tubes to form two channel types (a) where two fluids can be mixed (b) for single fluid.

---

### 3.4 Casting of the resin

The removal of the polyimide coating on the capillaries (in order to provide optical access to the flow in the channel) drastically reduces the pressure-resistance. Without the coating, the capillaries break at about 10 MPa. In order to reinforce the capillaries without hindering optical access, epoxy resin is cast inside the frame around the silica capillaries. This allows high-pressure resistance of the capillaries up to 30 MPa. The epoxy resin (FL-02) is a two component mixture, including the fixing agent and the resin itself. Special care is taken during the mixing step to ensure that the components are uniformly mixed. The proportion of each component to be used is described in the technical documentation of the resin. Both components are mixed and then placed in a vacuum at 400 mbar for one hour in order to remove the dissolved air. If the pressure is set below 400 mbar, the fixing agent is removed from the mixture and the hardening performance of the resin is reduced. Before casting the resin in the frame, the glass windows are cleaned with acetone (FL-04) to remove any epoxy glue residues or finger prints. The capillary tubes where the coating has been removed are also cleaned with ethanol (FL-03). These sections are checked under the microscope before casting the resin. The resin is cast in the frame and the microreactor is placed in an oven at 303 K for 20 hours. When the resin is poured into the frame, some air bubbles can be trapped and persist even after the venting chamber process. These bubbles can be removed with a small pencil during the first two hours in the oven. When the resin has set, the microreactor is ready for use. If the previous epoxy gluing step is not performed correctly, the resin, which is highly fluid can go through the holes and leak from the frame. In case resin does not sufficiently fill the frame after it hardens, it is still possible to cast extra resin since the interface between a previously hardened and a new resin layer is not visible. A photo of the final reactor is shown in Figure 3.7.

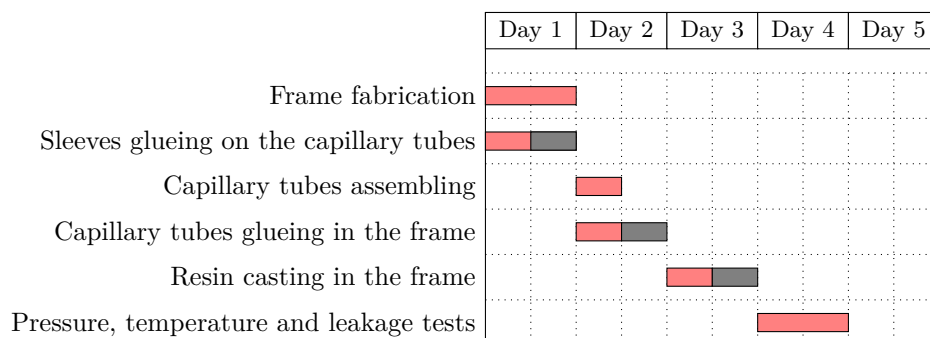


**Figure 3.7** – Photo of the microreactor after the fabrication steps. The final dimensions of the reactor are 50.2 cm×8.0 cm×2.0 cm.

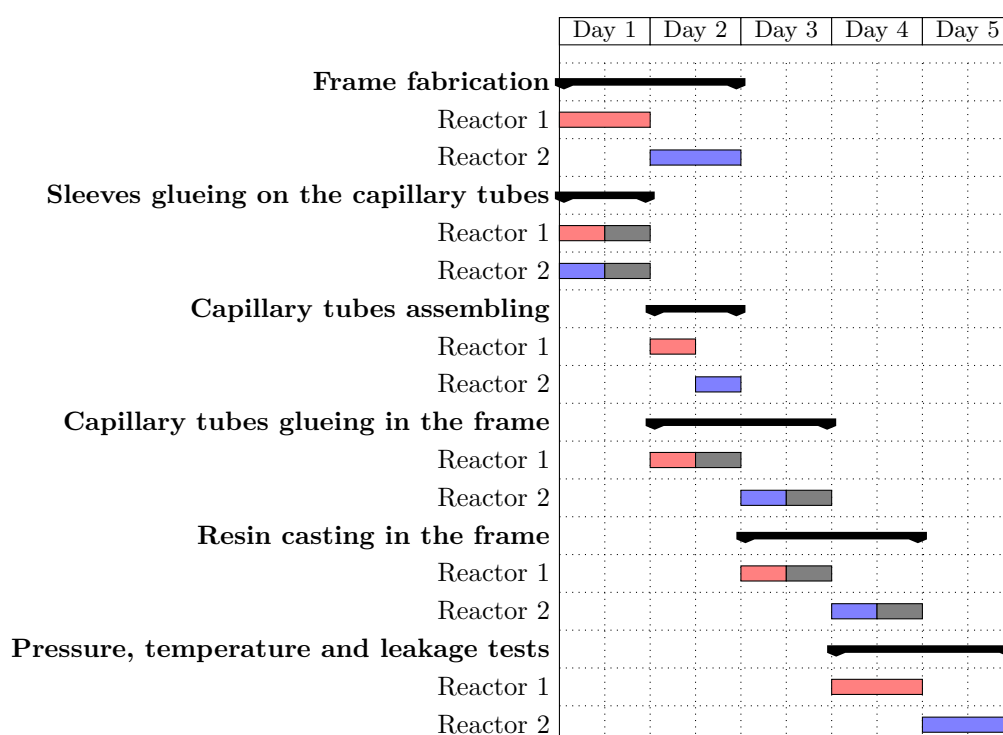
### 3.5 Manufacturing time

Figure 3.8 shows a Gantt diagram describing the duration of the manufacturing process. The fabrication of one microreactor take in average four days. The manufacturing time of this kind of reactor is relatively short compared with the procedure of purchasing a commercial microreactor from a supplier and allows flexibility in the design. However, even if a reactor can be manufactured in just four days, the development of the manufacturing process took

several months. Indeed, an error at one step often leads to failure of the pressure, temperature and/or leakage tests and a new reactor then has to be made. In order to anticipate this, two reactors can be manufactured in parallel in a total time of five days, as presented in Figure 3.9. It is rare to obtain a defective reactor; only one reactor in five fails the fabrication tests. The raw materials and elements required to manufacture one reactor cost in average 200 euros. However, the most expensive elements of the reactor (e.g. CO-01 and CO-02) can be reused so the fabrication process is also cost-efficient.



**Figure 3.8** – Reactor fabrication Gantt chart. The red symbol corresponds to the tasks related to the work on the reactor and the grey corresponds to drying periods.



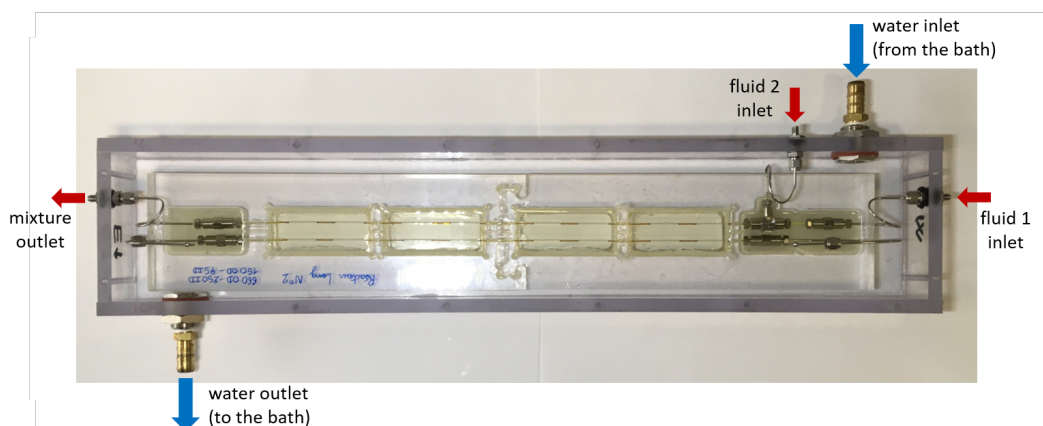
**Figure 3.9** – Reactor fabrication Gantt chart of two reactors simultaneously. The red bars corresponds to the tasks related to the first reactor, the blue ones to the second reactor and the grey ones corresponds to drying periods.

---

## 3.6 Manufacture of the temperature-controlled chamber

In order to maintain the temperature of the microreactor and the fluid within at a constant value, the microreactor is inserted in a chamber filled with temperature-controlled water as shown in Figure 3.10. The specifications of the conditioning chamber are the following:

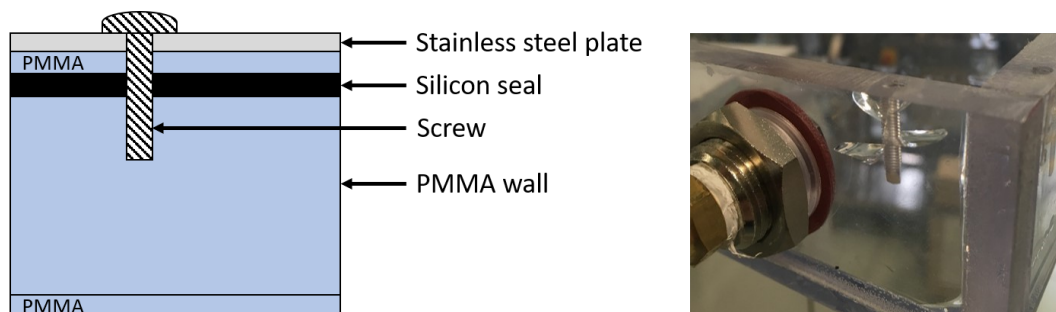
- Optical access from both sides.
- Access for an external bath.
- Resistance to water flow from the external bath.
- Resistance to temperature tested up to 333 K.
- Easy access to the microreactor in case it needs to be replaced.
- Pressure-resistant bulkhead in order to feed the reactor placed inside.



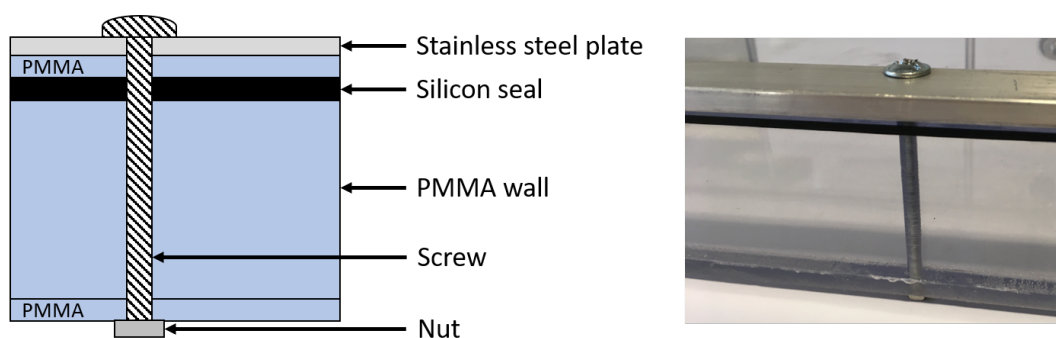
**Figure 3.10** – Top view of the temperature-controlled chamber with the reactor placed inside.

The chamber is made from PMMA plates with a thickness of 10 mm for the side walls, and of 5 mm for the top and the bottom walls of the chamber. The outer dimensions of the conditioning chamber are  $56.5 \times 11.6 \times 5.2 \text{ cm}^3$ . The PMMA walls are chemically bonded with chloroform, which provides a water-tight seal. The top of the chamber has three layers: the PMMA top part, a silicon black flat seal, and a stainless steel flat plate, which allows the silicon seal to be flattened lengthwise. The first attempt to consolidate these three layers to the walls of the chamber was to screw them together, as presented in the left part of Figure 3.11. However, the mechanical stress of the screw on the PMMA increased with temperature and caused the PMMA to crack as it can be observed in the right part of Figure 3.11. The solution to this problem was to completely cross the PMMA chamber wall with the screw and to add a nut as depicted in Figure 3.12. In this way, the mechanical stress of the screw

is no longer directly exerted on the PMMA.



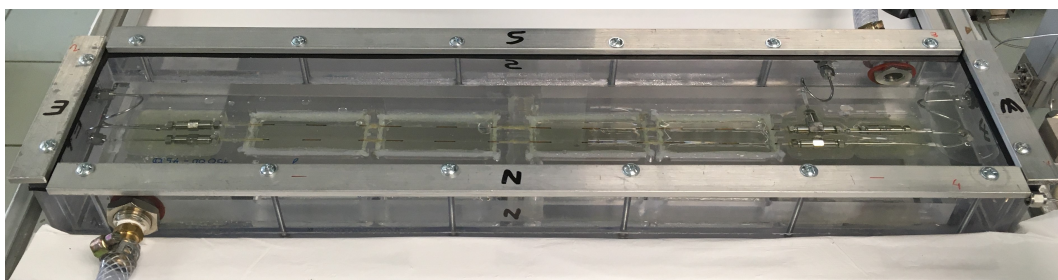
**Figure 3.11** – (Left) Temperature-controlled chamber closure with a simple screw system. (Right) Cracked PMMA due to the screw system closure.



**Figure 3.12** – Temperature-controlled chamber closure with a screw-nut assembling. The mechanical stress is applied on the nut instead of the PMMA wall.

The chamber is fed continuously with an external temperature controlled water bath. Several holes are drilled in the top of the chamber in order to purge air bubbles, which can perturb image acquisition. These holes are also used for inserting thermocouples to measure water temperature in the chamber. In addition, three holes are drilled through the side wall of the chamber for pressure-resistant bulkheads (CO-03). Bulkheads allow the reactor inside the chamber to be connected to the external pumps using a ferule-nut assembly.



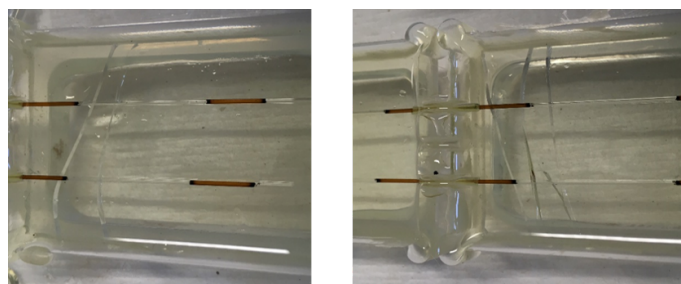


**Figure 3.13** – Top view of the entire microfluidic system, the reactor and the temperature-controlled chamber able to resist pressure up to 25 MPa and temperature up to 333 K.

The combination of the reactor and the conditioning chamber presented in Figure 3.13 is a complete setup which renders the investigation of two-phase flow possible at high pressure (tested up to 25 MPa) and temperature (tested up to 333 K). The optical access along the reactor allows the on-line characterization with methods based on image acquisition.

### 3.7 Pressure and temperature resistance tests

Prior to use, performance tests of the microreactor are carried out in order to evaluate the pressure -and temperature- resistance of the setup. To test the temperature-resistance of the microreactor and chamber, the entire setup is connected to pumps and the water bath at 333 K for eight hours. During the frame fabrication, a silicon seal (FL-05) is applied between the optical glass windows and the epoxy resin. This addition was made after the observation that an increase in temperature broke the glass windows as shown in Figure 3.14. After the use of the new conditioning chamber screw system and the addition of silicon seals, the temperature issue was completely solved. The setup has been proven to work correctly for temperatures up to 333 K (max temperature tested).

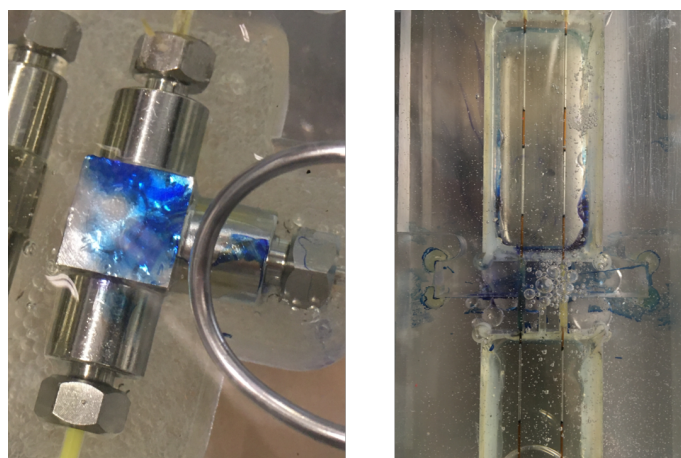


**Figure 3.14** – Broken glass slides observation due to a dilatation difference between the glass, the PMMA and the epoxy resin at 333 K.

The pressure-resistance of the reactor is tested at 333 K. To do this, the pressure is increased up to 25 MPa with water for eight hours. If the water leaks through the stainless steel connectors, the issue is fixed with extra clamping. However, if the water leaks through



the micro-system inside the resin, the microreactor is faulty. During the study, only one reactor was defective after a long period of use (around 300 hours). The diagnostic was that the epoxy glue used to fix the capillaries inside the frame was of poor quality<sup>1</sup>. The water permeated the epoxy glue near the T-junction and at the junction between the two parts of the reactor. The water causes the glue to soften and reduces its pressure-resistance. As a consequence, the reactor leaked and broke as depicted in Figure 3.15. The use of an epoxy glue of good quality (like the one listed in Table 3.3) solved the issue of water infiltration. The reactor presented in this chapter can be used for hundreds of hours if the pressure is slowly increased before use (2 MPa per minute) and decreased slowly after use (1 MPa per minute).



**Figure 3.15** – Coloured water leaking through the T-junction (left) and at the union of the parts of the microreactor due to a poor epoxy glue quality.

## Conclusion

This chapter presented the entire manufacture process of a temperature-controlled microreactor system made with capillary tubes that resists pressure up to 25 MPa and moderate temperature up to 333 K. The manufacture of the microreactor is cost-efficient with a price of 200 euros (materials only) where almost half of it is reusable. The fabrication time is reasonable since two reactors can be built in one week. The manufacture of the microreactor was fully described step by step in order to allow a reader to recreate such reactor by avoiding issues such as the non-compatibility between components or the low temperature and pressure resistance in some configurations. The disadvantages of such reactor could be the low resistance to temperatures higher than 348 K because of the dilatation difference of the components used (PMMA, glass and epoxy resin), and the small optical access zone which is around 50% of the entire capillary length. This reactor is employed in the colorimetric method presented in Chapter 5.

<sup>1</sup>It was a low quality epoxy adhesive, unsuitable for applications under water, inadvertently used.



# Determination of mass transfer coefficients using Raman Spectroscopy

Introduction . . . . .	110
4.1 Raman spectroscopy . . . . .	113
4.1.1 Raman Effect . . . . .	113
4.1.2 Principle of Raman spectroscopy . . . . .	113
4.1.3 Calibration step . . . . .	115
4.1.4 Raman spectra of pure $CO_2$ and pure $H_2O$ . . . . .	116
4.1.5 Raman spectra of $CO_2$ and $H_2O$ liquid mixture . . . . .	117
4.2 Experimental method . . . . .	119
4.2.1 Experimental setup . . . . .	119
4.2.2 Operating conditions . . . . .	123
4.2.3 Raman spectroscopy measurement setup . . . . .	124
4.2.4 Raman spectra measurements . . . . .	126
4.3 Determination of mass transfer . . . . .	127
4.3.1 Determination of $C_{CO_2}$ . . . . .	127
4.3.2 Determination of the volumetric mass transfer coefficient $k_L a_L$ . . . . .	129
4.4 Application of the experimental method to $CO_2$ - $H_2O$ mass transfer under high pressure . . . . .	130
4.4.1 Concentration profiles . . . . .	130
4.4.2 Effect of flow rate conditions on $k_L a_L$ . . . . .	133
Conclusion . . . . .	136

---

## Introduction

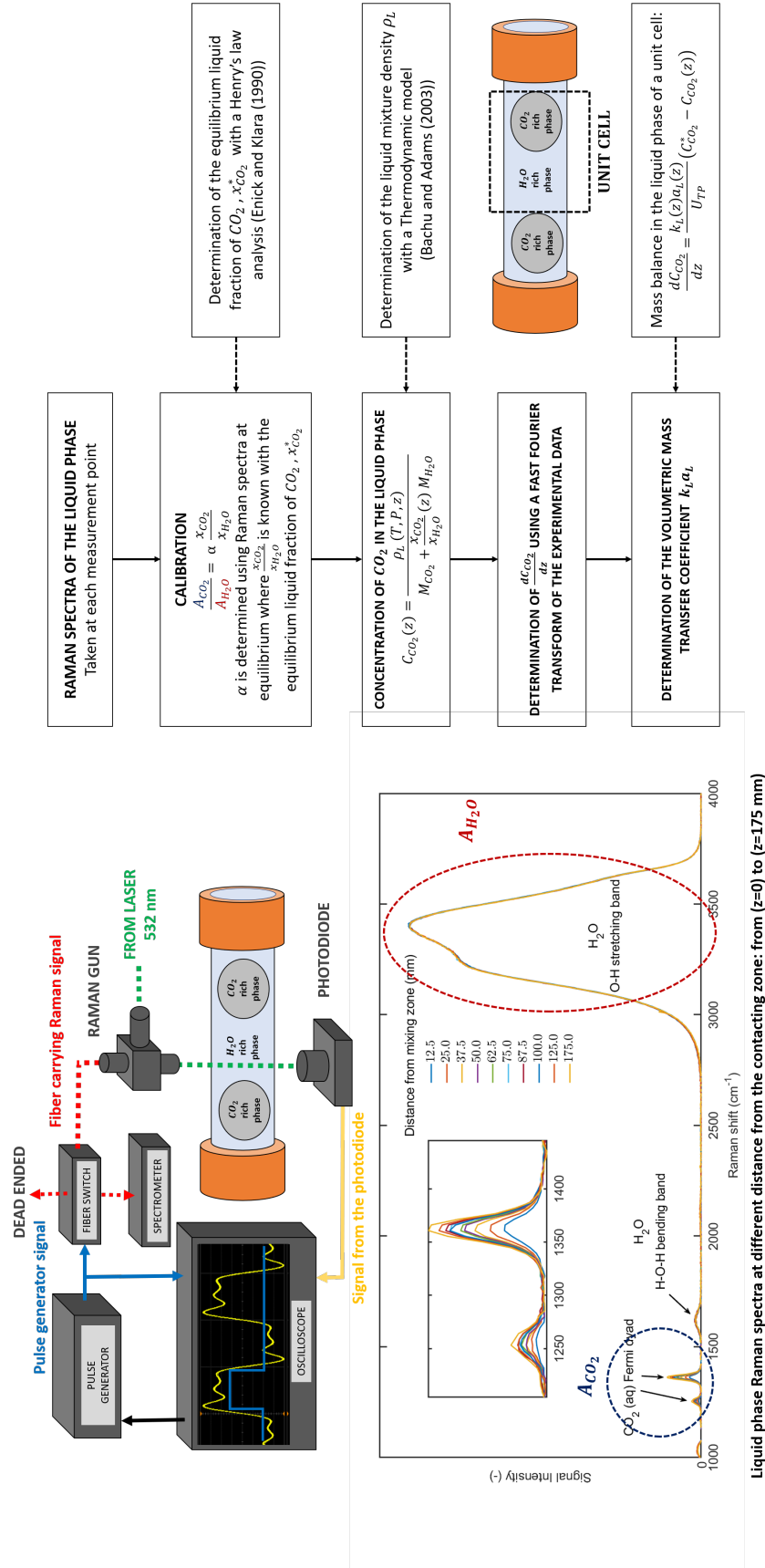
This chapter presents a new and rapid method for the determination of mass transfer coefficients using Raman spectroscopy that is applied to a high-pressure  $H_2O$  -  $CO_2$  system in a micro-capillary tube.  $H_2O$  and  $CO_2$  are fed at high pressure (between 8 MPa and 10 MPa) and moderate temperature (303 K) in the micro-capillary tube in order to obtain a segmented two-phase flow. The aim of the experiments is to characterise the mass transfer from the  $CO_2$ -rich phase towards the  $H_2O$ -rich phase during the bubble-drop formation process and after, by determining the liquid volumetric mass transfer coefficient.

The method presented in this chapter is based on the acquisition of Raman spectra inside the liquid phase of the segmented two-phase flow. After a preliminary calibration step, the measured Raman spectra give the molar ratio of the compounds within the liquid phase. Using a thermodynamic model for liquid mixtures that takes into account the density variation along the micro-capillary tube due to the gas dissolution, the concentration of gas dissolved in the liquid phase is determined. The discrete concentration values obtained from the Raman spectra are filtered with a Fast Fourier Transform in order to compute their first derivative. This is used as an input to the model presented in Chapter 2 which then allows the liquid volumetric mass transfer coefficient  $k_L a_L$  to be determined. The advantages of this Raman spectroscopy method for the determination of mass transfer coefficients are numerous:

- This method enables values of the volumetric mass transfer coefficient to be determined at different positions along the length of the tube rather than providing an average value between the inlet and the outlet of the tube (which is the case for most conventional measurement methods).
- This method is not intrusive and does not disturb the flow in the system.
- This method allows complex systems to be studied where the mass transfer occurs in both directions (from the dispersed to the continuous phase and from the continuous to the dispersed phase).
- This method takes into account a possible density change in both phases which can occur during the mass transfer process.

This chapter describes the different steps of the method, which are summarized in Figure 4.1. The first part of the chapter presents an overview of the Raman effect and the spectroscopic technique that results from it. The second part presents the experimental setup, which enables spectroscopic measurements to be performed in a specific phase of a  $H_2O$  –  $CO_2$  two-phase segmented flow at high pressure in a micro-capillary tube. The third part of the chapter describes and how the volumetric mass transfer coefficient is determined. The final part of the chapter presents the application of the experimental method to a two-phase segmented flow of  $CO_2$  and  $H_2O$  at varied flow rates and operating pressures.

The contents of this chapter have been published in Chemical Engineering Science (228, 115960, <https://doi.org/10.1016/j.ces.2020.115960>, 2020) provided in Appendix F.



**Figure 4.1** – Raman spectroscopy technique applied to the measurement of mass transfer coefficient in two phase segmented flow at high pressure.

## 4.1 Raman spectroscopy

This section presents the Raman effect and the related spectroscopic technique. The principle of the Raman effect is presented, as well as how Raman spectra are obtained experimentally. In addition, the Raman spectra of pure liquid  $H_2O$ , pure  $CO_2$  and a liquid  $H_2O$ -rich phase saturated with  $CO_2$  are presented and described with respect to the molecular bond vibrations of each molecules.

### 4.1.1 Raman Effect

The Raman Effect was discovered around 1930 by two Indian physicists, Sir Chandrashekhara Venkata Raman (1888-1970) and Sir Kariamanickam Srinivasa Krishnan (1898-1961), and at the same time by Leonid Mandelstam (1879-1944). The Raman effect is a phenomenon whereby the frequency (and hence wavelength) of light passing through a medium is slightly modified due to an energy exchange between the light and the media. When the light (like the laser beam in Figure 4.2) is passing through a medium, photons from the light source can be absorbed, transmitted or scattered. Photons can be scattered in two different ways. The first one is elastic scattering, whereby the photons are scattered with the same energy and momentum as the incident photon but with a different direction; this is called Rayleigh scattering. The second is inelastic scattering (and concern only one in a million photons) where the photons are scattered with slightly different energy and therefore wavelength; this is described as a shift.

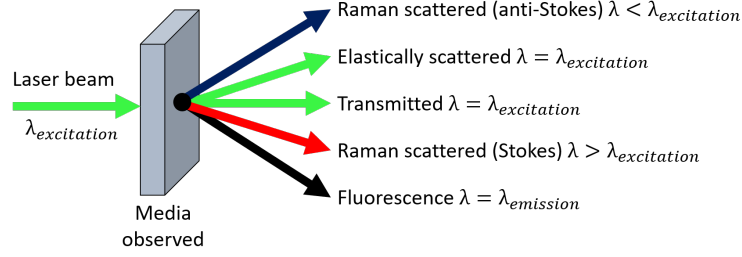
This shift can be quantified in terms of frequency. The frequency shift of a photon corresponds to the vibrational frequency of a specific molecular bond located in the medium. The electrical field from the excitation source creates an induced dipole for the molecule that depends on the type of molecule vibration (change of polarizability), like stretching and bending. Stokes scattering corresponds to when a photon is shifted to lower energy ( $\lambda > \lambda_{ex}$ ) and anti-Stokes scattering corresponds to when a photon is shifted to higher energy ( $\lambda < \lambda_{ex}$ ). As a consequence, Stokes radiation has lower energy compared with anti-Stokes radiation as presented in Equation (4.1)

$$E_{photon} = h\nu = h\frac{c}{\lambda} \quad (4.1)$$

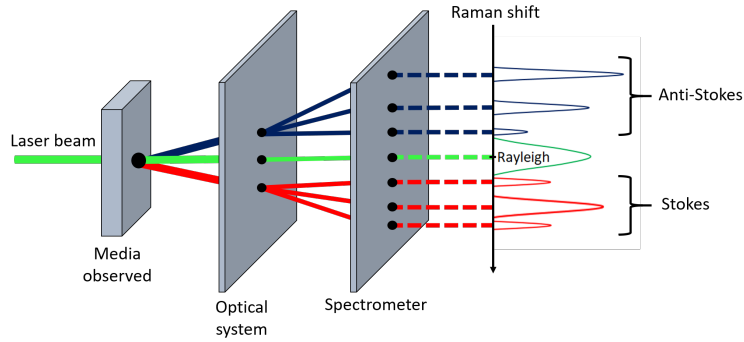
where  $h$  is the Planck constant,  $\nu$  the frequency,  $\lambda$  the wavelength and  $c$  the speed of light in vacuum.

### 4.1.2 Principle of Raman spectroscopy

Raman spectroscopy is based on the Raman effect. It is a non-destructive and non-invasive method that allows the observation and the characterization of the inner molecular composition and structure of the molecules within a medium. The non-elastic scattering of a photon is rare but with the use of a laser beam, the number of photons emitted is high



**Figure 4.2** – Different light interaction with matter when the photons are not absorbed by the medium.



**Figure 4.3** – Rayleigh, Stokes and anti-Stokes radiation and Raman spectroscopy technique.

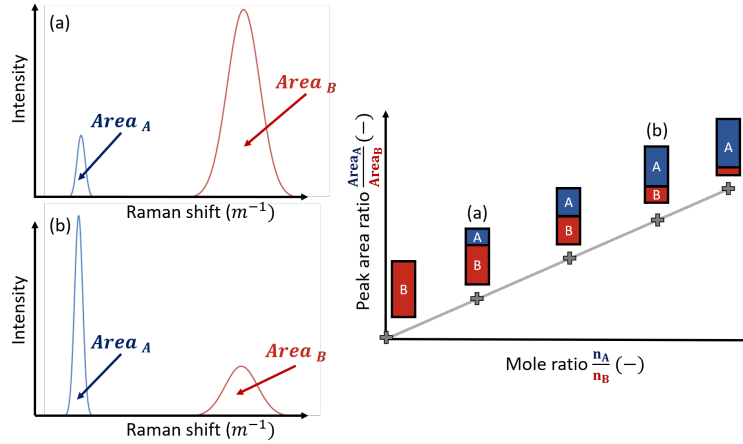
enough to detect Stokes or anti-Stokes radiations with a spectrometer. The wavelengths of the non-elastic radiations are characteristic of the vibrational frequencies of the molecules present in the medium observed. As a consequence, it is possible to identify the molecules present in the medium and also to quantify the number of molecules using a preliminary calibration.

With the use of a laser beam of a certain wavelength, the spectroscopic technique consists in the observation of the wavelength shift between the laser (Rayleigh emission) and the Stokes or anti-Stokes emission collected by the spectrometer (Figure 4.3). This shift is quantified in terms of Raman shift as presented in Equation (4.2), where  $\lambda_{ex}$  is the wavelength of the laser excitation and  $\lambda$  the wavelength of the Stokes or anti-Stokes emission from the media.

$$\text{Raman Shift} = \frac{1}{\lambda_{ex}} - \frac{1}{\lambda} \quad (4.2)$$

With an optical network of filters and lenses, the spectrometer only collects the photons of the non-elastically scattered signal. In practice, the spectrometer collects the Stokes or the anti-Stokes radiation only. For a fixed acquisition time, the more a certain molecule is present in the medium, the greater is the intensity of the signal collected by the spectrometer. It is therefore possible to quantify the number of a certain type of molecule compared with another by comparing the intensity of signals of their respective molecular vibrations. Most of the time, the ratio of the signal intensity of the two different molecules is proportional to





**Figure 4.4** – Example of a Raman spectroscopy calibration method for a binary system composed of molecules A and molecules B.

the molar ratio of these molecules in the medium. Nevertheless, in some cases, depending on the medium, the temperature or the pressure, the relationship between the intensity ratio and the molar ratio can be non-linear. This relationship can be determined with a calibration step.

### 4.1.3 Calibration step

Figure 4.4 gives the example of a binary mixture composed of molecules A and molecules B. Samples of different mole ratios  $n_A/n_B$  are prepared and their respective Raman spectra are obtained. In the intensity profiles of the example given, two areas can be distinguished: an area related to the vibrations of molecule A, noted  $Area_A$ , and an area related to the vibrations of molecule B, noted  $Area_B$ . The ratios of these areas  $Area_A/Area_B$  are plotted versus the molar ratios  $n_A/n_B$ <sup>1</sup>. The experimental data points are then fitted with a linear law described by Equation 4.3. This enables constant  $\alpha$  to be determined and a calibration curve to be obtained. This calibration curve allows the area ratio of a future sample measurement to be linked to the molar ratio of the molecules present in this new sample. Instead of computing areas, it is also possible to link the ratio of maximum intensity of the molecule vibrations to the molar ratio. Nevertheless, when a molecule has a wide Raman peak, it is more precise to make the calibration with the full area.

$$\frac{Area_A}{Area_B} = \alpha \frac{n_A}{n_B} \quad (4.3)$$

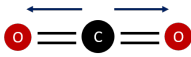
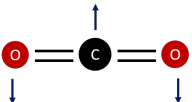
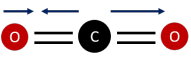
<sup>1</sup>The mole ratio is equal to the molar fraction ratio.

#### 4.1.4 Raman spectra of pure $CO_2$ and pure $H_2O$

##### Raman spectra of pure $CO_2$

The  $CO_2$  molecule has three types of molecular bond vibrations as presented in Table 4.1: the symmetrical stretch, the bending mode and the asymmetrical stretch. Since there is not a change of polarizability in the case of bending and asymmetrical stretching, these molecular vibrations are not Raman active. Symmetrical stretching is Raman active and is present in the  $CO_2$  spectra. However, in the case of  $CO_2$ , a resonance effect called the Fermi resonance occurs. The characteristic Raman shift of the pure spectra of  $CO_2$  is the Fermi dyad at  $1280\text{ cm}^{-1}$  and  $1380\text{ cm}^{-1}$ . This dyad is a combination of the symmetric stretching mode of the molecule,  $\nu_1$ , and the first overtone of the bending mode, noted  $2\nu_2$ . Even if the Fermi resonance was intensively investigated in the literature (Windisch et al. (2012), Basire et al. (2017), Nosenko et al. (2018)), there are still discussions about its source. The assignment of  $\nu_1$  and  $2\nu_2$  to the Fermi resonance has not been completely demonstrated. The  $CO_2$  Raman spectra obtained by N. Liu (2013) is presented in Figure 4.5. This figure presents the influence of pressure on the Raman spectra of  $CO_2$  at  $35\text{ }^\circ\text{C}$ . The intensities of peaks of the Fermi dyad both increase with a pressure increase. In general, an increase in pressure in a fluid reduces the distance between the molecules and then, for fixed measurement time and laser beam focus, increases the number of photons inelastically scattered and thus the intensity of the signal.

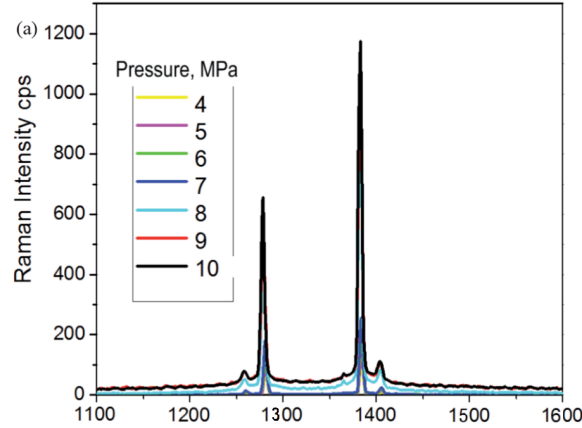
**Table 4.1** – Molecular bond vibrations of  $CO_2$  and their characteristics. Wave numbers are taken from Hollas (2013).

Molecule vibration			
Type	symmetrical stretch	bend	asymmetrical stretch
Wave number	$\nu_1 = 1388\text{ cm}^{-1}$	$\nu_2 = 667\text{ cm}^{-1}$	$\nu_3 = 2349\text{ cm}^{-1}$
Polarizability change?	Yes, Raman active	No, Raman inactive	No, Raman inactive

##### Raman spectra of pure liquid $H_2O$

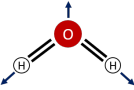
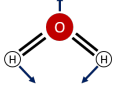
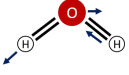
The  $H_2O$  molecule also presents three types of molecular bond vibrations presented in Table 4.2: the symmetric stretch, the bending mode and the asymmetrical stretch. All of them are Raman active since there is a polarizability change in each case.

The characteristic Raman spectra of liquid  $H_2O$  consists in one small band corresponding to the H-O-H bending around  $1600\text{ cm}^{-1}$  and a larger one corresponding to the H-O-H stretching band located between  $2700\text{ cm}^{-1}$  and  $3900\text{ cm}^{-1}$  as presented in Figure 4.6. In liquid water, the hydrogen bonds of one molecule of water interact with the other molecules



**Figure 4.5** – (a) Raman spectra of  $CO_2$  measured at 35 °C from 4 to 10 MPa from N. Liu (2013).

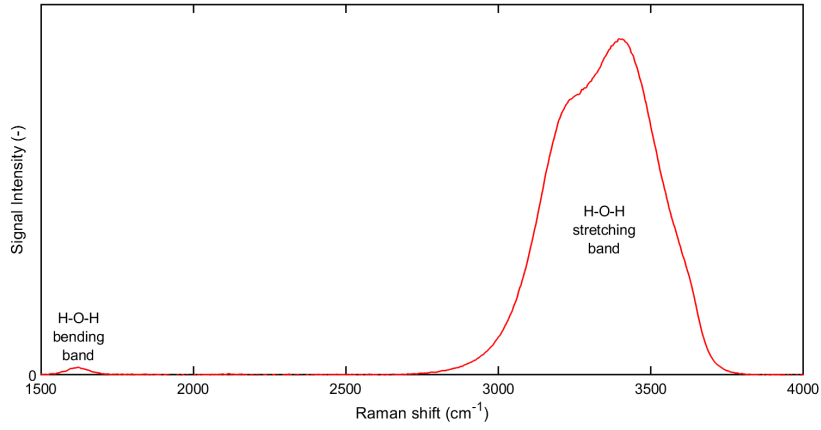
**Table 4.2** – Molecular bond vibrations of  $H_2O$  and their characteristics. Wave numbers are taken from Shimanouchi et al. (1978).

Molecule vibration			
Type	symmetrical stretch	bend	asymmetrical stretch
Wave number	$\nu_1 = 3657 \text{ cm}^{-1}$	$\nu_2 = 1595 \text{ cm}^{-1}$	$\nu_3 = 3756 \text{ cm}^{-1}$
Polarizability change?	Yes, Raman active	Yes, Raman active	Yes, Raman active

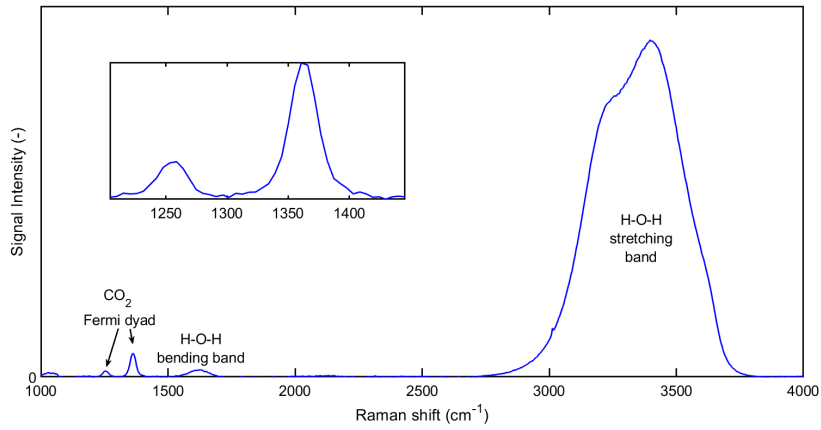
of water around it. As a consequence, the vibrational energy of each of the water molecules is function of these hydrogen bonds and results in a large distribution of vibrational energies for all the molecules of water. This effect explains the large band in the liquid water spectra. On the other hand, the Raman spectra of water vapour (not presented here) presents a narrow peak since the molecules of water interact less with each other.

#### 4.1.5 Raman spectra of $CO_2$ and $H_2O$ liquid mixture

An example of a Raman spectra of a liquid mixture of  $H_2O$  saturated by  $CO_2$  at 30 °C and 10 MPa is presented in Figure 4.7. The figure shows both the contributions of  $CO_2$  and  $H_2O$ , i.e. the Fermi dyad of  $CO_2$  and both the bands of liquid  $H_2O$ . The amount of  $H_2O$  compared with the amount of  $CO_2$  in  $H_2O$ -rich phase is determined by comparing the area of the Fermi dyad in the range  $[1200 \text{ cm}^{-1}; 1450 \text{ cm}^{-1}]$  and the area of the stretching molecule vibrations of  $H_2O$  in the range  $[2700 \text{ cm}^{-1}; 3900 \text{ cm}^{-1}]$ .



**Figure 4.6** – Raman spectra of  $H_2O$  measured at 30 °C and 10 MPa with the measurement setup used in this thesis work.

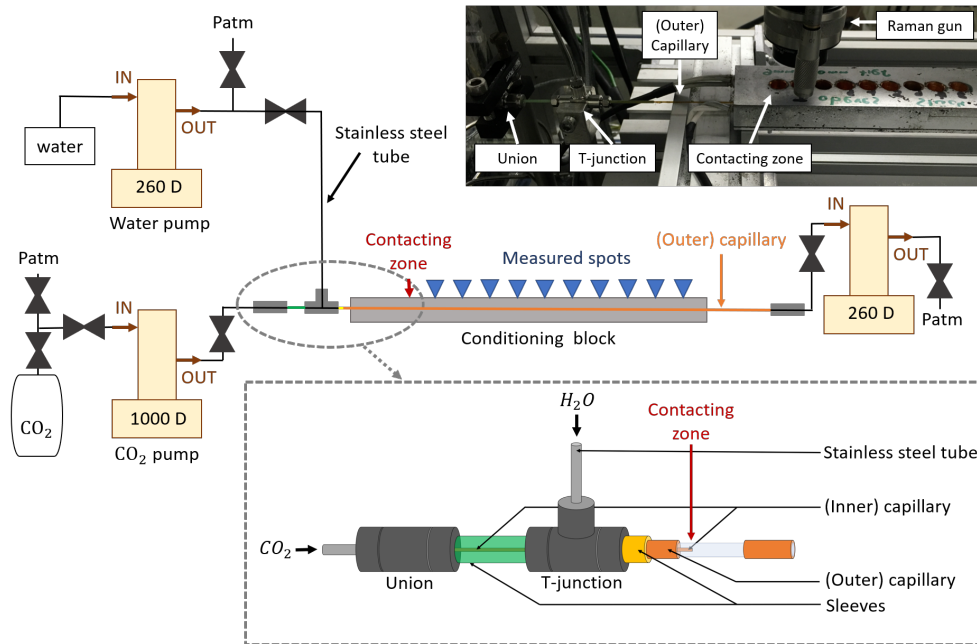


**Figure 4.7** – Raman spectra of  $CO_2-H_2O$  mixture measured at 30 °C and 10 MPa with the measurement setup used in this thesis work.

## 4.2 Experimental method

This section presents the experimental setup that is used to generate a segmented two-phase flow at high pressure and to perform Raman spectroscopy measurements in both phases of the segmented flow in a micro-capillary<sup>2</sup>. This setup involves a pressure and temperature controlled capillary micro-system, three high-pressure pumps, which are connected to the micro-system, and a specific Raman spectroscopy setup that enables measurement in each of the phases separately.

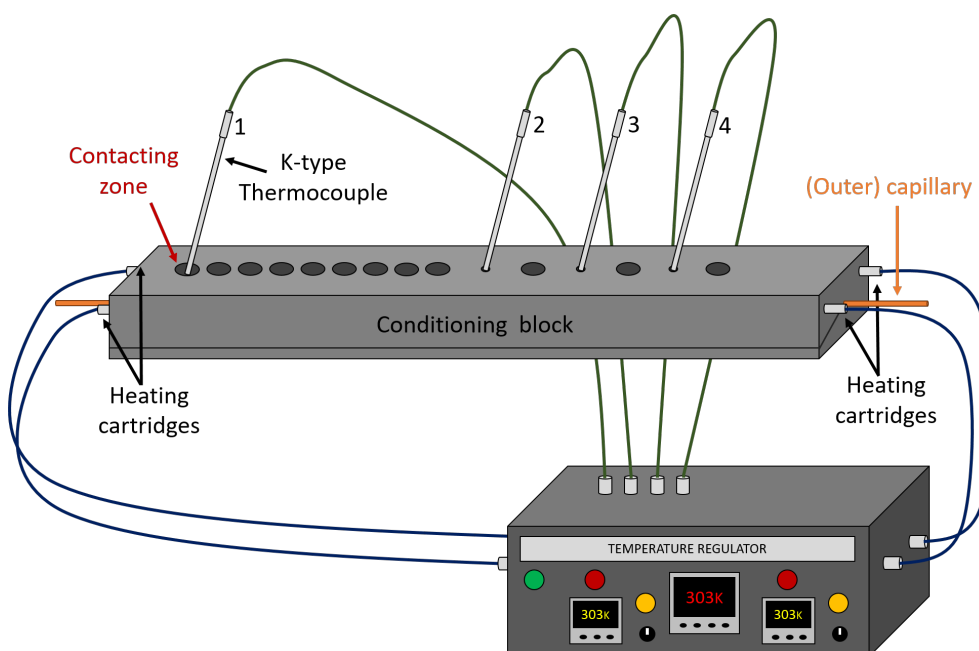
### 4.2.1 Experimental setup



**Figure 4.8** – Schematic diagram and photo of the experimental setup used to determine mass transfer coefficients in high-pressure two-phase flows.

Figure 4.8 shows the experimental setup used to measure the molar fraction of  $CO_2$  dissolved in the water-rich phase. It is composed of a capillary tube (60 cm in length) with a T-junction and high-pressure pumps. The capillaries used in the setup were purchased from Polymicro Technologies. Two sizes of capillary tubes made of silica with a polyimide coating are used for a coaxial injection. The smaller diameter tube, feeding the  $CO_2$ , is inserted in a larger diameter tube, feeding the water, as shown in the inset of Figure 4.8. The dimensions are listed in Table 4.3. These capillary tubes can withstand pressure and temperature up to 25 MPa at 700 K (Proctor et al., 1967). The connections between the silica capillaries and the other parts of the setup, which is composed of 1/16 inch stainless steel tubing, are made by assembling polymer sleeves, ferules, a stainless-steel T-junction and a simple union.

<sup>2</sup>For the  $CO_2$ - $H_2O$  system investigated in this thesis work, only the measurement in the liquid phase was necessary for the determination of the volumetric mass transfer coefficient



**Figure 4.9** – Conditioning block and temperature regulation.

**Table 4.3** – Dimensions of the capillary tubes used ( $\mu m$ ). ID=inner diameter, OD=outer diameter.

-	min ID	max ID	min OD	max OD
Inner capillary	74.9	75.3	151.3	151.5
Outer capillary	296.6	296.8	792.3	794.2

The fluids used are distilled  $H_2O$  (Standard DIN 43530) and  $CO_2 > 99.5\%$  in mole. Note that the  $H_2O$  is re-boiled before it is fed to the pump in order to reduce the amount of potentially dissolved compounds. Three Teledyne ISCO pumps are used to feed the fluids through the system. A 260D ISCO pump (capacity of 266 mL, a flow range of 0.001 to 107 mL min<sup>-1</sup>, a flow accuracy of 0.5% of the set point, a pressure accuracy of 0.5% of the full scale and a max pressure of 51.7 MPa) feeds the  $H_2O$ . A 1000D ISCO pump (capacity of 1015 mL, a flow range of 0.001 to 408 mL min<sup>-1</sup>, a flow accuracy of 0.5% of the set point, a pressure accuracy of 0.5% of the full scale and a max pressure of 13.4 MPa) feeds  $CO_2$ . The  $CO_2$  pump reservoir is cooled down to 278 K by circulating a cooling fluid from a temperature-regulated system (F12-Julabo) through its jacket. This ensures that the  $CO_2$  is in the liquid state inside the syringe pump. Another 260D ISCO pump is placed at the outlet of the capillary setup in order to maintain the pressure in the system and to collect the exiting mixture. The two feed pumps work in direct volumetric flow-rate-mode and the third pump at the outlet works in reverse volumetric flow rate mode. The flow rate of the reverse pump is calculated in order to maintain constant pressure in the system. All the pumps

are equipped with a pressure gauge. 1/16 inch stainless steel pipes are used to connect the pumps to the silica capillary tubes.

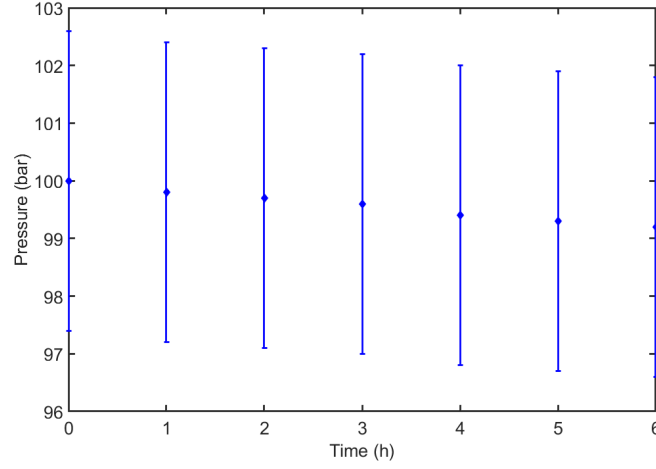
The capillary tube is placed in a copper temperature conditioning block (30 cm long), presented in Figure 4.9, which is heated with four electrical resistance heating rods. The temperature is measured with five thermocouples (K-type), which are in contact with the silica capillary tube through dedicated holes. The block is temperature-controlled with a precision of  $\pm 0.5$  K, which corresponds to the difference between the mean value and the extrema values obtained by the five thermocouples during the experiment. The coaxial contacting zone is placed 2.5 cm within the heating block to ensure the contact of  $H_2O$  and  $CO_2$  at the desired pressure and temperature. The assumption that 2.5 cm is long enough was verified with a computational fluid dynamic simulation. Ten holes are drilled in the temperature conditioning block at 1.25, 2.5, 3.75, 5, 6.25, 7.5, 8.75, 10, 12.5 and 17.5 cm from the contacting zone. The total investigable two-phase flow section is then 17.5 cm long. The brownish polymer coating of the silica capillary was removed at these spots in order to make the capillary accessible for Raman spectroscopy measurements.

### Pressure control

As mentioned before, the pressure is maintained constant by the reverse pump. Nevertheless, for long experimental times, depending on the flow rate fixed by the reverse pump, the pressure can slightly vary. Figure 4.10 shows the pressure variation for an experimental time of six hours for a fixed  $H_2O$  flow rate of  $110 \mu\text{L min}^{-1}$  and a  $CO_2$  flow rate of  $85 \mu\text{L min}^{-1}$  at 303 K and 10 MPa. It can be seen that the pressure in the system decreases by 0.1 MPa in six hours. This decrease has a negligible impact on the measurements performed in this study since the duration of an experiment time is less than 30 minutes, which corresponds to a pressure variation of less than 0.2 bar.

When a fluid flows through a tube, there is a pressure drop between the inlet and the outlet. If the pressure decreases significantly along the tube, this can reduce the solubility of the  $CO_2$  in the  $H_2O$ -rich phase. Hence, it is important that the microsystem is designed such the pressure drop is as small as possible. The pressure drop has been calculated in the system for the worst case scenario (where the pressure drop is the highest), i.e. when the outer capillary tube and the stainless steel tubes are filled with water and the total flow rate in the system is at the maximum value used in the experimental campaign ( $400 \mu\text{L min}^{-1}$ ). The pressure drop ( $\Delta P$ ) is calculated assuming that both the outer-capillary tube and the stainless steel tubes are completely smooth and that the flow is laminar. With these assumptions, the friction factor  $f$  for each tube can be calculated using Equation 4.4 where  $Re$  is the Reynolds number. The pressure drop in the inner-capillary is calculated in the same way assuming that the tube is filled with carbon dioxide flowing at the maximum flow rate in the experimental campaign ( $150 \mu\text{L min}^{-1}$ ).

$$f = \frac{64}{Re} \quad \text{for} \quad Re = \frac{\rho v D}{\mu} < 2000 \quad (4.4)$$



**Figure 4.10** – Pressure variation in the reverse pump (ISCO 260D) after six hours at 10 MPa, 303 K,  $\dot{V}_{H_2O} = 110 \mu\text{L min}^{-1}$  and  $\dot{V}_{CO_2} = 85 \mu\text{L min}^{-1}$ . The error bar corresponds to 0.5 % of the pump full scale.

Assuming that the flow is fully developed in the tubes, the pressure drop can be determined with Equation 4.5

$$\Delta P = f \frac{L \rho v^2}{2D} \quad (4.5)$$

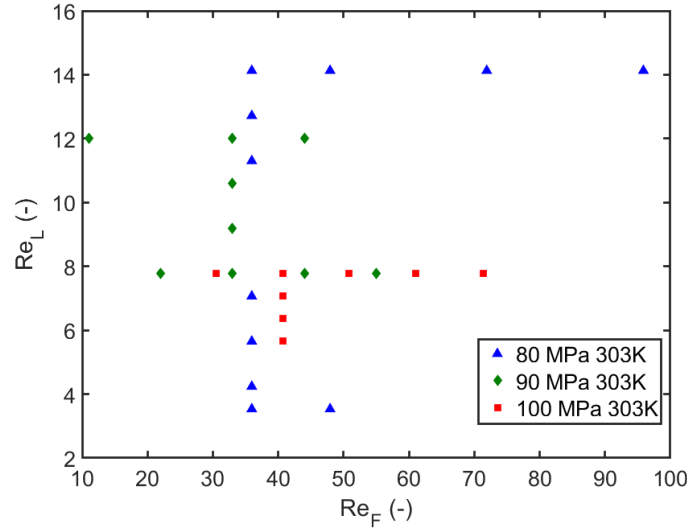
Combining Equations 4.4 and 4.5 gives Equation 5.1 which expresses the pressure drop  $\Delta P$  as a function of the viscosity  $\mu$ , the velocity  $v$ , the length of the tube  $L$ , and the diameter of the tube  $D$ . The maximum pressure drop values possible in the experimental system are presented in Table 5.1. The total pressure drop in the system does not exceed 0.35 bar, which can be considered negligible for the study presented here.

$$\Delta P = 32 \frac{\mu L v}{D^2} \quad (4.6)$$

**Table 4.4** – Pressure drop in different tubes of the system with  $\dot{V}_{H_2O} = 400 \mu\text{L min}^{-1}$  and  $\dot{V}_{CO_2} = 150 \mu\text{L min}^{-1}$ . The viscosities of  $CO_2$  and  $H_2O$  are computed at 8 MPa and 303 K with the models presented in Chapter 2.  $\mu_{CO_2} = 56.4 \mu\text{Pa s}$ ,  $\mu_{H_2O} = 799.2 \mu\text{Pa s}$ .

Tube	Stainless steel tube ( $H_2O$ )	Outer-capillary tube ( $H_2O$ )	Inner-capillary tube ( $CO_2$ )
Inner-diameter ( $\mu\text{m}$ )	1020	297	75
Length (m)	2.70	0.60	0.08
Velocity ( $\text{cm s}^{-1}$ )	0.8	9.6	56.8
Pressure drop (bar)	0.01	0.19	0.16





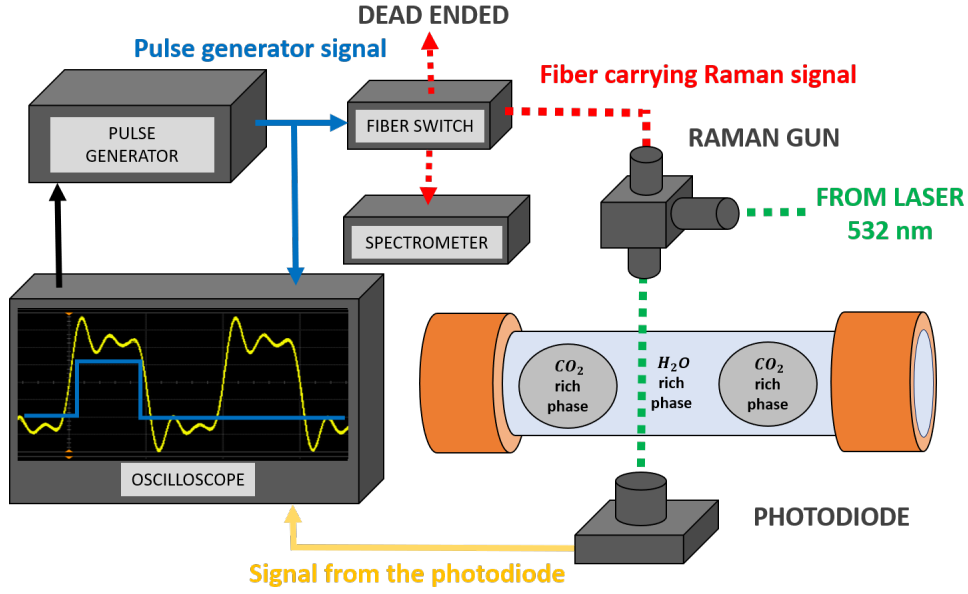
**Figure 4.11** – Operating conditions in term of Reynolds number for the  $H_2O$  flow rate (L) and  $CO_2$  flow rate (F).

### 4.2.2 Operating conditions

The operating pressures studied are 8, 9 and 10 MPa at a temperature of 303 K. The ISCO pumps are set to deliver a constant volumetric flow rate. However, since there is a temperature change – and therefore a density change of the fluids – between the pumps and the capillary tube, the volumetric flow rates in the capillary tube must be recalculated to take into account the change in density. For the sake of simplicity, since the  $CO_2$  can be either liquid or gas depending of the operating conditions, the  $CO_2$ -rich phase is called the fluid phase and the  $H_2O$ -rich phase is called the liquid phase. The fluid Reynolds numbers (for  $CO_2$ ) and the liquid Reynolds numbers (for  $H_2O$ ) are defined in Equation 4.7 and the values used in the experiments and presented in Figure 4.11.

$$Re_F = \frac{\rho_{CO_2} U_{CO_2} D}{\mu_{CO_2}} \quad \text{and} \quad Re_L = \frac{\rho_{H_2O} U_{H_2O} D}{\mu_{H_2O}} \quad (4.7)$$

These flow rates lead to residence times of the order of one second. Note that all the volumetric flow rates in this manuscript are given at the temperature and pressure of the microfluidic system. These flow rate ranges have been chosen such that there is a  $CO_2$ - $H_2O$  flow with a concentration gradient of  $CO_2$  in the  $H_2O$ -rich phase along the length of the capillary tube and that the  $H_2O$ -rich phase is not saturated with the  $CO_2$  at the final measurement point, i.e. at  $z = 175$  mm. The  $CO_2$  to  $H_2O$  flow rate ratio at the inlet is then varied in order to obtain thermodynamic equilibrium (i.e. where the  $H_2O$ -rich phase is saturated by  $CO_2$ ) at several measurement points. For each combination of pressure and temperature, the influence of the volumetric flow rate of one phase has been studied, whilst the volumetric flow rate of the other phase was kept constant.

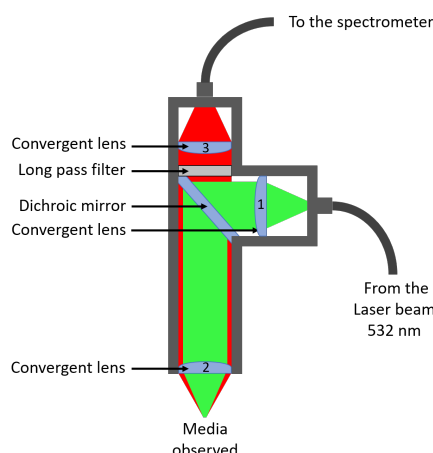


**Figure 4.12** – Schematic overview of the Raman spectroscopy measurement part of the experimental setup

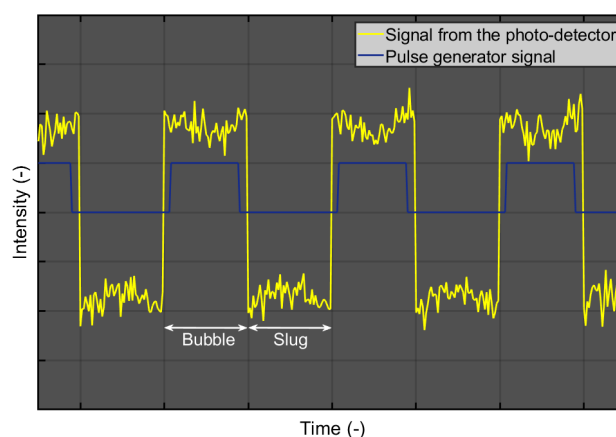
### 4.2.3 Raman spectroscopy measurement setup

The Raman spectroscopy measurement setup is based on the work of Luther et al. (2014). The measurement system, presented in Figure 4.12, allows the acquisition of a Raman spectra from one of the two phases of a fast segmented two-phase flow. The setup consists of a Raman gun presented in Figure 4.13, which allows the acquisition of a Raman signal in back-scattering mode. The signal from the laser Cobolt Samba (532 nm, 200 mW) enters the Raman gun via an optical fiber (M15 L02  $\varnothing$  105  $\mu$ m) and passes through a coated plano-convex lens (Thorlabs: LA 1131-A) noted "1" on Figure 4.13. The signal is reflected by a dichroic mirror adapted for 532 nm excitation with a cut-off of 550 nm. The signal goes through a second lens "2" (Thorlabs: AC254-030-A) in order to concentrate the signal on the medium observed within the capillary tube. The fluid medium scatters an inelastic signal that goes in all directions. This signal is collected by the lens "2" and a part of the signal (the Stokes radiation) passes through the dichroic mirror since the signal wavelength is higher than 550 nm. The signal then passes through a long-pass filter with a cut-off of 550 nm and is concentrated in an optical fiber with the third lens "3" (Thorlabs: AC254-060-A). The final signal collected here is an average signal of both phases present inside the micro-capillary.

In order to obtain only the signal from one of the two phases, the system is coupled with an avalanche photo-detector (Thorlabs: APD). The photo-detector detects the signal from the laser passing through the micro-capillary. The signal obtained by the photo-detector is presented in yellow on Figure 4.14. The signal is periodic since when a bubble or a droplet passes through the laser inside the capillary, the change of refractive index between the two phases leads to a bump or a crook in the intensity of the signal. A signal from a pulse generator (Model 9618 Quantum Composers) is created in order to fit with the phase selected

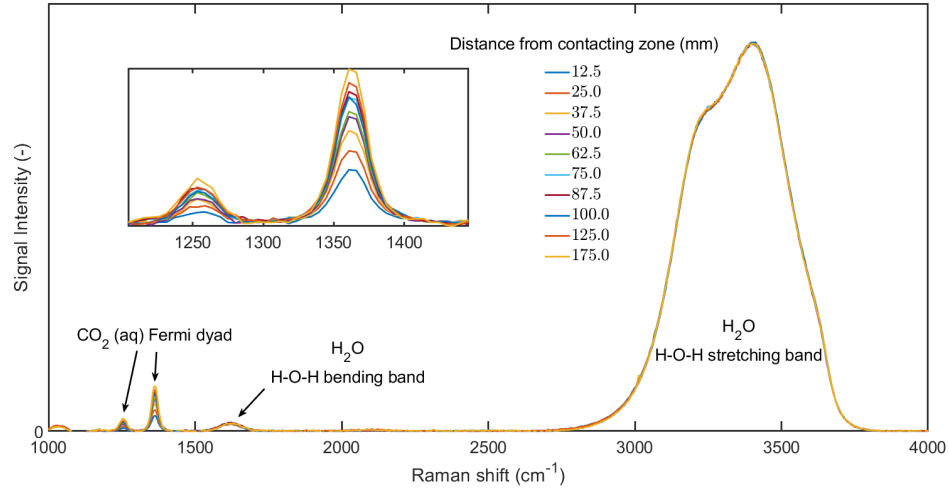


**Figure 4.13** – Schematic diagram of the Raman spectroscopy setup for obtaining spectra in a single phase of a segmented two-phase flow.



**Figure 4.14** – Oscilloscope visualisation of the photo-detector signal and the signal from the pulse generator.

for the measurement (blue on Figure 4.14). This electric signal is sent to a fiber switch (PiezoSystem Jena), which is composed of two inlets, one for the electric signal from the pulse generator and one for the Raman signal from the Raman gun. The fiber switch has two outlets, one dead ended and another one to the spectrometer (Ocean Optics QEpro). When the electric signal from the pulse generator is equal to zero, the outlet of the fiber switch is the dead ended fiber. However, when the electric signal is positive, the outlet of the fiber switch is the optical fiber connected to the spectrometer. Consequently, it is possible to obtain a Raman spectra from one of the phases only. The acquisition time for a clear Raman spectra in this micro-capillary setup is about 1 s. However, in this configuration, the spectrometer accumulates signals from one of the two phases. Therefore, the acquisition time is fixed to 3 s in order to obtain a clear spectra of the selected phase.



**Figure 4.15** – Raman spectra of the  $H_2O$ -rich phase at different axis location from the contacting point in the micro capillary. The operating conditions are  $P = 10$  MPa,  $T = 303$  K,  $\dot{V}_{H_2O} = 110 \mu\text{L min}^{-1}$  and  $\dot{V}_{CO_2} = 61.5 \mu\text{L min}^{-1}$ .

#### 4.2.4 Raman spectra measurements

At each measurement point, 16 spectra have been recorded, each with a signal integration time of 3 s. The mean of the 16 spectra is computed for each measurement point, the baseline is removed (using a spline method with the following node points [650, 930, 1150, 1200, 1300, 1420, 1470, 1530, 1800, 2000, 2300, 2500, 2600, 2700, 3850, 4000  $\text{cm}^{-1}$ ]) and the spectra are normalized by the  $H_2O$  band in order to visualize and compare the amount of  $CO_2$  in the  $H_2O$ -rich phase at each point. An example of the spectra obtained at the different measurement points is shown in Figure 4.15. The peak between 2700  $\text{cm}^{-1}$  and 3900  $\text{cm}^{-1}$  corresponds to the  $H_2O$  and the Fermi dyad of  $CO_2$  is present between 1200  $\text{cm}^{-1}$  and 1450  $\text{cm}^{-1}$ . As the distance of the measurement point from the contacting point of  $CO_2$  and  $H_2O$  increases, it can be seen that the signal intensity of the  $CO_2$  Fermi dyad increases, which corresponds to a greater amount of  $CO_2$  dissolved in the  $H_2O$ -rich phase.

## 4.3 Determination of mass transfer

The novelty of this work is to determine liquid local volumetric mass transfer coefficients  $k_L a_L$  in continuous high-pressure two-phase flows where the physical properties of the fluids vary. In order to do this, the Raman spectroscopy technique previously described is used to determine the  $CO_2$  to  $H_2O$  molar fraction ratio  $x_{CO_2}/x_{H_2O}$  at each measurement point. This ratio is then coupled with the density of the liquid mixture  $\rho_L$  to compute the concentration of  $CO_2$  dissolved in the  $H_2O$ -rich phase  $C_{CO_2}$  at each point. Following this, the concentration data is used with the unit cell model presented in Chapter 2, to calculate the volumetric mass transfer coefficient  $k_L a_L$  at each position in the capillary tube.

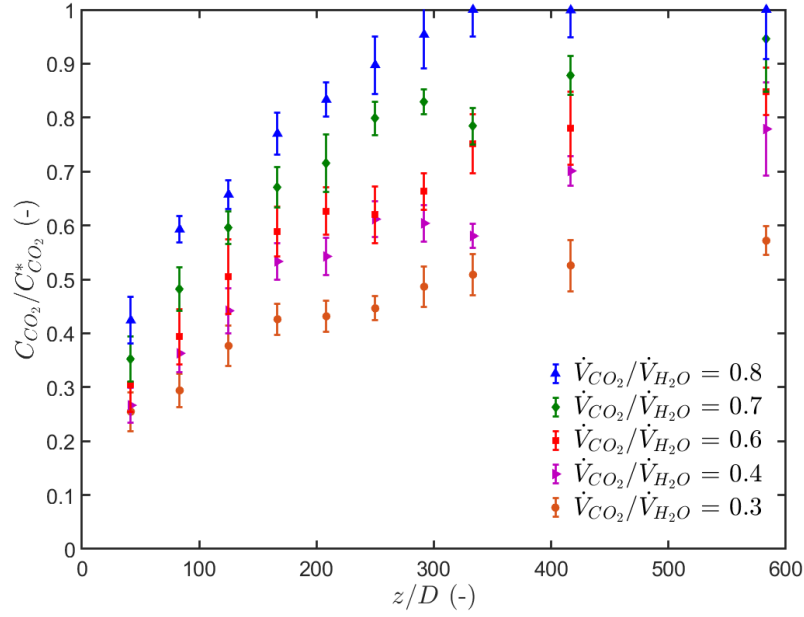
### 4.3.1 Determination of $C_{CO_2}$

The dissolution of  $CO_2$  into a  $H_2O$ -rich phase leads to the presence of  $H_2CO_3$ ,  $HCO_3^-$ ,  $CO_3^{2-}$  and  $CO_2$  in aqueous form in the  $H_2O$ -rich phase. Nevertheless, in the study of Anderson (1977), it has been shown that in the  $H_2O$ -rich phase, the amount of species other than  $CO_2$  is negligible at 283 K and 4.5 MPa and decreases further with an increase in pressure. Therefore, in this work, the total amount of  $CO_2$  dissolved in the  $H_2O$ -rich phase is considered to be present as dissolved molecular  $CO_2$ . The concentration of  $CO_2$  in the  $H_2O$ -rich phase  $C_{CO_2}$  is determined by Equation 4.8 where  $\rho_L$  is the liquid density of the  $H_2O$ -rich phase calculated with the model presented in Section 2.2.3 Chapter 2.  $V_L$  is the volume of the liquid slug,  $x_{CO_2}$  and  $x_{H_2O}$  are the molar fractions of  $CO_2$  and  $H_2O$  in the liquid slug respectively.

$$\begin{aligned}
 C_{CO_2} &= \frac{n_{CO_2}}{V_L} \\
 &= \frac{n_{CO_2} \rho_L}{m_{CO_2} + m_{H_2O}} \\
 &= \frac{\rho_L}{\left(\frac{n_{CO_2}}{n_{CO_2}}\right) M_{CO_2} + \left(\frac{n_{H_2O}}{n_{CO_2}}\right) M_{H_2O}} \\
 &= \frac{\rho_L}{M_{CO_2} + \left(\frac{n_{H_2O}}{n_{CO_2}}\right) M_{H_2O}} \\
 &= \frac{\rho_L}{M_{CO_2} + \left(\frac{x_{H_2O}}{x_{CO_2}}\right) M_{H_2O}}
 \end{aligned} \tag{4.8}$$

The molar fraction ratio is obtained from the Raman spectra and is proportional to the peak area ratio  $A_{CO_2}/A_{H_2O}$  at each measurement point as presented in Equation 4.9 (where  $A_{H_2O}$  and  $A_{CO_2}$  are the areas from the Raman spectra taken between 2700  $cm^{-1}$  to 3900  $cm^{-1}$  and 1200  $cm^{-1}$  to 1450  $cm^{-1}$  respectively):

$$\frac{A_{CO_2}}{A_{H_2O}} = \alpha \frac{x_{CO_2}}{x_{H_2O}} \tag{4.9}$$



**Figure 4.16** –  $CO_2$  normalized concentration in the  $H_2O$ -rich phase at different normalized axis location. The operating conditions are  $P = 10$  MPa,  $T = 303$  K and  $\dot{V}_{H_2O} = 110$   $\mu\text{L min}^{-1}$ . The error bar corresponds to  $\pm 3$  standard deviation.

The proportionality constant  $\alpha$  is determined by calculating the  $x_{CO_2}/x_{H_2O}$  ratio at equilibrium with the thermodynamic model for the solubility of  $CO_2$  in the  $H_2O$ -rich phase (presented in Section 2.2.1 Chapter 2) for experiments where thermodynamic equilibrium is achieved.  $\alpha$  is then used to determine  $x_{CO_2}/x_{H_2O}$  from  $A_{CO_2}/A_{H_2O}$  at each measurement point for the other experiments where thermodynamic equilibrium has not been achieved yet. The value  $\alpha$  was obtained with 43 equilibrium points. The final value was 0.239 with a standard deviation of 0.007 (2.9 %). The deviation obtained here can be drastically reduced with binary systems where the dispersed phase is more soluble in the continuous phase (thereby providing higher resolution of the calibration curve). In the case of  $CO_2$  and  $H_2O$ , the maximum amount of  $CO_2$  in the  $H_2O$ -rich phase is 3% in mass under the conditions presented in this thesis work. This value is low compared with other systems studied in the literature, such as  $CO_2$ - $EtOH$  and  $CO_2$ - $BMimPF_6$  as presented in Chapter 2.

Figure 4.16 presents an example of the results obtained at 10 MPa and 303 K for a fixed  $H_2O$  flow rate and varying  $CO_2$  flow rate. The dimensionless  $CO_2$  concentration in the  $H_2O$ -rich phase increases with the dimensionless location along the tube axis  $z/D$ . The effects of flow rate ratios will be discussed later in Section 4.4.1.

### 4.3.2 Determination of the volumetric mass transfer coefficient $k_L a_L$

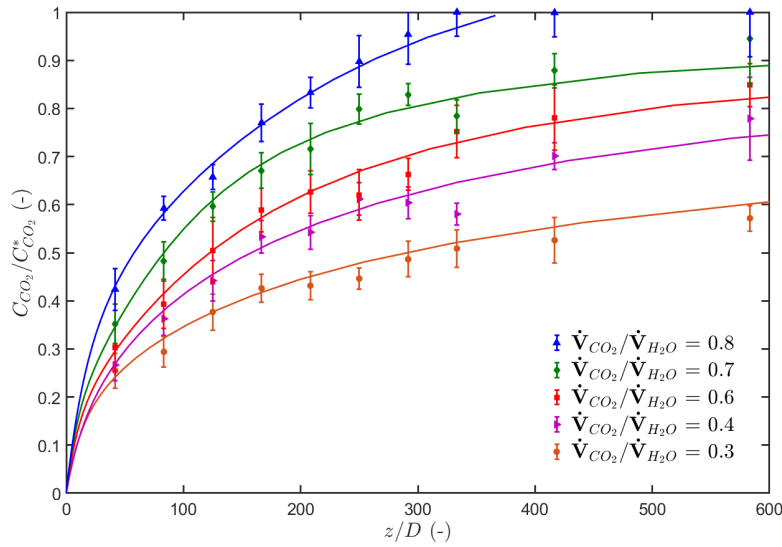
Equation 2.32 from the unit-cell model presented in Chapter 2 is used for the determination of the volumetric mass transfer coefficient:

$$k_L a_L = \frac{U_{TP}}{C_{CO_2}^*(T, P) - \langle C_{CO_2} \rangle(z)} \frac{d\langle C_{CO_2} \rangle}{dz} \quad (4.10)$$

The first derivative of the  $CO_2$  concentration in the  $H_2O$ -rich phase,  $\frac{d\langle C_{CO_2} \rangle}{dz}$ , is obtained by filtering the experimental concentration data using a Fast Fourier Transform (FFT). The FFT filtering method is presented in Appendix B.

## 4.4 Application of the experimental method to $CO_2$ - $H_2O$ mass transfer under high pressure

This section presents examples of Raman spectroscopy measurements and data analysis to obtain the volumetric mass transfer coefficient for a segmented flow composed of  $CO_2$ -rich and  $H_2O$ -rich phases in a capillary tube at pressures of 8 MPa, 9 MPa and 10 MPa, as well as a range of flow rates. Figure 4.17 shows an example of the experimental concentration data (normalised by the value at saturation) and the corresponding profiles obtained by FFT filtering as a function of the normalized axial distance from the contacting zone in the capillary tube for 10 MPa, 303 K and a constant  $H_2O$  flowrate ( $110 \mu\text{L min}^{-1}$ ). The error bars correspond to  $\pm 3$  standard deviations. The average deviation between the fitted concentrations and the experimental values of all the conditions studied in this chapter do not exceed 1%. This figure clearly shows that the FFT filtering method correctly represents the  $CO_2$  concentration in the  $H_2O$ -rich phase at each measurement point in the capillary tube. Considering this, in subsequent figures, only the fitted curves are shown in order to facilitate reading.

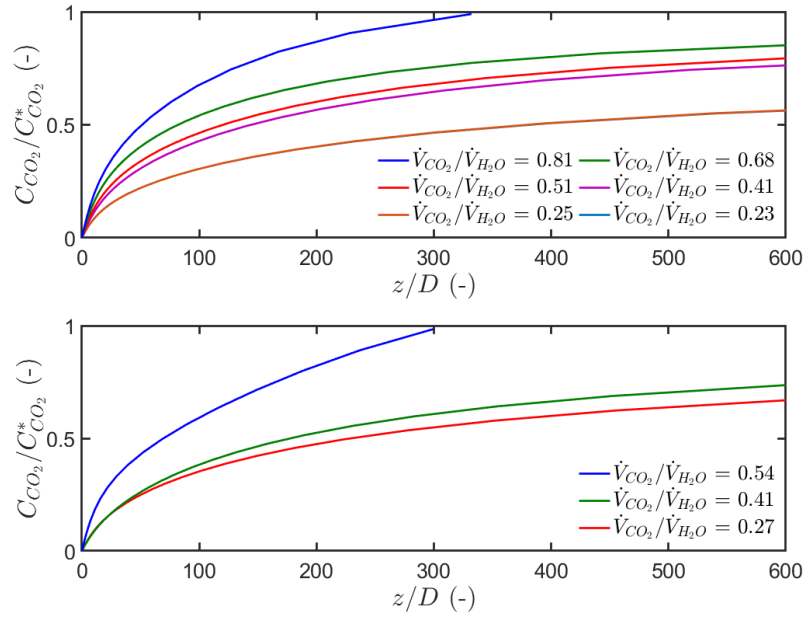


**Figure 4.17** –  $CO_2$  normalized concentrations in the  $H_2O$ -rich phase at different normalized axis locations and FFT filtered curves. The operating conditions are  $P = 10$  MPa,  $T = 303$  K,  $\dot{V}_{H_2O} = 110 \mu\text{L min}^{-1}$ . The average deviation between the fitted concentration profiles and the experimental points are 0.7%, 0.5%, 0.3%, 0.4% and 0.5%.

### 4.4.1 Concentration profiles

Figures 4.18 to 4.20 show the normalized fitted  $CO_2$  concentration profiles as a function of the normalized axial position in the capillary ( $z/D$ ) at 303 K and 8 MPa, 9 MPa and 10 MPa, respectively. At each pressure, either the volumetric flow rate of  $CO_2$  or of  $H_2O$  was kept constant, whilst the flow rate of the other phase was varied. The flow rate ratio



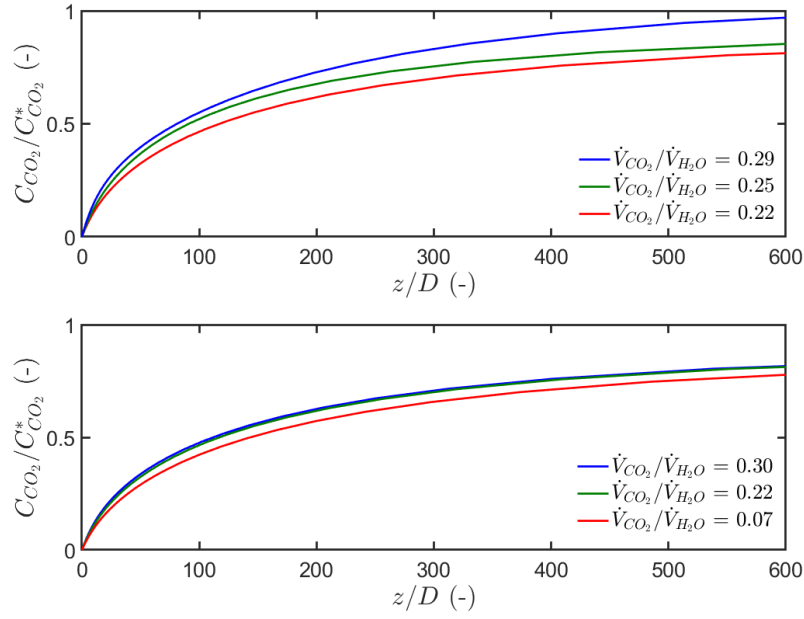


**Figure 4.18** – Normalized fitted concentrations profiles of  $CO_2$  in the  $H_2O$ -rich phase as a function of the normalized  $z$ -axis position at 8 MPa and 303 K where  $\dot{V}_{CO_2} = 40.5 \mu\text{L min}^{-1}$  (top) and  $\dot{V}_{H_2O} = 200 \mu\text{L min}^{-1}$  (bottom).

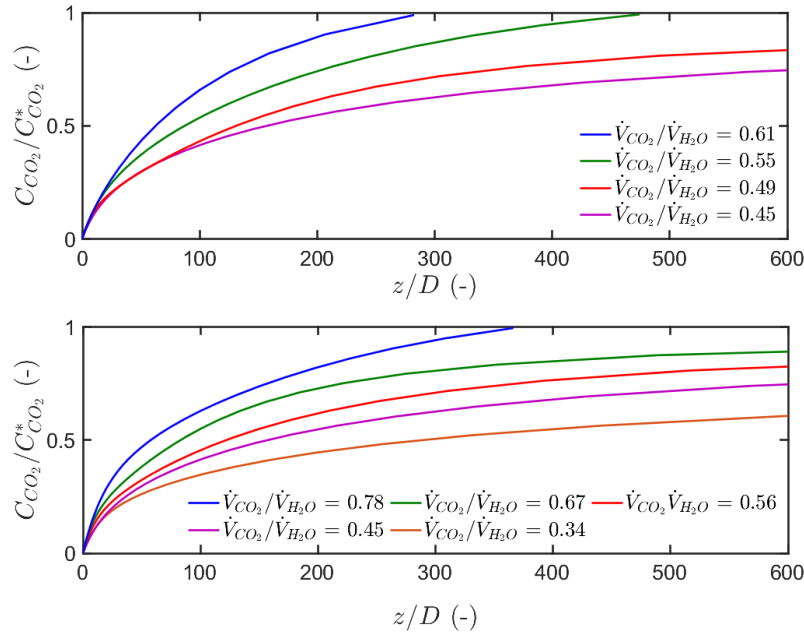
therefore provides the basis for comparison. Indeed, the volumetric flowrate ratio is a key parameter for characterizing hydrodynamics in segmented flows in small channels. Droplet and bubble growth mechanisms and lengths in microchannels have been widely studied as a function of flow rates (see for example the works of Garstecki et al. (2006), Steijn et al. (2007) and Abadie (2013) presented in Section 1.3.2 of Chapter 1). In such studies, it has been shown that bubble length,  $L_B$ , and liquid slug length,  $L_S$ , increase linearly with  $\dot{V}_{CO_2}/\dot{V}_{H_2O}$  and  $\dot{V}_{H_2O}/\dot{V}_{CO_2}$ , respectively.

For all pressures, it is observed that when  $\dot{V}_{CO_2}/\dot{V}_{H_2O}$  decreases, thermodynamic equilibrium is reached further along the capillary tube away from the contacting point. For example, in the top of Figure 4.18 for the experiment where  $\dot{V}_{CO_2}/\dot{V}_{H_2O} = 0.68$ , equilibrium is not reached in the measurement zone whereas for  $\dot{V}_{CO_2}/\dot{V}_{H_2O} = 0.81$ , equilibrium is reached at  $z/D = 320$ .

When  $\dot{V}_{CO_2}/\dot{V}_{H_2O}$  decreases, the bubble length  $L_B$  decreases and the slug length  $L_S$  increases. As a consequence, the interfacial area for mass transfer decreases. In addition, there is a larger amount of  $H_2O$  in a liquid slug to be saturated whereas a lesser amount of  $CO_2$  is available in the  $CO_2$ -rich bubble. Both of these contributions result in the fact that thermodynamic equilibrium is reached further along the capillary from the contacting zone.



**Figure 4.19** – Normalized fitted concentrations profiles of  $CO_2$  in the  $H_2O$ -rich phase as a function of the normalized  $z$ -axis position at 9 MPa and 303 K where  $\dot{V}_{CO_2} = 38.2 \mu\text{L min}^{-1}$  (top) and  $\dot{V}_{H_2O} = 170 \mu\text{L min}^{-1}$  (bottom).



**Figure 4.20** – Normalized fitted concentrations profiles of  $CO_2$  in the  $H_2O$ -rich phase as a function of the normalized  $z$ -axis position at 10 MPa and 303 K where  $\dot{V}_{CO_2} = 49.2 \mu\text{L min}^{-1}$  (top) and  $\dot{V}_{H_2O} = 110 \mu\text{L min}^{-1}$  (bottom).

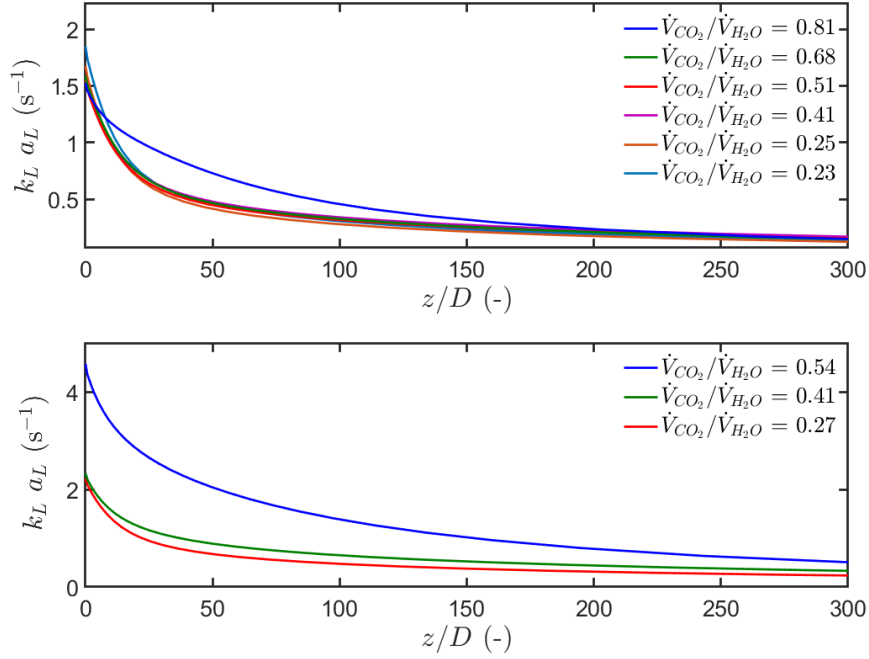
#### 4.4.2 Effect of flow rate conditions on $k_L a_L$

Figures 4.21 to 4.23 show the volumetric liquid mass transfer coefficient  $k_L a_L$ , determined with Equation 4.10, along the length of the capillary tube. Firstly, it is seen that  $k_L a_L$  is not constant along the capillary tube. This observation proves that the hypothesis that  $k_L a_L$  is constant along the tube, and either a decrease in  $a_L$  is compensated by an increase in  $k_L$ , or  $k_L$  and  $a_L$  are both assumed constant, which is often assumed in the plug flow unit-cell model, is here not valid. Indeed, when using this hypothesis, the value of  $k_L a_L$  at  $z/D = 100$  gives an average error of 35% compared with the value obtained in the hypothesis.  $k_L a_L$  decreases along the capillary tube between  $z/D = 0$  and  $z/D = 600$  by approximately a factor of 8. If this decrease in  $k_L a_L$  is due to a decrease in  $a_L$  only, then this corresponds to a decrease in the bubble diameter of a factor  $\sqrt{8} = 2.83$  (considering a spherical bubble and a water-rich slug with constant volume). However, such a significant decrease in bubble size between the contacting zone and the outlet of the capillary tube was not observed in the experiments as it can be seen from Figure 4.24. Hence, this implies that  $k_L$  must also be decreasing along the length of the capillary tube.

It can also be seen in Figures 4.21 to 4.23 that the rate of mass transfer is significantly higher closer to the contacting zone where  $CO_2$ -rich bubbles are formed. This is in agreement with the concentration profiles in Figures 4.18 to 4.20 where it can be seen that more than 20% of the thermodynamic equilibrium is reached during the bubble formation stage ( $z/D < 20$ ). The enhanced mass transfer at the bubble formation stage may be described by a difference in hydrodynamics between the bubble formation stage, which is a transient process, and the more or less stable segmented flow in the rest of the capillary tube. Indeed, in the transient bubble formation process, a bubble will grow and then be pinched-off, which will increase the liquid flow intermittently in the vicinity of the interface and consequently promote mass transfer.

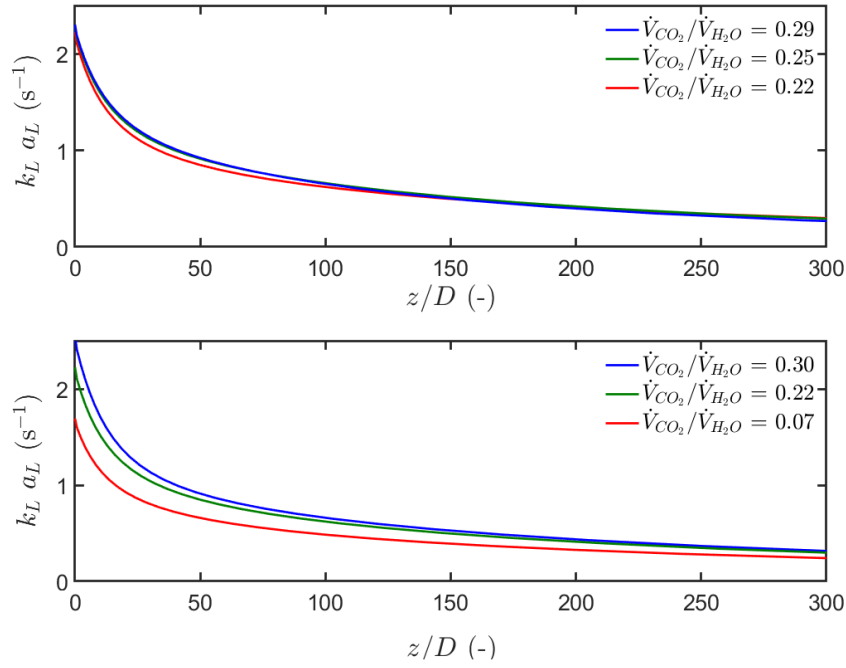
A comparison of the experiments also shows that for constant  $\dot{V}_{CO_2}$  or  $\dot{V}_{H_2O}$ , increasing  $\dot{V}_{CO_2}/\dot{V}_{H_2O}$  leads to an increase of  $k_L a_L$ . This may be explained by the fact that an increase in  $\dot{V}_{CO_2}/\dot{V}_{H_2O}$  results in an increase of the bubble length,  $L_B$ , (and consequently the bubble volume,  $V_B$ ) and a decrease of the liquid slug length,  $L_S$ . A decrease in slug length has previously been shown to increase the liquid slug recirculation (Leung et al. (2010), Zaloha et al. (2012), Abadie (2013)). It is expected that this would result in an enhanced renewal of the fluid-liquid interface and in turn increase the mass transfer coefficient  $k_L$ . Moreover, Abadie (2013) and Martin et al. (2018) showed that for both ambient pressure and high-pressure flows, the ratio between  $L_B$  and the total length of a unit cell,  $L_B + L_S$ , depends on  $U_F/U_L$ , and therefore  $\dot{V}_{CO_2}/\dot{V}_{H_2O}$  as described by Equation 4.11, where  $\beta$  is a constant.

$$\frac{L_B}{L_B + L_S} = \frac{\frac{\dot{V}_{CO_2}}{\dot{V}_{H_2O}}}{\beta + \frac{\dot{V}_{CO_2}}{\dot{V}_{H_2O}}} \quad (4.11)$$

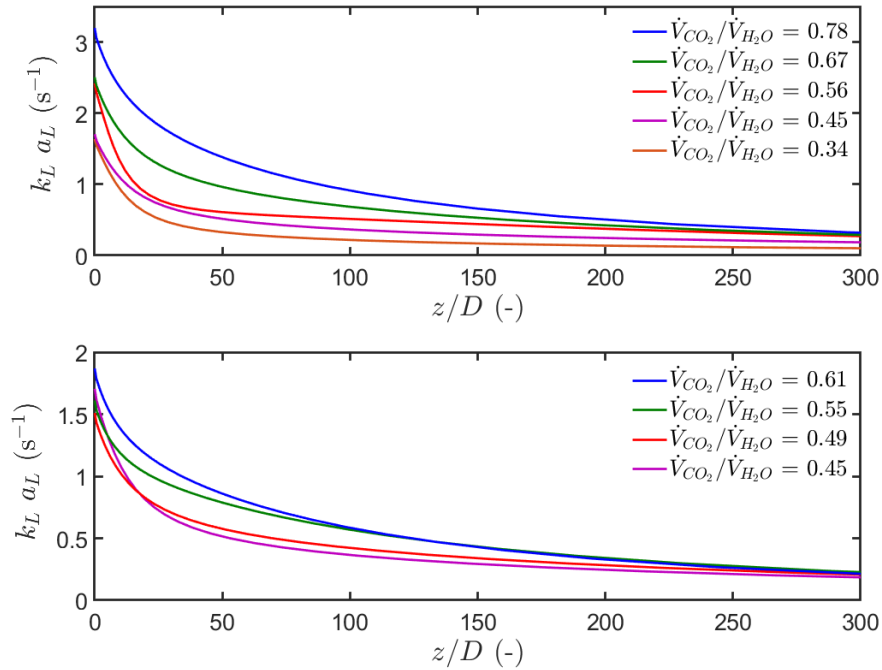


**Figure 4.21** – Volumetric liquid mass transfer coefficient profiles versus the normalized  $z$ -axis position at 8 MPa and 303 K where  $\dot{V}_{CO_2} = 40.5 \mu\text{L min}^{-1}$  (top) and  $\dot{V}_{H_2O} = 200 \mu\text{L min}^{-1}$  (bottom).

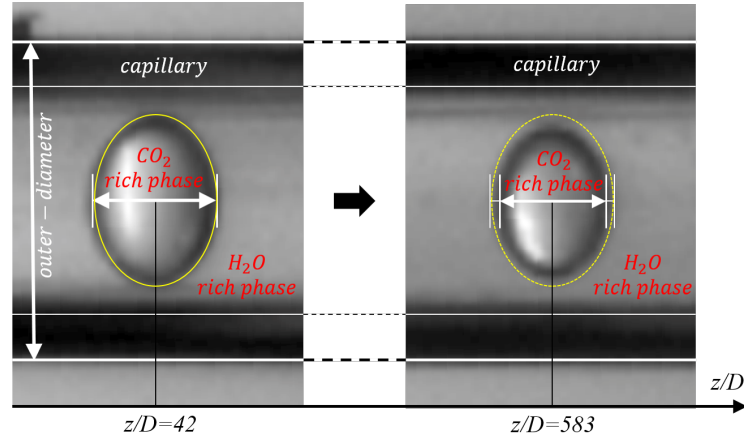
Equation 4.11 shows that when  $\dot{V}_{CO_2}/\dot{V}_{H_2O}$  increases,  $L_B/(L_B + L_S)$  also increases, which corresponds to an increase of  $a_L$ . Hence, an increase in  $\dot{V}_{CO_2}/\dot{V}_{H_2O}$  causes both  $k_L$  and  $a_L$  to increase, which is in agreement with the experimental observations that  $k_L a_L$  is higher when  $\dot{V}_{CO_2}/\dot{V}_{H_2O}$  is higher. Finally, it can be pointed out that values of the liquid volumetric mass transfer coefficients measured here are between  $0.2 \text{ s}^{-1}$  and  $4 \text{ s}^{-1}$ . In the work of Yao et al. (2017) where a segmented two-phase a flow of  $H_2O$  and  $CO_2$  is also investigated (at pressures up to 4 MPa at ambient temperature, in a square microchannel ( $300 \mu\text{m} \times 300 \mu\text{m}$ )), the  $k_L a_L$  values range between  $0.5 \text{ s}^{-1}$  and  $3.8 \text{ s}^{-1}$ . This gives the information that the order of magnitude presented with the method is correct. However, the values cannot be compared exactly. Indeed, in the work of Yao et al. (2017), the volumetric mass transfer coefficient  $k_L a_L$  is supposed to be constant along the microchannel, which is, according to our observations, not the case at the pressures investigated in this thesis work.



**Figure 4.22** – Volumetric liquid mass transfer coefficient profiles versus the normalized  $z$ -axis position at 9 MPa and 303 K where  $\dot{V}_{CO_2} = 38.2 \text{ } \mu\text{L min}^{-1}$  (top) and  $\dot{V}_{H_2O} = 170 \text{ } \mu\text{L min}^{-1}$  (bottom).



**Figure 4.23** – Volumetric liquid mass transfer coefficient profiles versus the normalized  $z$ -axis position at 10 MPa and 303 K where  $\dot{V}_{CO_2} = 49.2 \text{ } \mu\text{L min}^{-1}$  (top) and  $\dot{V}_{H_2O} = 110 \text{ } \mu\text{L min}^{-1}$  (bottom).



**Figure 4.24** – Image of bubbles at  $z/D = 42$  and  $z/D = 583$  at 10 MPa, 303 K,  $\dot{V}_{CO_2} = 73.7 \mu\text{L min}^{-1}$  and  $\dot{V}_{H_2O} = 110 \mu\text{L min}^{-1}$ . Note that the spherical bubble is deformed in the vertical direction because of the light refraction between the glass of the cylindrical capillary and the air. However, there is no deformation of the bubble diameter in line with the tube axis and of the outer diameter of the capillary. The bubble shrinkage is presented in yellow.

## Conclusion

In this chapter a new experimental method to determine volumetric mass transfer coefficients in segmented two-phase flow in a micro-capillary under high pressure using Raman spectroscopy has been presented. This method allows measurement of molar ratios of compounds present in both phases of a fast segmented two-phase flow and provides the opportunity to investigate of many binary systems. Moreover, the coupling of the measurement with a thermodynamic model allows the investigation of volumetric mass transfer coefficients of complex systems where the densities of the phases can change significantly with the molar ratios and where conventional imaging techniques that link mass transfer to a variation in bubble volume are not applicable. The method developed in this study allows the volumetric mass transfer coefficient at different axial positions along the micro-capillary to be determined by filtering the data with a Fast Fourier Transform algorithm. The method allows to get rid of the too strong hypothesis of the conventional unit-cell model described in the literature. The method has been applied to a  $H_2O - CO_2$  system at 303 K for 8,9 and 10 MPa. The values of the volumetric mass transfer coefficient obtained for this system were in the range  $0.2 \text{ s}^{-1}$  to  $4 \text{ s}^{-1}$ , which are in agreement with the literature and shows the accuracy of the method. This Raman spectroscopy method could be further improved by coupling it with an imaging method in order to obtain the surface area of bubbles ( $a_L$ ), liquid slug volumes ( $V_L$ ), as well as the velocities of both phases along the capillary in order to dissociate  $k_L$  and  $a_L$  and to develop dimensionless correlation of  $k_L a_L$  as a function of dimensionless parameters.

# Determination of liquid mass transfer coefficients in a $CO_2$ - $H_2O$ system using a colorimetric method

Introduction . . . . .	137
5.1 Experimental method . . . . .	139
5.1.1 Experimental setup . . . . .	139
5.1.2 Operating conditions . . . . .	144
5.1.3 Image acquisition setup . . . . .	146
5.1.4 Calibration of the method . . . . .	151
5.1.5 Image processing and analysis . . . . .	154
5.2 Determination of liquid-side volumetric mass transfer coefficients . . . . .	161
5.2.1 Determination of $C_{CO_2}$ . . . . .	161
5.2.2 Determination of the volumetric mass transfer coefficient $k_L a_L$ . . . . .	164
5.3 Application of the experimental method to $CO_2$ - $H_2O$ mass transfer under high pressure . . . . .	165
5.3.1 Characteristics of the gas-liquid flow . . . . .	165
5.3.2 Concentration profiles . . . . .	175
5.3.3 Effect of flow rate conditions on $k_L a_L$ . . . . .	176
Conclusion . . . . .	179

## Introduction

Chapter 2 presented a model that enables the liquid volumetric mass transfer coefficient in a two-phase segmented microflow at high-pressure to be calculated from experimental concentration data. This model takes into account the potential modifications of the physical properties of each phase along the reactor that are inherent to the change in pressure.

---

In a fluid-liquid flow <sup>1</sup> where the mass transfer occurs from the fluid phase to the liquid phase, the liquid mass transfer coefficient is calculated by Equation 2.32 in Chapter 2. In the case of a carbon dioxide and water flow, the calculation of the liquid mass transfer coefficient at different positions in the microreactor requires the knowledge of several variables. Firstly, it requires knowledge of the two-phase flow velocity,  $U_{TP}$ , which depends on the volumetric flow rates of  $CO_2$  and  $H_2O$  at the inlet of the microreactor. It is also necessary to know the concentration of carbon dioxide at equilibrium in the water-rich phase,  $C_{CO_2}^{L,*}$  at the operating pressure and temperature, the concentration of carbon dioxide in the liquid phase at each axial position  $z$  in the microreactor,  $C_{CO_2}^L$ , as well as the variation of this concentration with respect to the axial position in the microreactor  $C_{CO_2}^L/dz$ .

This chapter presents an experimental method for the acquisition of the parameters that are necessary for the calculation of the liquid mass transfer coefficient at different  $z$  positions for a two-phase flow of water and carbon dioxide under pressure. This method is based on the acidification of the  $H_2O$ -rich phase due to the dissolution of carbon dioxide. This leads to a decrease of the pH of water, which can decrease to values of less than 3, depending on the temperature and pressure. This method was inspired by the work of Andersson et al. (2018) in which the acidification of a  $H_2O$ -rich phase in contact with carbon dioxide was studied in a microreactor under high pressure. In the work of Andersson et al. (2018), the colored indicator bromophenol blue (BPB) was mixed with water before contacting  $CO_2$  inside a microreactor that allows optical access. The contact of the  $CO_2$ -rich phase and the  $H_2O$ -rich phase forms a segmented Taylor flow composed of  $H_2O$ -rich slugs and carbon dioxide bubbles that is observed with a high-speed camera. Bromophenol blue has a pH-dependent absorbance spectrum. Thus, by placing a lighting system below the microreactor and a band pass filter of the absorbance peak wavelength of bromophenol blue on the camera, it is possible to observe a change in absorbance along the microreactor. This change in absorbance, which corresponds to a change in the pH of the water-rich phase, is obtained using a calibration curve produced beforehand using pH buffer solutions. This method therefore makes it possible to determine the evolution of the pH in the  $H_2O$ -rich liquid slugs at different positions in the channel.

This colorimetric technique is used in this thesis work to follow the evolution of the carbon dioxide concentration in the water-rich phase along the microreactor at a pressure of 10 MPa and 303 K. However, in this work, the pH is linked to a greyscale value instead of an absorbance value. The crucial parameters for the implementation of this method are numerous: the operating parameters (i.e. flow rates of the two phases), the geometry of the microreactor (i.e. diameter), the quality of the image (i.e. shutter of the camera), the power of the lighting system and the concentration of bromophenol blue in water. It is also important to point out that these five parameters are not independent. For example, at a given lighting power, a BPB concentration exists for which it is no longer possible to observe a variation of greyscale

---

<sup>1</sup>The first phase is called “fluid” because it can be either in liquid form or gas form depending on the pressure and the temperature set in the microreactor.



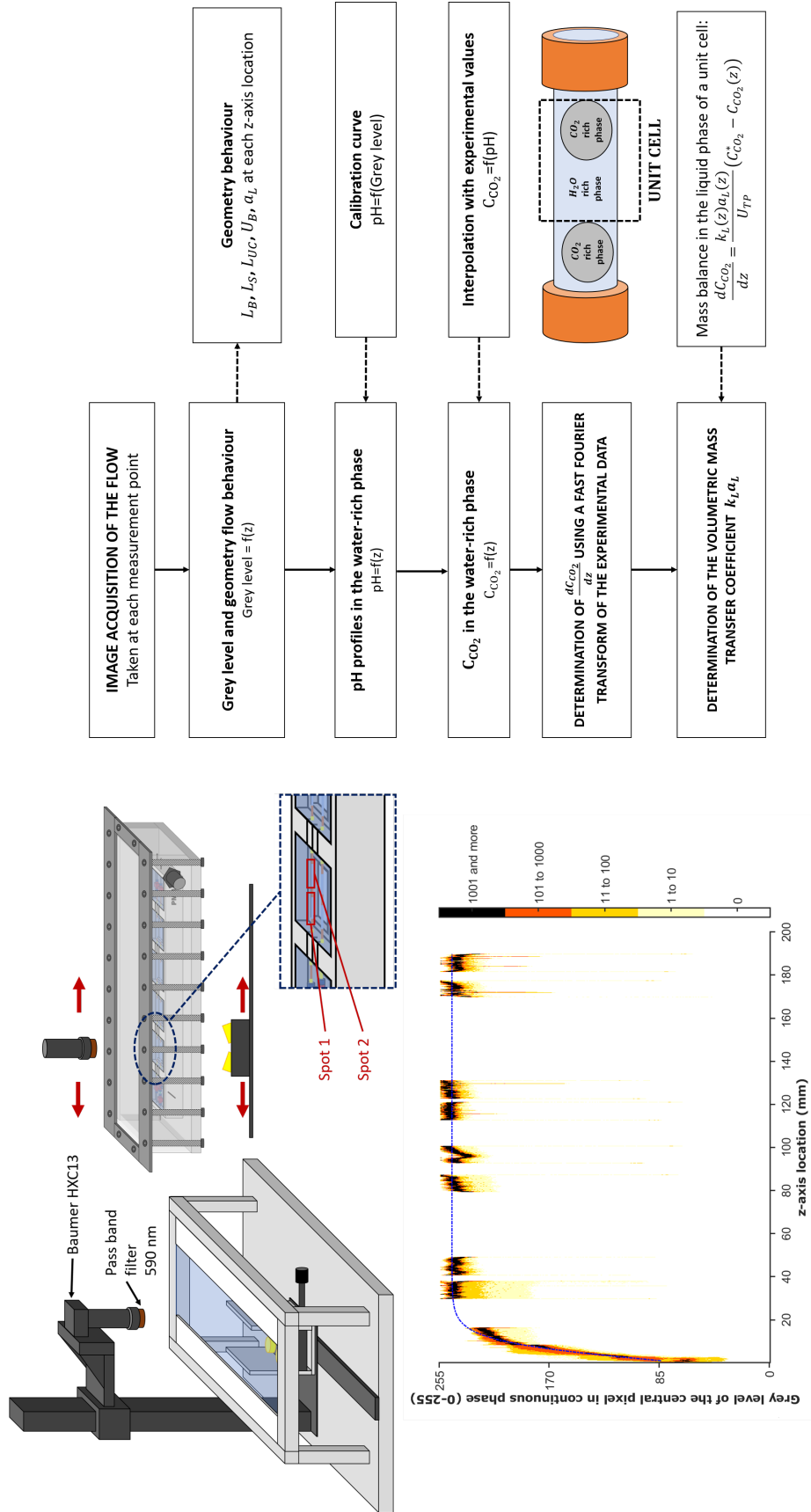
(and therefore of pH) with the camera. Moreover, at a given reactor diameter, if the BPB concentration is too high, it is difficult to find a camera shutter duration that allows both a clear image and a precise observation of the greyscale variation to be obtained. The method is therefore calibrated in order to obtain the set of these five parameters which allow the variation in pH along the microreactor to be detected in an optimal manner. Buffer solutions of different pH are then prepared from mixtures of citric acid and sodium citrate. Bromophenol blue is added to these buffer solutions, at the previously fixed concentration. These BPB solutions of different pH are fed into the microreactor where black and white images are acquired by the camera. The processing of these images allows to draw a calibration curve of the pH as a function of the greyscale. The microreactor is then used to acquire the two-phase flow images of  $CO_2$ - $H_2O$  at 10 MPa and 303 K at different flow rates. These images are processed using an image analysis program coded with Matlab software. This program was developed in order to obtain the geometric properties of bubbles and slugs along the flow such as their size and speed. This program also allows the greyscale of the liquid slugs along the microreactor to be obtained. The evolution of pH along the microreactor is thus determined from the previously established calibration curve. Using an experimental interpolation of pH as a function of  $CO_2$  concentration in the liquid phase, the pH is related to a  $CO_2$  concentration in the water-rich phase. Values of  $CO_2$  concentration in the  $H_2O$ -rich phase are then obtained as a function of the position of the  $H_2O$ -rich slug in the microreactor. These points are filtered using a fast Fourier transform method to obtain an analytical expression of these concentrations. Once these expressions are obtained, it is possible to analytically compute their derivatives and therefore to deduce the volumetric mass transfer coefficient using the model presented in Chapter 2. All of the method steps are summarized in Figure 5.1.

## 5.1 Experimental method

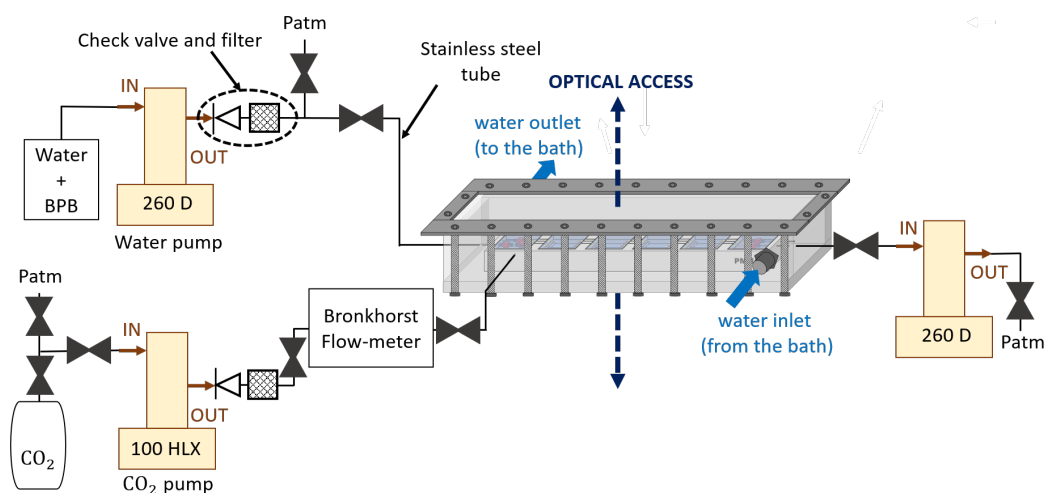
The experimental setup that is used to generate the segmented two-phase flow at high pressure and used to perform the image acquisition of the flow is firstly presented. The calibration of the colorimetric method is then detailed and the choice of BPB concentration in the  $H_2O$ -rich phase and camera shutter duration is explained. Finally, the image processing method is detailed, including the image acquisition of the flow and the greyscale profiles in the  $H_2O$ -rich phase that are used to the determination of  $CO_2$  concentration profiles in the  $H_2O$ -rich phase.

### 5.1.1 Experimental setup

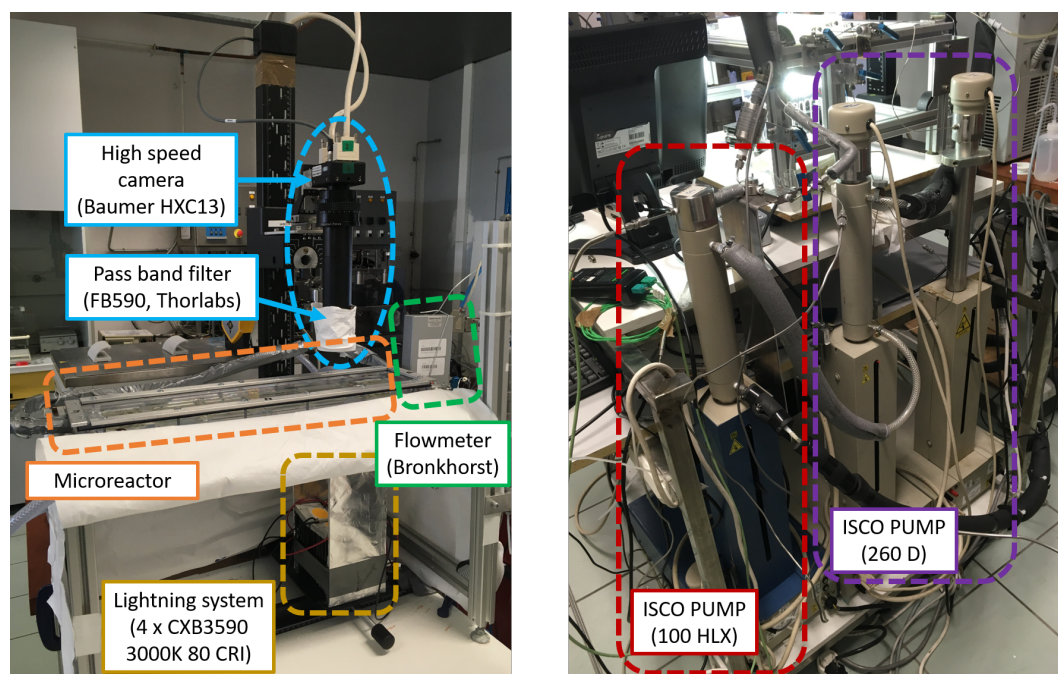
The experimental setup consists in the integration of the inhouse microreactor, which was presented in Chapter 3, in an environment that allows the fluids to be fed at high pressure in order to obtain a two-phase segmented flow. This setup guarantees a constant temperature and pressure and allows acquisition of images of the flow through the optical window. A schematic diagram of the complete setup is shown in Figure 5.2 and photos of the setup are presented in Figure 5.3.



**Figure 5.1** – Colorimetric technique applied to the measurement of mass transfer coefficient in two-phase segmented flow at high pressure.



**Figure 5.2** – Schematic diagram of the experimental setup used to determine mass transfer coefficients in high-pressure two-phase flows.



**Figure 5.3** – Photos of the experimental setup used to determine mass transfer coefficients in high-pressure two-phase flows.

---

## Fluids' feeding in the microreactor

Feeding of water and carbon dioxide at constant pressure in the microreactor is ensured using three high-pressure syringe pumps. An ISCO 260 D pump is used for water injection and an ISCO 100 HLX pump is used for  $CO_2$  injection. The range of flow rates used during the experimental campaign is 110-350  $\mu\text{L min}^{-1}$  for water and 59-112  $\mu\text{L min}^{-1}$  for  $CO_2$ <sup>2</sup>. A Coriolis effect mass micro-flowmeter (Bronkhorst) is placed between the  $CO_2$  injection pump and the microreactor in order to measure the mass flow rate entering the microreactor<sup>3</sup>. The connections between the pumps and the microreactor are made using stainless steel tubes with an internal diameter of 0.6 mm. The fluids are distributed using pressure-resistant valves. The stainless steel tubes are connected to the bulkheads of the temperature controlled chamber and the bulkheads are connected to the microreactor placed within the chamber. A third pump (ISCO 260 D) is connected in the same way at the outlet of the microreactor in order to collect the two-phase mixture and to maintain constant pressure within the microreactor. These three syringe pumps can operate in constant volumetric flow rate mode or in constant pressure mode. In this experimental campaign, the two pumps feeding  $H_2O$  and  $CO_2$  to the microreactor operated at fixed volumetric flow rate, while the outlet pump operated at constant pressure. Non-return valves are present between the fluid injection pumps and the microreactor in order to prevent back flow of water (or  $CO_2$ ) into the  $CO_2$  pump (or water pump) during the establishment of a stable periodic flow. In addition, filters (with an average pore diameter of 0.5  $\mu\text{m}$ ) are present at the same places in order to prevent the contamination of the microreactor with possible impurities from the injection pumps.

## Pressure control

As previously said, the pressure control of the microreactor is ensured using the two injection pumps and the outlet pump of the microreactor. The inlet pumps deliver a constant flow rate while the outlet pump is pressure controlled. The outlet pump therefore delivers a negative flow rate necessary to maintain this pressure. The precision on the outlet pressure (ISCO 260 D) is ensured by the manufacturer at  $\pm 0.26$  MPa, which corresponds to 0.5% of the full scale (51.7 MPa).

The pressure drop in the system has been calculated for the worst case (where the pressure drop is the highest), i.e. when the outer capillary tube (of the microreactor) and the stainless steel tubes are filled with water and when the total flow rate in the system is at the maximum value used in the experimental campaign (350  $\mu\text{L min}^{-1}$ ). The same method as the one presented in Chapter 4 is applied. The maximum pressure drop values possible in the experimental system are presented in Table 5.1. The total pressure drop in the system does

---

<sup>2</sup>These volumetric flow rates are given at pressure and temperature of the microreactor, here 10 MPa and 303 K.

<sup>3</sup>The density of  $CO_2$  varies between the pump and the microreactor because of the change in temperature, measurement of the mass flow rate is necessary in order to know the  $CO_2$  volumetric flow rate inside the microreactor with precision

not exceed 0.35 bar, which can be considered negligible for the study presented here.

$$\Delta P = 32 \frac{\mu L v}{D^2} \quad (5.1)$$

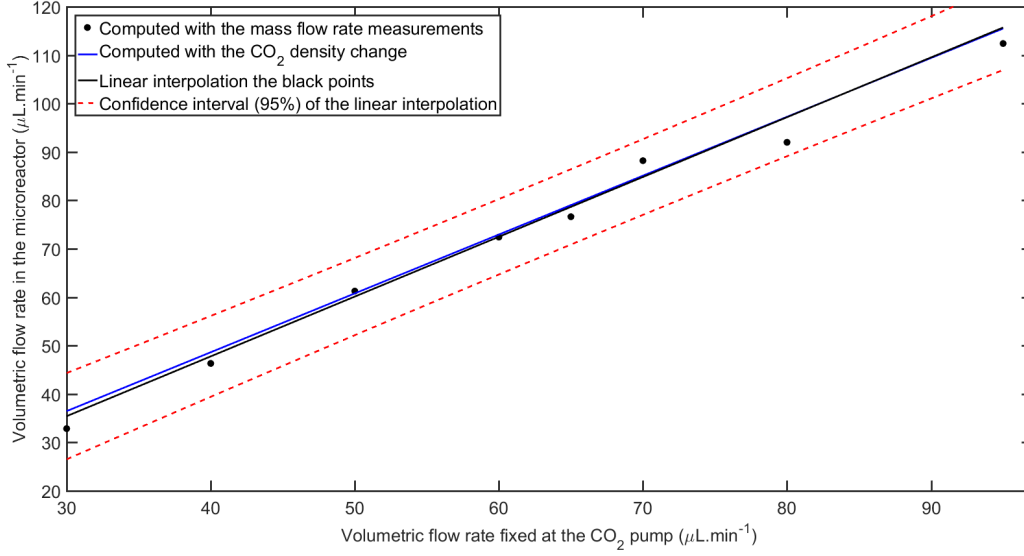
**Table 5.1** – Pressure drop in different tubes of the system with  $\dot{V}_{H_2O} = 350 \text{ } \mu\text{L min}^{-1}$  and  $\dot{V}_{CO_2} = 112 \text{ } \mu\text{L min}^{-1}$ . The viscosities of  $CO_2$  and  $H_2O$  are computed at 10 MPa and 303 K with the models presented in Chapter 2.  $\mu_{CO_2} = 66.3 \text{ } \mu\text{Pa s}$ ,  $\mu_{H_2O} = 796.7 \text{ } \mu\text{Pa s}$ .

Tube	Stainless steel tube ( $H_2O$ )	Outer-capillary tube ( $H_2O$ )	Inner-capillary tube ( $CO_2$ )
Inner-diameter ( $\mu\text{m}$ )	1020	250	75
Length (m)	1.2	0.38	0.08
Velocity ( $\text{cm s}^{-1}$ )	0.7	11.8	35.9
Pressure drop (bar)	0.002	0.20	0.12

## Temperature control

Temperature control is carried out at two strategic locations in the setup. On one hand within the microreactor in order to obtain an isothermal flow, and on the other hand, at the  $CO_2$  pump in order to keep a constant mass flow rate in the microreactor. The microreactor is placed in the temperature controlled chamber (cf. Figure 5.2). This chamber is connected to a thermostatically controlled bath (Lauda RE 2025G) using heat-insulated plastic tubes. The temperature in the bath is regulated at  $\pm 0.01 \text{ K}$ . However, the heat losses along the insulated tubes give an uncertainty on the water temperature on  $\pm 0.1 \text{ K}$ . Temperature tests of the microreactor submerged in the conditioning chamber were carried out. For a bath temperature set at 303 K, once the bath has reached this temperature (in 15 minutes), the microreactor reaches this same temperature in an average time of 10 minutes. The warm-up of the entire system is therefore estimated at 25 minutes.

The  $CO_2$  syringe pump is thermostatically controlled. A double jacket connected to an external bath (Lauda RE 104) surrounds the pump cylinder in order to maintain an injection at constant temperature. The  $CO_2$  pump bath is regulated at a temperature of 276 K. However, the thermal losses along the tubes connecting the bath to the jacket and through the pump cylinder give that for a bath temperature of 276 K, an injection temperature of  $CO_2$  at 282 K at the top of the cylinder pump (measured with type K thermocouples).



**Figure 5.4** –  $CO_2$  volumetric flow rates computed in the microreactor (at 10 MPa and 303 K) from the volumetric flow-rate in the ISCO pump and  $CO_2$  density change between the  $CO_2$  pump and the reactor (blue line).  $CO_2$  volumetric flow rate computed (at 10 MPa and 303 K) with the mass flow rates measurements (black points) and linear interpolation of these measurement values (black line).

### 5.1.2 Operating conditions

The operating pressure studied is 10 MPa for an operating temperature of 303 K. The ISCO pumps are set to deliver a constant volumetric flow rate. However, since there is a temperature change -and therefore a density change of the  $CO_2$  between the pumps and the microreactor, the volumetric flow rates have to be recalculated to take into account the change in density.

#### Volumetric $CO_2$ flow rate computation

The volumetric flow rates of  $CO_2$ ,  $\dot{V}_{CO_2}(microreactor)$ , are calculated from the knowledge of the mass flow rates measured with the mass flow-meter,  $\dot{M}_{CO_2}(Bronkhorst)$  with Equation 5.2 and the density change between the  $CO_2$  pump and the microreactor with Equation 5.3.

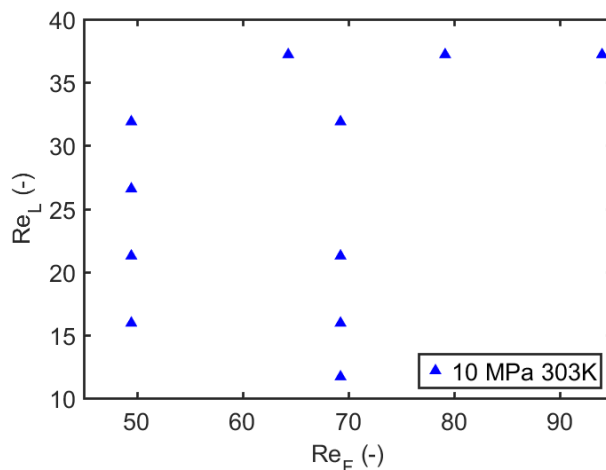
$$\dot{V}_{CO_2}(microreactor) = \frac{\dot{M}_{CO_2}(Bronkhorst)}{\rho_{microreactor}} \quad (5.2)$$

$$\dot{V}_{CO_2}(microreactor) = \dot{V}_{CO_2}(pump) \times \frac{\rho_{pump}(282\text{ K})}{\rho_{microreactor}(303\text{ K})} \quad (5.3)$$

The volumetric flow rates in the microreactor calculated using the mass flow rates measurements are in agreement with the density change calculations as presented in Figure 5.4. However, a small shift is noted for low volumetric flow rates.

### Range of Reynolds number

The fluid ( $CO_2$ ) and the liquid ( $H_2O$ ) Reynolds numbers of the experiments are presented in Figure 5.5. Detailed operating conditions are summarized in Table E.1 of Appendix E.



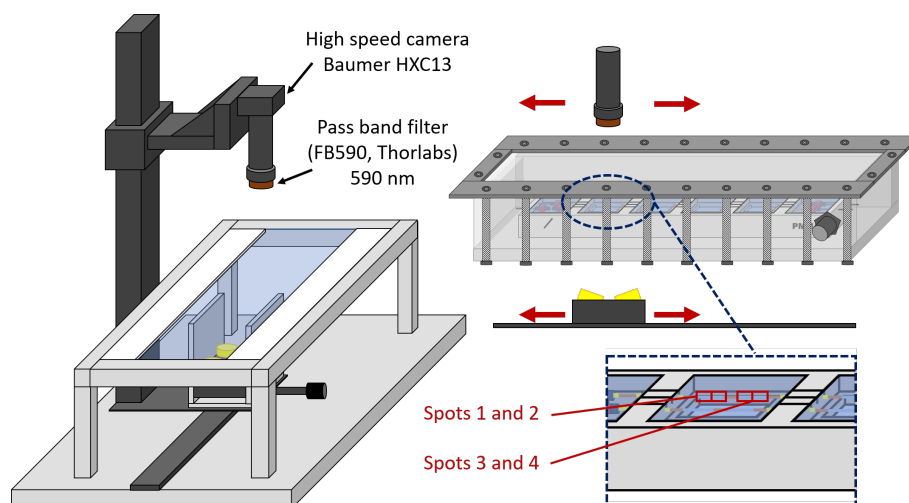
**Figure 5.5** – Operating conditions in term of Reynolds number for the  $H_2O$  flow rate (L) and the  $CO_2$  flow rate (F).

A comparison with the Reynolds number investigated in the Raman spectroscopy method (Figure 4.11 in Chapter 4) shows that the fluid and liquid Reynolds numbers investigated in the colorimetric method are higher. This is due to the fact that the fluid velocities investigated in the colorimetric method are higher, even if the capillary diameter is shorter (250  $\mu m$  compared with 300  $\mu m$  in the Raman method). In both cases, the Reynolds number investigated show that the flows obtained inside the capillary are laminar flows.

### Transient regime

In order to obtain the stable and periodic flow within the microreactor at working temperature and pressure, several steps are performed. Firstly, the bath that is connected to the temperature controlled chamber of the microreactor is set at the operating temperature. The microreactor reaches a fixed temperature after 25 minutes. During this time, the following steps are carried out:

- The inlet pump feeding the water and the outlet pump are connected to the microreactor (the valve of the  $CO_2$  pump is closed). Water is fed to the microreactor (500  $\mu L \min^{-1}$ ) in order to increase the pressure.
- Once the operating pressure is reached, the output pump is set in pressure control mode with the objective to maintain the operating pressure. At this time, if no leaks are present in the system, the flow rate displayed at the outlet pump is  $-500 \mu L \min^{-1}$ , i.e. the opposite of the water pump flow rate. The working water flow rate is then set to the water inlet pump.



**Figure 5.6** – Schematic overview of the optical measurement setup. A translating system makes it possible to acquire images at the different measurement spots.

- The  $CO_2$  pump is used in pressure control mode to reach the operating pressure. Once this pressure is reached, the operating  $CO_2$  flow rate is set to the pump and the valve connecting the  $CO_2$  pump to the microreactor is opened.
- After a certain amount of time (from ten minutes to two hours <sup>4</sup>), stable segmented flow is obtained. When one of the flow rates is modified, it is necessary to wait between two and five minutes (when changing the water flow rate) and between ten and fifteen minutes (when changing the  $CO_2$  flow rate) before the new flow conditions stabilize again.

### 5.1.3 Image acquisition setup

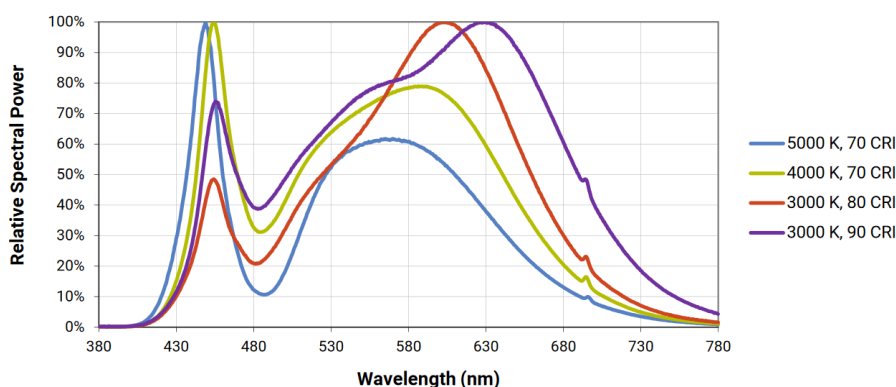
The microreactor is illuminated by transmitted light using a lighting system consisting of four LEDs (CXB3590 3000K 80 CRI). The images of the flow inside the microreactor are obtained using a high-speed camera (Baumer HXC13) with a band pass filter (590 nm  $\pm$  2 nm) which is placed directly above the LED system and the microreactor. This has a speed of 600 images per second for an image size of 1.8 mm  $\times$  7 mm. The microreactor has four viewing windows each comprising four measurement spots where capillary that is stripped of its protective coating is visible. The device is shown schematically in Figure 5.6. The assembly (camera + LED) is placed on a mobile rail in order to focus on the different measurement spots whilst maintaining the same lighting for each image.

#### Lighting system

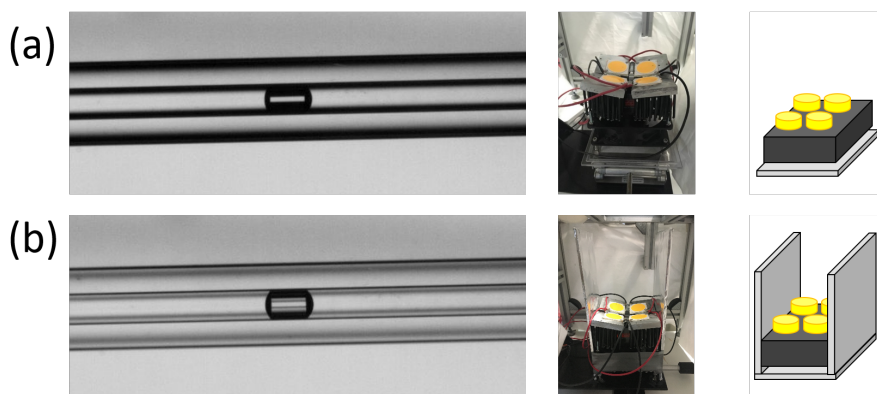
The lighting system is a key part of the colorimetry method. Since a band pass filter (590 nm) is used with the camera, the intensity of the light signal that reaches the camera is greatly

<sup>4</sup>At low working pressures, the time to obtain stable flow is high due to the  $CO_2$  low density, close to a gas density while this time will be shorter if the density of  $CO_2$  is high (i.e. at high pressure).





**Figure 5.7** – Relative spectra power of the different CXB3590 LED types as a function of the wavelength.



**Figure 5.8** – Images of an air bubble placed inside the microreactor filled with water when the lighting system is not equipped with reflectors (a) and when the lighting system is equipped with two reflectors (b).

reduced. To compensate for this lack of intensity, four high-intensity LEDs (CXB3590 3000K 80 CRI, 10000 lumens each) were combined to provide a sufficiently strong signal. These four LEDs are positioned in a concave way to achieve maximum illumination in the capillary tube. In addition, these LEDs have been chosen to have maximum intensity at the wavelength of the bandpass filter (590 nm), as shown in Figure 5.7 .

The four LEDs are placed on four static fans, which are placed on a dynamic fan in order to dissipate the heat produced by the LEDs. Two rectangular reflectors are placed on either side of the lighting system and parallel to the capillary. These reflectors allow to better define the contours of the capillary and the bubbles, as shown in Figure 5.8. This figure shows the image of an air bubble inside the microreactor filled with water in the case where there is no reflector (a) and in the case where two rectangular reflectors are used (b). In case (a), the outlines of the capillary and the bubble are coarse unlike in case (b) where the outlines are fine. The use of reflectors allows side lighting that brightens the areas where light does not pass when lighting is unidirectional (bottom to top). This is due to the change in the refractive index between glass, water and air that cause areas close to the glass-air, glass-water and air-water interfaces not to be illuminated adequately. The addition

---

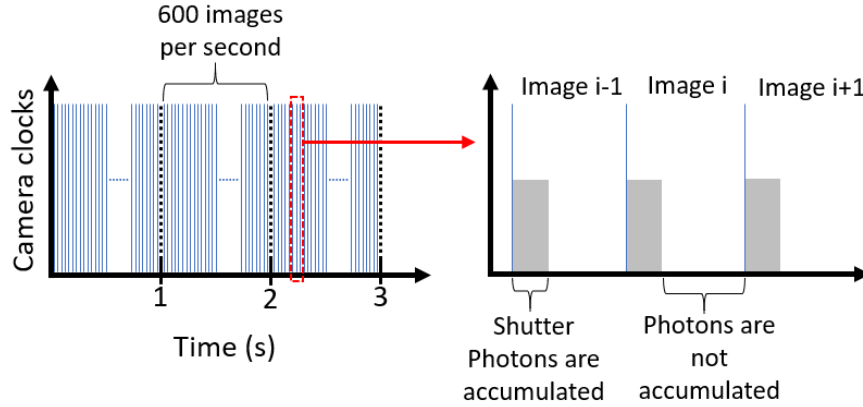
of reflectors therefore allows better precision on the measurements of the sizes, areas and volumes of the bubbles.

## Camera parameters

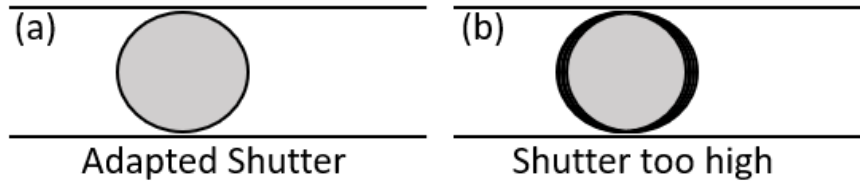
A camera enables the acquisition of an image using a photographic sensor, which converts electromagnetic radiation into an analog electrical signal. The processing of this signal allows to obtain a digital image which can be observed on a screen. The image resolution, which is  $256 \times 1024$  in this study, is the amount of pixels per row (256) and per column (1024) of the image. Thus, a digital image is a reconstruction of each of these independent pixels. A digital color image is conventionally called a 24-bit image. In this case, each pixel of the image is coded on 24 bits, i.e. 3 bytes, each being able to take for value an integer between 0 and 255, i.e. 256 different values. The space generally used is the Red-Green-Blue (RGB) space. Thus, depending on the intensity of each of the Red / Green / Blue colors received by the sensor, the 3 bytes take on the corresponding value, 0 corresponding to zero intensity and 255 to maximum intensity. This combination results in a color. There are therefore  $256 \times 256 \times 256 = 16.7$  million possible colors. The camera used here, Baumer HXC13, allows to acquire images only in shades of grey (generally called “black and white”). The principle is similar: each pixel is here coded on one byte, and the light intensity that is received corresponds to a shade of grey. An intensity of 0 (minimum intensity) corresponds to black and 255 (maximum intensity) corresponds to white. The resulting image is therefore a matrix whose size corresponds to the resolution of the image (here  $256 \times 1024$ ), and each of those elements has a value between 0 and 255.

A macro-type lens as well as an extension tube are inserted into the high-speed camera for macro photography. This type of photography allows to acquire images of small objects with a magnification ratio greater than 1:1. The distance between the camera lens, and the object observed inside the capillary, is 120 mm. The viewing field of the camera is  $1.8 \text{ mm} \times 7 \text{ mm}$  which corresponds to an image resolution of  $Resol = 6.8 \text{ }\mu\text{m}$  per pixel. The distance between the object inside the capillary and the lighting system is adjusted to obtain uniform illumination over the entire viewing field of the camera.

For each measurement spot, the camera records 1800 images, which corresponds to 600 images per second and 3 seconds of acquisition time. The value of the camera shutter, given in  $\mu\text{s}$ , corresponds to the duration of the shutter opening (for each camera clock cycle), located between the lens and the sensor. The shutter then allows to control the light intensity received by the sensor. The higher this value, the longer the shutter remains open, and the greater the light intensity received by the sensor. This therefore influences the measured greyscale: an object photographed with a high shutter will be brighter in the image than by selecting a low shutter, which results in a higher greyscale. Likewise, if the object is too dark (when the value of the greyscale is close to zero), it may be necessary to increase the value of the shutter in order to be able to observe it, when it is not possible to increase the incident light



**Figure 5.9** – Scheme describing the camera shutter.



**Figure 5.10** – Scheme of two bubble pictures inside a micro-capillary when the shutter of the camera is adapted (a) and when the shutter of the camera is too high (b).

intensity from the lighting system. In practice, this shutter closure is done digitally. The photons received by the camera are only counted during the shutter period, as shown in Figure 5.9.

For an acquisition of 600 images per second, the shutter cannot exceed  $1/600$ s, i.e.  $1666 \mu\text{s}$ . In practice, if the shutter is too high, the image may be saturated in white (all greyscales at 255). It is therefore necessary to first adjust the shutter and keep it for all image acquisitions. In addition, the blur linked to the bubble speed influences the shutter choice. If during the shutter period the bubble has time to move of more than one pixel, the resulting image will be blurred, as shown in Figure 5.10.

To calculate the limit shutter from which the image will start to blur, it is necessary to approximate the bubbles speed ( $U_B$ ) during the experiments, and the length of a pixel,  $L_{pix} = \text{Resol} \times 1$ . The limit shutter is calculated using the equation 5.4.

$$Shutter_{limit} = \frac{L_{pix}}{U_B} \quad (5.4)$$

In this study, in order to avoid image disturbance related to the speed of the bubbles, the shutter must be less than  $85 \mu\text{s}$ , which corresponds to a bubble speed of  $U_B = 8 \text{ cm s}^{-1}$  and a pixel length of  $L_{pix} = 6.8 \mu\text{m}$ . Using the 590 nm bandpass filter greatly reduces the amount of photons received by the CCD camera. As a consequence, it is necessary to work at higher shutters with the filter, in order to be able to acquire a sufficient number of photons and

---

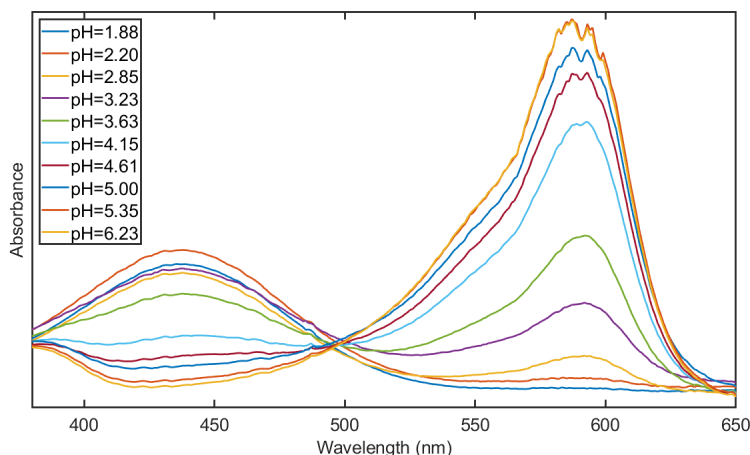
thus to observe an adequate variation of greyscale in the image.

Another important parameter is the depth of field (here inferior to 500  $\mu\text{m}$ ). This needs to be adjusted such that the focus avoids observation of both the inside of the capillary and any dust particles present in the resin or in the water of the thermostatic bath and creates a blurry image. In order to avoid blurry images, the focal length  $f$  of the camera can be adjusted. In the work of this thesis, the focal length is adjusted to  $f/2.4$  in order to obtain a clear image in the capillary plane only.

### 5.1.4 Calibration of the method

#### Bromophenol blue

The absorbance of Bromophenol blue (BPB) is a function of the pH of the aqueous solution, as shown in the visible absorbance spectra of BPB solutions at different values of pH presented in Figure 5.11.

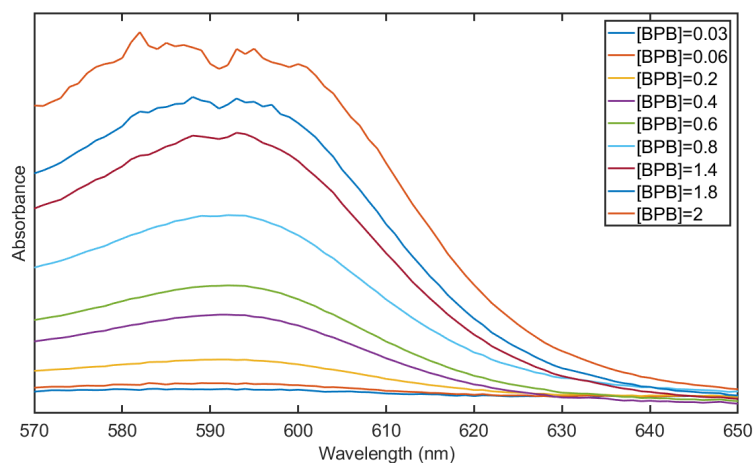


**Figure 5.11** – Visible absorbance spectra (Agilent Technologies Cary 8454) of pH buffer aqueous solutions (citric acid + sodium tri-citrate) with a bromophenol blue concentration equals to  $0.03 \text{ mmol L}^{-1}$ .

The absorption spectrum of BPB shows an acidic form with a maximum absorbance at 410 nm and a basic form with a maximum absorbance at 590 nm. These absorbance maxima are a function of the pH of the solution. An aqueous solution of BPB, observed in the capillary, will therefore exhibit a variation in greyscale if its pH is modified. In a two-phase flow of carbon dioxide and water mixed with bromophenol blue, the acidification of water due to the transfer of carbon dioxide is detected by means of a change in greyscale. This change in greyscale is detectable since the camera filter only allows light of a wavelength equal to the maximum peak absorbance of the basic form of BPB to pass through. This variation in greyscale is correlated with a variation of pH using a calibration curve  $pH = f(\text{greyscale})$  previously established with BPB buffer solutions.

The BPB concentration also influences the absorbance spectrum of the solution, as shown in Figure 5.12. It is therefore necessary to find the adequate concentration so that the entire pH range can be distinguished on the images taken in the microreactor. If the concentration is too high, there is black saturation of the images for a high pH range and if the concentration is too low, there is a white saturation of the images for a low pH range.

The adequate concentration of BPB to be used in water in order to be able to optimally visualize the variation of greyscale in the two-phase flow of  $CO_2$ - $H_2O$  is obtained by carrying



**Figure 5.12** – Visible absorbance spectra (Agilent Technologies Cary 8454) of a pH buffer solution (citric acid + sodium tri-citrate) at different BPB concentrations (in  $\text{mmol.L}^{-1}$ ). The pH of the buffer solution is 3.63.

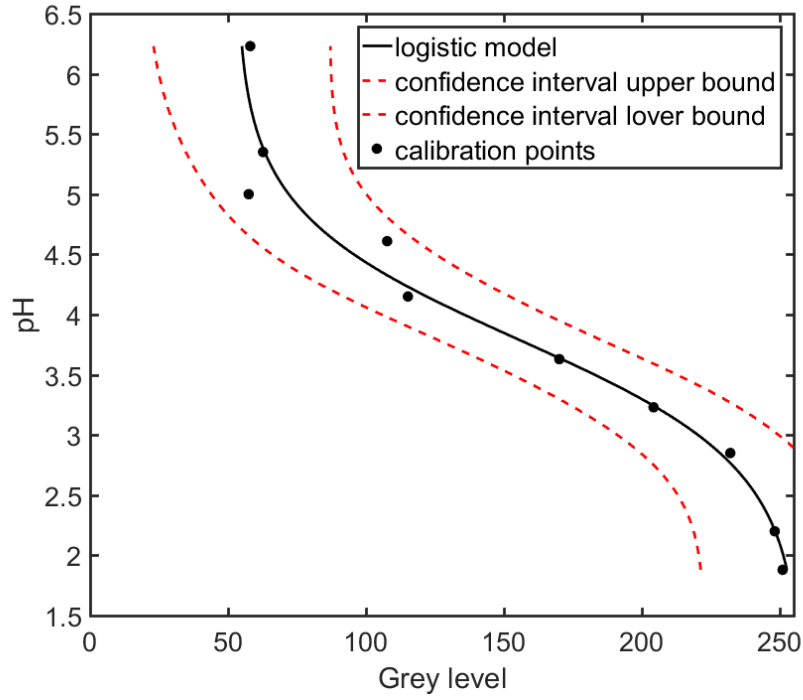
out the following parametric study. Ten buffer solutions composed of citric acid and sodium citrate are prepared for pH values ranging from 1.88 to 6.23. Using these solutions, three groups of ten solutions are prepared at three different BPB concentrations ( $0.2 \text{ mmol.L}^{-1}$ ,  $0.8 \text{ mmol.L}^{-1}$  and  $2 \text{ mmol.L}^{-1}$ ). The absorbance spectra of these solutions are then measured in order to determine whether it will be possible to differentiate them by the absorption peak of the basic form of BPB (590 nm).

### Calibration curve $\text{pH}=\text{f}(\text{greyscale})$

The previously prepared solutions are fed into the microreactor, in order to determine the pH calibration curves as a function of the greyscale observed in the images acquired by the camera. These images are taken at different camera shutter openings (100, 200, 300, 400 and 500  $\mu\text{s}$ ). If the shutter opening is too high, the solutions with low absorbance cannot be detected because the images are saturated in white. On the other hand, if the shutter opening is too low, it does not allow the solutions with high absorbance to be differentiated because the images obtained are black. Therefore, it is important to determine the combination of camera shutter opening and BPB concentration that allow the change in greyscale to be detected correctly for an entire given pH range, a given lighting power and for a fixed bubble speed range <sup>5</sup>. The different calibration curves are presented in Figures E.1, E.2 and E.3 in Appendix E. A "blank image"<sup>6</sup> has been removed from each of the images obtained of the BPB solutions. This allows to correct the fact that the thickness crossed by the light is not the same at the center of the capillary as near the capillary edges. The chosen pair of BPB concentration and optimal shutter opening are  $0.8 \text{ mmol.L}^{-1}$  and 300  $\mu\text{s}$ , respectively. This choice is detailed in the Appendix E. All experiments are therefore carried out for a

<sup>5</sup>The bubble speed conditions the acceptable shutter range in which the image is not too blurred

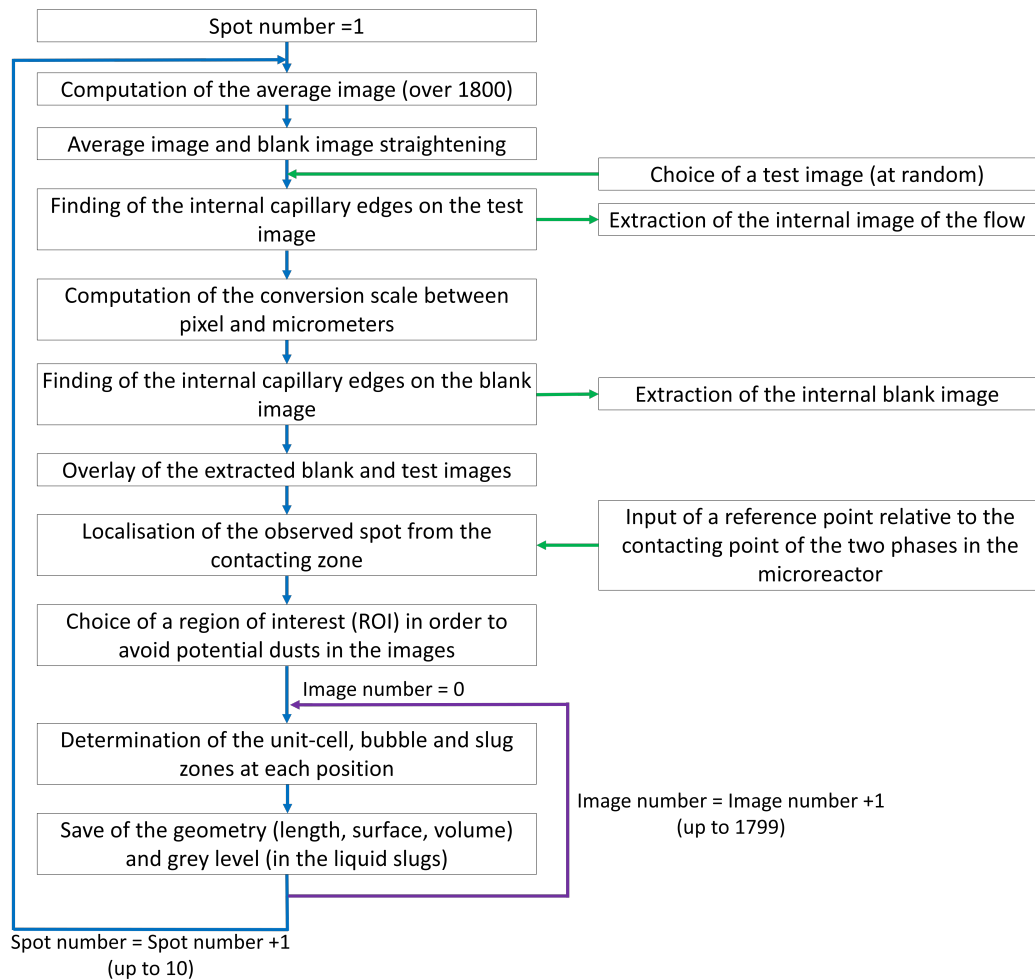
<sup>6</sup>The blank image corresponds to pure water circulating inside the capillary



**Figure 5.13** – Calibration curve linking the pH of the pH buffer solutions (citric acid + sodium tri-citrate) with the grey level of the images of these solutions placed inside the microreactor.  $[BPB]=0.8 \text{ mmol L}^{-1}$ , shutter= $300 \text{ } \mu\text{s}$ .

BPB concentration of  $0.8 \text{ mmol L}^{-1}$  in the water-rich phase and for a camera shutter of  $300 \text{ } \mu\text{s}$ . The calibration curve is shown in Figure 5.13. A logistic regression is used to fit the experimental points. It can be seen that for pH values higher than 5, the error on pH is quite significant. However, in this study, the  $H_2O$  is acidified by  $CO_2$  directly at the bubble generation process, and therefore pH higher than 5 are rarely investigated.

### 5.1.5 Image processing and analysis



**Figure 5.14** – Diagram of the image processing and analysis performed in the Matlab program.

During an experiment, for each of the 10 measurement spots observed (corresponding to a total length of 19 cm), 1800 images are obtained. These images are processed using Matlab software spot by spot by following the steps presented in Figure 5.14 in order to obtain the velocity, length, surface and volume of the bubbles, as well as the greyscale in the liquid slugs for the calculation of the concentration of  $CO_2$  solubilized in the  $H_2O$ -rich phase.

#### Computation of the average image

Figure 5.15 presents an image of the flow obtained at a measurement spot (a), the blank image where pure water is circulating at this measurement spot (b) and the average image of the 1800 images obtained at this measurement spot (c). The average image corresponds to the average greyscale obtained with 1800 images taken at this measurement spot. This





**Figure 5.15** – (a) Image of a two-phase segmented flow of  $CO_2 + H_2O + BPB$  at 10 MPa and 303 K. (b) blank image in the bubble generation zone (spot 1). (c) Averaged image of the 1800 images taken in spot 1.

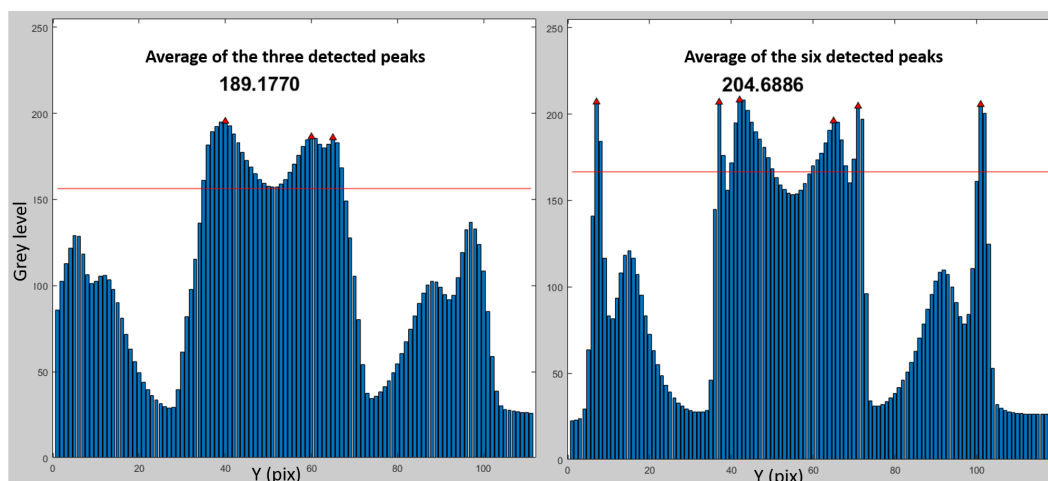
average image is used for the straightening process of the images. Indeed, it is observable that the capillary is tilted in the image and therefore it is necessary to straighten it in order to be able to set the position of the bubbles and liquid slugs.

### Average image and blank image straightening

To perform the rectification, the negative image of the average image is computed (black therefore corresponds to 255 in greyscale) and an average is calculated over the length direction of the image. The result is presented in Figure 5.16 (a). It can be seen that the inner and outer edges of the capillary give a maximum in greyscale. A step by step image rotation is then carried out and the same average as before is calculated until the highest greyscale values for the edges of the capillaries are obtained. When this maximum value is obtained, it can be assumed that the image is straightened. This step is also carried out for the blank image in order to be able to later superimpose the images of the flow with the blank image.

### Processing of the internal capillary edges

The relevant image area that has to be analysed to follow the evolution of the flow and the greyscale is that corresponding to the inner part of the capillary. It is therefore necessary to clearly identify the edges of the internal capillary in the image. Figure 5.17 presents the step that consists in detecting the contours of the test image (and therefore of the other images). In practice, the maximum greyscales obtained during the straightening process are detected and the corresponding pixels are assumed to correspond to the inner capillary. The edge of the capillary is therefore identified at the next line of pixels and the result is verified on a test image selected randomly from the 1800 images. Once the edges of the capillary are detected, the same process is carried out for the blank image and the interiors of the capillaries are extracted to create new images. This step also allows to give the scale, namely



**Figure 5.16** – Average in the z-direction of the negative average image when the image is not straightened (a) and when the image is straightened (b).

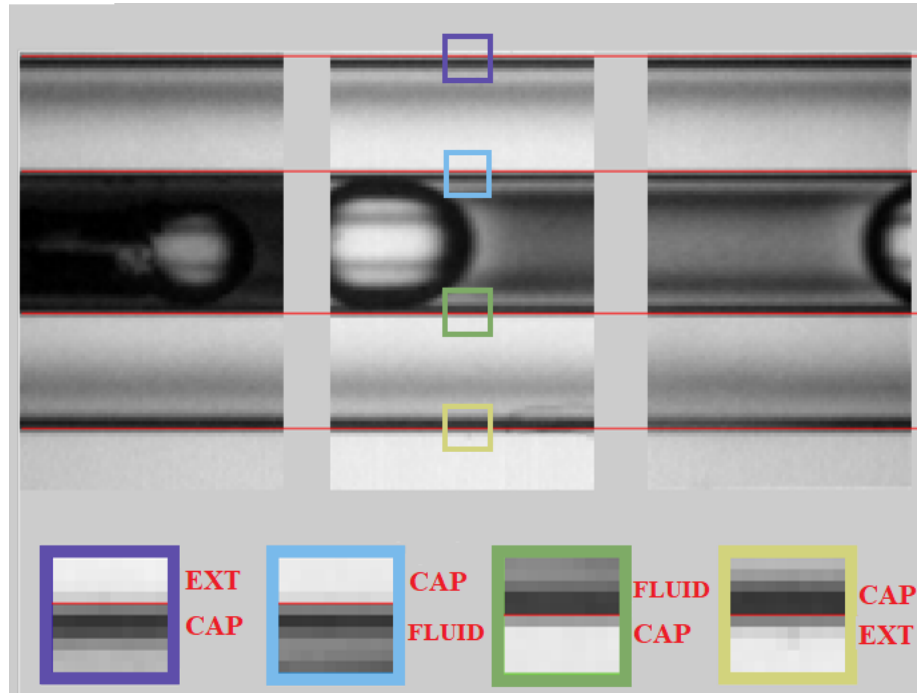
the real size of a pixel. Indeed, the height of the extracted image in pixels corresponds to the internal diameter of the capillary, which is known in micrometers. The scale obtained here is 6.8  $\mu\text{m}$  per pixel.

## Overlay of the extracted blank and test images

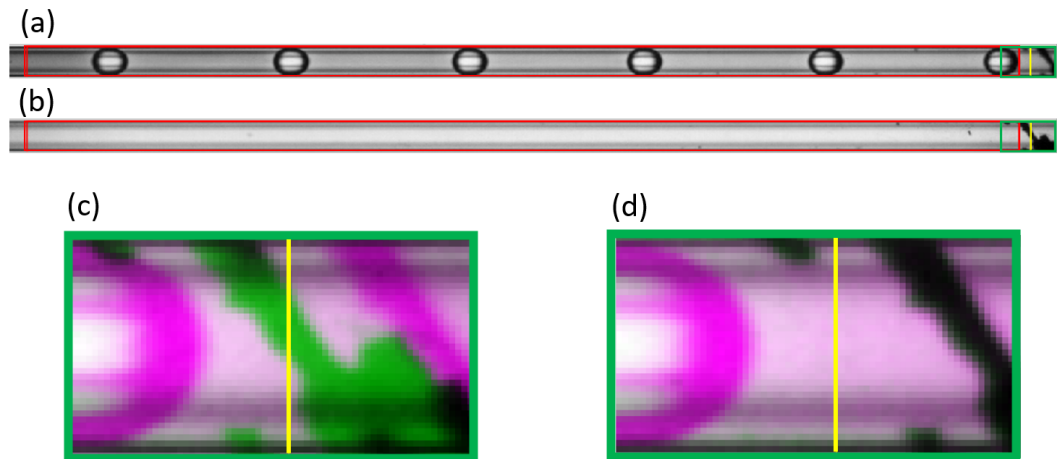
This step consists of superimposing the blank image and the test image extracted from the previous step. Since these images correspond to the extraction of the interior of the capillary, these images are already aligned vertically. However, it is also necessary to align these two images horizontally. Figure 5.18 presents this step. The carbon residue (due to coating removal by combustion) present on the capillary at this spot allows this alignment to be made. Figure 5.18 (c) and (d) show the overlay of the test image and the blank image (the test image is purple and the blank image is green). In Figure 5.18 (c), the images are not perfectly superimposed. It is therefore possible to shift one image relative to the other to obtain perfect alignment, as in Figure 5.18 (d). The yellow line in Figure 5.18 is used to locate the measurement spot with respect to the fluids contacting zone at the entrance of the microreactor. In fact, the yellow line corresponds to the black residue visible from the outside of the reactor for which the distance to the fluids contacting zone was measured.

## Determination of the unit-cell, bubble and liquid slug zones

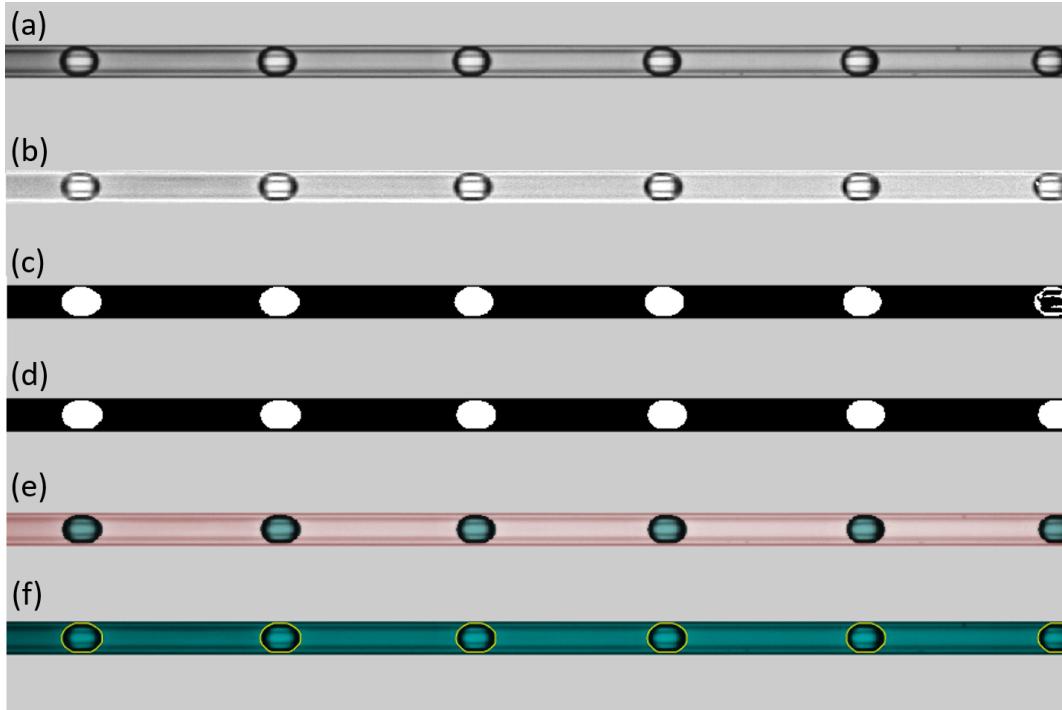
When the test and blank images are perfectly aligned, it is possible to perform the following operation, the test image and the blank image were subtracted from the maximum grey-level of 255, in order to remove the effect of depth that is present in the center of capillary. This is because the light from the illumination passes through a greater amount of liquid in the center of the capillary than near the edges, and therefore the greyscale obtained is not the same. With this operation, the effect of liquid thickness is greatly reduced. The result is presented in Figure 5.19 (b). It can be observed that the effect of the liquid depth effect is



**Figure 5.17** – Determination of the capillary edges. A test image is displayed in order to verify the capillary limit detected by the Matlab program.



**Figure 5.18** – Overlay of the extracted test (a) and blank (b) images when they are not well superimposed (c) and when they are well superimposed (d).

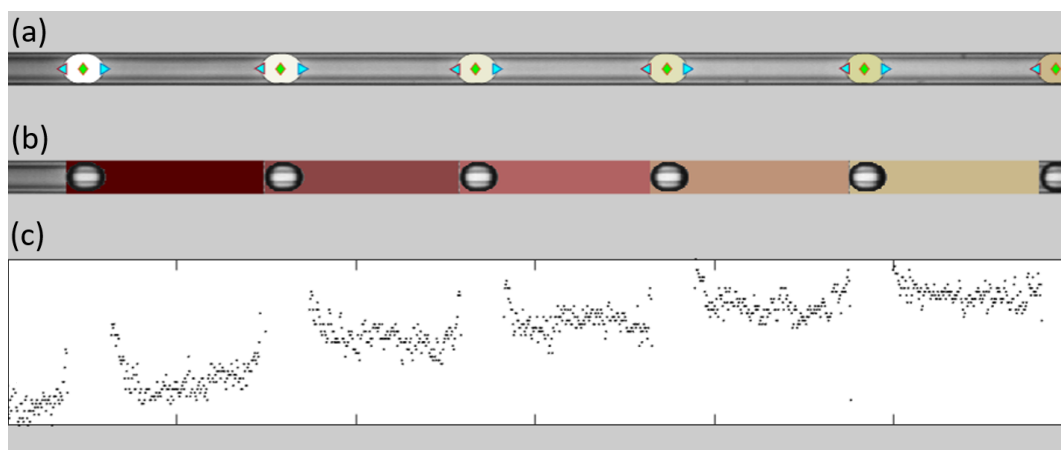


**Figure 5.19** – Successive steps for the acquisition of the bubble geometry and the greyscale in the liquid slugs. (a) test image. (b) 255-(blank image-test image). (c) Binarization with a variable threshold and opening (erosion + dilatation). (d) Convexity filter and gap filling. (e) and (f) visual verification.

less important for image (b) than for the test image (a). In addition, image (b) facilitates the detection of bubble edges. Figure 5.19 (c) represents image (b) after several successive steps. These steps correspond to binarization of the image (with a variable threshold), as well as an opening which is the succession of an erosion and a dilation in order to remove potential artefacts. Figure 5.19 (d) is the result of a filter that ensure the convexity of the bubble and a filling of the bubbles that are not yet completely white in Figure 5.19 (c). Steps (e) and (f) serve as a visual check on the correct detection of the bubble edges.

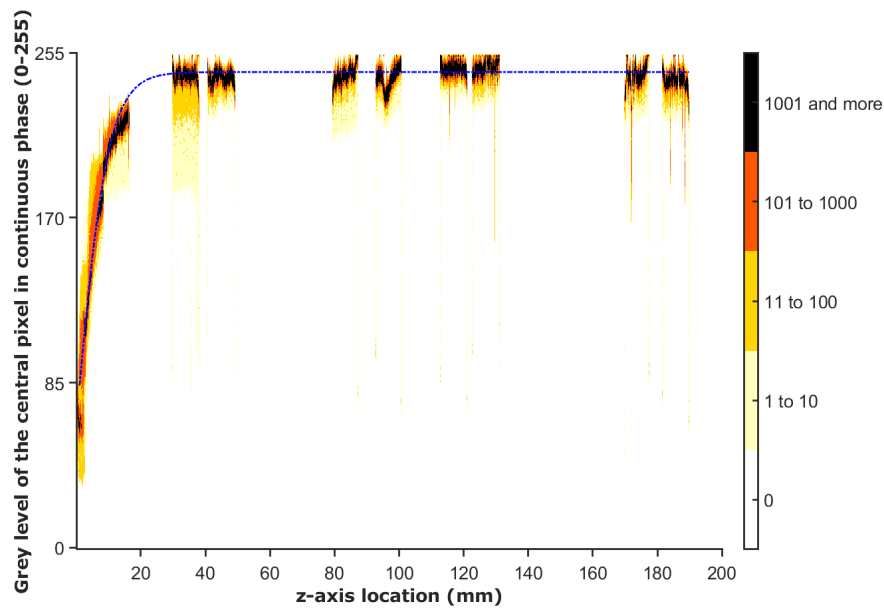
Once the previous step has been visually validated, the bubble outlines are detected ((a) in Figure 5.20), as well as the areas delimiting the unit cell ((b) in Figure 5.20). The delimitation of the unit-cells and the bubbles therefore makes it possible to delimit the liquid slugs and to extract the grey level in the center of the capillary ((c) in Figure 5.20).

The last step is performed for each of the 1800 images obtained at one measurement spot. There are two program output files (disp and cont). Examples of these files are shown in Figures E.4 and E.5 in Appendix E. For each measurement spot, these two files allow the evolution of the flow geometry and the evolution of the greyscale from the contacting zone of the fluids ( $z = 0$ ) until the end of the tenth spot ( $z=19$  cm) to be followed. Figure 5.21 presents the evolution of the greyscale of the water-rich phase at the center of the microreactor capillary as a function of the  $z$ -axis location in the microreactor. The color level is the number of greyscale values obtained at a certain distance  $z$ . The darker the color, the

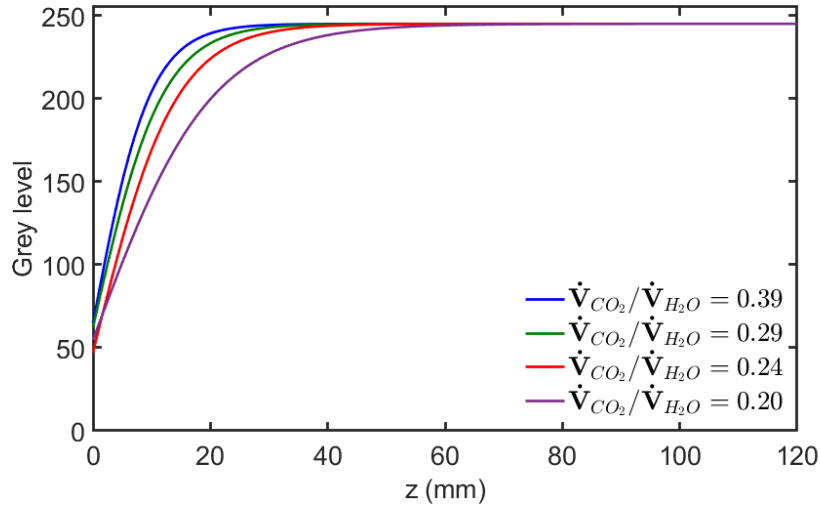


**Figure 5.20** – Successive steps for the acquisition of the bubble geometry and the greyscale in the liquid slugs. (a) Detection of the bubble positions. (b) Detection of the unit-cell positions. (c) Greyscale at the capillary center inside the liquid slugs.

more values obtained for the point shown on the figure. The dashed blue line corresponds to an exponential type model for the grey level along the microreactor. It is this model that will be processed to obtain the concentrations of  $CO_2$  dissolved in the  $H_2O$ -rich phase.



**Figure 5.21** – Greyscale at the center of the capillary inside the liquid slugs along the entire microreactor. The operating conditions are  $P = 10$  MPa,  $T = 303$  K,  $\dot{V}_{H_2O} = 150 \text{ } \mu\text{L min}^{-1}$  and  $\dot{V}_{CO_2} = 58.9 \text{ } \mu\text{L min}^{-1}$ . The color level is the number of greyscale values obtained at a certain distance  $z$ . The darker the color, the more values were obtained for the point displayed in the figure. The dashed blue line corresponds to an exponential type model for the greyscale along the microreactor weighted with the color density. The number of greyscale values is equal to 1767540.



**Figure 5.22** – Greyscale profiles obtained in the  $H_2O$ -rich slugs versus the  $z$ -axis position at 10 MPa and 303 K where  $\dot{V}_{CO_2} = 58.9 \mu\text{L min}^{-1}$ .

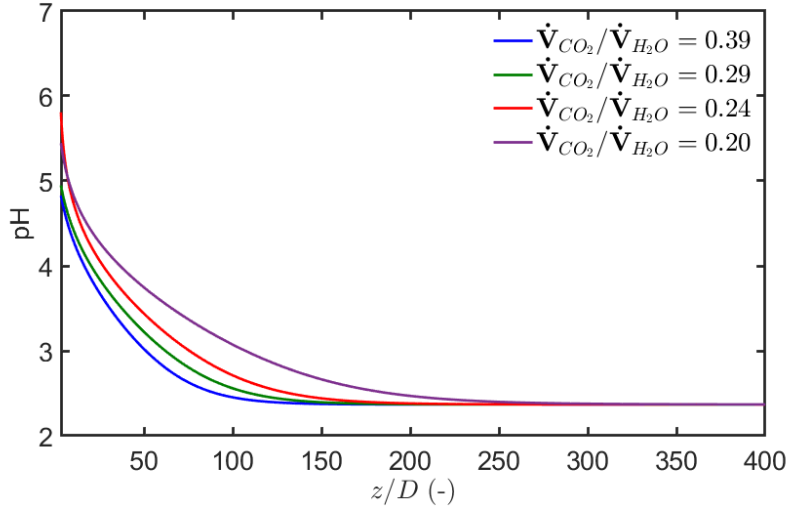
## 5.2 Determination of liquid-side volumetric mass transfer coefficients

The colorimetric method developed in this work enables the determination of the volumetric mass transfer coefficient  $k_L a_L$  at different locations along the length of the microreactor. In order to do this, the evolution of the greyscale in the  $H_2O$ -rich slugs recorded with the camera along the microreactor are transformed into pH values using the calibration curve. Hence, using experimental data linking pH and the concentration of  $CO_2$  dissolved in the  $H_2O$ -rich phase, the evolution of the  $CO_2$  concentration in the  $H_2O$ -rich phase can be computed along the microreactor. Like for Raman spectroscopy method, the concentration data are filtered with a fast Fourier transform (FFT) in order to compute the first derivative of the concentration  $dC_{CO_2}/dz$  which is used to deduce the volumetric mass transfer coefficient along the microreactor.

### 5.2.1 Determination of $C_{CO_2}$

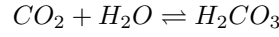
Figure 5.22 shows the evolution of greyscales in the liquid phase along the microreactor at 10 MPa and 303 K for  $\dot{V}_{CO_2} = 58.9 \mu\text{L min}^{-1}$  at various volumetric flow rates of  $H_2O$  and the corresponding pH profiles are presented in Figure 5.23.

$CO_2$  in aqueous solution is present under different forms: carbonic acid  $H_2CO_3$ , bicarbonate ions  $HCO_3^-$ , and carbonate ions  $CO_3^{2-}$ . Hence, different chemical equilibria occur simultaneously:

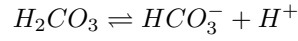


**Figure 5.23** – pH profiles obtained in the  $H_2O$ -rich slugs versus the  $z$ -axis position at 10 MPa and 303 K where  $\dot{V}_{CO_2} = 58.9 \text{ } \mu\text{L min}^{-1}$ .

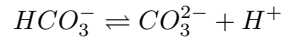
- The chemical balance between carbonic acid and carbon dioxide:



- The first dissociation reaction of carbonic acid into bicarbonate ions:



- The second reaction of dissociation of the bicarbonate ions into carbonate ions:



These chemical equilibria are described by the following equations:

- The equilibrium hydration constant:

$$K_h = \frac{[H_2CO_3]}{[CO_2]} \quad (5.5)$$

- From the first dissociation reaction:

$$[H^+][HCO_3^-] = K_{a1}[H_2CO_3] \quad (5.6)$$

- From the second dissociation reaction:

$$K_{a2} = \frac{[H^+][CO_3^{2-}]}{[HCO_3^-]} \quad (5.7)$$



- The equilibrium constant of water:

$$K_e = [H^+][OH^-] \quad (5.8)$$

- The electrical neutrality of the solution:

$$[H^+] = [HCO_3^-] + [HO^-] + 2[CO_3^{2-}] \quad (5.9)$$

In addition, the concentration of  $CO_2$  in the aqueous phase includes the concentration of pure  $CO_2$ , but also of the elements formed during dissociation equilibria. Thus, the neutrality equation gives:

$$[H^+] - \frac{K_e}{[H^+]} = [HCO_3^-] + 2 \times [CO_3^{2-}] \quad (5.10)$$

$$[CO_2]_{aq} = [HCO_3^-] + [H_2CO_3] + [CO_2] + [CO_3^{2-}] \quad (5.11)$$

By replacing the concentrations in  $HCO_3^-$ ,  $CO_3^{2-}$  and  $CO_2(aq)$  by their expressions, it gives:

$$[H^+] - \frac{K_e}{[H^+]} = \frac{K_{a1}[H_2CO_3]}{[H^+]} + 2 \times \frac{K_{a1}K_{a2}[H_2CO_3]}{[H^+]^2} \quad (5.12)$$

Finally, by isolating the concentration in  $CO_2$ :

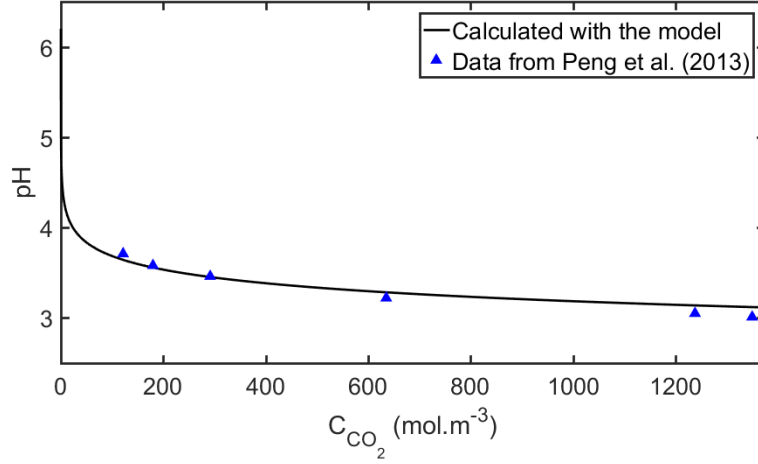
$$[H^+] - \frac{K_e}{[H^+]} = [CO_2] \left[ \frac{K_{a1}K_h}{[H^+]} + 2 \times \frac{K_{a1}K_{a2}K_h}{[H^+]^2} \right] \quad (5.13)$$

Equation 5.13 allows the concentration of  $CO_2$  dissolved in water to be determined from the knowledge of pH value. However, this equation overestimates the concentration of  $CO_2$  dissolved. This observation was also done in the work of Toews et al. (1995) where pH are measured in water acidified with  $CO_2$ . At 10 MPa and 303 K, the pH was overestimated: 3.31 with the previous model and 2.83 for the experimental value obtained by Toews et al. (1995). In a reverse way, the pH obtained at equilibrium at 10 MPa, 303 K gives a  $CO_2$  concentration in the  $H_2O$ -rich phase five times higher<sup>7</sup> than the  $CO_2$  concentration calculated with the model of Enick et al. (1990) presented in Section 2.2.1 of Chapter 2. Since the model is not well adapted for high-pressure studies, the experimental data from the work of Peng et al. (2013) are used to link the pH values measured with the  $CO_2$  concentration in the  $H_2O$ -rich phase. The pH values measured in this thesis work are interpolated with the experimental data of Peng et al. (2013), presented in Figure 5.24<sup>8</sup>. An additional point is added, that corresponds to the minimum pH value obtained in Figure 5.23 and the  $CO_2$  concentration at equilibrium calculated with the model presented in Section 2.2.1 of Chapter 2.

The  $CO_2$  concentrations obtained are therefore discrete values. In order to obtain concentration curves, and therefore calculate the first derivative of the concentration needed in the

<sup>7</sup>With the model, a small variation in pH corresponds to a significant variation in  $CO_2$  concentration.

<sup>8</sup>Interpolation with the experimental data to link the pH to  $CO_2$  concentration is therefore the highest contribution to the  $CO_2$  concentration uncertainty of this method. The method could be improved with precise measurements of pH for given  $CO_2$  concentrations in a  $H_2O$ -rich phase at 10 MPa and 303 K.



**Figure 5.24** – pH as a function of  $CO_2$  concentrations in the  $H_2O$ -rich phase, calculated from Equation 5.13 and experimental values from Peng et al. (2013).

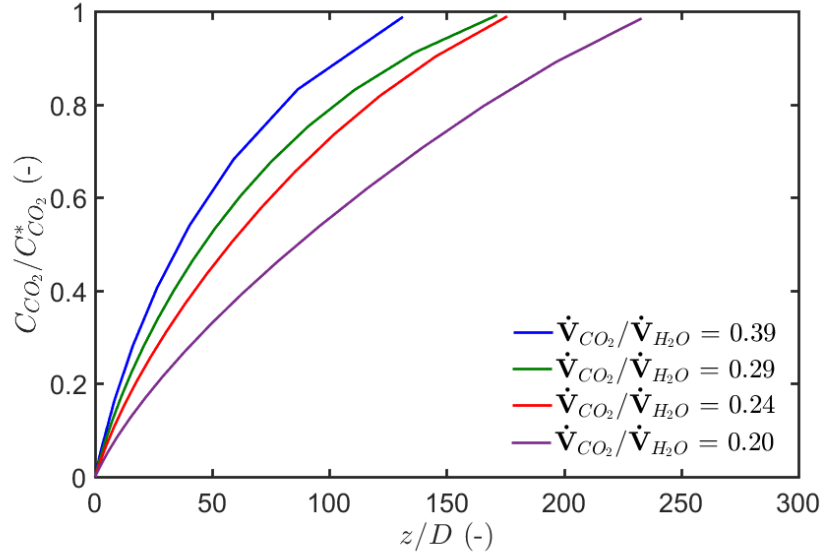
volumetric mass transfer coefficient computation, the discrete  $CO_2$  concentrations values are filtered with a fast Fourier transform method (FFT) described in Appendix B. The normalized concentration profiles obtained with the fast Fourier transform are presented in Figure 5.25. It can be seen that the thermodynamic equilibrium ( $C_{CO_2}/C_{CO_2}^* = 1$ ) is reached nearer to the contacting zone compared with the concentration profiles obtained with the Raman spectroscopy method. This difference is due to the change in capillary diameter employed for the method. Since the capillary diameter employed in the colorimetric method is 17% smaller than the one employed in the Raman spectroscopy method, the mass transfer rate is higher. Indeed, the characteristic time of mass transfer is proportional to the square of the capillary diameter which corresponds here to a characteristic time 1.44 times smaller.

## 5.2.2 Determination of the volumetric mass transfer coefficient $k_L a_L$

The Equation 2.32 from the unit-cell model presented in Chapter 2 is used for the determination of the volumetric mass transfer coefficient:

$$k_L a_L = \frac{U_{TP}}{C_{CO_2}^*(T, P) - \langle C_{CO_2} \rangle(z)} \frac{d\langle C_{CO_2} \rangle}{dz} \quad (5.14)$$

The first derivative of the  $CO_2$  concentration in the  $H_2O$ -rich phase,  $\frac{d\langle C_{CO_2} \rangle}{dz}$ , is obtained with the  $CO_2$  concentration curves obtained from the fast Fourier transform filtering (FFT)



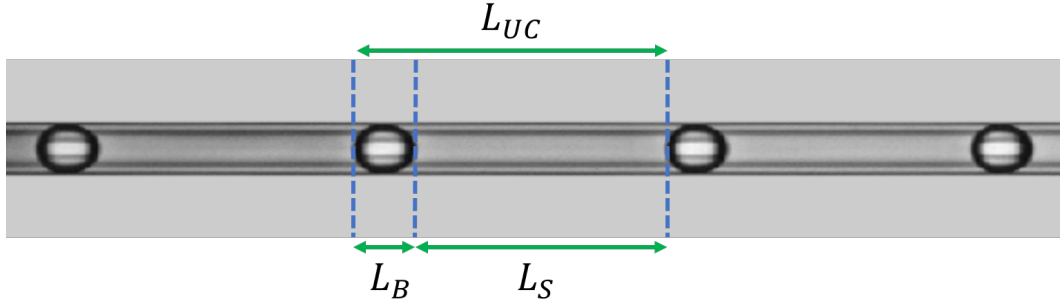
**Figure 5.25** – Normalized fitted concentrations profiles of  $CO_2$  in the  $H_2O$ -rich phase versus the normalized  $z$ -axis position at 10 MPa and 303 K where  $\dot{V}_{CO_2} = 58.9 \mu\text{L min}^{-1}$ .

## 5.3 Application of the experimental method to $CO_2$ - $H_2O$ mass transfer under high pressure

The experimental method presented in this chapter is applied to a two-phase segmented flow of  $CO_2$  and  $H_2O$  for various volumetric flow rates at a pressure of 10 MPa and a temperature of 303 K. This section presents the results on the physical characteristics of the flow in the microreactor, the  $CO_2$  concentration profiles in the  $H_2O$ -rich phase and the liquid volumetric mass transfer coefficient profiles.

### 5.3.1 Characteristics of the gas-liquid flow

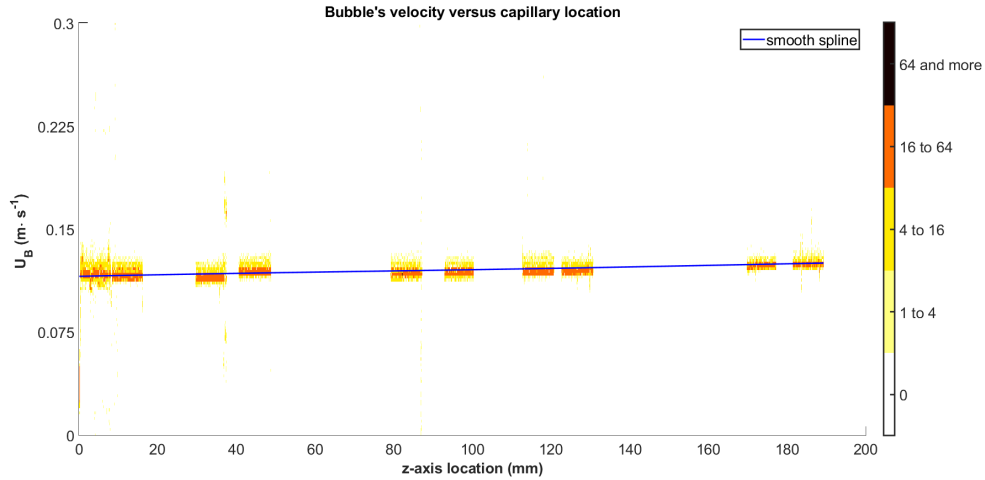
Analysis of the images obtained at each measurement spot enables different characteristics of the flow to be examined as a function of the axial distance  $z$  in the capillary. The evolution of  $CO_2$  bubble velocity ( $U_B$ ),  $CO_2$  bubble length ( $L_B$ ), liquid slug length ( $L_S$ ), as well as the unit-cell length ( $L_{UC}$ ) as a function of operating conditions will be presented in this section. These parameters are depicted in Figure 5.26. In addition, the specific area,  $a_L$  defined by the bubble surface divided by the volume of liquid slug of the same unit-cell, is calculated at different  $z$ -axis location. The specific area is an indicator of the mass transfer performance. The larger the specific area, the faster the transfer. The image analysis method presented above allows around 18000 values of each of the parameters (speed, lengths and specific area) to be obtained for each measurement spot. The figure in this section are presented in number of values obtained per pixel. The higher the number of values, the greater the confidence in the value obtained.



**Figure 5.26** – Characteristics of two-phase segmented flow in the microreactor.  $L_B$  is the bubble length,  $L_S$  the liquid slug length and  $L_{UC}$  the unit-cell length.

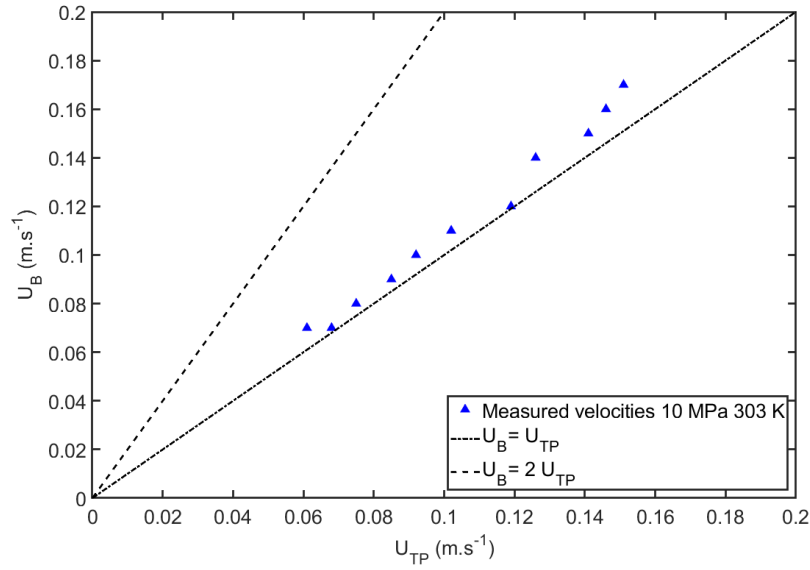
### Evolution of the bubble velocity

Figure 5.27 presents the evolution of the bubble velocity along the microchannel for  $\dot{V}_{CO_2} = 58.9 \mu\text{L min}^{-1}$  and  $\dot{V}_{H_2O} = 250 \mu\text{L min}^{-1}$  ( $\dot{V}_{CO_2}/\dot{V}_{H_2O} = 0.24$ ). At these flow conditions, the velocity of the two-phase flow  $U_{TP} = U_G + U_L$  is equal to  $0.10 \text{ m s}^{-1}$ . The bubble velocity is equal to  $U_B = 0.11 \text{ m s}^{-1}$  at the inlet and slightly increases along the channel length. This means that the  $CO_2$  bubble is spherical with a diameter decreasing along the channel length. When the spherical  $CO_2$  bubble decreases in size, its velocity increases. If the bubble were very small, its speed would be equal to the speed at the center of the tube,  $2 \times U_{TP}$ .



**Figure 5.27** – Bubble velocity  $U_B$  measured at different positions along the microreactor at 10 MPa and 303 K for  $\dot{V}_{CO_2} = 58.9 \mu\text{L min}^{-1}$  and  $\dot{V}_{H_2O} = 250 \mu\text{L min}^{-1}$ .

Figure 5.28 presents the bubble velocity of the experiments performed,  $U_B$ , as a function of the two-phase flow  $U_{TP}$ . The bubble velocity evolves linearly with the velocity of the two-phase flow and is slightly greater than the velocity of the two-phase flow. If  $U_B = U_{TP}$ , there is no liquid film. Here,  $U_B$  is about  $1.1 U_{TP}$  which means that there is a thin liquid film. This in turn can be confirmed by Equation 1.7 in Chapter 1 that gives a liquid film around  $7 \mu\text{m}$  for the operating conditions investigated here.



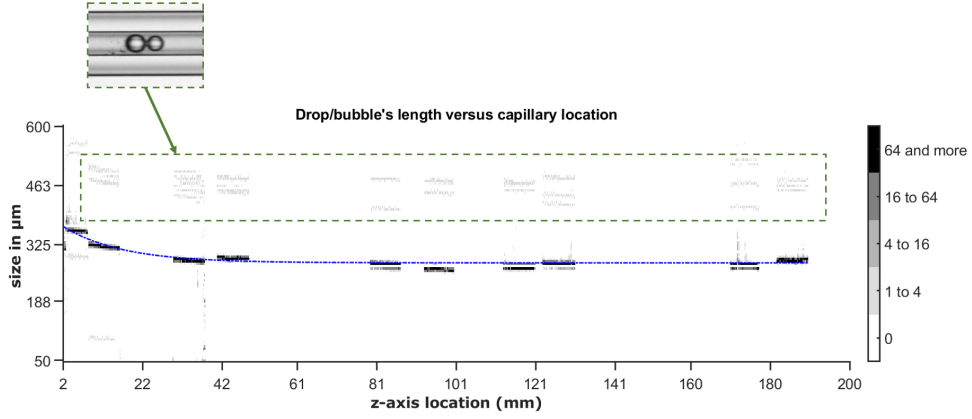
**Figure 5.28** – Comparison of the bubble velocity  $U_B$  and the two-phase velocity  $U_{TP}$  for each experiment at 10 MPa and 303 K.

## Evolution of the bubble, slug and unit-cell lengths

Figure 5.29 shows an example of the evolution of the bubble length along the microreactor for  $\dot{V}_{CO_2} = 58.9 \mu\text{L min}^{-1}$  and  $\dot{V}_{H_2O} = 250 \mu\text{L min}^{-1}$ <sup>9</sup>. It can be observed that the bubble length  $L_B$  decreases along the microreactor and then becomes stable after about 40 mm<sup>10</sup> (from 372  $\mu\text{m}$  to around 250  $\mu\text{m}$  at equilibrium). The decrease in bubble size is due to the transfer of  $CO_2$  in the  $H_2O$ -rich phase, then when the thermodynamic equilibrium is reached, the bubble length becomes stable. It can be noticed that there is scattered data of bubble lengths that are significantly greater than the average trend. These values are due to the rare presence of small bubbles generated in the two-phase flow which flow faster than the bigger bubbles. These small bubbles are located next to bigger bubbles as presented in the insert in Figure 5.29. Unfortunately the image analysis program cannot differentiate the two bubbles and measures the length of the ensemble of both bubbles. However, since the number of these small bubbles is negligible compared with the total number of bubbles, the exponential fitting model presented by the blue line in Figure 5.29 is not affected.

<sup>9</sup> $\dot{V}_{CO_2}/\dot{V}_{H_2O} = 0.24$ .

<sup>10</sup>Equal to  $z/D = 160$ . This observation is in agreement with the distance where the equilibrium is reached for the red curve in Figure 5.25.

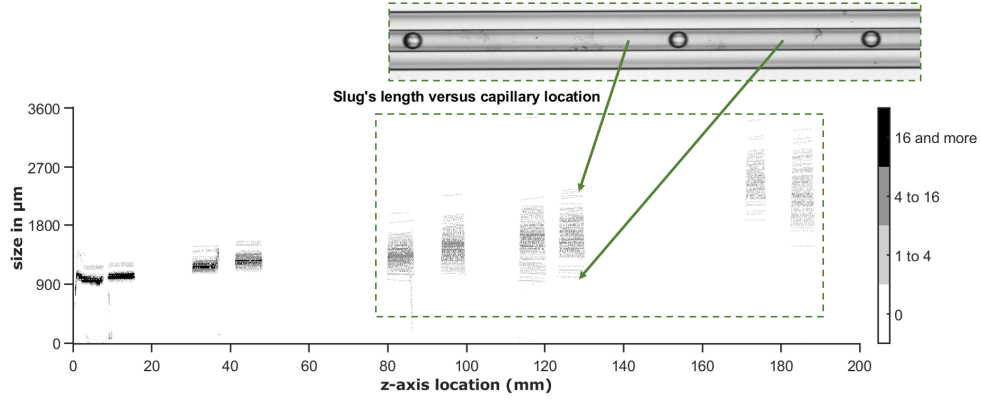


**Figure 5.29** – Bubble length  $L_B$  measured at different positions along the microreactor at 10 MPa and 303 K for  $\dot{V}_{CO_2} = 58.9 \mu\text{L min}^{-1}$  and  $\dot{V}_{H_2O} = 250 \mu\text{L min}^{-1}$ . The bubble length  $L_B$  decreases from 372  $\mu\text{m}$  to 250  $\mu\text{m}$ .

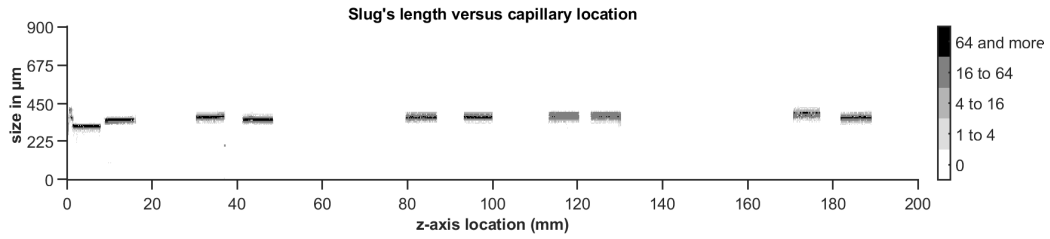
The evolution of the liquid slug length  $L_S$  is presented in Figure 5.30 for the same flow conditions. It is observed that the liquid slug length increases slightly up to a distance of 40 mm from the  $CO_2$ - $H_2O$  contacting zone (from 1019  $\mu\text{m}$  to around 1275  $\mu\text{m}$  at  $z = 40 \text{ mm}$ )<sup>11</sup>. After this distance, the slug length size at each position becomes more and more scattered. This observation is due to the fact that once equilibrium is reached (i.e. when the bubble size is stable from about  $z=40 \text{ mm}$ , certain bubbles accelerate and thereby irregular slug lengths can be seen as shown in the insert of Figure 5.30. These bubbles leave behind a longer liquid slug, and shorten the liquid slug in front of them. This phenomenon is observed as soon as equilibrium is reached for some flow conditions. Such a phenomenon is linked to the fact that in these flow conditions, the sizes of  $CO_2$  bubbles are in the same order of magnitude as the diameter of the microreactor capillary, 250  $\mu\text{m}$ <sup>12</sup>. For flow rates ranges where the bubbles have sizes several times greater than the diameter of the capillary, this phenomenon cannot occur since even at thermodynamic equilibrium the bubble length is greater than the capillary diameter that creates resistance for the bubble to flow. An example is presented in Figure 5.31 where the bubble length  $L_B$  is around 350  $\mu\text{m}$  at equilibrium.

<sup>11</sup>This observation is in agreement with Figure 2.22 in Chapter 2. This figure shows that a volume of pure water increases when it is saturated with  $CO_2$ .

<sup>12</sup>When this acceleration of the bubbles and the irregularity of the slug length are observed, it is a sign that the flow regime has changed from Taylor flow to isolated bubble flow.

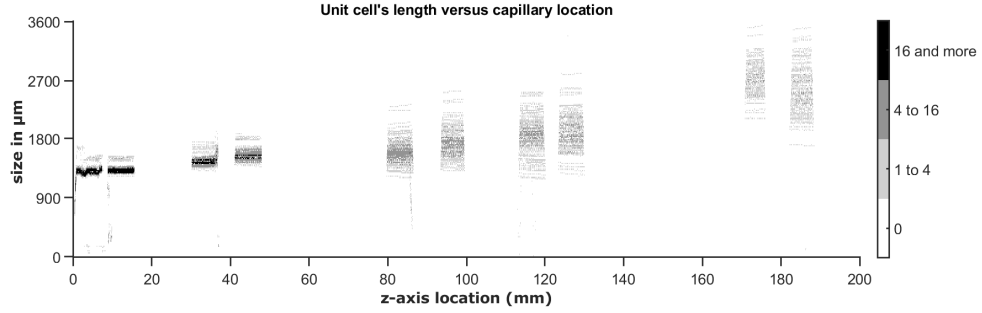


**Figure 5.30** – Liquid slug length  $L_S$  measured at different positions along the microreactor at 10 MPa and 303 K for  $\dot{V}_{CO_2} = 58.9 \mu\text{L min}^{-1}$  and  $\dot{V}_{H_2O} = 250 \mu\text{L min}^{-1}$ .



**Figure 5.31** – Liquid slug length  $L_S$  measured at different positions along the microreactor at 10 MPa and 303 K for  $\dot{V}_{CO_2} = 82.5 \mu\text{L min}^{-1}$  and  $\dot{V}_{H_2O} = 110 \mu\text{L min}^{-1}$ .

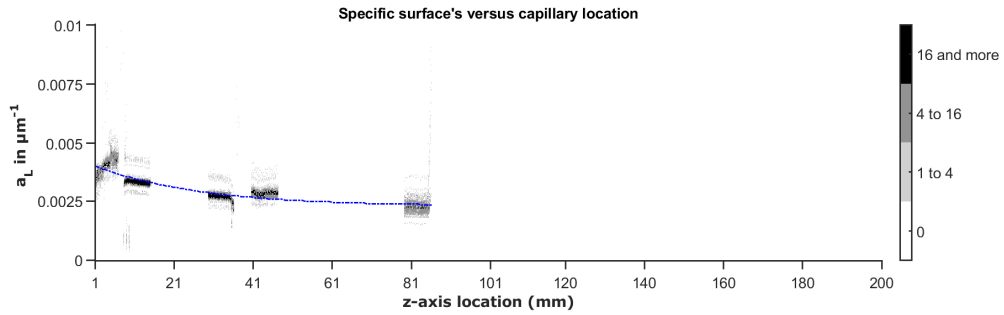
The evolution of the unit-cell length  $L_{UC}$  for the same flow conditions is presented in Figure 5.32. Before thermodynamic equilibrium is reached (i.e. at  $z < 40$  mm, the unit-cell length is slightly increasing, from 1317  $\mu\text{m}$  to 1567  $\mu\text{m}$ . Indeed, the decrease in  $CO_2$  bubble size does not compensate the increase in size of the  $H_2O$ -rich slugs. Once equilibrium is reached, the phenomenon explained for variation in the length of the liquid slugs has repercussions on the length of the unit-cell as well. Thus, the unit-cell length values become rather scattered.



**Figure 5.32** – Unit-cell length  $L_{UC}$  measured at different positions along the microreactor at 10 MPa and 303 K for  $\dot{V}_{CO_2} = 58.9 \text{ } \mu\text{L min}^{-1}$  and  $\dot{V}_{H_2O} = 250 \text{ } \mu\text{L min}^{-1}$ .

### Evolution of the specific surface $a_L$

The specific surface, defined by the area of the bubble divided by the volume of liquid slug is presented in Figure 5.33 for the same flow conditions. It can be seen that the specific area decreases in the zone where equilibrium is not yet reached. This observation is explained by the simultaneous decrease in bubble size (and therefore bubble surface area of the gas-liquid interface) and increase in the length of liquid slug (and therefore liquid volume).



**Figure 5.33** – Specific surface  $a_L$  measured at different positions along the microreactor at 10 MPa and 303 K for  $\dot{V}_{CO_2} = 58.9 \text{ } \mu\text{L min}^{-1}$  and  $\dot{V}_{H_2O} = 250 \text{ } \mu\text{L min}^{-1}$ .

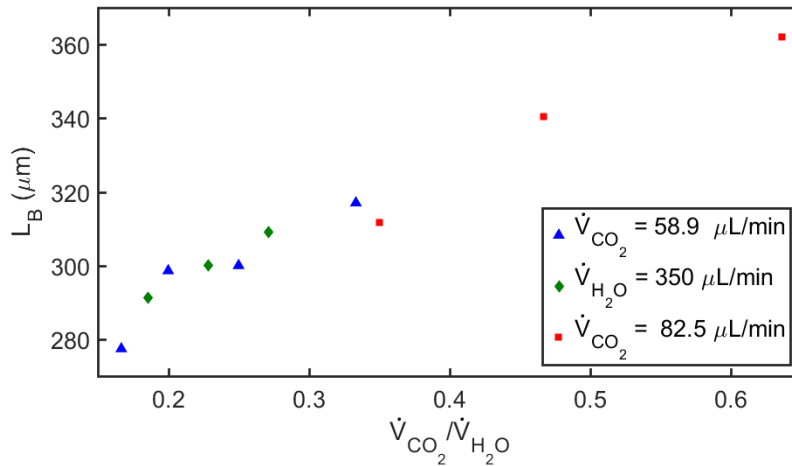
### Effects of the volumetric flow rates ratio $\dot{V}_{CO_2}/\dot{V}_{H_2O}$ on $a_L$ , $L_B$ and $L_S$

Figures 5.34, 5.35 and 5.36 present the influence of the ratio of volumetric flow rates of  $CO_2$  and  $H_2O$  on the bubble length  $L_B$ , the slug length  $L_S$  and the specific surface  $a_L$  at



$z = 2.95 \text{ cm}^{13}$ . The colors correspond to experiments when either the volumetric flow rate of  $CO_2$  or  $H_2O$  was kept constant, whilst the flow rate of the other phase was varied. Firstly, it is observed that when the volumetric flow rate ratio  $\dot{V}_{CO_2}/\dot{V}_{H_2O}$  increases, the bubble length  $L_B$  and the specific surface  $a_L$  increase. When the ratio  $\dot{V}_{H_2O}/\dot{V}_{CO_2}$  increases, the liquid slug length  $L_S$  increases.

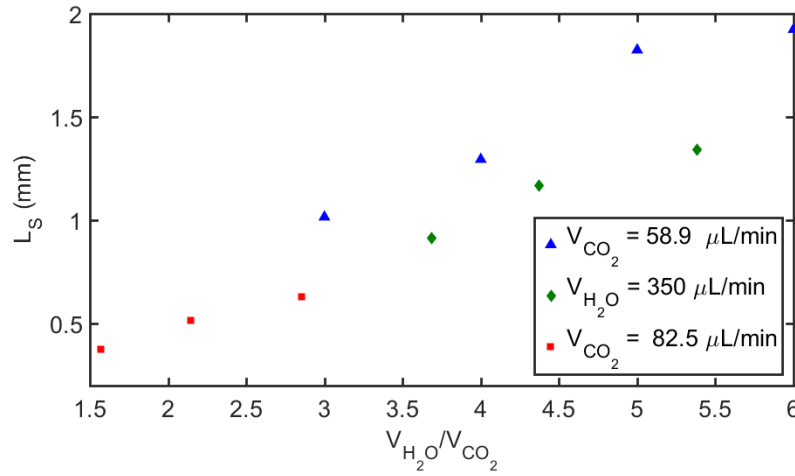
Figure 5.34 shows that the bubble length  $L_B$  evolves linearly with the volumetric flow rate ratio  $\dot{V}_{CO_2}/\dot{V}_{H_2O}$  when the  $CO_2$  volumetric flow rate is taken constant and when the  $H_2O$  volumetric flow rate is taken constant. Even if the values are taken far from the bubble generation zone, the bubbles length evolution is in agreement with the correlations of Garstecki et al. (2006) and Steijn et al. (2007), respectively Equations 1.2 and 1.3 in Chapter 1. Figure 5.35 shows that the liquid slug length  $L_S$ , increases linearly with  $\dot{V}_{H_2O}/\dot{V}_{CO_2}$  as in the correlation developed by Völkel (2009), presented in Equation 1.4 in Chapter 1. Figure 5.36 shows that the specific surface  $a_L$  increases linearly with the volumetric flow rate ratio  $\dot{V}_{CO_2}/\dot{V}_{H_2O}$ . However, the blue set of data for which the volumetric  $CO_2$  flow rate is constant and equal to  $\dot{V}_{CO_2} = 58.9 \text{ } \mu\text{L min}^{-1}$ , has a different slope. This can also be seen in Figure 5.35 with the liquid slug length. Additional experiments with various volumetric flow rates are needed to give with certitude a reason to this difference.<sup>14</sup>



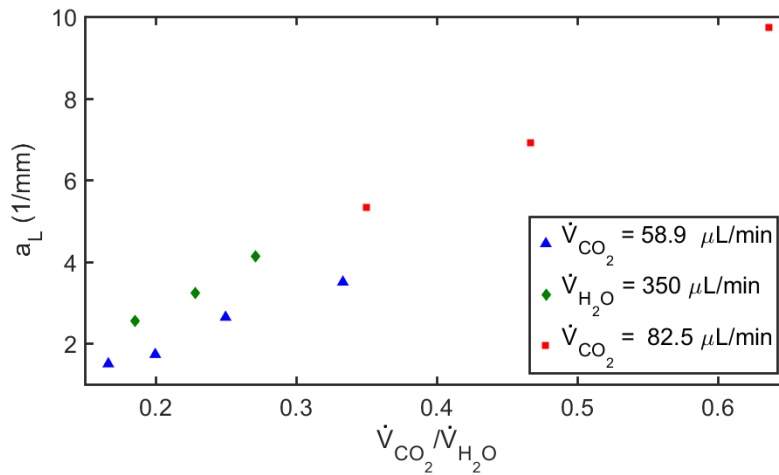
**Figure 5.34** – Bubble length  $L_B$  at  $z = 2.95 \text{ cm}$  at 10 MPa and 303 K as a function of the volumetric flow rate ratio  $\dot{V}_{CO_2}/\dot{V}_{H_2O}$ .

<sup>13</sup>This distance is far from the bubble generation zone where the bubbles and liquids slugs vary a lot due to the bubble formation and far from the thermodynamic equilibrium zone where the lengths are scattered.

<sup>14</sup>The comparison between carried out experiments based on the dimensionless numbers Re and Ca, the volumetric flow rates  $\dot{V}_{CO_2}$  and  $\dot{V}_{H_2O}$ , the ratio  $C_{CO_2}/C_{CO_2}^*$  at  $z = 2.95 \text{ cm}$ , the two-phase velocity  $U_{TP}$  as well as images of the flow, does not allow to explain this difference.



**Figure 5.35** – Slug length  $L_S$  at  $z=2.95$  cm at 10 MPa and 303 K as a function of the volumetric flow rate ratio  $\dot{V}_{H_2O}/\dot{V}_{CO_2}$ .

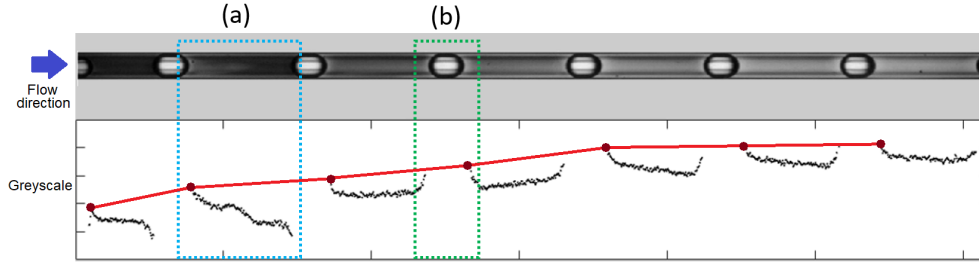


**Figure 5.36** – Specific surface  $a_L$  at  $z=2.95$  cm at 10 MPa and 303 K as a function of the volumetric flow rate ratio  $\dot{V}_{CO_2}/\dot{V}_{H_2O}$ .

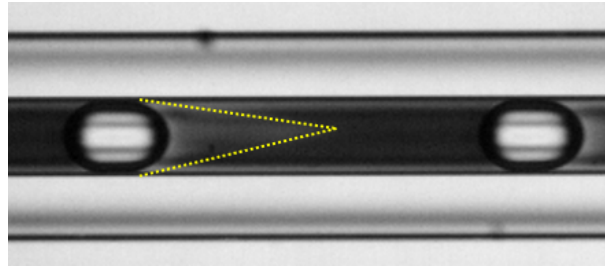
## Bubble generation zone

The figure 5.37 presents an image of the two-phase segmented flow of  $CO_2$  and  $H_2O$  at the inlet of the microreactor (i.e. at the first measurement spot) where the  $CO_2$  bubbles are generated. This image gives information about the mass transfer in the bubble generation process. Zone (a) indicated in this figure shows the propagation of the  $CO_2$  dissolved inside the  $H_2O$ -rich liquid slug. Indeed, a triangular-shaped zone of higher greyscale intensity is located in the left part of the liquid slug (a zoom is presented in Figure 5.38). The greyscale is more greater ahead of the moving bubble compared with in the wake of the previous bubble where the greyscale intensity is lower. This reveals a zone of higher  $CO_2$  concentration in front of the bubble. Further along the microchannel, the greyscale and therefore the  $CO_2$

concentration in the liquid slug becomes almost uniform. Zone (b) of the figure presents the greyscale around a  $CO_2$  bubble. It can be observed that the region near the bubble is lighter when compared with the center of the liquid slug. The evolution of the  $CO_2$  concentration at the interface is presented in the figure with the red line. It can be seen that the concentration at the interface is always higher compared with the liquid slug bulk. However, this concentration gradient is quickly uniform.

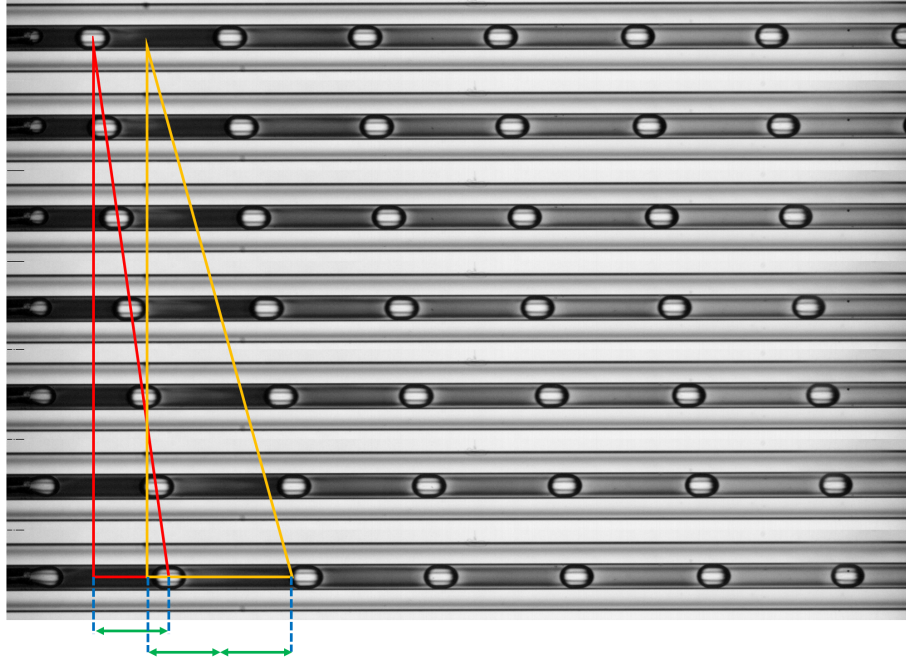


**Figure 5.37** – Evolution of the greyscale in the bubble generation zone at 10 MPa and 303 K for  $\dot{V}_{CO_2} = 58.9 \mu\text{L min}^{-1}$  and  $\dot{V}_{H_2O} = 250 \mu\text{L min}^{-1}$ .



**Figure 5.38** – Zoom in a liquid slug in the bubble generation zone at 10 MPa and 303 K for  $\dot{V}_{CO_2} = 58.9 \mu\text{L min}^{-1}$  and  $\dot{V}_{H_2O} = 250 \mu\text{L min}^{-1}$ . The triangular-shaped zone of higher greyscale intensity (in yellow) shows the mass transfer of  $CO_2$  inside the liquid slug

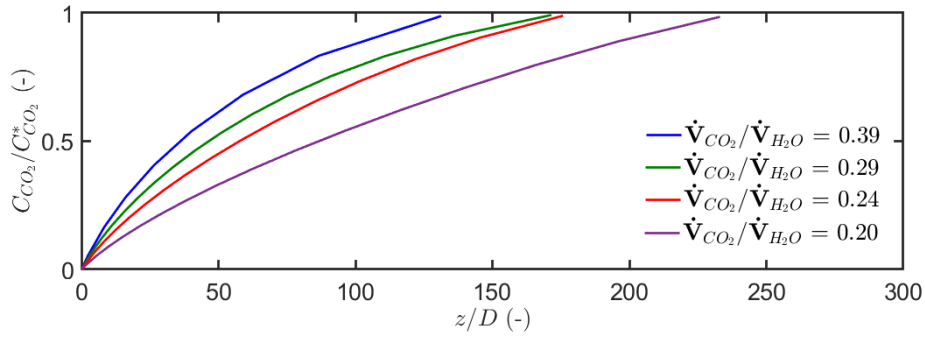
Figure 5.39 presents the evolution of the flow in the bubble generation zone. It can be seen that the lighter triangle in the liquid slug is moving at twice the bubble velocity. The hypotenuse of the red right-angled triangle crosses all the bubble centers of the same  $CO_2$  bubble presented at different positions along the microchannel (1/600 second between each image). In a similar way, the hypotenuse of the orange right-angled triangle crosses all the lighter triangle peaks inside the same liquid slug on each image. The comparison between these two triangles provides a comparison of the velocity of the  $CO_2$  bubble and the velocity of the lighter triangle peak. It is therefore observable that the velocity of the light triangle peak is twice the velocity of the  $CO_2$  bubble. This observation is in agreement with the fact that relative to the ground, the velocity of the recirculation in the liquid slug is equal to twice the velocity of the bubble.



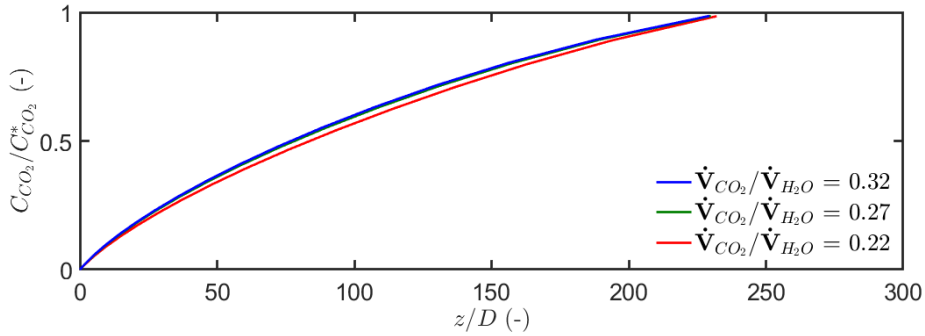
**Figure 5.39** – Flow evolution in the bubble generation zone at 10 MPa and 303 K for  $\dot{V}_{CO_2} = 58.9 \text{ } \mu\text{L min}^{-1}$  and  $\dot{V}_{H_2O} = 250 \text{ } \mu\text{L min}^{-1}$ .

### 5.3.2 Concentration profiles

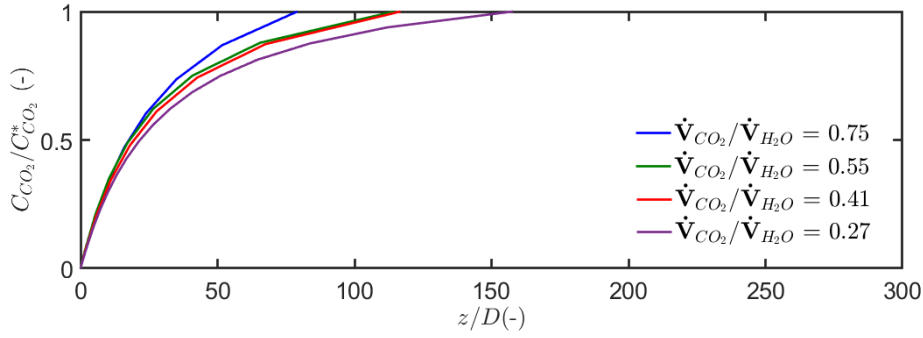
Figure 5.40, 5.41 and 5.42 present the normalized fitted concentration profiles obtained with the fast Fourier transform versus the normalized axial position in the microreactor ( $z/D$ ). On each figure, either the volumetric flow rate of  $CO_2$  or the one of  $H_2O$  was kept constant, whilst the flow rate of the other phase was varied. It is observed that when the volumetric flow rate ratio  $\dot{V}_{CO_2}/\dot{V}_{H_2O}$  increases, the thermodynamic equilibrium is reached closer to the bubble generation zone. This observation can be explained by the physical characteristics of the two-phase flow. Indeed, when the ratio  $\dot{V}_{CO_2}/\dot{V}_{H_2O}$  increases, both the bubble length  $L_B$  and the surface area available for mass transfer increase, as shown in Figure 5.34 and Figure 5.36. Furthermore, for increasing  $\dot{V}_{CO_2}/\dot{V}_{H_2O}$ , the liquid slug length  $L_S$  decreases and therefore, the amount of water to be saturated (i.e. the liquid slug volume) is smaller. The mass transfer rate increases and the liquid slugs are saturated more quickly (and therefore closer to the contacting zone in the microreactor).



**Figure 5.40** – Normalized fitted concentrations profiles of  $CO_2$  in the  $H_2O$ -rich phase versus the normalized  $z$ -axis position at 10 MPa and 303 K at  $\dot{V}_{CO_2} = 58.9 \mu\text{L min}^{-1}$ .



**Figure 5.41** – Normalized fitted concentrations profiles of  $CO_2$  in the  $H_2O$ -rich phase versus the normalized  $z$ -axis position at 10 MPa and 303 K at  $\dot{V}_{H_2O} = 350 \mu\text{L min}^{-1}$ .



**Figure 5.42** – Normalized fitted concentrations profiles of  $CO_2$  in the  $H_2O$ -rich phase versus the normalized  $z$ -axis position at 10 MPa and 303 K at  $\dot{V}_{CO_2} = 82.5 \mu L \min^{-1}$ .

### 5.3.3 Effect of flow rate conditions on $k_L a_L$

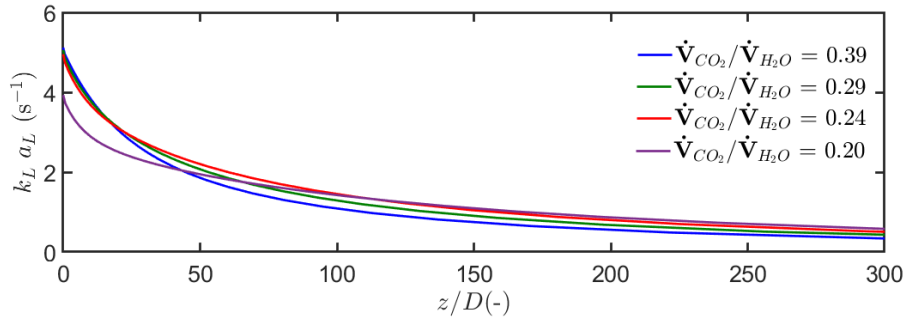
Figure 5.43, 5.44 and 5.45 show the volumetric liquid mass transfer coefficient  $k_L a_L$ , determined with Equation 5.14, versus the normalized axial position in the microreactor ( $z/D$ ). Firstly, it can be seen that  $k_L a_L$  is not constant along the microreactor, as it was the case with the  $k_L a_L$  measured with the Raman spectroscopy method. It can also be seen that the  $k_L a_L$  values decrease by about a factor of 5 between the inlet of the reactor and the end of the observation zone. However, the values of  $a_L$  obtained with the high-speed camera decreases by about a factor 1.4 in the experiments. This suggest that the values of  $k_L$  also must decrease along the microreactor. Indeed, it can be expected that  $k_L$  is significantly different in the bubble generation zone, where a transient process is occurring, than in the other part of the capillary, where the flow is stable. This possible difference in  $k_L$  could also explain why the contribution of the mass transfer process in the bubble generation zone has been found to contribute to around 20-40% of the total mass transfer process in the operating conditions investigated in this thesis work. This observation is in agreement with the literature presented in Section 1.4.2 of Chapter 1 for studies where the bubble generation process duration is in the same order of magnitude (Tan et al. (2012), Baten et al. (2004)).

A comparison between the experiments also shows that for constant  $\dot{V}_{CO_2}$  or  $\dot{V}_{H_2O}$ , increasing  $\dot{V}_{CO_2}/\dot{V}_{H_2O}$  leads to an increase of  $k_L a_L$ . This statement was also observed on results obtained with the Raman spectroscopy method presented in Chapter 4 and may be explained in a similar manner:

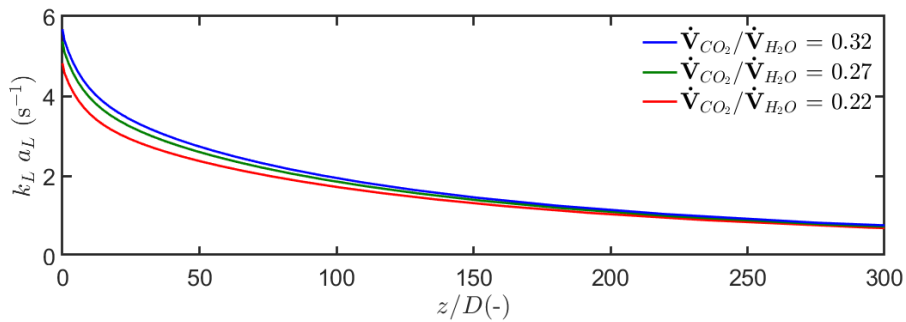
- An increase in  $\dot{V}_{CO_2}/\dot{V}_{H_2O}$  results in an increase of the bubble length,  $L_B$ , (and consequently the bubble volume,  $V_B$ ) and a decrease of the liquid slug length,  $L_S$ . A decrease in slug length has previously been shown to increase the liquid slug recirculation (Leung et al. (2010), Zalloha et al. (2012), Abadie (2013)). It is expected that this would result in an enhanced renewal of the fluid-liquid interface and in turn increase the mass transfer coefficient  $k_L$ .
- An increase in  $\dot{V}_{CO_2}/\dot{V}_{H_2O}$  leads to an increase in  $a_L$  as shown in Figure 5.36.

Both the decrease in slug length and the increase in specific area lead to an increase in  $k_L a_L$  when  $\dot{V}_{CO_2}/\dot{V}_{H_2O}$  increases for a fixed  $H_2O$  or  $CO_2$  flow rate.

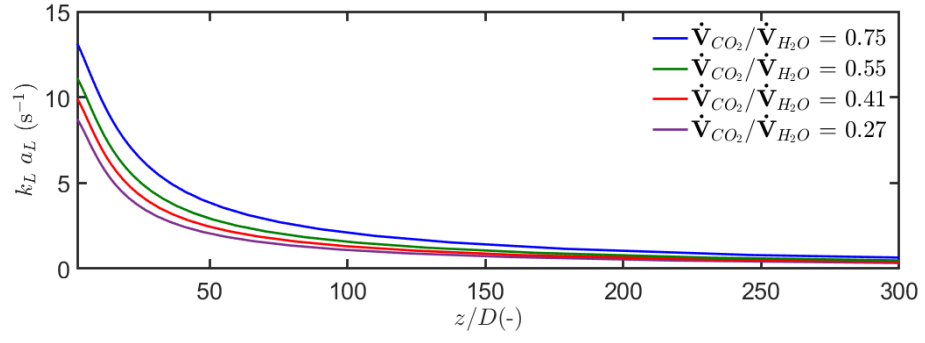
The values of the volumetric mass transfer coefficients measured here are between  $1 \text{ s}^{-1}$  and  $13 \text{ s}^{-1}$ . The order of magnitude presented with this method is similar to that obtained with the Raman spectroscopy method ( $0.2 \text{ s}^{-1}$  -  $4 \text{ s}^{-1}$ ), although slightly higher. This difference is probably due to the difference of capillary diameters employed in the methods. A diameter of  $300 \text{ }\mu\text{m}$  was employed for the Raman spectroscopy method and a diameter of  $250 \text{ }\mu\text{m}$  was employed for the colorimetric method. It has been demonstrated in the literature (see Section 1.4.2 of Chapter 1) that a smaller diameter of channel leads to higher mass transfer rates (the mass transfer characteristic time is 1.4 times higher with a diameter of  $250 \text{ }\mu\text{m}$  compared with the diameter of  $300 \text{ }\mu\text{m}$ ).



**Figure 5.43** – Volumetric liquid mass transfer coefficient profiles versus the normalized  $z$ -axis position at 10 MPa and 303 K at  $\dot{V}_{CO_2} = 58.9 \text{ }\mu\text{L min}^{-1}$ .



**Figure 5.44** – Volumetric liquid mass transfer coefficient profiles versus the normalized  $z$ -axis position at 10 MPa and 303 K at  $\dot{V}_{H_2O} = 350 \text{ }\mu\text{L min}^{-1}$ .



**Figure 5.45** – Volumetric liquid mass transfer coefficient profiles versus the normalized  $z$ -axis position at 10 MPa and 303 K at  $\dot{V}_{CO_2} = 82.5 \text{ } \mu\text{L min}^{-1}$ .



## Conclusion

In this chapter a colorimetric method was developed to determine the liquid volumetric mass transfer coefficient in a two-phase segmented flow at high pressure in a microreactor. Since the method is visual technique, it also allows the physical characteristics of the two-phase flow (i.e. such as the bubble, slug and unit-cell lengths, the bubble velocity and the specific surface) to be determined along the microchannel length at the same time as mass transfer data. The colorimetric method can be applied to any aqueous systems that can be acidified with carbon dioxide at high pressure. This opens the possibility to investigate the acidification of water and brine with carbon dioxide for geology purposes, for example. This method could also be used for any systems where a mass transfer is observable with a color change.

The method also allows the volumetric mass transfer coefficient at different axial positions in the microchannel to be determined. The method has been applied to study flow and mass transfer in a  $H_2O$ - $CO_2$  system at 10 MPa and 303 K. The values obtained for the volumetric mass transfer coefficient were in the range  $1\text{ s}^{-1}$ - $13\text{ s}^{-1}$ . It was observed that the volumetric mass transfer coefficient  $k_L a_L$  decreases along the flow as well as  $k_L$  since the decrease in  $a_L$  observed is not sufficient to explain the decrease in  $k_L a_L$ .

An improvement of this method would be the investigation of a model linking the pH of aqueous solutions acidified with  $CO_2$ , with the  $CO_2$  concentration in the aqueous solution. Indeed, the model commonly employed at ambient conditions do not fit well the experimental data obtained at high pressure (the pH is overestimated). The utilization of such model taking into account the high-pressure specificities could be an important improvement of the colorimetric method presented in this chapter.

In comparison with the Raman spectroscopy method, the material used in this method is less expensive. However, the calibration of the method with the finding of the five optimal parameters (shutter duration, lighting power, BPB concentration, capillary diameter and operating conditions) is more laborious as well as the image processing compared with the Raman spectra processing. With a camera of greater resolution, it could be possible to determine  $CO_2$  concentration profiles in the bubble generation zone, to compute  $k_L$  with precision along the flow, and, with the knowledge of the velocity profiles, to compute diffusion coefficient.





# General conclusion and outlooks

## Summary

This thesis work was devoted to fulfilling the primary objective of the MuSyS project, namely, the determination of mass transfer coefficients in high-pressure two-phase flow in microreactors. To do this, a microfluidic platform was fabricated, allowing the study of two-phase segmented flows at constant pressure and temperature under high-pressure conditions. A theoretical model was set up in order to compute the liquid volumetric mass transfer coefficient  $k_L a_L$  of a two-phase segmented flow of  $CO_2$  and  $H_2O$ . In addition, two experimental methods based on the visualization of a color change in the flow and on Raman spectroscopy have been developed for the measurement of local values of  $CO_2$  concentration in the  $H_2O$ -rich phase of the segmented flow. This data is used as input to the theoretical model in order to determine the volumetric mass transfer coefficient. The experiments were carried out at 10 MPa and 303 K for the colorimetric method and at 303 K and 8 MPa, 9 MPa and 10 MPa using the Raman spectroscopy method.

Chapter 2 of this thesis work was devoted to the thermodynamics and mass transfer in high-pressure flows. It demonstrates the significant impact of pressure on the physical properties of the two phases in the flow. These changes affect the thermodynamic equilibrium via increased solubility of the gas in the liquid phase but also the mass transfer via changes in mixture viscosity and density along the length of the microchannel. A unit-cell type model was presented and aims at calculating mass transfer coefficients in the liquid phase in a two-phase flow at high pressure. However, the model can also be adapted to determine the mass transfer coefficient in the gas phase or in both phases simultaneously. This model is then applied to the case of a  $CO_2$ - $H_2O$  flow. All the assumptions of this model have also been discussed relative to other binary systems, such as  $CO_2$ - $EtOH$  and  $CO_2$ - $BMimPF_6$  systems, which have different properties.

---

Chapter 3 described the fabrication process of a microfluidic platform that enables optical measurements of two-phase flow under high pressure at constant temperature and pressure. The microfluidic platform therefore enables the investigation of hydrodynamics and mass transfer of two-phase segmented flow at high-pressure at the same time. This platform consists of a microreactor, which is placed in a temperature-controlled chamber while ensuring optical access to the flow. Focus was given to the details of the manufacturing process so that it can be repeated by future readers. The manufacturing method can easily be adapted to cope with different inner diameters of the capillary, capillary lengths, addition of optical access in a specific capillary area and also the addition of capillaries inside the microreactor, in order to observe two different flows simultaneously or investigate a multitube microreactor.

Chapters 4 and 5 presented the two experimental methods that were developed for the measurement of the concentration of carbon dioxide dissolved in the  $H_2O$ -rich phase of the segmented flow under high-pressure inside a micro-capillary:

- The Raman spectroscopy method is based on the acquisition of Raman spectra in the liquid phase of the flow. This measurement in the liquid phase is possible by coupling the spectrometer with a photodetector, which detects the passage of bubbles. Therefore, it is not necessary to stop the flow to obtain spectral data in the liquid phase. These spectral data allow  $CO_2$  concentrations in the liquid phase to be obtained along the microchannel using a thermodynamic model to calculate the density of the liquid phase as a function of the amount of dissolved  $CO_2$ . In addition, this method can be performed not only in the liquid phase, but also in the gas phase. This means that concentrations can be obtained in systems where mass transfer between phases occurs in both directions. This method requires that the spectra of the two fluids do not overlap. If they partially overlap (as it is the case for the  $CO_2$ - $EtOH$  system with a green laser of 532 nm), it is possible to carry out additional processing of the signals to obtain a coherent result. In the case of the  $CO_2$ - $BMimPF_6$  system, the fluorescence obtained by the presence of  $BMimPF_6$  does not allow the use of this method with the current laser. However, the use of a laser which has a longer wavelength (e.g. 785 nm) could allow this experimental method to be used for this system.
- The colorimetric method, presented in Chapter 5, is based on the change in color of the pH indicator bromophenol blue (BPB) due to the acidification of water by solubilized carbon dioxide. The colored indicator allows the degree of acidification to be quantified by image acquisition and enables  $CO_2$  concentration values along the flow to be obtained. This imaging method also allows observation and quantification of the physical characteristics of the flow, such as bubbles lengths and velocities at the same time as the mass transfer measurement. This makes it possible to quantify the specific surface area  $a_L$ , which is a very effective indicator of the potential mass transfer rate in a two-phase flow. In addition, the colorimetric method allows observation of the evolution of the concentration profiles of the dissolved gas in the liquid slugs at the bubble generation zone. This method could be improved by further investigating

models that could better relate the  $CO_2$  concentration in aqueous solution acidified by  $CO_2$  and the corresponding pH. Indeed, an accurate model would directly give concentration curves instead of discrete values after the calibration. The colorimetric method presented in this thesis work can only be used for binary systems that are composed of an aqueous solution that can be acidified by a compound present in the second phase. This limitation greatly restricts the range of systems that can be studied with this method. In addition, the pH range that can be studied is conditioned by the color indicator used. However, this method could be adapted for any system where species dissolution is characterized by a color change (with or without a colored indicator).

Using the model developed in Chapter 2 and the experimental data obtained by the developed experimental methods presented in Chapters 4 and 5, it is possible to compute the liquid volumetric mass transfer coefficient  $k_L a_L$  along the microchannel, and thus achieve the primary objective of the MuSyS project. The first observation made is that the volumetric mass transfer coefficient  $k_L a_L$  is not constant along the flow, although a constant mass transfer coefficient is a common assumption in conventional models in the literature. It was found that  $k_L a_L$  decreases from the inlet until it reaches a stable value and approximately 20-30% of the mass transfer occurs in the bubble generation zone. It was also shown that the  $k_L a_L$  increases with  $\dot{V}_{CO_2}/\dot{V}_{H_2O}$  when one volumetric flow rate is fixed. The theoretical thermodynamic study of  $CO_2$ - $EtOH$  and  $CO_2$ - $BMimPF_6$  systems suggests that the change in  $k_L a_L$  along the microchannel would be even more important for such systems because of the drastic change in physical properties when compared with the  $CO_2$ - $H_2O$  system. The volumetric mass transfer coefficient  $k_L a_L$  in the two-phase segmented flow of  $CO_2$  and  $H_2O$  was determined to be in the range  $1\text{ s}^{-1}$ - $13\text{ s}^{-1}$  using the colorimetric method and in the range  $0.2\text{ s}^{-1}$ - $4\text{ s}^{-1}$  using the Raman method<sup>15</sup>. For tube diameters close to 250-300  $\mu\text{m}$ , these  $k_L a_L$  values are in the same order of magnitude as those in the literature. In addition, literature values are average values between the inlet and outlet of the microchannel whilst in this thesis work, the values of  $k_L a_L$  are local values obtained along the length of the microchannel.

The two experimental methods developed in this thesis work are thus considered to be consistent for the calculation of the liquid volumetric mass transfer coefficient in a high pressure two-phase flow for  $CO_2$ - $H_2O$  systems.

## Outlooks

The colorimetric and Raman spectroscopy methods presented in this thesis enable the measurement of the volumetric mass transfer coefficient in two-phase segmented flow at high-pressure  $k_L a_L$ . However, the influence of operating parameters such as temperature,

<sup>15</sup>This change from one method to another is justified by the fact that the tube diameter used in the colorimetric method is smaller than that used in the Raman method, which therefore leads to an increase in the mass transfer rate.

---

pressure and flow rates has only been briefly studied. Therefore, in order to attain a deeper scientific understanding of the mass transfer process it would be necessary to measure  $k_L a_L$  for a wider range of flow rates, temperatures, and pressures, and for different diameters of capillary tubes. These measurements would make it possible to determine correlations of the volumetric mass transfer coefficient as a function of the dimensionless numbers such as Re, Ca, Sc and Sh. The development of such correlations would provide a reliable design method for the intensification of segmented flow under pressure in microreactors.

In addition, the colorimetric method allows the mass transfer coefficient  $k_L$  to be measured since the values of the specific surface  $a_L$  are obtained by analyzing the bubble size in the flow. These values of  $k_L$  could thus be obtained and compared with data from the literature. On the other hand, the acquisition of velocity profiles inside the liquid slugs by experimental methods such as micro particle image velocimetry or by simulation of segmented flows (Computational Fluid Dynamics tools) could be developed. This comparison would then make it possible to fulfill the ultimate objective of the MuSyS project, namely the determination of diffusion coefficients of  $CO_2$  in the liquid phase at high pressure. Since diffusion coefficients are independent of the scale of the device in which they are calculated, diffusion coefficients of new investigated fluids could be more easily measured and then used for the sizing of high-pressure processes.

The colorimetric method provides additional information that was not investigated further in this thesis work. On the basis of the bubble volume measurement, frequency, liquid slug volume measurement and the  $CO_2$  concentration in the liquid slug, it is possible to perform a mass balance between the mass of  $CO_2$  and  $H_2O$  injected at the inlet of the microreactor and the amount that goes out at the microreactor outlet. This computation also provides the quality of the permanent flow regime obtained in the microreactor.

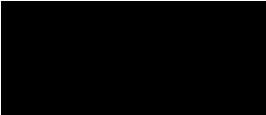
During the experimental campaign, it was noticed in some mass transfer experiments, for the Reynolds ranges investigated, that the flow behaviour changed from slug flow to spherical bubble-confined flow. It could therefore be interesting to separate the investigation where the  $CO_2$  slugs remain slugs when the thermodynamic equilibrium is reached and the other regime where the  $CO_2$  segments becomes spherical bubbles during the mass transfer process.

It would also be of interest to couple the Raman spectroscopy method with image acquisition of the flow in order to link the concentrations data in each phase with the change in bubble volume and the velocity of each phase, like done for the colorimetric method. This would allow one to verify whether the material balance is consistent between the fluid quantities fed into the microreactor and the those present in each phase once thermodynamic equilibrium has been reached, as well as to link the physical aspects of the flow with transport phenomena.

The Raman spectroscopy method can be applied to systems such as  $CO_2$ - $EtOH$  and  $CO_2$ - $BMimPF_6$  for which the dimensionless numbers  $Re_L$ ,  $Ca_L$  and  $Bo_L$  change significantly between the moment when the fluids are brought into contact and the moment when thermodynamic equilibrium is achieved. The study of the volumetric mass transfer coefficients  $k_L a_L$  would require the development of a new type of correlation since the dimensionless numbers are no longer a constant of the flow.







# Nomenclature

Symbol	Description	Unit
$A_1, A_2$	Constants	m
$a$	Specific surface	$\text{m}^{-1}$
$A$	Capillary cross-section	$\text{m}^2$
$Bo$	Bond number	-
$C$	Concentration	$\text{mol m}^{-3}$
$c$	Speed of light in a vacuum	$\text{m s}^{-1}$
$Ca$	Capillary number	-
$D$	Capillary diameter	m
$\mathcal{D}$	Diffusion coefficient	$\text{m}^2 \text{s}^{-1}$
$d_h$	Hydraulic diameter	m
$f$	Fugacity	Pa
$Fo$	Fourier number	-

---

$G$	Optical magnification	-
$H$	Henry constant	Pa
$h$	Planck constant	J s
$ID$	Inner diameter	m
$J^*$	Diffusion molar flux	$\text{mol m}^{-2} \text{s}^{-1}$
$k$	Local mass transfer coefficient	$\text{m s}^{-1}$
$K$	Global mass transfer coefficient	$\text{m s}^{-1}$
$L$	Length	m
$Li$	Li number	-
$L_{pix}$	Pixel length	m
$M$	Molar mass	$\text{kg mol}^{-1}$
$\dot{M}$	Mass flow rate	$\text{kg s}^{-1}$
$N$	Diffusion and convection combined flux	$\text{mol m}^{-2} \text{s}^{-1}$
$n$	Number of moles	mol
$\mathbf{n}$	Unit vector	-
$OD$	Outer diameter	m
$P$	Pressure	Pa
$Pe$	Peclet number	-
$R$	Ideal gas law constant	$\text{J mol}^{-1} \text{K}^{-1}$
$r$	Molar ratio in the liquid phase	-
$Re$	Reynolds number	-
$S$	Surface	$\text{m}^2$

$Sc$	Schmidt number	-
$Sh$	Sherwood number	-
$T$	Temperature	K
$t$	Time	s
$U$	Superficial velocity	$\text{m s}^{-1}$
$V$	Volume	$\text{m}^3$
$v$	Velocity	$\text{m s}^{-1}$
$v^*$	Molar average velocity	$\text{m s}^{-1}$
$\dot{V}$	Volumetric flowrate	$\text{m}^3 \text{s}^{-1}$
$w$	Mass fraction	-
$We$	Weber number	-
$x$	Molar fraction	-
$z$	Axis-location	m

---

Greek Symbol	Description	Unit
$\alpha$	Constant	-
$\gamma$	Constant	$\text{m}^{-1}$
$\delta$	Film thickness	m
$\epsilon$	Void fraction	-
$\theta$	Temperature	$^{\circ}\text{C}$
$\lambda_1, \lambda_2$	Constants	-
$\lambda$	Wavelength	m
$\mu$	Viscosity	$\text{Pa}\cdot\text{s}$
$\nu$	Frequency	$\text{s}^{-1}$
$\rho$	Density	$\text{kg}\cdot\text{m}^{-3}$
$\sigma$	Interfacial tension	$\text{N}\cdot\text{m}^{-1}$

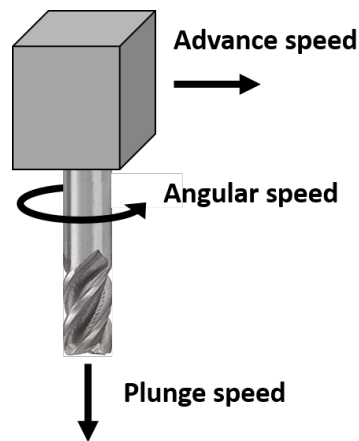
Superscript	Description
$\infty$	At infinite dilution
$a$	Apparent
$o$	Pure
$L$	Liquid
$*$	At equilibrium
$cap$	Capillary

Subscript	Description
$\phi$	Phase: liquid or gas
$B$	Bubble
$c$	Critical
$film$	Related to the liquid film
$F$	Fluid
$G$	Gas
$i$	Related to the $i$ molecules
$L$	Liquid
$S$	Slug
$TP$	Two-phase

---

Abbreviation	Description
<i>BPB</i>	BromoPhenol Blue
<i>CFD</i>	Computational Fluid Dynamics
<i>LIF</i>	Laser Induced Fluorescence
<i>PEEK</i>	PolyEtherEtherKetone
<i>PGSS</i>	Particles from Gas Saturated Solutions
<i>PMMA</i>	Poly(MethylMethAcrylate)
<i>RESS</i>	Rapid Expansion of Supercritical Solutions
<i>SAS</i>	Supercritical Anti-Solvent
<i>sCO<sub>2</sub></i>	Supercritical carbon dioxide
$\mu - PIV$	Microscopic Particle Image Velocimetry

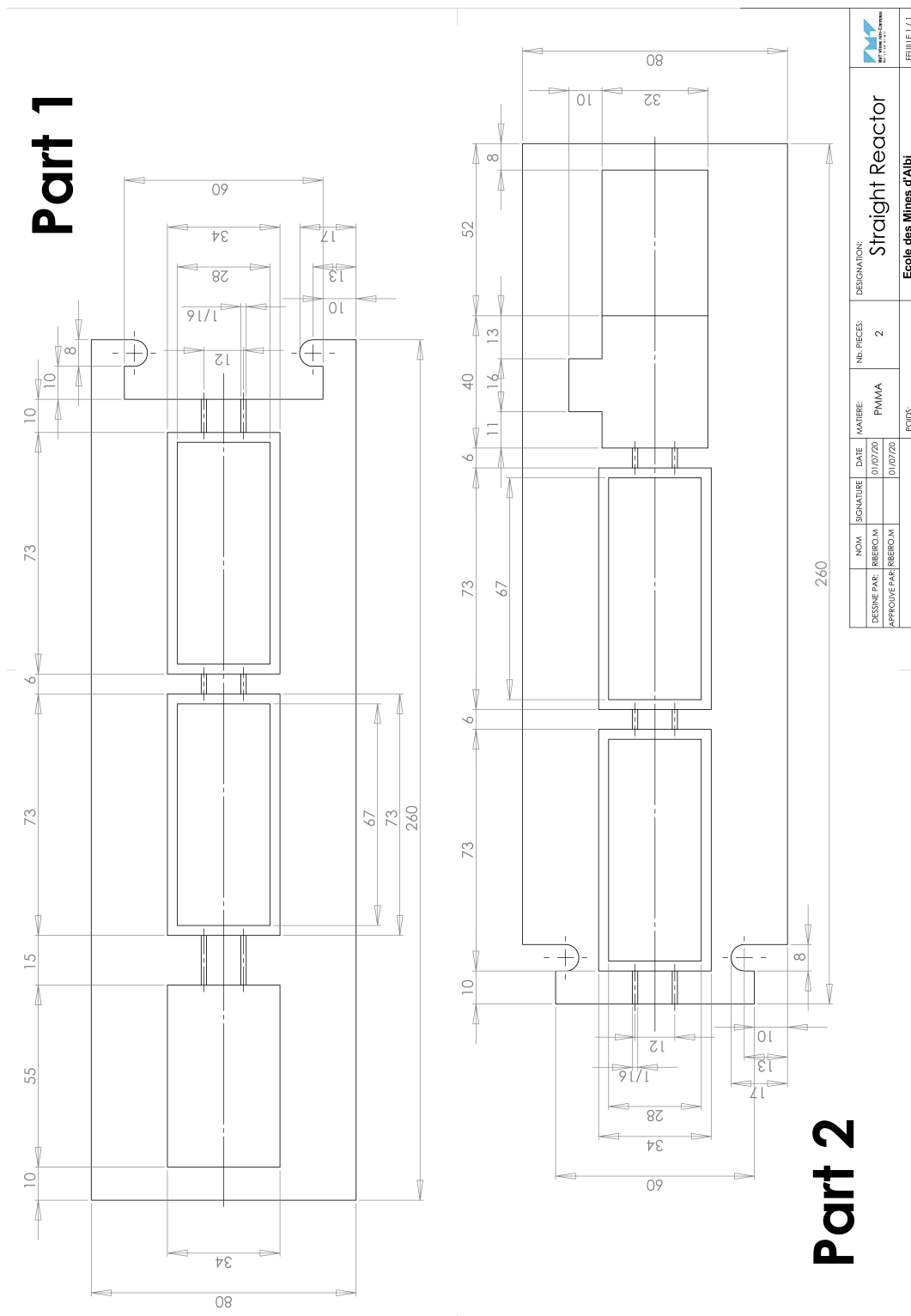
# Straight reactor dimensions and drilling parameters



**Figure A.1** – Scheme describing the drilling speeds.

**Table A.1** – Drill parameters used for the frame fabrication with the digital milling machine (TL-01).

Code	Drill diameter	Angular speed	Advance speed	Plunge speed
DRL-01	1/16 inch	19000 rpm	10 mm s <sup>-1</sup>	10 mm s <sup>-1</sup>
DRL-02	5 mm	15500 rpm	15 mm s <sup>-1</sup>	10 mm s <sup>-1</sup>
DRL-03	6 mm	14500 rpm	15 mm s <sup>-1</sup>	10 mm s <sup>-1</sup>
DRL-04	10 mm	10000 rpm	20 mm s <sup>-1</sup>	5 mm s <sup>-1</sup>



**Figure A.2** – Dimensions of the microreactor divided in part 1 and part 2. Each dimensions are given in mm.



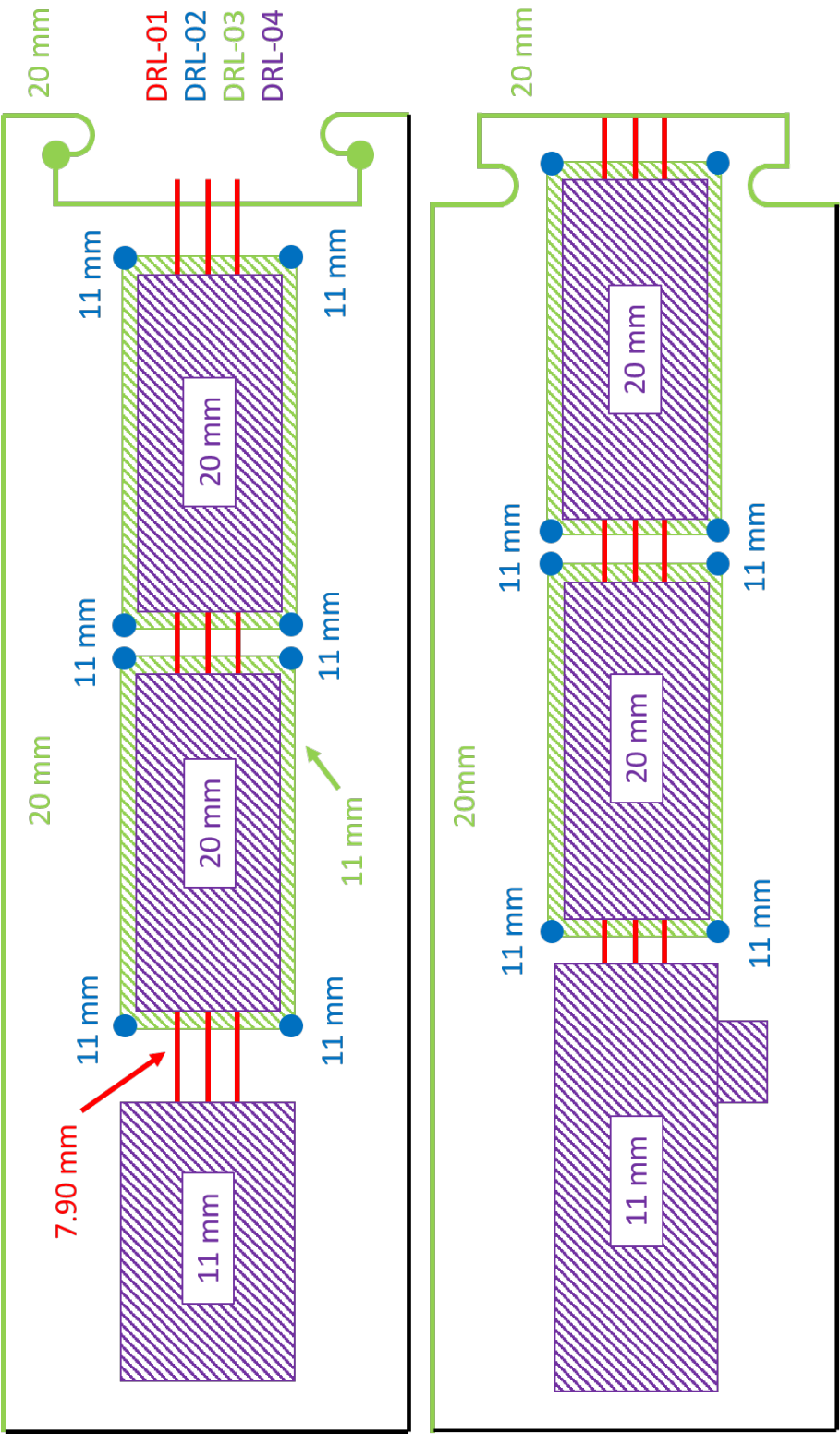


Figure A.3 – Drilling depth for the microreactor.

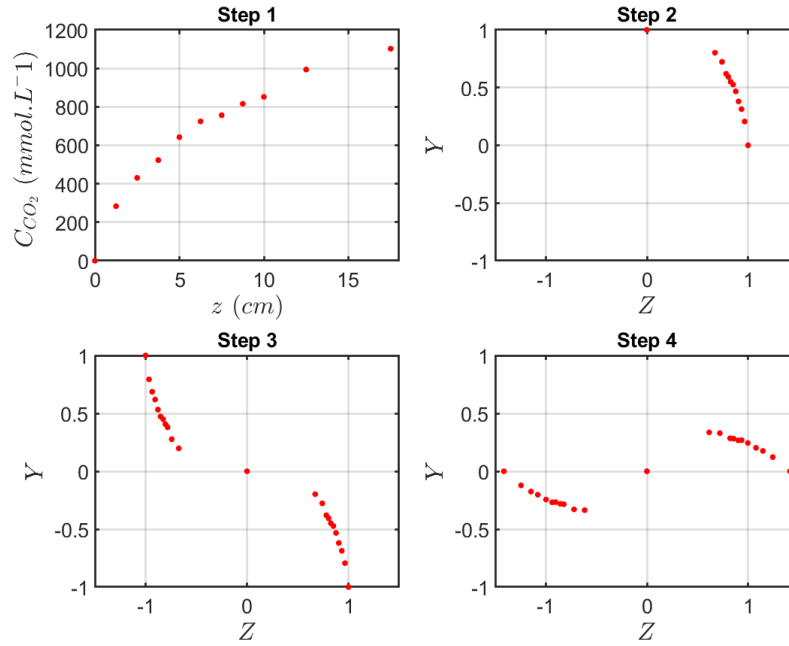


## Fast Fourier Transform method

The determination of the volumetric mass transfer coefficient requires the first derivative of the  $CO_2$  concentration in the  $H_2O$ -rich phase. However, the determination of this derivative with experimental discrete points leads to a significant error. The Fast Fourier Transform (FFT) consists in filtering the discrete points previously obtained from the temporal domain, transforming them into the frequency domain following a transformation algorithm. The FFT algorithm is presented in Balac (2011). By choosing the number of frequencies that provide the least error on the experimental values, the experimental points are fitted. The following steps enable a filtered and smoothed signal for fixed temperature, pressure,  $H_2O$  flow rate and  $CO_2$  flow rate to be obtained:

The first four steps consist in obtaining a periodic signal and are presented in Figure B.1.

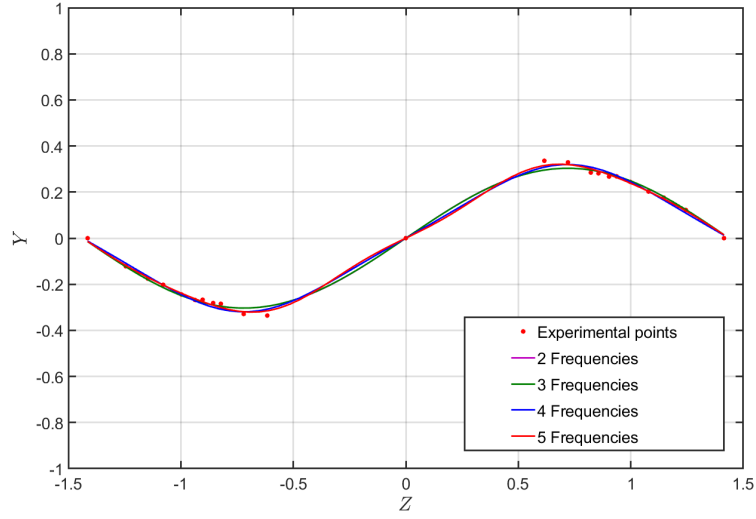
- **Step 1:** Two points are added to each set of  $CO_2$  concentrations  $(z, C_{CO_2})$ . The initial point  $(0, 0)$  and a theoretical final one  $(\infty, C_{CO_2}^*)$  where  $C_{CO_2}^*$  is the concentration of the  $H_2O$ -rich phase saturated with  $CO_2$ .
- **Step 2:** The variable substitutions  $Z = 1/(1 + \gamma z)$  and  $Y = C_{CO_2}/C_{CO_2}^*$  are performed where  $\gamma < 1$  is a constant that allows more points to be taken near  $z = 0$  in the FFT transform algorithm. The data points are all in the range  $[0; 1] \times [0; 1]$ .
- **Step 3:** The data points are translated  $(Y) \rightarrow (Y - 1)$  and the number of points are doubled by adding  $(-Z, -Y)$ .
- **Step 4:** The curve is rotated by  $-\pi/4$  around  $(0, 0)$ . Therefore, a continuous periodic curve is obtained that greatly improves the number of frequencies selection after the FFT.
- **Step 5:** The FFT algorithm necessitates to respect the Shannon theorem which consists in re-sampling the data  $(Z, Y)$  by linear interpolation taking a certain number of points. The number of points is equal to the first power of two superior to the number of data points, which is  $2^5$  in this study.
- **Step 6:** A discrete Fourier transform is carried out using the FFT algorithm.



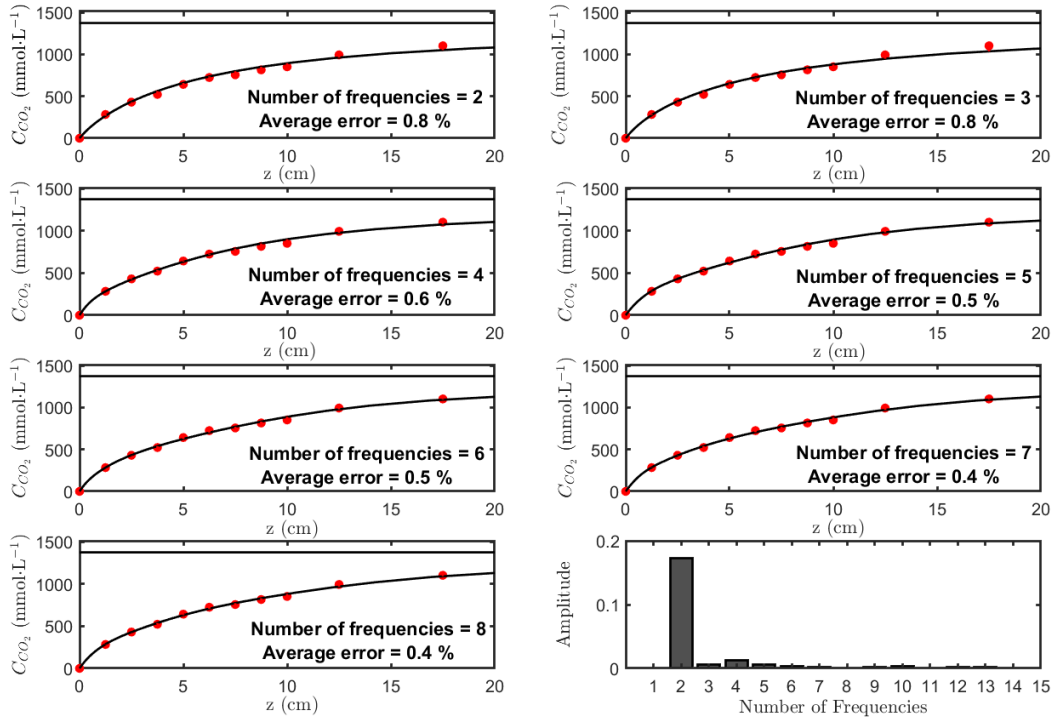
**Figure B.1** – The first four steps of the Fast Fourier Transform (FFT). The operating conditions are  $P = 10$  MPa,  $T = 303$  K,  $\dot{V}_{H_2O} = 110 \mu\text{L min}^{-1}$  and  $\dot{V}_{CO_2} = 49 \mu\text{L min}^{-1}$ .

- **Step 7:** Using the amplitude spectrum of the Fourier transform, a number of frequencies has to be taken. Figure B.2 shows the experimental data points and the fitting curves obtained with 2,3,4 and 5 frequencies. As shown, it is difficult to select a number of frequencies just by looking at the curve.
- **Step 8:** Steps 1,2,3 and 4 are performed in the reverse manner in order to look at the fitting with the original data point. The results are presented in Figure B.3. The number of frequencies is selected taking the smallest objective criteria, which is the weighted least squares (square root of the sum of the square residuals between experimental and fitting values weighted by the inverse of the standard deviation). However, only the frequencies of high amplitude are considered in order to avoid a change in the second derivative of the concentration values. In practice, the number of frequencies varies between two and four.
- **Step 9:** A curve of filtered point are obtained and allows the computation of the first derivative of  $CO_2$  concentrations in the  $H_2O$ -rich phase with precision.

In Chapter 4 where the Raman spectroscopy method is presented, figure 4.17 presents the concentration experimental data points previously presented in Figure 4.16 with the addition of the filtered curves obtained by the Fast Fourier Transform. This figure shows that the FFT fitting method correctly represents the  $CO_2$  concentrations in the  $H_2O$ -rich phase. Note that other fitting methods have been tested like Taylor expansion of exponentials, but the results were not as precise as the FFT method. This FFT algorithm has been applied to the discrete



**Figure B.2** – Experimental data points of  $CO_2$  concentrations and FFT fitting for different number of frequencies selected. The operating conditions are  $P = 10$  MPa,  $T = 303$  K,  $\dot{V}_{H_2O} = 110 \text{ } \mu\text{L min}^{-1}$  and  $\dot{V}_{CO_2} = 49 \text{ } \mu\text{L min}^{-1}$ .



**Figure B.3** – Determination of the number of frequencies for the FFT fitting. The operating conditions are  $P = 10$  MPa,  $T = 303$  K,  $\dot{V}_{H_2O} = 110 \text{ } \mu\text{L min}^{-1}$  and  $\dot{V}_{CO_2} = 49 \text{ } \mu\text{L min}^{-1}$ .

---

concentration values obtained in the colorimetric method. However, the average errors obtained were higher compared with those obtained in the Raman spectroscopy method. In the Raman spectroscopy method, the average error between the fitted concentrations and the experimental values of all the conditions studied do not exceed 1% where the average errors are around 10% in the colorimetric method. This difference is due to the transition between pH values to  $CO_2$  concentration values. As mentioned before, this transition can be greatly improved with further investigations of a model linking pH and  $CO_2$  concentrations in the  $H_2O$ -rich phase.

# Raman spectroscopy method supplements

**Table C.1** – Operating conditions employed in the Raman spectroscopy method at 303 K.

$P$	$\dot{V}_{H_2O}$	$\dot{V}_{CO_2}$	$U_G$	$U_L$	$Re_L$	$Re_G$	$Ca_L$	$Ca_G$	$U_{TP}$	$\frac{U_G}{U_L}$
MPa	$\mu\text{L min}^{-1}$	$\mu\text{L min}^{-1}$	$\text{m s}^{-1}$	$\text{m s}^{-1}$	-	-	-	-	$\text{m s}^{-1}$	-
8	50	40,5	0,010	0,012	4,4	35,9	$3,00 \times 10^{-4}$	$1,71 \times 10^{-5}$	0,021	0,81
8	60	40,5	0,010	0,014	5,3	35,9	$3,60 \times 10^{-4}$	$1,71 \times 10^{-5}$	0,024	0,68
8	80	40,5	0,010	0,019	7,1	35,9	$4,80 \times 10^{-4}$	$1,71 \times 10^{-5}$	0,028	0,51
8	100	40,5	0,010	0,024	8,9	35,9	$6,00 \times 10^{-4}$	$1,71 \times 10^{-5}$	0,033	0,41
8	160	40,5	0,010	0,038	14,2	35,9	$9,60 \times 10^{-4}$	$1,71 \times 10^{-5}$	0,047	0,25
8	180	40,5	0,010	0,042	16,0	35,9	$1,08 \times 10^{-3}$	$1,71 \times 10^{-5}$	0,052	0,23
8	200	54,1	0,013	0,047	17,7	47,9	$1,20 \times 10^{-3}$	$2,28 \times 10^{-5}$	0,060	0,27
8	200	81,1	0,019	0,047	17,7	71,8	$1,20 \times 10^{-3}$	$3,42 \times 10^{-5}$	0,066	0,41
8	200	108,1	0,025	0,047	17,7	95,7	$1,20 \times 10^{-3}$	$4,56 \times 10^{-5}$	0,073	0,54
9	130	38,2	0,009	0,031	11,5	32,5	$7,88 \times 10^{-4}$	$1,79 \times 10^{-5}$	0,040	0,29
9	150	38,2	0,009	0,035	13,3	32,5	$9,09 \times 10^{-4}$	$1,79 \times 10^{-5}$	0,044	0,25
9	170	38,2	0,009	0,040	15,1	32,5	$1,03 \times 10^{-3}$	$1,79 \times 10^{-5}$	0,049	0,22
9	170	51	0,012	0,040	15,1	43,4	$1,03 \times 10^{-3}$	$2,40 \times 10^{-5}$	0,052	0,30
9	170	38,2	0,009	0,040	15,1	32,5	$1,03 \times 10^{-3}$	$1,79 \times 10^{-5}$	0,049	0,22
9	170	12,7	0,003	0,040	15,1	10,8	$1,03 \times 10^{-3}$	$5,98 \times 10^{-5}$	0,043	0,07
10	110	36,9	0,009	0,026	9,8	30,5	$6,82 \times 10^{-4}$	$1,89 \times 10^{-5}$	0,035	0,34
10	110	49,2	0,012	0,026	9,8	40,6	$6,82 \times 10^{-4}$	$2,52 \times 10^{-5}$	0,038	0,45
10	110	61,5	0,015	0,026	9,8	50,8	$6,82 \times 10^{-4}$	$3,16 \times 10^{-5}$	0,040	0,56
10	110	73,7	0,017	0,026	9,8	60,9	$6,82 \times 10^{-4}$	$3,78 \times 10^{-5}$	0,043	0,67
10	110	86	0,020	0,026	9,8	71,0	$6,82 \times 10^{-4}$	$4,42 \times 10^{-5}$	0,046	0,78
10	110	49,2	0,012	0,026	9,8	40,6	$6,82 \times 10^{-4}$	$2,52 \times 10^{-5}$	0,038	0,45
10	100	49,2	0,012	0,024	8,9	40,6	$6,20 \times 10^{-4}$	$2,52 \times 10^{-5}$	0,035	0,49
10	90	49,2	0,012	0,021	8,0	40,6	$5,58 \times 10^{-4}$	$2,52 \times 10^{-5}$	0,033	0,55
10	80	49,2	0,012	0,019	7,1	40,6	$4,96 \times 10^{-4}$	$2,52 \times 10^{-5}$	0,030	0,61



# Uncertainty calculations

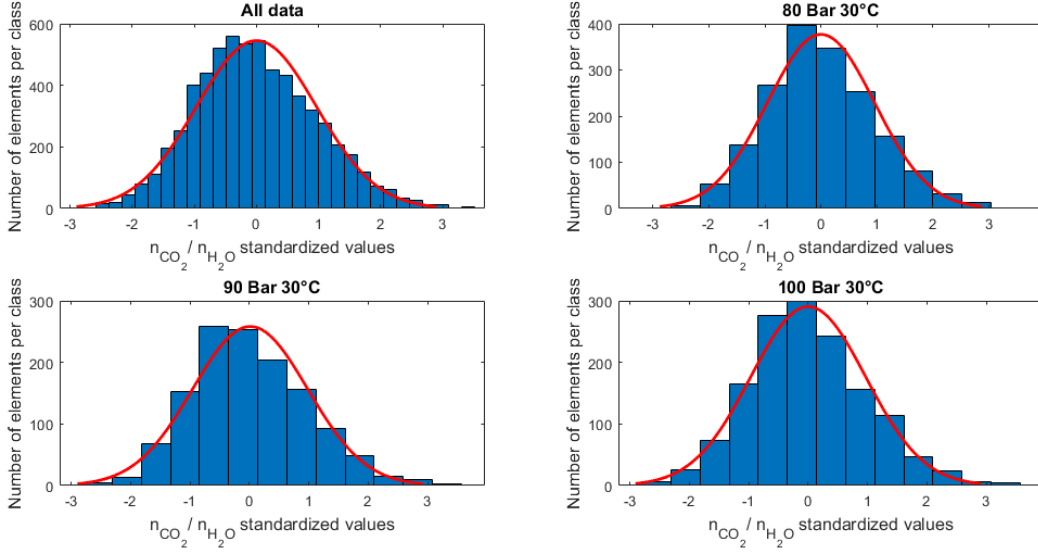
## D.1 Uncertainty calculations on the $CO_2$ concentrations in the Raman spectroscopy method

The concentrations in Figure 4.16 are given with error bars. The error bars calculation is treated using an uncertainty propagation from the raw Raman spectra giving the molar ratios to the  $CO_2$  concentrations calculations. At each measurement spot, 16 spectra are obtained. Thus, the molar ratios are averaged using 16 values. First of all, a standard normal distribution test is performed for all molar ratios  $r = n_{CO_2}/n_{H_2O}$  obtained for each pressure and temperature as presented in Figure D.1. Each set of data follows a normal law distribution. Consequently, the standard deviation  $\sigma_r$  can be seen as a standard deviation of a normal distribution. Equation 4.8 gives the computation of the  $CO_2$  concentration in the  $H_2O$ -rich phase as a function of the molar ratio  $r$  (here equal to the molar fraction ratio) and the liquid mixture density  $\rho_L$ . This function is called  $f$  as presented in Equation D.1

$$C_{CO_2} = \frac{\rho_L}{M_{CO_2} + \left(\frac{n_{H_2O}}{n_{CO_2}}\right)M_{H_2O}} = f\left(\frac{n_{CO_2}}{n_{H_2O}}, \rho_L\right) = f(r, \rho_L) \quad (D.1)$$

The standard deviation of the  $CO_2$  concentrations can be written as Equation D.2 assuming the following hypothesis:

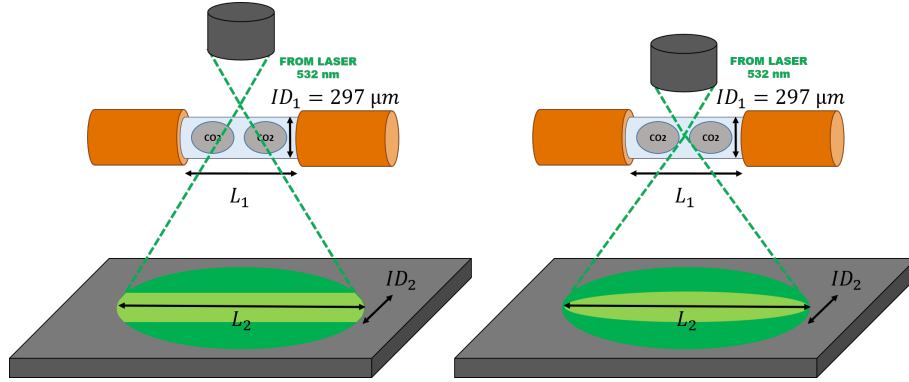
- $r$  and  $\rho_L$  are near their mean values noted  $\tilde{r}$  and  $\tilde{\rho}_L$ .
- $\sigma_r$  and  $\sigma_{\rho_L}$  are small compared with  $r$  and  $\rho_L$ .
- $\partial f/\partial r$  (respectively  $\partial f/\partial \rho_L$ ) are linear inside the interval  $\pm\sigma_r$  ( $\pm\sigma_{\rho_L}$ ) about  $\tilde{r}$  ( $\tilde{\rho}_L$ ).



**Figure D.1** – Standardized class distributions of molar ratios in the  $H_2O$ -rich phase (blue) and standardized normal distribution (red) for all data and for each couple of pressure/temperature.

$$\sigma_{C_{CO_2}} = \sqrt{\left(\frac{\partial f}{\partial r}\right)_{r=\bar{r}}^2 \sigma_r^2 + \left(\frac{\partial f}{\partial \rho_L}\right)_{\rho_L=\bar{\rho}_L}^2 \sigma_{\rho_L}^2} \quad (D.2)$$

Following a Monte Carlo statistical method, a random draw of thousands of values in the normal distribution of  $r$  and  $\rho_L$  gives a distribution of  $C_{CO_2}$  with Equation D.1. It has been demonstrated that the  $C_{CO_2}$  distribution follows a normal law as well. Consequently, the standard deviation  $\sigma_{C_{CO_2}}$  computed with Equation D.2 can be seen as a standard deviation of a normal law distribution. For a normal distribution, 95% of the entire population are within  $\pm$  two standard deviations. The value of the standard deviation  $\sigma_{C_{CO_2}}$  which take into account the variations of the molar ratios (including the error during the calibration step) and the variations of the mixture density, does not exceed 7% of the concentration value. However, this deviation can be drastically reduced with a binary system where the calibration step is easier than the one with the  $CO_2$ - $H_2O$  system because the solubility of  $CO_2$  in the  $H_2O$  rich phase is small (and therefore reduces the resolution of the calibration curve). The contribution of temperature and pressure measurements on the concentrations obtained with this method was verified by a random sampling in the normal distribution of T and P. The results show that the concentration values are shifted by less than 0.05% of the mean value, which is highly negligible compared with error from the molar ratio and from the density model.



**Figure D.2** – Sketches of the laser passing through the capillary tube when the laser is not well focused inside the capillary (left) and when the laser is well focused (right).

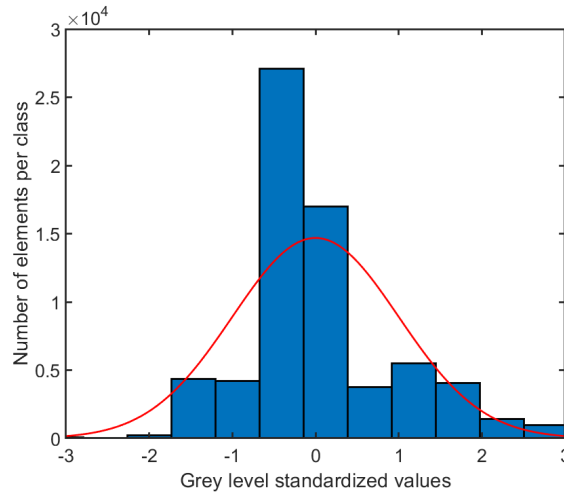
## D.2 Uncertainty calculations on the $z$ -axis position in the capillary in the Raman spectroscopy method

As the  $CO_2$  concentration in the  $H_2O$ -rich phase is computed at different  $z$ -axis positions, it is important to know the precision on the  $z$ -axis position. In order to do this, the technique presented in Figure D.2 is used. On the left part of the figure, the laser is not well focused inside the capillary and therefore, the image on the black table represents the capillary with a certain magnification. The diameter of the measurement spot is known ( $L_1 = 1$  cm) as the inner diameter of the capillary ( $ID_1 = 297$  μm). The magnification  $G$  is computed using Equation D.3. When the laser is well focused in the capillary, the image on the black table is ellipsoidal. If the laser is positioned in the middle of the measurement spot, the ellipsoid is symmetrical and the  $z$ -axis position of the measurement corresponds to the middle of the measurement spot. Assuming that the error on the symmetric ellipsoid is 1 cm at naked eye on the black table, this leads to an error of 333 μm on the  $z$ -axis position in the capillary, which is negligible compared with the distance between two measurement spots.

$$G = \frac{L_2}{L_1} = \frac{ID_2}{ID_1} = 30 \quad (D.3)$$

## D.3 Uncertainty calculations on the $CO_2$ concentrations in the colorimetric method

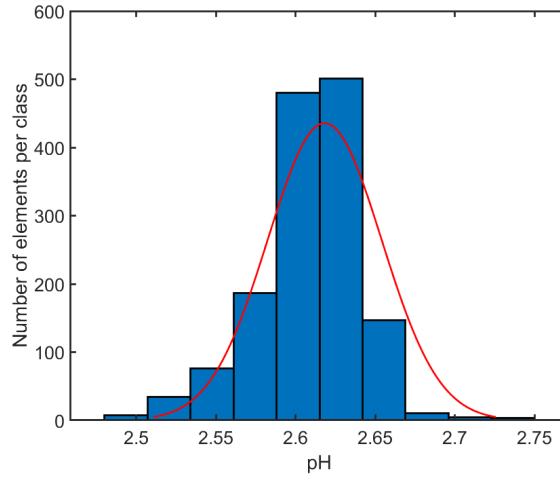
The uncertainty calculation on the  $CO_2$  concentrations in the colorimetric method is performed with the same procedure as the uncertainty calculation in the Raman spectroscopy method. The greyscale values of all the measurement spots were standardized ((value-average)/standard deviation) and a normal distribution test was performed. The result is presented in Figure D.3. It can be seen that the greyscale standardized values distribution is not scattered. This observation shows that the precision on the greyscale values is significant.



**Figure D.3** – Standardized class distribution of greyscale values of all the measurement spots at 10 MPa, 303 K,  $\dot{V}_{CO_2} = 58.9 \text{ } \mu\text{L min}^{-1}$  and  $\dot{V}_{H_2O} = 150 \text{ } \mu\text{L min}^{-1}$ .

A Monte Carlo statistical method has been applied at fixed  $z$ -axis positions, a random draw of thousands of values taken from the distribution of the greyscales is performed. For each greyscale obtained, a random draw in the corresponding possible<sup>1</sup> pH values from the calibration curve is performed. This method allows to take into account the uncertainty in the calibration curve. An example is given in Figure D.4 which presents the pH distribution obtained at  $z=33.7 \text{ mm}$  for the experiment at 10 MPa, 303 K where  $\dot{V}_{CO_2} = 58.9 \text{ } \mu\text{L min}^{-1}$ ,  $\dot{V}_{H_2O} = 150 \text{ } \mu\text{L min}^{-1}$ .

<sup>1</sup>The corresponding pH value is taken in the confident interval of the calibration curve assuming that the distribution follows a normal law



**Figure D.4** – pH class distribution at  $z=33.7$  mm, 10 MPa, 303 K,  $\dot{V}_{CO_2} = 58.9 \text{ } \mu\text{L min}^{-1}$  and  $\dot{V}_{H_2O} = 150 \text{ } \mu\text{L min}^{-1}$ .

The standard deviation of the pH distribution in Figure D.4 is equal to 0.036. The same treatment has been performed for hundred values of  $z$ -axis position linearly spaced between  $z=0$  and  $z=18.9$  cm. The maximum standard deviation obtained was 0.15, in the bubble generation zone<sup>2</sup>. This method allows to give uncertainty on the pH values obtained. However, since the  $CO_2$  concentrations are interpolated with experimental values from Peng et al. (2013), it is not possible to give an uncertainty on the  $CO_2$  concentrations in the  $H_2O$ -rich phase. However, average errors on the  $CO_2$  concentration filtered curves obtained with the Fast Fourier Transform of discrete values are calculated, as shown in Appendix B.

## D.4 Uncertainty calculations on the $z$ -axis position in the capillary in the colorimetric method

The  $z$ -axis position of bubbles or liquid slugs in the colorimetric method is obtained by measuring the distance between the contacting point of the two phases ( $z = 0$ ) and the carbon residues at the measurement spots. This measurement is performed with the camera of the setup and a graduated scale. The uncertainty on this measurement is around  $\pm 250 \text{ } \mu\text{m}$ . The Matlab program allows to compute the distance between the bubbles and the carbon residue at a measurement spot, the uncertainty on this measurement is around 5 pixels, which is equal to  $35 \text{ } \mu\text{m}$ . It is therefore assumed that the uncertainty on the  $z$ -axis position is around  $\pm 285 \text{ } \mu\text{m}$  in the colorimetric method.

<sup>2</sup>This result is due to the wide greyscale distribution during the bubble generation process and to the large confident interval in the calibration curve for pH values superior to 5.



# Colorimetric method supplements

## E.1 Operating Conditions

**Table E.1** – Operating conditions employed in the colorimetric method at 10 MPa and 303 K.

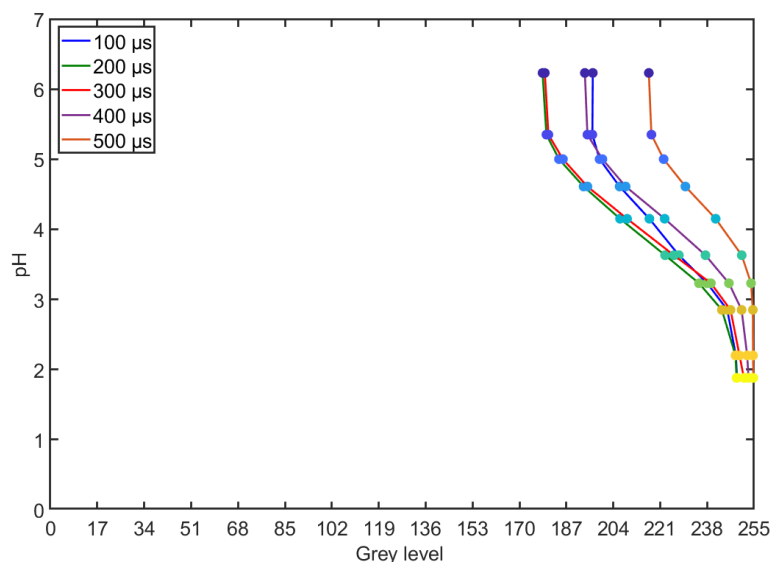
$\dot{V}_{H_2O}$	$\dot{V}_{CO_2}$	$U_G$	$U_L$	$Re_L$	$Re_G$	$Ca_L$	$Ca_G$	$U_{TP}$	$U_B$	$\frac{U_G}{U_L}$
$\mu\text{L min}^{-1}$	$\mu\text{L min}^{-1}$	$\text{m s}^{-1}$	$\text{m s}^{-1}$	-	-	-	-	$\text{m s}^{-1}$	$\text{m s}^{-1}$	-
150	58.9	0.017	0.051	15.9	49.5	0.0014	$3.8 \times 10^{-5}$	0.068	0.07	0.33
200	58.9	0.017	0.068	21.3	49.5	0.0018	$3.8 \times 10^{-5}$	0.085	0.09	0.25
250	58.9	0.017	0.085	26.6	49.5	0.0023	$3.8 \times 10^{-5}$	0.102	0.11	0.20
300	58.9	0.017	0.102	31.9	49.5	0.0027	$3.8 \times 10^{-5}$	0.119	0.12	0.17
350	76.6	0.022	0.119	37.2	64.3	0.0032	$4.9 \times 10^{-5}$	0.141	0.15	0.19
350	94.2	0.027	0.119	37.2	79.2	0.0032	$6.0 \times 10^{-5}$	0.146	0.16	0.23
350	111.9	0.032	0.119	37.2	94.0	0.0032	$7.1 \times 10^{-5}$	0.151	0.17	0.27
110	82.5	0.024	0.037	11.7	69.3	0.0010	$5.3 \times 10^{-5}$	0.061	0.07	0.64
150	82.5	0.024	0.051	15.9	69.3	0.0014	$5.3 \times 10^{-5}$	0.075	0.08	0.47
200	82.5	0.024	0.068	21.3	69.3	0.0018	$5.3 \times 10^{-5}$	0.092	0.1	0.35
300	82.5	0.024	0.102	31.9	69.3	0.0027	$5.3 \times 10^{-5}$	0.126	0.14	0.23

---

## E.2 Choice of BPB concentration

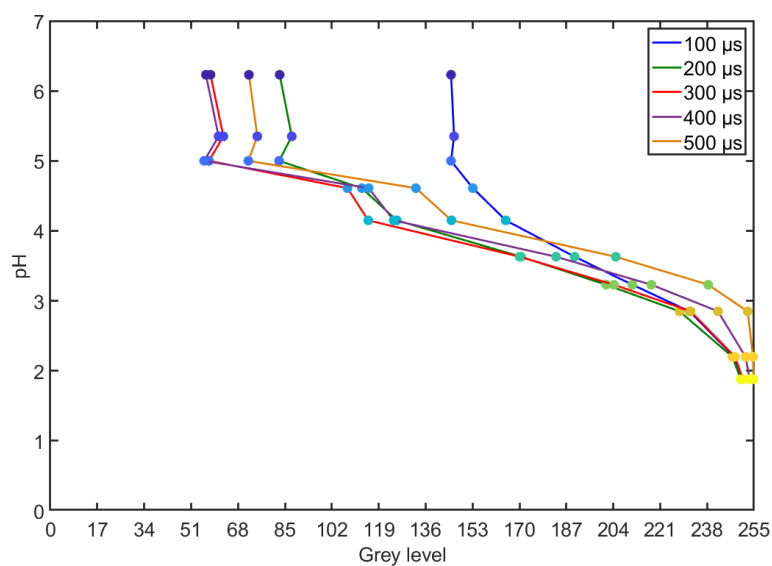
The optimal choice of shutter and BPB concentrations of  $0.8 \text{ mmol L}^{-1}$  and  $300 \mu\text{s}$  for the calibration curve has been carried out with Figures E.1 to E.3 and the following arguments:

- For all the concentrations, It can be seen that for shutters  $100 \mu\text{s}$ ,  $200 \mu\text{s}$  and  $500 \mu\text{s}$  the curve are shifted compared with the other shutters. This is due to the fact that the blank images at a shutter of  $500 \mu\text{s}$  is saturated with blank (greyscale=255) and saturated with black (greyscale=0) for the shutters of  $100 \mu\text{s}$  and  $200 \mu\text{s}$ . Therefore these shutters cannot be selected.
- For BPB concentration of  $0.2 \text{ mmol L}^{-1}$ , low pH values cannot be differentiated since the images are saturated with blank (greyscale=255). For a BPB concentration of  $2 \text{ mmol L}^{-1}$ , pH values superior to 4 cannot be differentiated since the images are saturated with black (greyscale near zero).
- For BPB concentration of  $0.8 \text{ mmol L}^{-1}$ , shutters of  $300 \mu\text{s}$  and  $400 \mu\text{s}$  are adapted. However, in order to obtain the lowest blur motion due to the bubble speed, the smallest shutter is selected.

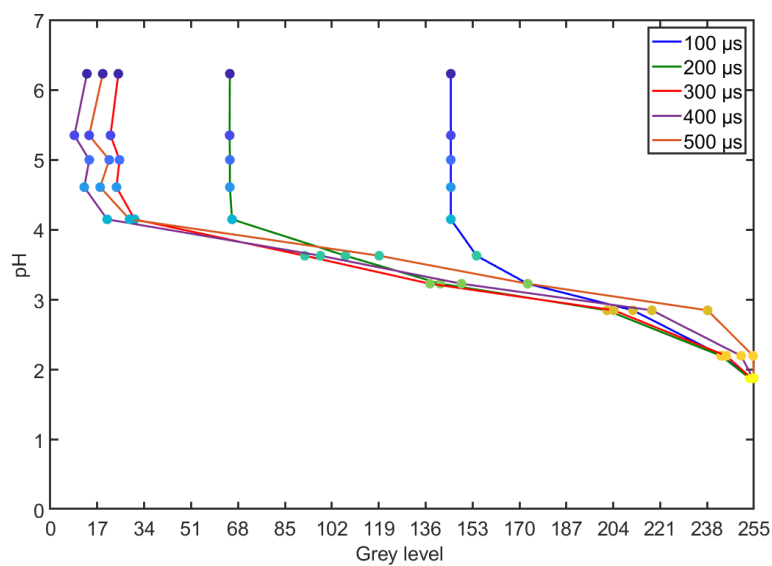


**Figure E.1** – Calibration curves linking pH of the buffer solutions (citric acid + sodium tri-citrate) with the greyscale of the images of these solutions placed inside the microreactor.  $[\text{BPB}] = 0.2 \text{ mmol L}^{-1}$  and shutters =  $[100 \mu\text{s}, 200 \mu\text{s}, 300 \mu\text{s}, 400 \mu\text{s}, 500 \mu\text{s}]$ .





**Figure E.2** – Calibration curves linking pH of the buffer solutions (citric acid + sodium tri-citrate) with the greyscale of the images of these solutions placed inside the microreactor.  $[\text{BPB}] = 0.8 \text{ mmol L}^{-1}$  and shutters =  $[100 \mu\text{s}, 200 \mu\text{s}, 300 \mu\text{s}, 400 \mu\text{s}, 500 \mu\text{s}]$ .



**Figure E.3** – Calibration curves linking pH of the buffer solutions (citric acid + sodium tri-citrate) with the greyscale of the images of these solutions placed inside the microreactor.  $[\text{BPB}] = 2 \text{ mmol L}^{-1}$  and shutters =  $[100 \mu\text{s}, 200 \mu\text{s}, 300 \mu\text{s}, 400 \mu\text{s}, 500 \mu\text{s}]$ .

## E.3 Output files of the Matlab software

```
%
%                               10-Sep-2020 : Creation date
% ../data-test/E10/Sequence_2020_07_08_13_24_47_SPOT1 : Raw images directory
% ../data-test/E10/PARAM_2020_07_08_13_24_47_SPOT1.m : Parameters file
%                               ImageXXXX.tif : Image name type
%                               6.7835 µm/pix : Scale
%                               37  1235 : Number of pixels (height, width)
%-----
%ima drop Dout      Lx      Ly      Rx      Ry      Bx      By      Tx      Ty      per2D  surf2D  surfrev  volrev
% #   #   log    pix    pix    pix    pix    pix    pix    pix    pix    pix    pix2    pix2    pix3
%-----
  0    1    0   40.5   21.0   87.5   19.5   66.5   35.5   65.5   2.5  131.88   1310   5242.74  33533.87
  0    2    0   234.5  24.0  280.5   19.0  254.0   35.5  252.5   2.5  130.47   1315   5074.20  32011.45
  0    3    0   413.5  14.0  469.5   19.0  436.5   36.5  441.0   2.5  140.61   1496   5581.09  37054.93
  0    4    0   609.5  19.0  662.5   19.5  629.0   36.5  635.0   2.5  135.47   1432   5369.13  35300.25
  0    5    0   798.5  19.0  851.5   18.5  817.5   36.5  824.5   2.5  135.46   1426   5325.31  34883.57
  0    6    0   985.5  19.0 1038.5   19.5 1005.0   36.5 1011.0   2.5  134.91   1408   5306.72  34746.16
  0    7    0  1175.5  19.5 1227.5   19.0 1201.0   35.5 1201.5   2.5  133.01   1387   5115.50  32674.26
  1    1    0   58.5   19.5  104.5   19.0   84.0   34.5   77.5   1.5  131.02   1303   5143.79  32607.73
  1    2    0  251.5   20.0  298.5   17.5  270.5   34.5  270.5   1.5  131.69   1335   5143.91  32640.19
  1    3    0   434.5  19.0  489.5   17.5  466.5   35.5  459.5   1.5  146.94   1489   5634.00  37410.25
  1    4    0   626.5  18.5  679.5   19.0  652.5   35.5  652.5   1.5  135.28   1440   5316.68  34737.69
  1    5    0   815.5  19.5  868.5   19.0  835.0   35.5  842.0   1.5  135.09   1423   5329.15  34951.21
  1    6    0  1003.5  18.5 1055.5   19.0 1029.0   35.5 1024.0   1.5  133.32   1396   5223.03  33973.74
  1    7    1 1192.5  17.5 1235.5   25.5 1213.0   35.5 1218.0   1.5  126.18   1225   -666.00   -666.00

1797   5    0   743.5  18.0  796.5   19.0  769.0   35.5  769.5   2.5  135.15   1420   5215.96  33539.25
1797   6    0   931.5  18.5  983.5   19.0  951.0   35.5  952.0   1.5  133.88   1392   5292.61  34734.94
1797   7    0  1117.5  19.0 1169.5   19.5 1142.5   35.5 1137.0   1.5  133.87   1405   5274.38  34459.89
1798   1    0   22.5   20.0   68.5   20.0   54.0   34.5   42.0   2.5  126.12   1208   4649.78  28320.98
1798   2    0   209.5  19.0  258.5   20.5  235.5   35.5  228.5   2.5  135.25   1365   5262.60  33613.48
1798   3    0   387.5  19.0  439.5   19.0  419.5   35.5  413.0   2.5  134.31   1397   5232.60  33774.48
1798   4    0   574.5  19.0  627.5   18.5  594.0   35.5  594.0   1.5  135.83   1426   5387.33  35574.57
1798   5    0   759.5  18.5  812.5   19.0  785.5   35.5  786.0   2.5  135.16   1420   5225.66  33630.89
1798   6    0   948.5  19.0 1000.5   19.0  974.0   35.5  974.0   2.5  133.02   1390   5123.37  32763.91
1798   7    0  1133.5  18.5 1186.5   18.5 1159.0   35.5 1153.5   1.5  134.72   1406   5265.06  34360.42
1799   1    0   39.5   18.5   85.5   20.0   71.0   34.5   58.5   2.5  126.03   1214   4724.45  29261.47
1799   2    0   226.5  20.5  272.5   19.5  245.5   35.5  246.0   2.5  131.12   1326   5125.63  32469.32
1799   3    0   404.5  19.0  459.5   15.5  435.5   35.5  430.0   2.5  137.96   1430   5305.30  34079.17
1799   4    0   590.5  19.5  644.5   19.5  617.0   35.5  611.0   1.5  136.50   1444   5379.46  35337.38
1799   5    0   776.5  19.5  829.5   19.0  802.0   35.5  802.5   2.5  135.53   1428   5263.47  33963.62
1799   6    0   965.5  19.0 1017.5   18.5  990.0   35.5  991.0   2.5  133.02   1389   5116.66  32699.87
1799   7    0  1150.5  16.0 1202.5   19.0 1176.0   35.5 1174.5   2.5  138.36   1451   5424.72  35199.64
```

**Figure E.4** – Output file of the Matlab program containing the data on the bubbles of each image: the number of the working image (ima), the number of the bubble in this image (drop), a boolean which is true if the bubble touches the edge of the image (Dout), the coordinates (in pixel) of the ends of the bubble (Lx, Ly, Rx, Ry, Bx, By, Tx, Ty) where L is for left, R for right, B for bottom and T for top. It also contains the perimeter (per2D) and surface (surf2D) of the bubble on the image, as well as the surface (surfrev) and volume (volrev) of the real bubble obtained by the Guldin's theorem.

```
%
%          10-Sep-2020 : Creation date
% ../data-test/E10/Sequence_2020_07_08_13_24_47_SPOT1 : Raw images directory
% ../data-test/E10/PARAM_2020_07_08_13_24_47_SPOT1.m : Parameters file
%          ImageXXXX.tif : Image name type
%          6.7835 µm/pix : Scale
%          37 1235 : Number op pixels (height, width)
```

```
%-----
%image      x      Greylevel
% #         pix      0-255
%-----
%
%      0      1      70
%      0      2      74
%      0      3      81
%      0      4      81
%      0      5      80
%      0      6      77
%      0      7      76
%      0      8      79
%      0      9      79
%      0     10      76
%      0     11      79
%      0     12      83
%      0     13      82
%      0     14      77
%
%      .
%      .
%      .
%
% 1799    1219    187
% 1799    1220    188
% 1799    1221    187
% 1799    1222    187
% 1799    1223    187
% 1799    1224    189
% 1799    1225    191
% 1799    1226    193
% 1799    1227    188
% 1799    1228    184
% 1799    1229    185
% 1799    1230    189
% 1799    1231    188
% 1799    1232    186
% 1799    1233    188
% 1799    1234    190
% 1799    1235    191
```

**Figure E.5** – Output file of the Matlab program containing the number of the image (image), a position in pixels (x) and an associated greyscale (Greylevel).

---

## E.4 Images of two-phase segmented flow of $CO_2$ and $H_2O$



**Figure E.6** – Images of two-phase segmented flow of  $CO_2$  and  $H_2O$  at the first measurement spot for 10 MPa and 303 K where  $\dot{V}_{CO_2} = 58.9 \mu\text{L min}^{-1}$ : (a)  $\dot{V}_{H_2O} = 150 \mu\text{L min}^{-1}$ , (b)  $\dot{V}_{H_2O} = 200 \mu\text{L min}^{-1}$  and (c)  $\dot{V}_{H_2O} = 300 \mu\text{L min}^{-1}$ .



**Figure E.7** – Images of two-phase segmented flow of  $CO_2$  and  $H_2O$  at the first measurement spot for 10 MPa and 303 K where  $\dot{V}_{H_2O} = 350 \mu\text{L min}^{-1}$ : (a)  $\dot{V}_{CO_2} = 76.6 \mu\text{L min}^{-1}$ , (b)  $\dot{V}_{CO_2} = 94.2 \mu\text{L min}^{-1}$  and (c)  $\dot{V}_{CO_2} = 111.9 \mu\text{L min}^{-1}$ .



**Figure E.8** – Images of two-phase segmented flow of  $CO_2$  and  $H_2O$  at the first measurement spot for 10 MPa and 303 K where  $\dot{V}_{CO_2} = 82.5 \mu\text{L min}^{-1}$ : (a)  $\dot{V}_{H_2O} = 110 \mu\text{L min}^{-1}$ , (b)  $\dot{V}_{H_2O} = 150 \mu\text{L min}^{-1}$ , (c)  $\dot{V}_{H_2O} = 200 \mu\text{L min}^{-1}$  and (d)  $\dot{V}_{H_2O} = 300 \mu\text{L min}^{-1}$ .



**Figure E.9** – Images of a two-phase segmented flow evolution of  $CO_2$  and  $H_2O$  at the first measurement spot for 10 MPa and 303 K where  $\dot{V}_{CO_2} = 82.5 \mu\text{L min}^{-1}$  and  $\dot{V}_{H_2O} = 300 \mu\text{L min}^{-1}$  (1/600 second between each image).



# Chemical Engineering Science, Deleau et al. (2020)

# Determination of mass transfer coefficients in high-pressure two-phase flows in capillaries using Raman spectroscopy

T. Deleau <sup>a,b</sup>, M.H.H. Fechter <sup>c</sup>, J.-J. Letourneau <sup>a</sup>, S. Camy <sup>b</sup>, J. Aubin <sup>b,\*</sup>, A.S. Braeuer <sup>c</sup>, F. Espitalier <sup>a</sup>

<sup>a</sup> Université de Toulouse, Mines Albi, Centre RAPSODEE UMR CNRS 5302, Campus Jarlard, Albi, France

<sup>b</sup> Université de Toulouse, Laboratoire de Génie Chimique, UMR CNRS 5503, INPT, Toulouse, France

<sup>c</sup> Institute of Thermal, Environmental, and Resources' Process Engineering (ITUN), Technische Universität Bergakademie Freiberg (TUBAF), Leipziger Strasse 28, 09599 Freiberg, Germany

## H I G H L I G H T S

- Mass transfer of CO<sub>2</sub> into a H<sub>2</sub>O-rich phase at high pressure in a capillary is studied.
- A method for the determination of volumetric mass transfer coefficient is presented.
- A thermodynamic model and Raman spectroscopy are coupled to obtain CO<sub>2</sub> concentrations.
- The influence of flow rates on the volumetric mass transfer coefficient is studied.
- The mass transfer coefficient varies along the length of the micro-capillary tube.

## A B S T R A C T

This study presents a method for the experimental determination of local volumetric mass transfer coefficients  $k_L a_L$  in a high-pressure two-phase flow of water (H<sub>2</sub>O) and carbon dioxide (CO<sub>2</sub>) in a micro-capillary using Raman spectroscopy. H<sub>2</sub>O and CO<sub>2</sub> are continuously and co-currently fed at high pressure (8, 9 and 10 MPa) and moderate temperature (303 K) into a fused silica micro-capillary. A segmented two-phase flow is obtained therein and the fraction of CO<sub>2</sub> in the water-rich phase is measured *in-situ* at different points along the capillary using Raman spectroscopy. A modified Henry's law is used to compute the equilibrium compositions of the water-rich phase at the desired pressure and temperature. A mixture density model is used to convert the fraction of CO<sub>2</sub> in the water-rich phase into a CO<sub>2</sub> concentration. The volumetric liquid mass transfer coefficient is computed at various axial locations along the capillary, from the contacting zone to the end of the capillary. Experimentally derived  $k_L a_L$  values range between  $2.10^{-3}$  and  $5.10^{-3} \text{ s}^{-1}$ .

### Keywords:

Mass transfer  
High pressure  
Microfluidics  
Two phase flow  
Raman spectroscopy

## 1. Introduction

There is an increasing number of supercritical fluid (SCF) applications in diverse industries such as food (Perrut and Perrut, 2019; Brunner, 2005; Ben-Nasr and Coenen, 1994; Lehotay, 1997; Kim et al., 1999; Lumia et al., 2007), cosmetics (Temelli, 2009) and biomedical (Masmoudi et al., 2011; Tsai and Wang, 2019). Moreover, new applications are in development in laboratories (Perrut and Perrut, 2018; Knez et al., 2018). This increasing number of

applications involves new fluid mixtures and therefore knowledge of the physical and thermodynamic mixture properties (e.g. density, viscosity, surface tension, diffusion coefficient, thermodynamic equilibrium compositions) at high pressure and temperature is essential for designing industrial-scale equipment. Many industrial applications involve two-phase systems where the mass transfer behaviour is a key parameter for the performance of the process. Tools that enable mass transfer coefficients to be measured and quantified are therefore required. Conventional techniques for the time-resolved measurement of phase composition in high-pressure vessels, which resist elevated pressure and temperature often require high investment costs, large quantities of product, specific safety precautions, as well as cumbersome experimental campaigns. These disadvantages can be largely overcome by the use of microfluidic systems. Indeed, the small

\* Corresponding author.

E-mail addresses: thomas.deleau@mines-albi.fr (T. Deleau), michael.fechter@tu-freiberg.de (M.H.H. Fechter), jean-jacques.letourneau@mines-albi.fr (J.-J. Letourneau), severine.camy@ensiacet.fr (S. Camy), joelle.aubin@ensiacet.fr (J. Aubin), andreas.braeuer@tu-freiberg.de (A.S. Braeuer), fabienne.espitalier@mines-albi.fr (F. Espitalier).



## Nomenclature

$A$	area of Raman peak, $m^2$
$a$	specific surface area, $m^{-1}$
$C$	concentration, $mol/m^3$
$f$	fugacity, $Pa$
$G$	optical magnification
$H$	Henry's law constant, $Pa$
$D$	diameter, $m$
$K$	overall mass transfer coefficient, $m/s$
$k$	local mass transfer coefficient, $m/s$
$L$	length, $m$
$N$	molar density flux, $mol/m^2/s$
$n$	number of moles, $mol$
$p$	pressure, $Pa$
$R$	ideal gas constant, $J/mol/K$
$Re$	Reynolds number $\frac{U D \rho}{\mu}$
$r$	molar ratio in the liquid phase
$S$	capillary cross section, $m^2$
$T$	temperature, $K$
$U$	velocity, $m/s$
$V$	volume, $m^3$
$\dot{V}$	volumetric flow rate, $m^3/s$
$v$	partial molar volume, $m^3/mol$
$w$	mass fraction
$x$	mole fraction
$z$	position in the capillary, $m$

## Greek symbols

$\rho$	density, $kg/m^3$
$\alpha$	constant, $m^2/mol$
$\beta, \gamma$	constant
$\vartheta$	temperature, $^{\circ}C$
$\mu$	viscosity, $Pa \cdot s$
$\sigma$	standard deviation

## Subscripts

$cap$	capillary
$CO_2$	carbon dioxide
$F$	fluid
$H_2O$	water
$L$	liquid
$m$	molar
$S$	liquid slug
$TP$	two-phase

## Superscripts

$a$	apparent
$\infty$	at infinite dilution
$*$	at equilibrium
$o$	pure
$\sim$	mean value

characteristic length scale of microfluidic devices, i.e. capillary diameter, enables experimental mass-transfer times to be drastically reduced. This is because the characteristic times for heat and mass transport are proportional to the square of characteristic length, which is ten orders of magnitude smaller in microfluidic systems than in standard pressurized vessels. This then results in characteristic experimental times – on the order of a few minutes – in microsystems compared with hours in conventional systems. Moreover, small quantities of products are used due to the reduced volume of microfluidic devices, thereby limiting operating costs and increasing safety when using toxic compounds. Risks related to high-pressure operation are also reduced. Microfluidic devices made with capillary tubes are also inexpensive compared with conventional high-pressure cells. Several types of microfluidic systems for high-pressure applications have been developed (Marre et al., 2010), including those using micro-capillary tubes (Macedo Portela da Silva et al., 2014) and polymers (Martin et al., 2016), both of which are fast and inexpensive to make.

Multiphase flow in microfluidic systems has largely been described in the literature, highlighting the enhancement of mass and heat transfer rates and the possibility for process intensification (Peters et al., 2017; Luther et al., 2013). Segmented flow, such as Taylor flow, is mainly studied due to its specific characteristics: quasi homogeneous mixing in both phases and a highly regular flow pattern with large interfacial area. Several experimental methods have been proposed to determine volumetric mass transfer coefficients in gas–liquid flow or liquid–liquid flow at atmospheric pressure and ambient temperature and are classified into two types: online methods and global methods. Online methods include optical techniques that enable the measurement of bubble or drop volumes where the bubble/drop shrinkage is linked to mass transfer rates (Tan et al., 2012; Lefortier et al., 2012; Yao et al., 2014; Zhang et al., 2018), as well as colorimetric (Dietrich et al., 2013) and laser induced fluorescence methods (Kuhn and Jensen, 2012) where concentration data in the liquid phase are

obtained. Global methods consist in determining mass transfer coefficients by measuring a solute concentration in both phases at the system inlet and outlet (Irandoost et al., 1992; Bercic and Pintar, 1997; Heiszwolf et al., 2001; Yue et al., 2009; Vandu et al., 2005; Ren et al., 2012) or by pressure drop measurements, which link the pressure drop to the mass transfer coefficient (Yue et al., 2007; Ganapathy et al., 2014; Yao et al., 2017). Global methods allow the determination of average mass transfer coefficients over the length of the microsystem, whereas online methods enable the measurement of values of the mass transfer coefficient at different positions along the microsystem. Data from these experimental studies at atmospheric pressure and ambient temperature have been used to validate mass transfer models and to develop dimensionless correlations (van Baten and Krishna, 2004; Liu and Wang, 2011; Eskin and Mostowfi, 2012). Most mass transfer models in the literature are based on the ‘unit-cell model’ for segmented flow and the theory of the unit-cell model will be given below.

The objective of this paper is to present a new method for the determination of local mass transfer coefficients in high-pressure two-phase flows in micro-channels using a Raman spectroscopy technique (Klima and Braeuer, 2019), which allows measurement of the molar fraction of  $CO_2$  dissolved in the water-rich phase in segmented flow at elevated pressure without sampling. The proposed new method does not rely on as many hypotheses as there are fixed in the unit cell model and thus features a more general applicability. The novelty of the presented method is the combination of these measurements with a thermodynamic model and a specific density mixture model, which are used to firstly compute the concentration of  $CO_2$  in the water-rich phase and to secondly compute local values of the mass transfer coefficient along the capillary tube, downstream from the contacting zone. The following sections describe the experimental setup and Raman spectroscopy technique, as well as the models and the calculation of dissolved fluid concentration and mass transfer coefficients. For the sake of

simplicity, the CO<sub>2</sub>-rich phase is called the “fluid” phase since this phase can be either liquid or gas depending on the operating conditions. The H<sub>2</sub>O-rich phase is called the liquid phase. Finally, a demonstration of the method to determine mass transfer coefficients in CO<sub>2</sub>-H<sub>2</sub>O flows at 8, 9 and 10 MPa and moderate temperature 303 K is provided.

## 2. Experimental setup

Fig. 1 shows the experimental setup used to measure the molar fraction of CO<sub>2</sub> dissolved in the water-rich phase. It is composed of a capillary tube (60 cm in length) with a T-junction inlet and high-pressure pumps.

The capillaries used in the setup were purchased from Polymicro Technologies. Two sizes of capillary tubes made of silica with a polyimide coating are used for a coaxial injection, where a smaller diameter tube, guiding the CO<sub>2</sub>, is inserted in a larger diameter tube, guiding the water, as shown in the inset of Fig. 1. The dimensions are listed in Table 1. These capillary tubes can withstand pressure and temperature up to 25 MPa at 700 K (Proctor et al., 1967). The connections between the silica capillaries and the other parts of the setup, which is composed of 1/16 in. stainless steel tubing, are made by assembling polymer sleeves, ferules, a stainless-steel T-junction and a simple union.

The fluids used are distilled H<sub>2</sub>O (Standard DIN 43530) and CO<sub>2</sub> < 99.5% in mole. Note that the H<sub>2</sub>O is re-boiled before it is fed to the pump in order to reduce the amount of potentially dissolved compounds. Three Teledyne ISCO pumps are used to feed the fluids through the system. A 260D ISCO pump (capacity of 266 mL, a flow range of 0.001–107 mL/min, a flow accuracy of 0.5% of the set point, a pressure accuracy of 0.5% of the full scale and a max pressure of 51.7 MPa) feeds the H<sub>2</sub>O. A 1000D ISCO pump (capacity of 1015 mL, a flow range of 0.001 to 408 mL/min, a flow accuracy of 0.5% of the set point, a pressure accuracy

of 0.5% of the full scale and a max pressure of 13.4 MPa) feeds CO<sub>2</sub>; this pump reservoir is cooled down to 278 K by circulating a temperature conditioning fluid from a conditioning system (F12-Julabo) through its double wall jacket. This measure ensures that the CO<sub>2</sub> is in the liquid state inside the syringe pump. Another 260D ISCO pump is placed at the end of the capillary setup in order to maintain the pressure in the system and to take up the mixture. The two feed pumps work in direct volumetric flow-rate-mode and the third pump at the outlet works in reverse volumetric flow rate mode. The flow rate of the reverse pump is calculated in order to maintain constant pressure in the system. All the pumps are equipped with a pressure gauge. 1/16 in. stainless steel pipes are used to connect the pumps to the silica capillary tubes. The lengths of the piping system is short enough to neglect pressure drop, which is not greater than 0.05 MPa over the whole system between the feed pumps and the up-taking pump. The capillary tube is placed in a copper temperature conditioning block (30 cm long), which is heated with four electrical resistance heating rods. The temperature is measured with 5 thermocouples (K-type), which are in contact with the silica capillary tube through dedicated holes. The block is temperature-controlled with a precision of ±0.5 K, which corresponds to the difference between the mean value and the extrema values obtained by the 5 thermocouples during the experiment. The coaxial contacting zone is placed 2.5 cm within the heating block to ensure the contact of H<sub>2</sub>O and CO<sub>2</sub> at the desired pressure and temperature. The assumption that 2.5 cm is long enough was verified with a computational fluid dynamic simulation. Ten holes are drilled in the temperature conditioning block at 1.25, 2.5, 3.75, 5, 6.25, 7.5, 8.75, 10, 12.5 and 17.5 cm from the contacting zone. The total investigable two-phase flow section is then 17.5 cm long. The brownish polymer coating of the silica capillary was removed at these spots in order to make the capillary accessible for Raman spectroscopy measurements.

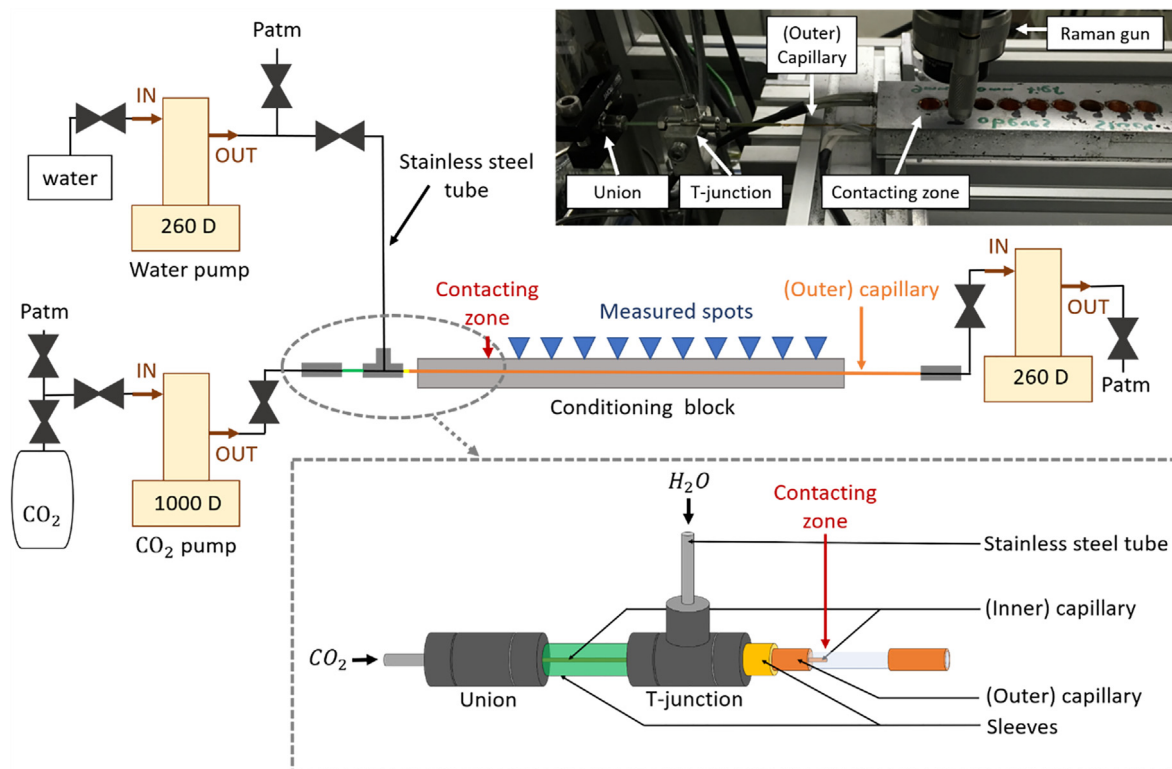


Fig. 1. Schematic diagram and picture of the experimental setup used to determine mass transfer coefficients in high-pressure two-phase flows.

**Table 1**Dimensions of the capillary tubes used ( $\mu\text{m}$ ). ID = inner diameter, OD = outer diameter.

	min ID	max ID	min OD	max OD
Inner capillary	74.9	75.3	151.3	151.5
Outer capillary	296.6	296.8	792.3	794.2

### 3. Unit-cell model

Fig. 2 depicts a unit cell for segmented fluid-liquid flow. The unit cell comprises one element of the dispersed fluid phase (called from now on “bubble” for the sake of simplicity), the liquid film surrounding it and one liquid slug. As can be seen in the lower part of Fig. 2, the unit cell model simplifies the segmented flow pattern based on a certain number of assumptions, which will be described below.

According to the double resistance diffusion model, which is given in Fig. 3, the molar flux of  $\text{CO}_2$  can be written considering the continuity of flux at the interface

$$\dot{N}_{\text{CO}_2} = k_L^m (x_{\text{CO}_2,i} - x_{\text{CO}_2}) = K_L^m (x_{\text{CO}_2}^* - x_{\text{CO}_2}) \quad (1)$$

where the lowercase  $k_L^m$  is the liquid local mass transfer coefficient ( $\text{mol} \cdot \text{m}^{-2} \cdot \text{s}^{-1}$ ) and the capital letter  $K_L^m$  the liquid global mass transfer coefficient ( $\text{mol} \cdot \text{m}^{-2} \cdot \text{s}^{-1}$ ).

The main hypotheses of the unit cell model are the following:

- There is no mass transfer between two consecutive unit cells, the overall amount of substance in one unit cell is constant. (H1)
- The fluid and liquid are in equilibrium at the interface, the two-film model is applied. (H2)
- Mass transfer occurs from the fluid phase to liquid phase only (Fig. 3(b)) (H3), which implies that  $k_L^m = K_L^m$  (because the mass transport resistance in the fluid phase is approximated zero) and then  $x_{\text{CO}_2}^* = x_{\text{CO}_2,i}$ . This assumption is only valid when the fluid compound is soluble in the liquid phase and the compound in the liquid phase is not or slightly soluble in the fluid phase. This is the case in this study where the amount of  $\text{H}_2\text{O}$  soluble in the  $\text{CO}_2$ -rich phase is negligible compared with the solubility of  $\text{CO}_2$  in the  $\text{H}_2\text{O}$ -rich phase. Consequently, only the migration of  $\text{CO}_2$  from the  $\text{CO}_2$ -rich phase to the  $\text{H}_2\text{O}$ -rich phase has an effect on the concentration of  $\text{CO}_2$  in the  $\text{H}_2\text{O}$ -rich phase.

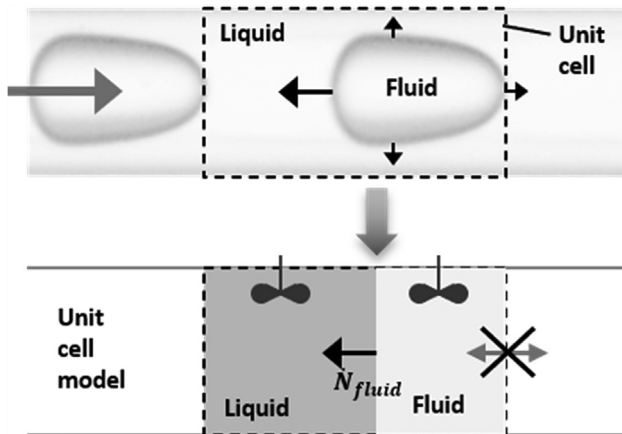


Fig. 2. Unit cell model of fluid-liquid segmented flow where  $\dot{N}_{\text{fluid}}$  is the molar density flux of fluid in  $\text{mol} \cdot \text{m}^{-2} \cdot \text{s}^{-1}$ .

- Fluid and liquid phases are perfectly mixed (H4), i.e. the phases are considered as homogeneous and described by average bulk fractions  $x$  and  $y$  are taken. Therefore, the greyish gradients in Fig. 3 can be represented by straight horizontal dashed black lines. There is no liquid film surrounding the bubble (film separating the bubble from the inner wall), the camera observation showed that the bubble occupies almost the entire cross section of the capillary tube and that the liquid film is negligible in the current conditions). Therefore both the bubbles and liquid slugs are assumed to have the same velocity (H5). This velocity is equal to the velocity of the two-phase flow at the inlet  $U_{TP} = \frac{\dot{V}_{\text{CO}_2} + \dot{V}_{\text{H}_2\text{O}}}{S} = \frac{dz}{dt}$  where  $\dot{V}_{\text{CO}_2}$  and  $\dot{V}_{\text{H}_2\text{O}}$  are the volumetric flow rates of the fluid and liquid phases at conditions prevailing inside the capillary,  $S$  is the inner cross section of the capillary tube and  $z$  is the length along the capillary from the contacting zone of  $\text{H}_2\text{O}$  and  $\text{CO}_2$ . This velocity allows the transformation from the temporal to the spatial scale.

Following these hypotheses, the evolution of the concentration of  $\text{CO}_2$  in the  $\text{H}_2\text{O}$ -rich phase as a function of the distance downstream of the contacting point  $z = 0$  can be derived:

$$\frac{dC_{\text{CO}_2}}{dz} = \frac{k_L a_L}{U_{TP}} (C_{\text{CO}_2}^* - C_{\text{CO}_2}(z)) \quad (2)$$

where  $k_L$  is the liquid local mass transfer coefficient ( $\text{m} \cdot \text{s}^{-1}$ ),  $a_L$  is the specific surface (equal to the ratio of the area available for mass transfer over the volume of the liquid slug),  $C_{\text{CO}_2}(z)$  is the concentration of  $\text{CO}_2$  in the liquid slug ( $\text{mol} \cdot \text{m}^{-3}$ ) at a certain distance  $z$  downstream of the contacting location and  $C_{\text{CO}_2}^*$  is the concentration of  $\text{CO}_2$  in the liquid slug in thermodynamic equilibrium with the  $\text{CO}_2$ -rich phase.

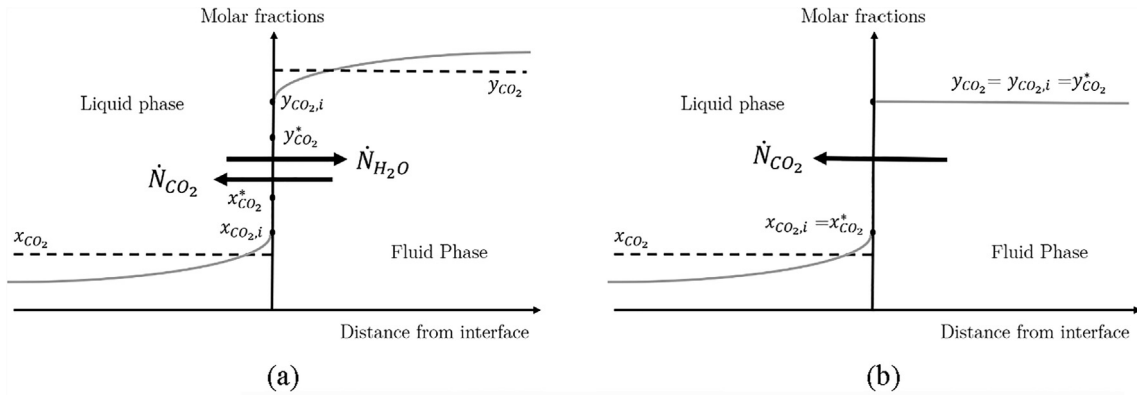
- A final assumption commonly used is that the volumetric mass transfer coefficient  $k_L a_L$  is constant along the length of the capillary tube (or microchannel) (H6). This assumption is used when the mass transfer coefficient is determined by global methods based on inlet and outlet concentration measurements.

If  $k_L a_L$  is constant, Eq. (2) can be integrated:

$$k_L a_L = \frac{U_{TP}}{z} \ln \left( \frac{C_{\text{CO}_2}^* - C_{\text{CO}_2}(z=0)}{C_{\text{CO}_2}^* - C_{\text{CO}_2}(z)} \right) \quad (3)$$

Eq. (3) is used for the determination of the volumetric mass transfer coefficients using global measurement methods where the concentration of the  $\text{CO}_2$  dissolved in the liquid phase is measured at the outlet of the system. At ambient pressure and for gases, it is also possible to correlate the bubble dimension with the mass transfer coefficient using the ideal gas law. This technique then allows to compute mass transfer coefficient to be calculated from images of bubble/drop sizes.

Most of the conventional methods at ambient conditions are based on the previous hypothesis. When operating at high-pressure, however, the conventional experimental methods, models and assumptions, which have been developed for ambient conditions, are no longer well suited. This is due to a number of



**Fig. 3.** Two-film model with mass transfer in both directions (a) and fluid to liquid only (b) where  $y_{CO_2}$  is the molar fraction of CO<sub>2</sub> in the bulk of CO<sub>2</sub>-rich phase,  $y_{CO_2,i}$  is the molar fraction of CO<sub>2</sub> at the interface in equilibrium with  $x_{CO_2,i}$  and  $y_{CO_2,i}^*$  is the molar fraction of CO<sub>2</sub> in the CO<sub>2</sub>-rich phase in equilibrium with the liquid phase with the molar fraction of CO<sub>2</sub> in the bulk,  $x_{CO_2}$ . Adapted from (Bird, 2002).

reasons. Under elevated pressure the behaviour of many gases cannot be described by the ideal gas law; this is particularly the case for CO<sub>2</sub>. As a result, a thermodynamic model is required in order to link the bubble volume and the number of moles in the fluid phase. Furthermore, the physical properties, such as density and viscosity, of the liquid phase and the fluid phase can change along the length of the microchannel because they are highly dependent on the amount of compounds dissolved in the liquid or the fluid phase. Taking samples of each of the phases at the outlet of the system is also difficult since the system is operating under high-pressure and also since undesired mass transfer between the fluid and liquid phases may occur in basic fluid-liquid separators. For these reasons, it is often very difficult to link a change in bubble volume to mass transfer rates in high-pressure systems and the application of existing correlations for mass transfer coefficients are not well adapted since they also are based on the simplifying hypothesis (H1-H6).

### 3.1. Operating conditions

The operating pressures studied are 8, 9 and 10 MPa at a temperature of 303 K. The ISCO pumps are set to deliver a constant volumetric flow rate. However, since there is a temperature change – and therefore a density change of the fluids – between the pumps and the capillary tube, the volumetric flow rates in the capillary tube must be recalculated to take into account the change in density. The volumetric flow rates in the capillary tube range from 50  $\mu\text{L}/\text{min}$  to 200  $\mu\text{L}/\text{min}$  for H<sub>2</sub>O ( $Re_L = \rho_L U_L D / \mu_L = 4\text{--}22$ ) and from 37  $\mu\text{L}/\text{min}$  to 108  $\mu\text{L}/\text{min}$  for CO<sub>2</sub> ( $Re_F = \rho_F U_F D / \mu_F = 11\text{--}96$ ). These flow rates lead to residence times of the order of one second. Note that all the volumetric flow rates in this paper are given at the temperature and pressure of the microfluidic system. These flow rate ranges have been chosen such that there is a CO<sub>2</sub>-H<sub>2</sub>O flow with a concentration gradient of CO<sub>2</sub> in the H<sub>2</sub>O-rich phase along the length of the capillary tube and that the H<sub>2</sub>O-rich phase is not saturated with the CO<sub>2</sub> at the final measurement point, i.e. at  $z = 175\text{ mm}$ . The CO<sub>2</sub> to H<sub>2</sub>O ratio at the inlet is then varied in order to obtain thermodynamic equilibrium (i.e. where the H<sub>2</sub>O-rich phase is saturated by CO<sub>2</sub>) at several measurement points. For each combination of pressure and temperature, the influence of the volumetric flow rate of one phase has been studied, whilst the volumetric flow rate of the other phase was kept constant.

## 4. Raman spectra measurements

The Raman spectroscopy setup given in Fig. 4 is that developed by Klima and Braeuer (2019). This setup has previously been used

to obtain thermodynamic equilibrium data of two-phase fuel-nitrogen systems under engine-like conditions (i.e. at high pressure and high temperature). In particular, the setup enables Raman spectra to be measured in one of the fluids of a fast moving segmented two-phase flow (the measurement is possible in both phases). A Cobolt Samba™ 532 nm laser (green, operated with 150 mW) is connected to a Raman gun (Braeuer-engineering) with an optical fiber and is focused in the capillary tube at the measurement point. The inelastic Raman signal (red shifted) is collected in back-scattering mode passing through a dichroic mirror and a long-pass filter where the elastic signal, which corresponds to the laser excitation wavelength is separated. The inelastic Raman signal is then focused into an optical fiber that goes to a fiber switch and then to a spectrometer (Ocean Optics QEpro), which receives the signal. In parallel, a photodiode is aligned with the laser beam under the capillary tube in order to receive the signal from the laser beam transmitted through the capillary. When a bubble is passing through the capillary at the measurement point, the laser bends and alters the intensity signal received by the photodiode. This intensity signal is recorded on an oscilloscope and corresponds to the periodicity of the segmented flow. A pulse generator (Model 9618, Quantum Composers) is used to create an electric signal that is positive during the bump or the crook (corresponding to the H<sub>2</sub>O-rich phase or the CO<sub>2</sub>-rich phase) of the photodiode intensity signal. This electric signal is sent to the fiber switch (PiezoSystem Jena), which has one optical fiber inlet (from the Raman probe) and two outlets (one to the spectrometer and one dead ended). Depending on the electrical signal sent to the fiber switch, the signal from the Raman probe will go to the dead ended outlet or to the spectrometer. This is what allows the signal in either the H<sub>2</sub>O-rich phase or the CO<sub>2</sub>-rich phase to be obtained.

At each measurement point, 16 spectra have been recorded, each with a signal integration time of 3 s. However, the signal arrives in small increments (signal from the H<sub>2</sub>O-rich phase only). Nevertheless, the signal integration time is long enough to obtain a clear spectrum. The mean of the 16 spectra is computed for each measurement point, the baseline is removed (using a spline method with the following node points [650, 930, 1150, 1200, 1300, 1420, 1470, 1530, 1800, 2000, 2300, 2500, 2600, 2700, 3850, 4000  $\text{cm}^{-1}$ ]) and the spectra are normalized by the H<sub>2</sub>O band in order to visualize and compare the amount of CO<sub>2</sub> in the H<sub>2</sub>O-rich phase at each point. An example of the spectra obtained at the different measurement points is shown in Fig. 5. The peak between 2700  $\text{cm}^{-1}$  and 3900  $\text{cm}^{-1}$  corresponds to the H<sub>2</sub>O and the Fermi dyad of CO<sub>2</sub> is present between 1200  $\text{cm}^{-1}$  and 1450  $\text{cm}^{-1}$ . As the distance of the measurement point from the contacting point of CO<sub>2</sub> and H<sub>2</sub>O increases, it



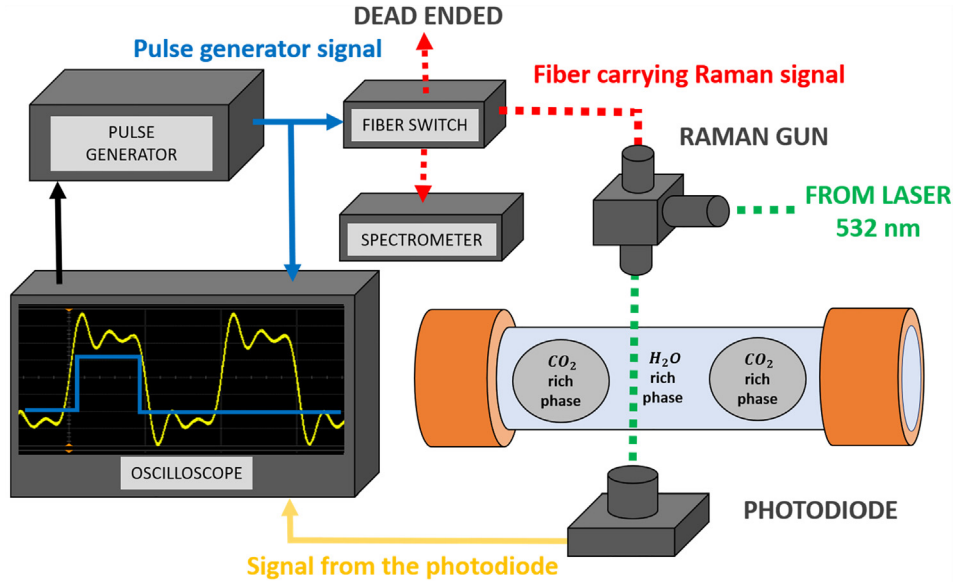


Fig. 4. Schematic diagram of the Raman spectroscopy setup for obtaining spectra in a single phase of a segmented two-phase flow.

can be seen that the signal intensity of the CO<sub>2</sub> Fermi dyad increases, which corresponds to a greater amount of CO<sub>2</sub> dissolved in the H<sub>2</sub>O-rich phase.

## 5. Determination of mass transfer

The novelty of this work is to determine local volumetric mass transfer coefficients  $k_L a_L$  in continuous high-pressure two-phase flows where the physical properties of the fluids vary. In order to do this, the Raman spectroscopy technique described in Section 4 is used to determine the CO<sub>2</sub> to H<sub>2</sub>O molar fraction ratio  $\frac{x_{CO_2}}{x_{H_2O}}$  at each measurement point. This ratio is then coupled with the density of the liquid mixture  $\rho_L$  to compute the concentration of CO<sub>2</sub> dissolved in the H<sub>2</sub>O-rich phase  $C_{CO_2}$  at each point. Following this, the concentration data is used with the unit cell model to calculate the volumetric mass transfer coefficient  $k_L a_L$  at each position in the capillary tube.

### 5.1. Determination of $C_{CO_2}$

The dissolution of CO<sub>2</sub> into a H<sub>2</sub>O-rich phase leads to the presence of H<sub>2</sub>CO<sub>3</sub>, HCO<sub>3</sub><sup>-</sup>, CO<sub>3</sub><sup>2-</sup> and CO<sub>2</sub> in aqueous form in the H<sub>2</sub>O-rich phase. Nevertheless, in the study of Anderson (1977), it has been shown that in the H<sub>2</sub>O-rich phase, the amount of species other than CO<sub>2</sub> is negligible at 283 K and 4.5 MPa and decreases further with an increase in pressure. Therefore, in this work, the total amount of CO<sub>2</sub> dissolved in the H<sub>2</sub>O-rich phase is considered to be present as dissolved molecular CO<sub>2</sub>. The concentration of CO<sub>2</sub> in the H<sub>2</sub>O-rich phase  $C_{CO_2}$  is determined by Eq. (4).

$$C_{CO_2} = \frac{\rho_L(T, P, x_{CO_2})}{M_{CO_2} + \frac{x_{H_2O}}{x_{CO_2}} M_{H_2O}} \quad (4)$$

where  $\rho_L(T, P, x_{CO_2})$  is the liquid density of the H<sub>2</sub>O-rich phase,  $x_{CO_2}$  is the molar fraction of CO<sub>2</sub> and  $M_{CO_2}$  and  $M_{H_2O}$  are the molar mass of CO<sub>2</sub> and H<sub>2</sub>O, respectively. The ratio of molar fraction of CO<sub>2</sub> to H<sub>2</sub>O is obtained from the Raman spectra and is proportional to

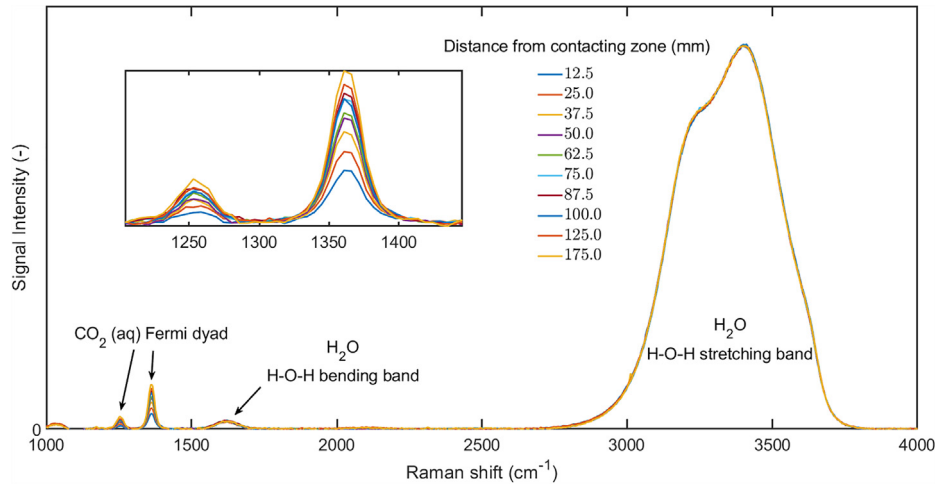


Fig. 5. Raman spectra of the H<sub>2</sub>O-rich phase normalized to the intensity of the peak of the H-O-H stretching (H<sub>2</sub>O).  $p = 10$  MPa,  $T = 303$  K,  $\dot{V}_{H_2O} = 110 \mu L \cdot min^{-1}$ ,  $\dot{V}_{CO_2} = 61.5 \mu L \cdot min^{-1}$ .

the peak area ratio  $\frac{A_{CO_2}}{A_{H_2O}}$  at each measurement point (where  $A_{H_2O}$  and  $A_{CO_2}$  are the areas from the Raman spectra taken between 2700  $cm^{-1}$  to 3900  $cm^{-1}$  and 1200  $cm^{-1}$  to 1450  $cm^{-1}$  respectively):

$$\frac{A_{CO_2}}{A_{H_2O}} = \alpha \frac{x_{CO_2}}{x_{H_2O}} \quad (5)$$

The proportionality constant  $\alpha$  is determined by calculating the  $\frac{x_{CO_2}}{x_{H_2O}}$  ratio at equilibrium with a thermodynamic model for the solubility of  $CO_2$  in  $H_2O$ -rich phase (as described in Section 5.1.1) for experiments where thermodynamic equilibrium is achieved.  $\alpha$  is then used to determine  $\frac{x_{CO_2}}{x_{H_2O}}$  from  $\frac{A_{CO_2}}{A_{H_2O}}$  at each measurement point for the other experiments where thermodynamic equilibrium has not been achieved yet. The value  $\alpha$  was obtained with 43 equilibrium points. The final value was 0.239 with a standard deviation of 0.007 (2.9%). The deviation obtained here can be drastically reduced with binary systems where the dispersed phase is more soluble in the continuous phase (thereby providing higher resolution of the calibration curve). In the case of  $CO_2$  and  $H_2O$ , the maximum amount of  $CO_2$  in the  $H_2O$ -rich phase is 3% in mass under the conditions presented in this paper. This value is low compared with other systems studied in the literature, such as  $CO_2$  and ethanol.

#### 5.1.1. Determination of the equilibrium fraction of $CO_2$ in the $H_2O$ -rich phase, $x_{CO_2}^*$

In this paper, the equilibrium fraction of  $CO_2$  in the  $H_2O$ -rich phase,  $x_{CO_2}^*$ , is calculated using the work of Enick and Klara (1990) with the exception that the fugacity of  $CO_2$ ,  $f_{CO_2}$ , is calculated from the Span and Wagner (1996) equation of state. In the work of Enick and Klara (1990), a Henry's law analysis is used with a Poynting correction, as given in Eq. (6).

$$\frac{f_{CO_2}}{x_{CO_2}^*} = H_{CO_2}^* \exp\left(\frac{v_{CO_2}^\infty P}{RT}\right) \quad (6)$$

Enick and Klara (1990) compiled 110 solubility data points for a range of temperature from 298 K to 523 K and pressure from 3.40 MPa to 72.41 MPa, and regressed both the reference Henry's law constant,  $H_{CO_2}^*$ , and the partial molar volume of  $CO_2$  at infinite

dilution,  $v_{CO_2}^\infty$ , with Eq. (6) in order to fit with the experimental solubility data. Empirical correlations for each of the parameters are given below in Eqs. (7) and (8).

$$H_{CO_2}^* = -5032.99 + 30.74113T - 0.052667T^2 + 2.630218 \times 10^{-5}T^3 \quad (7)$$

$$v_{CO_2}^\infty = 1799.36 - 17.8218T + 0.0659297T^2 - 1.05786 \times 10^{-4}T^3 + 6.200275 \times 10^{-8}T^4 \quad (8)$$

where  $T$  is the temperature in Kelvin.

#### 5.1.2. Determination of the liquid mixture density of the $H_2O$ -rich phase, $\rho_L$

Mixture densities are computed following the methodology of Bachu and Adams (2003). In the case of non-ideal solutions such as  $H_2O$  and  $CO_2$  mixtures, it is assumed that the volume of the liquid mixture is the sum of two contributions: the volume occupied by the solvent in its pure state (i.e. pure  $H_2O$ ) and the apparent volume occupied by the solute (i.e.  $CO_2$ ).

The total volume of the solution is then written using the partial molar volume of each component as shown in Equation (9).

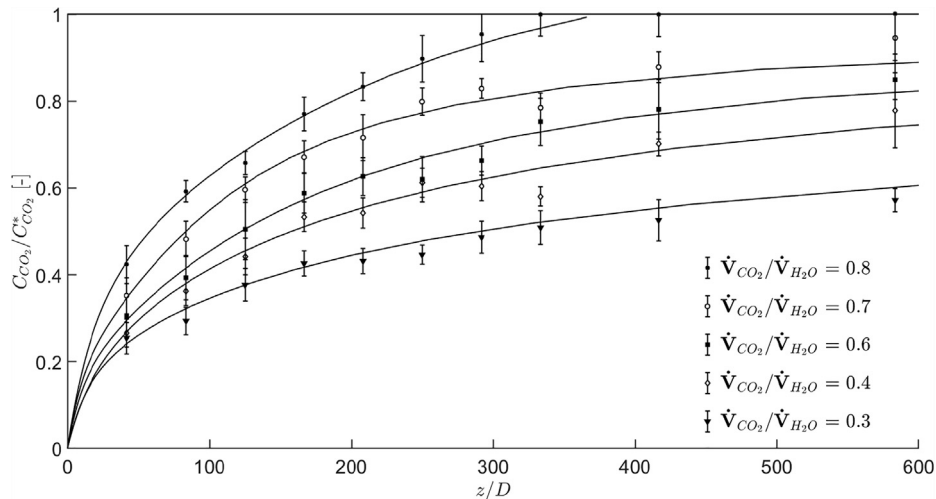
$$V_L = n_{H_2O} \left( \frac{\partial V}{\partial n_{H_2O}} \right)_{T,P,n_{CO_2}} + n_{CO_2} \left( \frac{\partial V}{\partial n_{CO_2}} \right)_{T,P,n_{H_2O}} = n_{H_2O} v_{H_2O} + n_{CO_2} v_{CO_2} \quad (9)$$

The apparent molar volume of  $CO_2$ ,  $v_{CO_2}^a$ , defined in Equation (10) is the difference between the total volume and the molar volume of pure  $H_2O$ ,  $v_{H_2O}^0$ , multiplied by the number of moles of  $H_2O$  and divided by the number of moles of  $CO_2$ . The apparent molar volume is different to the partial molar volume,  $v_{H_2O}$ , as shown in Equation (11).

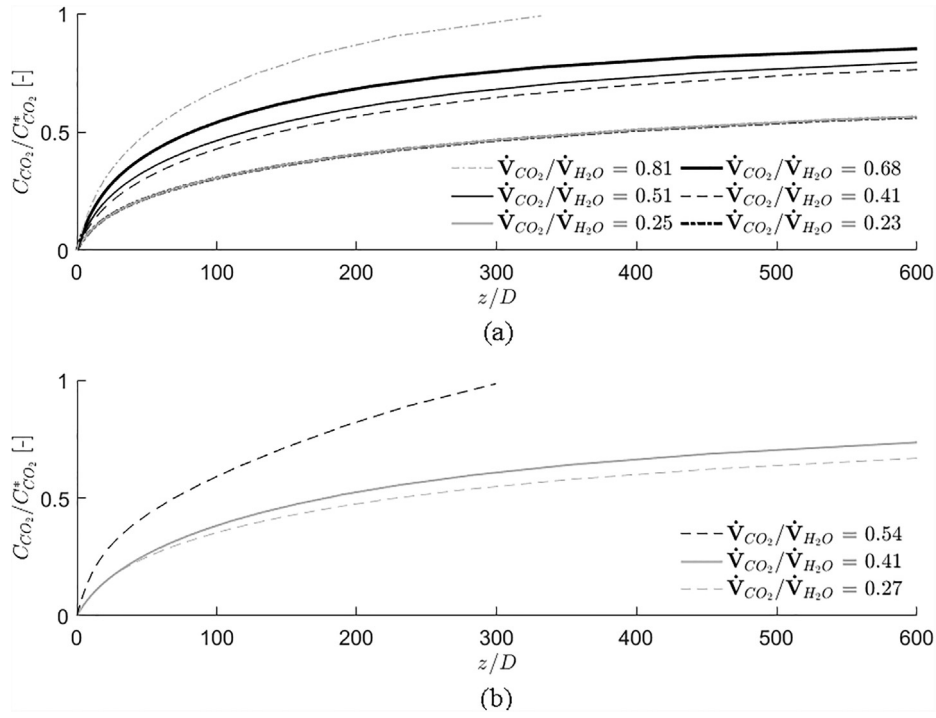
$$v_{CO_2}^a = \frac{V_L - n_{H_2O} v_{H_2O}^0}{n_{CO_2}} \quad (10)$$

$$V_L = n_{CO_2} v_{CO_2} + n_{H_2O} v_{H_2O} = n_{CO_2} v_{CO_2}^a + n_{H_2O} v_{H_2O}^0 \quad (11)$$

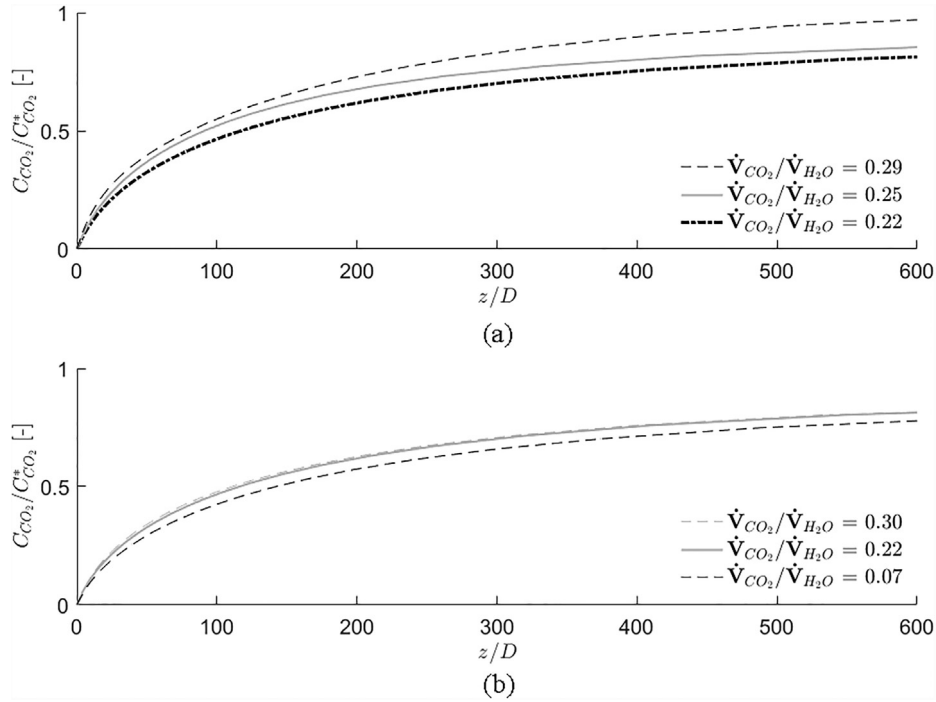
For  $CO_2$  and  $H_2O$  mixtures, numerous correlations for  $v_{CO_2}^a$  can be found in the literature due to their use in geology (Andersen et al., 1992; Enick and Klara, 1990). In this work, the correlation



**Fig. 6.** Fitted normalized  $CO_2$  concentration profiles and experimental points along the length of the capillary tube at 10 MPa, 303 K and  $\dot{V}_{H_2O} = 110 \mu L \cdot min^{-1}$ . The average deviation between the fitted concentration profiles and the experimental points are respectively 0.7%, 0.5%, 0.3%, 0.4% and 0.5%.



**Fig. 7.** Fitted normalized CO<sub>2</sub> concentration profiles at 8 MPa 303 K. (a)  $\dot{V}_{CO_2} = 40.5 \mu\text{L}\cdot\text{min}^{-1}$  (b)  $\dot{V}_{H_2O} = 200 \mu\text{L}\cdot\text{min}^{-1}$ .



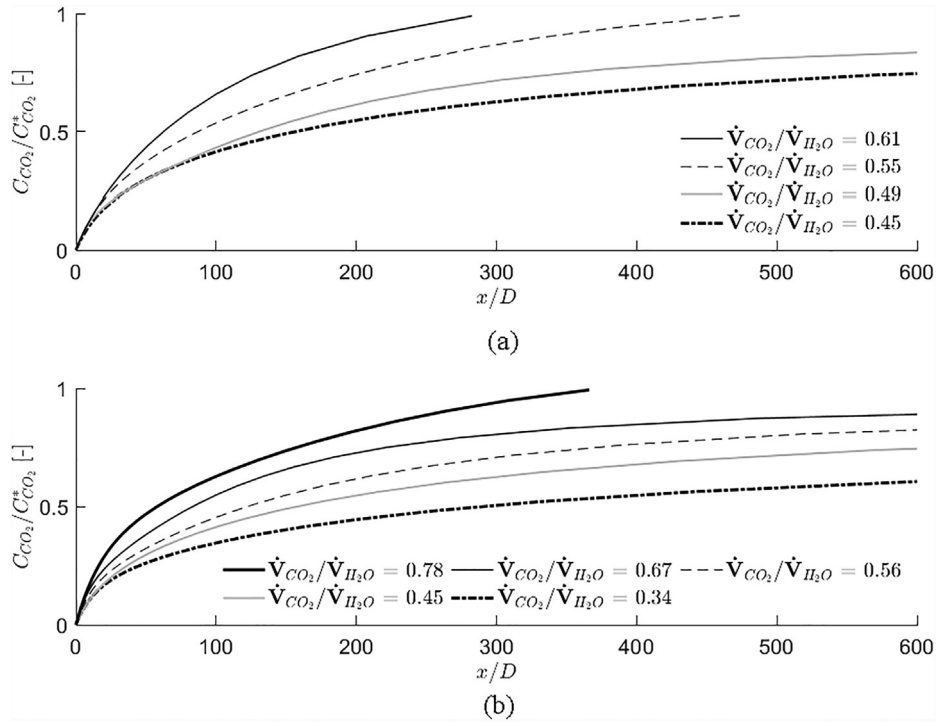
**Fig. 8.** Fitted normalized CO<sub>2</sub> concentration profiles at 9 MPa 303 K. (a)  $\dot{V}_{CO_2} = 38.2 \mu\text{L}\cdot\text{min}^{-1}$  (b)  $\dot{V}_{H_2O} = 170 \mu\text{L}\cdot\text{min}^{-1}$ .

from [Garcia \(2001\)](#) given by Eq. (12) is employed. It is based on 54 data points obtained for temperature and pressure ranges of 278 K to 573 K and 0.2 MPa to 35 MPa, respectively.

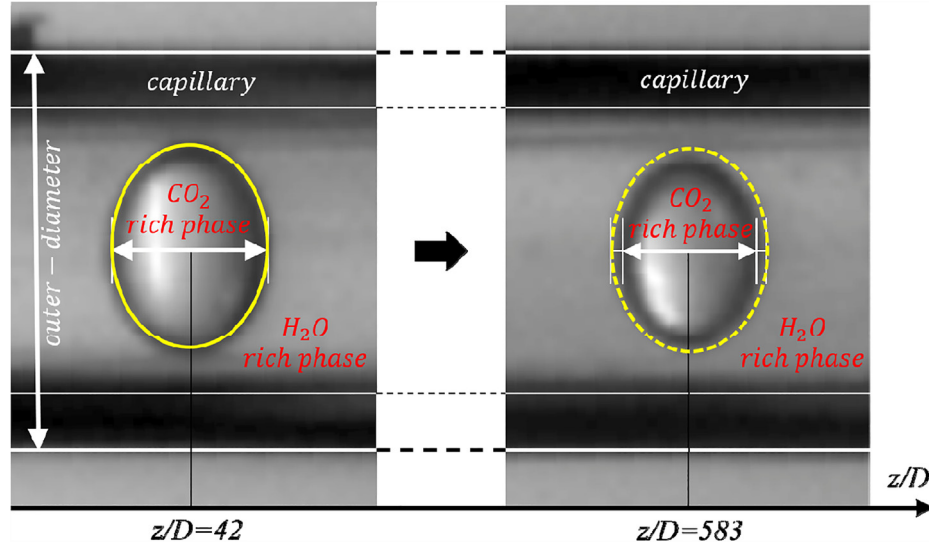
$$v_{CO_2}^l = 37.51 - 9.585 \times 10^{-2} \vartheta + 8.740 \times 10^{-4} \vartheta^2 - 5.044 \times 10^{-7} \vartheta^3 \quad (12)$$

where  $\vartheta$  is temperature in °C and  $v_{CO_2}^l$  in cm<sup>3</sup>/mol. [Garcia \(2001\)](#) demonstrated that the influence of pressure is negligible when the temperature is lower than 573 K, which is the case in the current work.

Eq. (13) gives the liquid density of the H<sub>2</sub>O and CO<sub>2</sub> mixture,  $\rho_L(T, P, x_{CO_2})$  derived from Eq. (11):



**Fig. 9.** Fitted normalized CO<sub>2</sub> concentration profiles at 10 MPa 303 K. (a)  $\dot{V}_{CO_2} = 49.2 \mu\text{L}\cdot\text{min}^{-1}$  (b)  $\dot{V}_{H_2O} = 110 \mu\text{L}\cdot\text{min}^{-1}$ .



**Fig. 10.** Image of bubbles at  $z/D = 42$  and  $z/D = 583$  at 10 MPa, 303 K,  $\dot{V}_{CO_2} = 73.7 \mu\text{L}\cdot\text{min}^{-1}$  and  $\dot{V}_{H_2O} = 110 \mu\text{L}\cdot\text{min}^{-1}$ . Note that the spherical bubble is deformed in the vertical direction because of the light refraction between the glass of the cylindrical capillary and the air. However, there is no deformation of the bubble diameter in line with the tube axis and of the outer diameter of the capillary. The bubble shrinkage is presented in yellow.

$$\rho_L(T, P, x_{CO_2}) = \frac{\rho_{H_2O}^0(T, P)}{1 - w_{CO_2} \left( 1 - \frac{\nu_{CO_2}^a(T) \rho_{H_2O}^0(T, P)}{M_{CO_2}} \right)} \quad (13)$$

where  $w_{CO_2}$  is the mass fraction of CO<sub>2</sub> and  $\rho_{H_2O}^0(T, P)$  is the density of pure H<sub>2</sub>O which is determined using the correlation of [Batze and Wang \(1992\)](#) given by Eq. (14)

$$\rho_{H_2O}^0(T, P) = 1 + 10^{-6} \times (-80 T - 3.3 \vartheta^2 + 0.00175 \vartheta^3 + 489 p - 2 \vartheta p + 0.016 \vartheta^2 p - 1.3 \times 10^{-5} \vartheta^3 p - 0.333 p^2 - 0.002 \vartheta p^2) \quad (14)$$

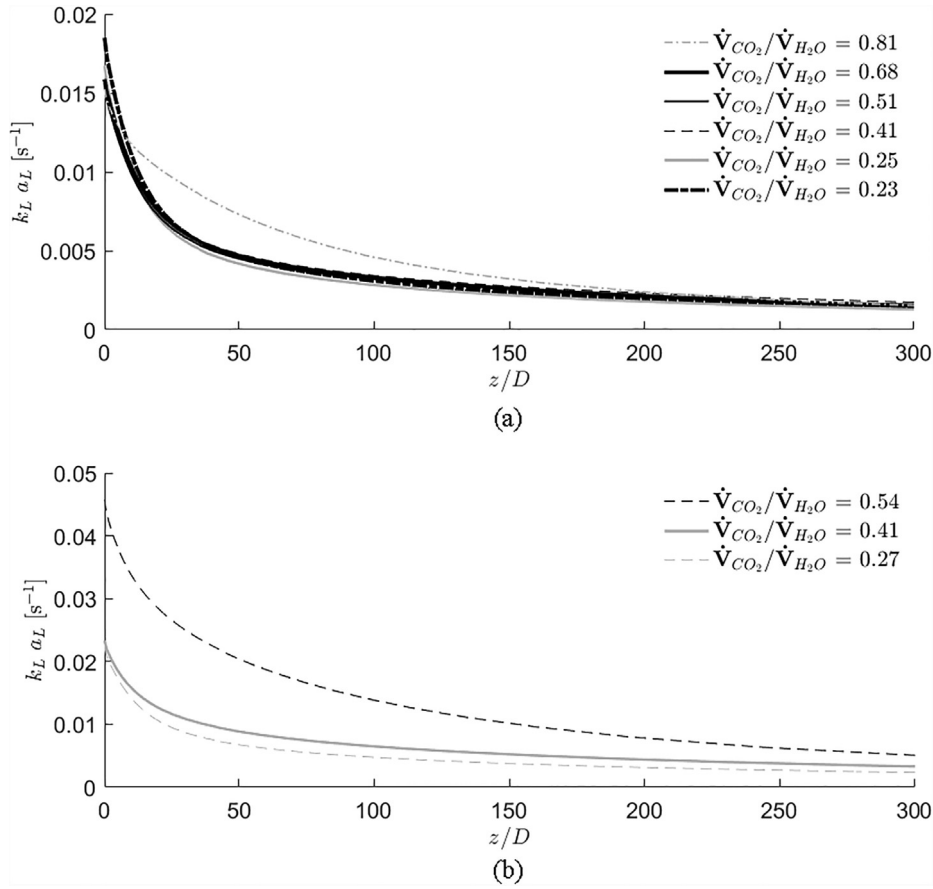
where  $p$  is pressure in MPa,  $\vartheta$  is temperature in °C and  $\rho_{H_2O}^0$  in g/cm<sup>3</sup>.

## 5.2. Determination of the volumetric mass transfer coefficient $k_L a_L$

From Eq. (2), the volumetric mass transfer coefficient can be expressed as Eq. (15).

$$k_L a_L = \frac{U_{TP}}{(C_{CO_2}^* - C_{CO_2})} \frac{dC_{CO_2}}{dz} \quad (15)$$





**Fig. 11.** Volumetric mass transfer coefficient profiles at 8 MPa and 303 K. (a)  $\dot{V}_{\text{CO}_2} = 40.5 \mu\text{L}\cdot\text{min}^{-1}$ , (b)  $\dot{V}_{\text{H}_2\text{O}} = 200 \mu\text{L}\cdot\text{min}^{-1}$ .

This equation is based on the unit cell model assuming (H1) to (H5) only. It will be shown that the hypothesis (H6), i.e. assuming that  $k_L a_L$  is constant along the length of the capillary tube, results in significant error on the  $k_L a_L$  values in the case of this study. The first derivative of the  $\text{CO}_2$  concentration in the  $\text{H}_2\text{O}$ -rich phase,  $\frac{dC_{\text{CO}_2}}{dz}$ , is obtained by filtering the experimental concentration data using fast Fourier transform (FFT) as shown in Appendix B.

## 6. Application of the experimental method to $\text{CO}_2$ - $\text{H}_2\text{O}$ mass transfer under high-pressure conditions

In order to demonstrate the use of the experimental method presented here, this section presents examples of Raman spectroscopy measurements and data analysis to obtain the volumetric mass transfer coefficient for a segmented flow composed of  $\text{CO}_2$ -rich and  $\text{H}_2\text{O}$ -rich phases in a capillary tube at pressures of 8 MPa, 9 MPa and 10 MPa, as well as a range of flow rates.

Fig. 6 shows an example of the experimental concentration data (normalised by the value at saturation) and the corresponding profiles obtained by FFT filtering as a function of the axial distance from the contacting zone in the capillary tube for 10 MPa, 303 K and a constant  $\text{H}_2\text{O}$  flowrate ( $110 \mu\text{L}\cdot\text{min}^{-1}$ ). The error bars correspond to  $\pm 3$  standard deviations (see Appendix A for uncertainty calculations). The average deviation between the fitted concentrations and the experimental values of all the conditions studied in this paper do not exceed 1%. This figure clearly shows that the FFT filtering method correctly represents the  $\text{CO}_2$  concentration in the  $\text{H}_2\text{O}$ -rich phase at each measurement point in the capillary tube. Considering this, in subsequent Figs. 7–9, only the fitted curves are shown in order to facilitate reading.

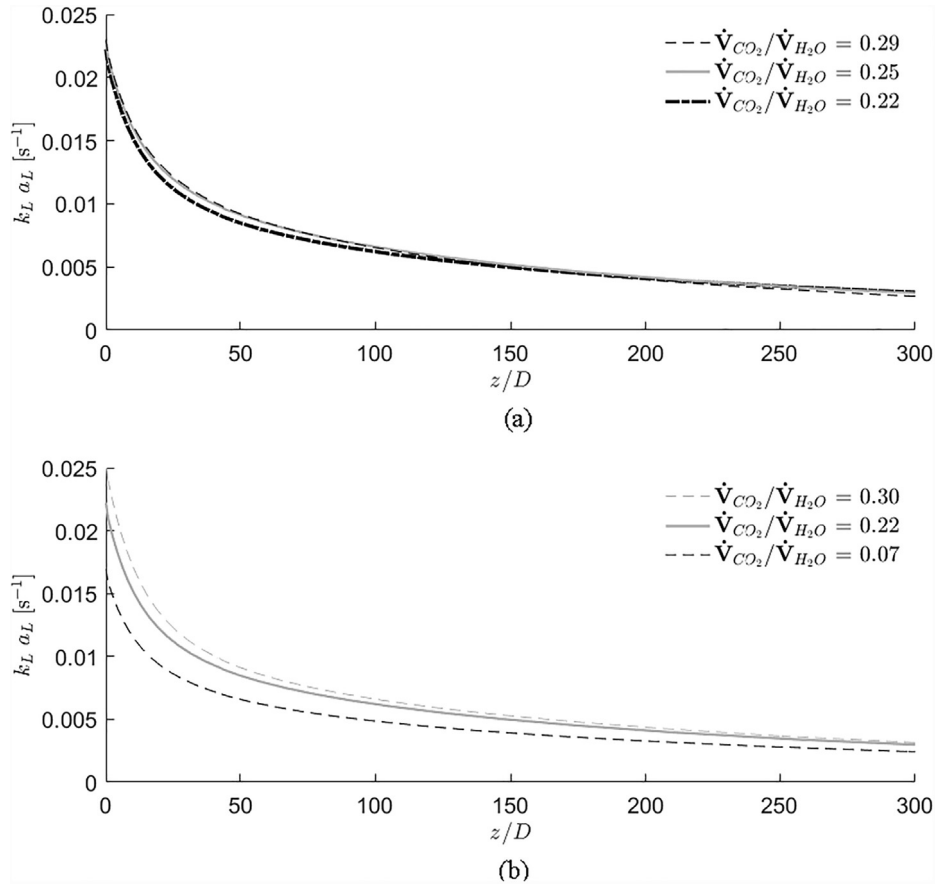
### 6.1. Concentration profiles

Figs. 7–9 show the normalized fitted  $\text{CO}_2$  concentration profiles versus the normalized axial position in the capillary ( $z/D$ ) at 303 K and 8 MPa, 9 MPa and 10 MPa, respectively. At each pressure, either the volumetric flow rate of  $\text{CO}_2$  or of  $\text{H}_2\text{O}$  was kept constant, whilst the flow rate of the other phase was varied. The flow rate ratio therefore provides the basis for comparison. Indeed, the volumetric flowrate ratio is a key parameter for characterising hydrodynamics in segmented flows in small channels. Droplet and bubble growth mechanisms and lengths in microchannels have been widely studied (see for example Garstecki et al. (2006), van Steijn et al. (2007), Abadie et al. (2012)). In such studies, it has been shown that bubble length,  $L_B$ , and liquid slug length,  $L_S$ , increase linearly with  $\frac{\dot{V}_{\text{CO}_2}}{\dot{V}_{\text{H}_2\text{O}}}$  and  $\frac{\dot{V}_{\text{H}_2\text{O}}}{\dot{V}_{\text{CO}_2}}$ , respectively.

For all pressures, it is observed that when  $\frac{\dot{V}_{\text{CO}_2}}{\dot{V}_{\text{H}_2\text{O}}}$  decreases, thermodynamic equilibrium is reached further along the capillary tube away from the contacting point. When  $\frac{\dot{V}_{\text{CO}_2}}{\dot{V}_{\text{H}_2\text{O}}}$  decreases, the bubble length  $L_B$  decreases and the slug length  $L_S$  increases. As a consequence, the interfacial area for mass transfer decreases. In addition, there is a larger amount of  $\text{H}_2\text{O}$  in a liquid slug to be saturated whereas a lesser amount of  $\text{CO}_2$  is available in the  $\text{CO}_2$ -rich bubble. Both of these contributions result in the fact that thermodynamic equilibrium is reached further along the capillary from the contacting zone.

### 6.2. Volumetric mass transfer coefficient profiles

Figs. 11–13 show the volumetric liquid mass transfer coefficient  $k_L a_L$ , determined with Eq. (15), along the length of the capillary



**Fig. 12.** Volumetric mass transfer coefficient profiles at 9 MPa and 303 K. (a)  $\dot{V}_{CO_2} = 38.2 \mu\text{L}\cdot\text{min}^{-1}$ , (b)  $\dot{V}_{H_2O} = 170 \mu\text{L}\cdot\text{min}^{-1}$ .

tube. Firstly, it is seen that  $k_L a_L$  is not constant along the capillary tube. This observation proves that hypothesis (H6) (i.e.  $k_L a_L$  is constant along the tube, and either a decrease in  $a_L$  is compensated by an increase in  $k_L$ , or  $k_L$  and  $a_L$  are both assumed constant, which is often assumed in the unit cell model), is not valid. Indeed, when using hypothesis (H6), the value of  $k_L a_L$  at  $z/D = 100$  gives an average error of 35% compared with the value obtained without (H6).  $k_L a_L$  decreases along the capillary tube between  $z/D = 0$  and  $z/D = 600$  by approximately a factor of 8. If this decrease in  $k_L a_L$  is due to a decrease in  $a_L$  only, then this corresponds to a decrease in the bubble diameter of a factor  $\sqrt{8} \approx 2.83$  (considering a spherical bubble and a water-rich slug with constant volume). However, such a significant decrease in bubble size between the contacting zone and the outlet of the capillary tube was not observed in the experiments as it can be seen from Fig. 10. Hence, this implies that  $k_L$  must also be decreasing along the length of the capillary tube.

It can also be seen in Figs. 11–13 that the rate of mass transfer is significantly higher closer to the contacting zone where  $CO_2$ -rich bubbles are formed. This is in agreement with the concentration profiles in Figs. 7–9 where it can be seen that more than 20% of the thermodynamic equilibrium is reached during the bubble formation stage ( $z/D < 20$ ). The enhanced mass transfer at the bubble formation stage may be described by a difference in hydrodynamics between the bubble formation stage, which is a transient process, and the more or less stable segmented flow in the rest of the capillary tube. Indeed, in the transient bubble formation process, a bubble will grow and then be pinched-off, which will increase the liquid flow intermittently in the vicinity of the interface and consequently promote mass transfer.

A comparison of the experiments also shows that for constant  $\dot{V}_{CO_2}$  or  $\dot{V}_{H_2O}$ , increasing  $\frac{\dot{V}_{CO_2}}{\dot{V}_{H_2O}}$  leads to an increase of  $k_L a_L$ . This may

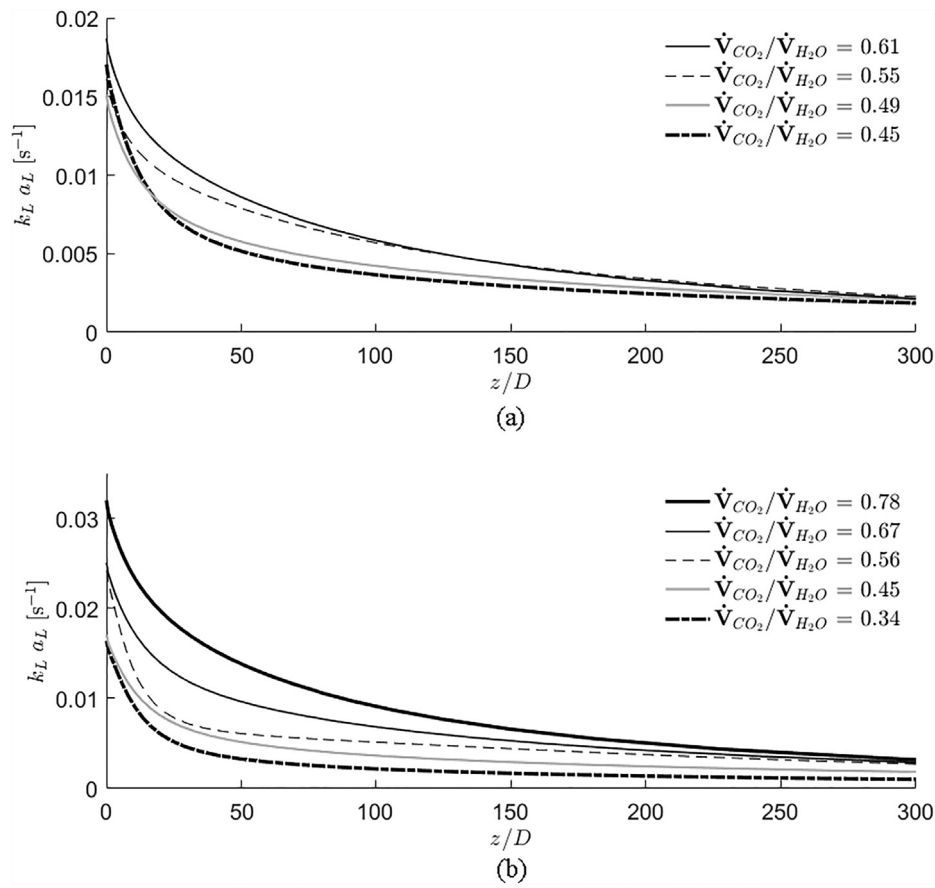
be explained by the fact that an increase in  $\frac{\dot{V}_{CO_2}}{\dot{V}_{H_2O}}$  results in an increase of the bubble length,  $L_B$ , (and consequently the bubble volume,  $V_B$ ) and a decrease of the liquid slug length,  $L_S$ . A decrease in slug length has previously been shown to increase the liquid slug recirculation (Leung et al., 2010, Zaloha et al., 2012, Abadie, 2013). It is expected that this would result in an enhanced renewal of the fluid-liquid interface and in turn increase the mass transfer coefficient  $k_L$ . Moreover, Abadie (2013) and Martin et al. (2018) showed that for both ambient pressure and high-pressure flows, the ratio between  $L_B$  and the total length of a unit cell,  $L_B + L_S$ , depends on  $\frac{U_F}{U_L}$ , and therefore  $\frac{\dot{V}_{CO_2}}{\dot{V}_{H_2O}}$  as described by Eq. (16):

$$\frac{L_B}{L_B + L_S} = \frac{\frac{U_F}{U_L}}{\beta + \frac{U_F}{U_L}} \quad (16)$$

where  $\beta$  is a constant.

Eq. (16) shows that when  $\frac{\dot{V}_{CO_2}}{\dot{V}_{H_2O}}$  increases,  $\frac{L_B}{L_B + L_S}$  also increases, which corresponds to an increase of  $a_L$ . Hence, an increase in  $\frac{\dot{V}_{CO_2}}{\dot{V}_{H_2O}}$  causes both  $k_L$  and  $a_L$  to increase, which is in agreement with the experimental observations that  $k_L a_L$  is higher when  $\frac{\dot{V}_{CO_2}}{\dot{V}_{H_2O}}$  is higher.

Finally, it can be pointed out that values of the volumetric mass transfer coefficients measured here are between  $2 \cdot 10^{-3} \text{ s}^{-1}$  and  $5 \cdot 10^{-2} \text{ s}^{-1}$ , which are the same order of magnitude as values obtained in other microfluidic systems of this diameter and in the same range of Reynolds number (Susanti et al., 2016).



**Fig. 13.** Volumetric mass transfer coefficient profiles at 10 MPa and 303 K. (a)  $\dot{V}_{CO_2} = 49.2 \mu\text{L}\cdot\text{min}^{-1}$ , (b)  $\dot{V}_{H_2O} = 110 \mu\text{L}\cdot\text{min}^{-1}$ .

## 7. Conclusion

A new experimental method to determine mass transfer coefficients in two-phase flow at elevated pressure and moderate temperature in a micro-capillary tube has been presented. It is based on the measurement of the molar ratio of different species in one of the phases using Raman spectroscopy. The species concentration, mixture density and the mass transfer coefficient are then determined using appropriate thermodynamic models and the unit cell model for mass transfer in segmented two-phase flow. The novelty of this method is that it allows the measurement of local values of the mass transfer coefficient at different positions along capillary tube and it takes into account variations in fluid properties due to high-pressure conditions. The results obtained with this technique can serve as a design tool for new types of microreactors where mass transfer is a key parameter and also as a fundamental tool in order to investigate mass transfer behaviour of different binaries in high-pressure systems.

The method has been applied to a  $CO_2$ - $H_2O$  flow at 303 K and pressures of 8 MPa, 9 MPa and 10 MPa. The  $k_L a_L$  values obtained are in the range  $10^{-3}$ – $10^{-2} \text{ s}^{-1}$ , which agree with the values in the literature and illustrate the reliability of the technique. It has also been shown that  $k_L a_L$  is not constant and that it decreases along the length of the capillary tube; this decrease is expected to be due to both a decrease in  $k_L$  and  $a_L$ . This result clearly shows that the assumption that  $k_L a_L$  is constant along the tube length, which is commonly used in the unit cell model, is in fact incorrect (35% of error in average).

Future studies will focus on the effects of pressure and the temperature on mass transfer with an objective of developing dimen-

sionless correlations of the volumetric mass transfer coefficient. Indeed, this technique will be of significant interest for studying mass transfer in other binary systems such as ethanol and  $CO_2$  by measuring in both phases. In ethanol and  $CO_2$  systems, mass transfer occurs from the liquid phase to the fluid phase, also from the fluid phase to the liquid phase and the density of both phases change during the mass transfer. Further developments of this technique will include the combination of the Raman spectroscopy measurements with high speed imaging of the flow. This will enable the volume of the bubbles and their velocities at each position in the capillary tube to be measured. The former will give the access to the specific surface  $a_L$  of the dispersed phase and allow the individual contributions of  $k_L$  and  $a_L$  in the volumetric mass transfer coefficient  $k_L a_L$  to be assessed.

## CRedit authorship contribution statement

**T. Deleau:** Conceptualization, Data curation, Formal analysis, Investigation, Methodology, Writing - original draft. **M.H.H. Fechter:** Data curation, Investigation. **J.-J. Letourneau:** Conceptualization, Formal analysis, Supervision, Writing - review & editing, Funding acquisition. **S. Camy:** Conceptualization, Supervision, Writing - review & editing, Funding acquisition. **J. Aubin:** Conceptualization, Supervision, Writing - review & editing, Funding acquisition. **A.S. Braeuer:** Conceptualization, Formal analysis, Supervision, Writing - review & editing. **F. Espitalier:** Conceptualization, Supervision, Writing - review & editing, Funding acquisition.

## Declaration of Competing Interest

The authors declare that they have no known competing financial interests or personal relationships that could have appeared to influence the work reported in this paper.

## Acknowledgements

The project leading to this result has received funding from the Occitanie region (France), MUSYS project (ALDOCT-000149-2017 001788). The authors also gratefully acknowledge the doctoral school MEGeP for funding relating to T.D.'s stay at the Institute of Thermal, Environmental, and Resources Process Engineering, ITUN (Germany) and ITUN for access to the experimental setup.

## Appendix A. Uncertainty calculations

This section deals with the propagation of uncertainties from the acquisition of the Raman spectra to the concentration calculations. In each experiment, 16 spectra have been recorded for each of the ten measurement points. From these,  $16 \times 10$  molar ratios  $\frac{n_{\text{CO}_2}}{n_{\text{H}_2\text{O}}}$  (or molar fraction ratio) are obtained.

### A.1. Experimental uncertainty of the z-position in the capillary tube

In order to compute the error of the z-position where the measurement is made, the following method was used.

Fig. 14 shows the observed image of the laser passing through the capillary tube on the black optical table. The length of the measurement spot is known ( $L_1 = 1 \text{ cm}$ ) and the length of the image,  $L_2$ , is measured. The magnification of the capillary tube image,  $G$ , is then computed with Eq. (17).

$$G = \frac{L_2}{L_1} = \frac{ID_2}{ID_1} \approx 30 \quad (17)$$

When the laser is focused in the capillary (right sketch of Fig. 14), the image is checked to be symmetrical, which means that the laser is well positioned in the measurement spot. It is considered that the maximum error here is 2 cm, which corresponds to an error of  $667 \mu\text{m}$  in the z-position. This error is negligible and does not affect the concentration measurements.

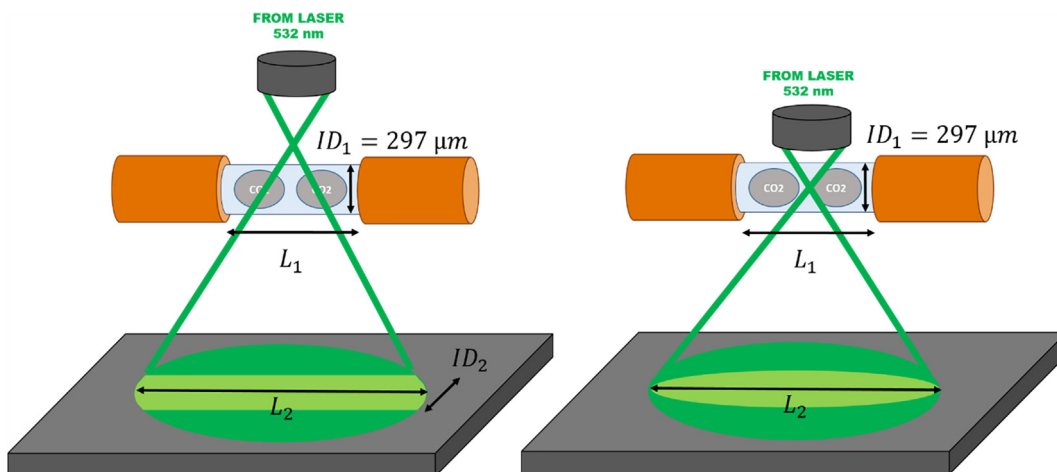


Fig. 14. Sketches of the laser passing through the capillary tube when the laser is not focused in the capillary tube (left) and when it is focused in the capillary tube (right).

### A.2. Experimental uncertainty on concentration

For each experiment, a standard normal distribution test is performed on the molar ratio values ( $r = \frac{n_{\text{H}_2\text{O}}}{n_{\text{CO}_2}}$ ), the results are shown in Fig. 15. Each group of data follows a standard normal distribution, hence, the standard deviation  $\sigma_r$  can be interpreted as a standard deviation of a normal distribution.

Eq. (19) gives the approximation of the standard deviation  $\sigma_{C_{\text{CO}_2}}$  calculated with the standard deviations of both the molar ratio,  $r$ , and the liquid mixture density,  $\rho_L$ . This approximation is taken because the values of  $r$  and  $\rho_L$  are near their mean values and  $\sigma_r$  (respectively  $\sigma_{\rho_L}$ ) is small compared with  $r$  ( $\rho_L$ ). Furthermore,  $\frac{\partial f}{\partial r}$  (respectively  $\frac{\partial f}{\partial \rho_L}$ ) are linear within the interval  $\pm \sigma_r$  ( $\pm \sigma_{\rho_L}$ ) about  $r$  ( $\rho_L$ ).

$$C_{\text{CO}_2} = \frac{\rho_L(T, P, x_{\text{CO}_2})}{M_{\text{CO}_2} + \frac{n_{\text{H}_2\text{O}}}{n_{\text{CO}_2}} M_{\text{H}_2\text{O}}} = f\left(\frac{n_{\text{H}_2\text{O}}}{n_{\text{CO}_2}}, \rho_L\right) = f(r, \rho_L) \quad (18)$$

$$\sigma_{C_{\text{CO}_2}}^2 = \left(\frac{\partial f}{\partial r}\right)_{r=r}^2 \sigma_r^2 + \left(\frac{\partial f}{\partial \rho_L}\right)_{\rho_L=\rho_L}^2 \sigma_{\rho_L}^2 \quad (19)$$

Random sampling in the normal distribution of  $r$  and  $\rho_L$  allows computation of a representative sample of  $C_{\text{CO}_2}$ . It has been shown that the concentration distribution also follows a normal law. Consequently, the standard deviation  $\sigma_{C_{\text{CO}_2}}$  represented in Fig. 6 can be interpreted as the standard deviation of a normal distribution. The value of the standard deviation  $\sigma_{C_{\text{CO}_2}}$  which take into account the variations of the molar ratios (including the error during the calibration step) and the variations of the mixture density, does not exceed 7% of the concentration value. However, this deviation can be drastically reduced with a binary system where the calibration step is easier than the one with the  $\text{CO}_2$ - $\text{H}_2\text{O}$  system because the solubility of  $\text{CO}_2$  in the  $\text{H}_2\text{O}$  rich phase is small (and therefore reduces the resolution of the calibration curve). The contribution of temperature and pressure measurements on the concentrations obtained with this method was verified by a random sampling in the normal distribution of  $T$  and  $P$ . The results show that the concentration values are shifted by less than 0.05% of the mean value, which is highly negligible compared with error from the molar ratio and from the density model.

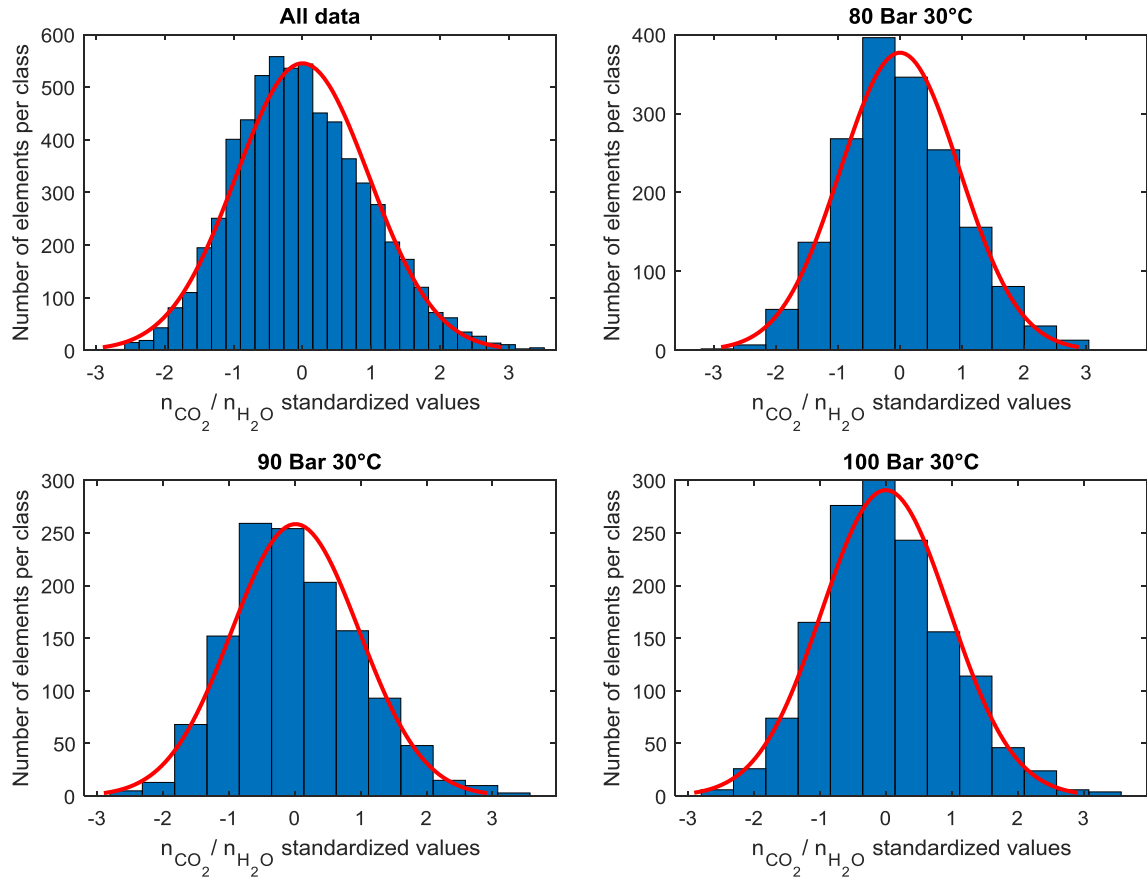


Fig. 15. Standardized class distribution of  $\frac{n_{CO_2}}{n_{H_2O}}$  values (blue) and standardized normal distribution (red).

## Appendix B. Fast Fourier transform (FFT) filtering

As it can be observed from Eq. (15), the  $k_L a_L$  calculation requires estimation of the value of the first derivative at each point of the curve  $C_{CO_2}$  versus  $z$ . The precision of a derivative between two experimental data points is not sufficient to proceed to a raw calculation of these derivatives. In fact, as shown on Fig. 6, the data present Gaussian “noise” in the  $C_{CO_2}$  versus  $z$  curves. These curves therefore have to be filtered and smoothed before any estimation of the derivative. Several filtering and smoothing techniques have been tested. The best results have been obtained with the Fast Fourier Transform (Balac, 2011). The selection was based on the visual smoothing appearance and objective criteria consisting in the weighted least squares (square root of the sum of the square residuals between experimental and filtering values weighted by the inverse of the standard deviation). This technique consists of several steps.

- Firstly, two points are added to each set of results ( $z, C_{CO_2}$ ): the initial point (0, 0) and a theoretical final one ( $+\infty, C_{CO_2}^*$ ).
- The following variable substitutions are then performed:  $Z = 1/(1 + \gamma z)$  and  $Y = C_{CO_2}/C_{CO_2}^*$ . The new variables are confined in the range  $[0, 1] \times [0, 1]$ , and the parameter  $\gamma$  ( $0 < \gamma < 1$ ) allows a better spreading of these new data on  $[0, 1]$ .
- The values used for the discussion on the comparative experimental results mostly concern the first part of the curve, i.e. near the point (0, 0). Therefore, care should be taken when fitting data in this region. This is why the third step consists in the doubling of the number of points by adding  $(-Z, -Y)$  to

the curve. This way, the region of interest is located in the middle of the curve, far from eventual boundaries ending point problems.

- The fourth step consists in rotating the curve centred at (0, 0) by an angle of  $-\pi/4$ . Following this, a continuous periodic curve is obtained that greatly improves the selection of frequencies after the FFT.
- Resampling is carried out at the points ( $Z, Y$ ) of this curve by linear interpolation in order to obtain a new set of equally-spaced points on the  $z$ -axis. In order to respect the Shannon theorem,  $2^5$  points were taken. A discrete Fourier transform using a FFT algorithm is then performed.
- From the amplitude spectrum of the Fourier transform, between 2 and 4 frequencies of greater amplitudes are selected (taking the smallest objective criteria). The inverse Fourier transform is then carried out with these selected pairs of frequency and amplitude, leading to a new set of filtered ( $Z, Y$ ).
- Finally, a reverse rotation and a reverse variable substitution is performed and the final filtered and smoothed curve of  $C_{CO_2}$  versus  $z$  is obtained. These filtered points are used to estimate the first derivative of  $C_{CO_2}$  needed for  $k_L a_L$  calculation.

## References

- Abadie, Thomas, 2013. Hydrodynamics of Gas-Liquid Taylor Flow in Microchannels. Phd. <http://ethesis.inp-toulouse.fr/archive/00002504/>.
- Abadie, T., Aubin, J., Legendre, D., Xuereb, C., 2012. Hydrodynamics of Gas-Liquid Taylor Flow in Rectangular Microchannels. *Microfluid. Nanofluid.* 12 (January), 355–369. <https://doi.org/10.1007/s10404-011-0880-8>.



- Andersen, G., Probst, A., Murray, L., Butler, S., 1992. An Accurate PVT Model for Geothermal Fluids as Represented by H<sub>2</sub>O-NaCl-CO<sub>2</sub>. In: *Mixtures, Proceedings 17th Workshop on Geothermal Reservoir Engineering*, pp. 239–248.
- Anderson, G.R., 1977. The Raman Spectra of Carbon Dioxide in Liquid Water and Water-D<sub>2</sub>. *J. Phys. Chem.* 81 (3), 273–276. <https://doi.org/10.1021/j100518a017>.
- Bachu, S., Adams, J.J., 2003. Sequestration of CO<sub>2</sub> in Geological Media in Response to Climate Change: Capacity of Deep Saline Aquifers to Sequester CO<sub>2</sub> in Solution. *Energy Convers. Manage.* 44 (20), 3151–3175. [https://doi.org/10.1016/S0196-8904\(03\)00101-8](https://doi.org/10.1016/S0196-8904(03)00101-8).
- Balac, Stéphane, 2011. La transformée de Fourier vue sous l'angle du calcul numérique, January. <https://cel.archives-ouvertes.fr/cel-01862054>.
- van Baten, J.M., Krishna, R., 2004. CFD Simulations of Mass Transfer from Taylor Bubbles Rising in Circular Capillaries. *Chem. Eng. Sci.* 59 (12), 2535–2545. <https://doi.org/10.1016/j.ces.2004.03.010>.
- Batzle, M., Wang, Z., 1992. Seismic Properties of Pore Fluids. *Geophysics* 57 (11), 1396–1408. <https://doi.org/10.1190/1.1443207>.
- Ben-Nasr, Hedi, Coenen, Hubert, 1994. Process for the quasi-continuous decaffeination of raw coffee. United States US5338575A, filed 5 May 1993, and issued 16 August 1994. <https://patents.google.com/patent/US5338575A/en>.
- Bercic, G., Pintar, A., 1997. The Role of Gas Bubbles and Liquid Slug Lengths on Mass Transport in the Taylor Flow through Capillaries. *Chem. Eng. Sci.* 52 (21), 3709–3719. [https://doi.org/10.1016/S0009-2509\(97\)00217-0](https://doi.org/10.1016/S0009-2509(97)00217-0).
- Bird, R.B., 2002. Transport Phenomena. *Appl. Mech. Rev.* 55 (1), R1–R4. <https://doi.org/10.1115/1.1424298>.
- Brunner, G., 2005. Supercritical fluids: technology and application to food processing. *J. Food Eng.* 67 (1–2), 21–33. <https://linkinghub.elsevier.com/retrieve/pii/S0260877404003383>. <https://doi.org/10.1016/j.jfoodeng.2004.05.060>.
- Dietrich, N., Loubière, K., Jimenez, M., Hébrard, G., Gourdon, C., 2013. A New Direct Technique for Visualizing and Measuring Gas-Liquid Mass Transfer around Bubbles Moving in a Straight Millimetric Square Channel. *Chemical Engineering Science*, 11th International Conference on Gas-Liquid and Gas-Liquid-Solid Reactor Engineering, 100 (August), 172–82. <https://doi.org/10.1016/j.ces.2013.03.041>.
- Enick, R.M., Klara, S.M., 1990. CO<sub>2</sub> Solubility in Water and Brine under Reservoir Conditions. *Chem. Eng. Comm.* 90 (1), 23–33. <https://doi.org/10.1080/00986449008940574>.
- Eskin, D., Mostowfi, F., 2012. A Model of a Bubble Train Flow Accompanied with Mass Transfer through a Long Microchannel. *Int. J. Heat Fluid Flow* 33 (1), 147–155. <https://doi.org/10.1016/j.ijheatfluidflow.2011.11.001>.
- Ganapathy, H., Shoostari, A., Dessiatoun, S., Alshehhi, M., Ohadi, M., 2014. Fluid Flow and Mass Transfer Characteristics of Enhanced CO<sub>2</sub> Capture in a Minichannel Reactor. *Appl. Energy* 119, 43–56. <https://doi.org/10.1016/j.apenergy.2013.12.047>.
- García, Julio E., 2001. Density of Aqueous Solutions of CO<sub>2</sub>, October. <https://escholarship.org/uc/item/6dn022hb>.
- Garstecki, P., Fuerstman, M.J., Stone, H.A., Whitesides, G.M., 2006. Formation of Droplets and Bubbles in a Microfluidic T-Junction—Scaling and Mechanism of Break-Up. *Lab Chip* 6 (3), 437–446. <https://doi.org/10.1039/B510841A>.
- Heiszwolf, J.J., Kreutzer, M.T., van den Eijnden, M.G., Kapteijn, F., Moulijn, J.A., 2001. Gas-Liquid Mass Transfer of Aqueous Taylor Flow in Monoliths. *Catal. Today, Structured Catalysts and Reactors* 69 (1), 51–55. [https://doi.org/10.1016/S0920-5861\(01\)00354-6](https://doi.org/10.1016/S0920-5861(01)00354-6).
- Irandoust, S., Ertlé, S., Andersson, B., 1992. Gas-liquid mass transfer in Taylor flow through a capillary. *Can. J. Chem. Eng.* 70 (1), 115–119. <https://doi.org/10.1002/cjce.5450700116>.
- Kim, H.-J., Lee, S.-B., Park, K.-A., Hong, I.-K., 1999. Characterization of Extraction and Separation of Rice Bran Oil Rich in EPA Using SFE Process. *Sep. Purif. Technol.* 15 (1), 1–8. [https://doi.org/10.1016/S1383-5866\(98\)00048-3](https://doi.org/10.1016/S1383-5866(98)00048-3).
- Klima, T.C., Braeuer, A.S., 2019. Vapor-Liquid-Equilibria of Fuel-Nitrogen Systems at Engine-like Conditions Measured with Raman Spectroscopy in Micro Capillaries. *Fuel* 238 (February), 312–319. <https://doi.org/10.1016/j.fuel.2018.10.108>.
- Knez, Ž., Hrnčič, M.K., Čolnik, M., Škerget, M., 2018. Chemicals and Value Added Compounds from Biomass Using Sub- and Supercritical Water. *J. Supercrit. Fluids* 133 (March), 591–602. <https://doi.org/10.1016/j.supflu.2017.08.011>. Biomass Fractionation by Subcritical and Supercritical Water.
- Kuhn, S., Jensen, K.F., 2012. A pH-Sensitive Laser-Induced Fluorescence Technique To Monitor Mass Transfer in Multiphase Flows in Microfluidic Devices. *Ind. Eng. Chem. Res.* 51 (26), 8999–9006. <https://doi.org/10.1021/ie300978n>.
- Lefortier, S.G.R., Hamersma, P.J., Bardow, A., Kreutzer, M.T., 2012. Rapid Microfluidic Screening of CO<sub>2</sub> Solubility and Diffusion in Pure and Mixed Solvents. *Lab Chip* 12 (18), 3387–3391. <https://doi.org/10.1039/C2LC40260B>.
- Lehotay, S.J., 1997. Supercritical Fluid Extraction of Pesticides in Foods. *J. Chromatogr. A* 785 (1), 289–312. [https://doi.org/10.1016/S0021-9673\(97\)00461-5](https://doi.org/10.1016/S0021-9673(97)00461-5).
- Leung, S.S.Y., Liu, Y., Fletcher, D.F., Haynes, B.S., 2010. Heat Transfer in Well-Characterised Taylor Flow. *Chem. Eng. Sci.* 65 (24), 6379–6388. <https://doi.org/10.1016/j.ces.2010.09.014>.
- Liu, D., Wang, S., 2011. Gas-Liquid Mass Transfer in Taylor Flow through Circular Capillaries. *Ind. Eng. Chem. Res.* 50 (4), 2323–2330. <https://doi.org/10.1021/ie902055p>.
- Lumia, Guy, Perre, Christian, Aracil, Jean-Marie, 2007. Method for treating and extracting cork organic compounds, with a dense fluid under pressure. United States US7192490B1, filed 26 September 2000, and issued 20 March 2007. <https://patents.google.com/patent/US7192490B1/en>.
- Luther, S.K., Schuster, J.J., Leipertz, A., Braeuer, A., 2013. Microfluidic Investigation into Mass Transfer in Compressible Multi-Phase Systems Composed of Oil, Water and Carbon Dioxide at Elevated Pressure. *J. Supercrit. Fluids* 84 (December), 121–131. <https://doi.org/10.1016/j.supflu.2013.10.002>.
- Portela, M., da Silva, N., Letourneau, J.-J., Espitalier, F., Prat, L., 2014. Transparent and Inexpensive Microfluidic Device for Two-Phase Flow Systems with High-Pressure Performance. *Chem. Eng. Technol.* 37 (11), 1929–1937.
- Marre, S., Adamo, A., Basak, S., Aymonier, C., Jensen, K.F., 2010. Design and Packaging of Microreactors for High Pressure and High Temperature Applications. *Ind. Eng. Chem. Res.* 49 (22), 11310–11320. <https://doi.org/10.1021/ie101346u>.
- Martin, A., Camy, S., Aubin, J., 2018. Hydrodynamics of CO<sub>2</sub>-Ethanol Flow in a Microchannel under Elevated Pressure. *Chem. Eng. Sci.* 178 (March), 297–311. <https://doi.org/10.1016/j.ces.2017.12.046>.
- Martin, A., Teychené, S., Camy, S., Aubin, J., 2016. Fast and Inexpensive Method for the Fabrication of Transparent Pressure-Resistant Microfluidic Chips. *Microfluid. Nanofluid.* 20 (6), 92. <https://doi.org/10.1007/s10404-016-1757-7>.
- Masmoudi, Y., Ben Azzouk, L., Forzano, O., Andre, J.-M., Badens, E., 2011. Supercritical impregnation of intraocular lenses. *J. Supercrit. Fluids* 60, 98–105. <https://linkinghub.elsevier.com/retrieve/pii/S089684461100372X>. <https://doi.org/10.1016/j.supflu.2011.08.014>.
- Perrut, M., Perrut, V., 2018. Towards Ingredients by Combining Supercritical Fluids with Other Processes. *J. Supercrit. Fluids*, 30th Year Anniversary Issue of the Journal of Supercritical Fluids 134 (April), 214–219. <https://doi.org/10.1016/j.supflu.2017.11.019>.
- Perrut, Michel, Perrut, Vincent, 2019. Chapter 7.7 - Supercritical Fluid Applications in the Food Industry. In: Cachon, Rémy, Girardon, Philippe, Voilley, Andrée (Eds.), *Gases in Agro-Food Processes*. Academic Press, pp. 483–509. <https://doi.org/10.1016/B978-0-12-812465-9.00020-7>.
- Peters, C., Wolff, L., Haase, S., Thien, J., Brands, T., Koß, H.-J., Bardow, A., 2017. Multicomponent Diffusion Coefficients from Microfluidics Using Raman Microspectroscopy. *Lab Chip* 17 (16), 2768–2776. <https://doi.org/10.1039/C7LC00433H>.
- Proctor, B.A., Whitney, I., Johnson, J.W., 1967. The Strength of Fused Silica. *Proc. R. Soc. Lond. A* 297 (1451), 534–557. <https://doi.org/10.1098/rspa.1967.0085>.
- Ren, J., He, S., Ye, C., Chen, G., Sun, C., 2012. The Ozone Mass Transfer Characteristics and Ozonation of Pentachlorophenol in a Novel Microchannel Reactor. *Chem. Eng. J.* 210 (November), 374–384. <https://doi.org/10.1016/j.cej.2012.09.011>.
- Span, R., Wagner, W., 1996. A New Equation of State for Carbon Dioxide Covering the Fluid Region from the Triple-Point Temperature to 1100 K at Pressures up to 800 MPa. *J. Phys. Chem. Ref. Data* 25 (6), 1509–1596. <https://doi.org/10.1063/1.555991>.
- Steijn, Volkert van, Kreutzer, Michiel T., Kleijn, Chris R., 2007.  $\mu$ -PIV Study of the Formation of Segmented Flow in Microfluidic T-Junctions. *Chemical Engineering Science*, 8th International Conference on Gas-Liquid and Gas-Liquid-Solid Reactor Engineering, 62(24), 7505–14. <https://doi.org/10.1016/j.ces.2007.08.068>.
- Susanti, J.G.M., Winkelmann, B.S., Heeres, H.J., Yue, J., 2016. Lactic Acid Extraction and Mass Transfer Characteristics in Slug Flow Capillary Microreactors. *Ind. Eng. Chem. Res.* 55 (16), 4691–4702. <https://doi.org/10.1021/acs.iecr.5b04917>.
- Tan, J., Lu, Y.C., Xu, J.H., Luo, G.S., 2012. Mass Transfer Characteristic in the Formation Stage of Gas-Liquid Segmented Flow in Microchannel. *Chem. Eng. J.* 185–186 (March), 314–320. <https://doi.org/10.1016/j.cej.2012.01.054>.
- Temelli, F., 2009. Perspectives on supercritical fluid processing of fats and oils. *J. Supercrit. Fluids* 47 (3), 583–590. <https://linkinghub.elsevier.com/retrieve/pii/S0896844608003598>. <https://doi.org/10.1016/j.supflu.2008.10.014>.
- Tsai, W.-C., Wang, Y., 2019. Progress of Supercritical Fluid Technology in Polymerization and Its Applications in Biomedical Engineering. *Prog. Polym. Sci.* 98, (November). <https://doi.org/10.1016/j.progpolymsci.2019.101161>.
- Vandu, C.O., Liu, H., Krishna, R., 2005. Mass transfer from Taylor bubbles rising in single capillaries. *Chem. Eng. Sci.* 60 (22), 6430–6437. <https://linkinghub.elsevier.com/retrieve/pii/S0009250905000813>. <https://doi.org/10.1016/j.ces.2005.01.037>.
- Yao, C., Dong, Z., Zhao, Y., Chen, G., 2014. An Online Method to Measure Mass Transfer of Slug Flow in a Microchannel. *Chem. Eng. Sci.* 112 (June), 15–24. <https://doi.org/10.1016/j.ces.2014.03.016>.
- Yao, C., Zhu, K., Liu, Y., Liu, H., Jiao, F., Chen, G., 2017. Intensified CO<sub>2</sub> Absorption in a Microchannel Reactor under Elevated Pressures. *Chem. Eng. J.* 319 (July), 179–190. <https://doi.org/10.1016/j.cej.2017.03.003>.
- Yue, J., Chen, G., Yuan, Q., Luo, L., Gonthier, Y., 2007. Hydrodynamics and Mass Transfer Characteristics in Gas-Liquid Flow through a Rectangular Microchannel. *Chem. Eng. Sci.* 62 (7), 2096–2108. <https://doi.org/10.1016/j.ces.2006.12.057>.
- Yue, J., Luo, L., Gonthier, Y., Chen, G., Yuan, Q., 2009. An Experimental Study of Air-Water Taylor Flow and Mass Transfer inside Square Microchannels. *Chem. Eng. Sci.* 64 (16), 3697–3708. <https://doi.org/10.1016/j.ces.2009.05.026>.
- Zaloha, P., Kristal, J., Jiricny, V., Völkel, N., Xuereb, C., Aubin, J., 2012. Characteristics of Liquid Slugs in Gas-Liquid Taylor Flow in Microchannels. *Chem. Eng. Sci.* 68 (1), 640–649. <https://doi.org/10.1016/j.ces.2011.10.036>.
- Zhang, P., Yao, C., Ma, H., Jin, N., Zhang, X., Lü, H., Zhao, Y., 2018. Dynamic Changes in Gas-Liquid Mass Transfer during Taylor Flow in Long Serpentine Square Microchannels. *Chem. Eng. Sci.* 182 (June), 17–27. <https://doi.org/10.1016/j.ces.2018.02.018>.

# List of Figures

1.1	(Pressure, Temperature) diagram of a substance with its three states (solid, liquid, gas) and its supercritical region. . . . .	22
1.2	Simplified scheme of the Rapid Expansion of Supercritical Solution process (RESS). The solute can be either a liquid or a solid such as drugs, polymers and fat. . . . .	24
1.3	Simplified scheme of the Particle Generation From gas Saturated Solution process (PGSS). . . . .	25
1.4	Simplified scheme of Supercritical Anti-Solvent process (SAS). . . . .	26
1.5	Number of Google Scholar results per half decade for publications containing the keyword "Microfluidics". The data between 2015 and 2020 are taken at the end of July in 2020. . . . .	27
1.6	[Left] 3D printing of biological constructions with heterogeneous and complex structures. Photographs of the 3D-printed (a) a mandible bone construct, (b) an ear cartilage with ear lobule, (c) a kidney with renal pelvis, (d) a liver, (e) a heart cross-section, and (f) an arterial tree, taken from Yi et al. (2017). [Right] Fully soft and autonomous robot controlled via the embedded microfluidic soft controller and powered by monopropellant decomposition, taken from Wehner et al. (2016). . . . .	28
1.7	Maximum experiment pressure and temperature of microreactors providing an optical access, shown in the litterature and their maximum linear strength applied on their inner surfaces. Presentation adapted from Marre et al. (2010). . . . .	30
1.8	(a) Silicon/pyrex microreactor for supercritical extraction of vanilin (Assmann et al. (2012)); (b) Glass/ostemer microreactor for gas liquid mass transfer investigation (Martin et al. (2016)); (c) Metal microreactor for liquid fractionation with supercritical carbon dioxide (Campos Domínguez et al. (2016)); (d) Glass/glass microreactor for analytical chemistry (Oosterbroek et al. (2006)); (e) Capillary - An emulsion [ethyl-acetate 15 $\mu\text{L min}^{-1}$ - water 90 $\mu\text{L min}^{-1}$ ] is injected into a flow of supercritical $\text{CO}_2$ 300 $\mu\text{L min}^{-1}$ at 311 K and 8 MPa . . . . .	31
1.9	Summary of the main advantages of combining supercritical fluids to microfluidics systems. Taken from Marre et al. (2012). . . . .	34

---

1.10	Schematic diagram of the high pressure plant, into which the microreactor was integrated. It consists of high pressure piston pumps and an elaborated sampling system. Taken from Assmann et al. (2012).	34
1.11	Description of the mixing principles studied in the work of Campos Domínguez et al. (2016): multi-lamination (A) and T-type lamination (B). Taken from Campos Domínguez et al. (2016).	35
1.12	Micro reactor employed for esterification of oleic acid with methanol where supercritical carbon dioxide acts as a solvent at a pressure of 10 MPa and temperatures between 333 K and 393 K. Taken from Quitain et al. (2018).	36
1.13	Micro reactor employed in the griseofulvin particle generation from a solution of griseofulvin and dimethylformamide with carbon dioxide as antisolvent. Taken from Arora et al. (2020).	36
1.14	Microfluidic approach for the determination of $CO_2$ solubility into a $H_2O$ and brine liquid solution at high pressure. Taken from N. Liu et al. (2012).	37
1.15	Determination of the vapor-liquid equilibria for fuel-nitrogen systems at pressures between 3 MPa and 8 MPa, temperature up to 593 K, in a microcapillary where a Raman spectroscopy technique is employed. Taken from Klima et al. (2019).	37
1.16	Flow patterns obtained at 1 MPa with a 1.10 mm internal diameter tube. Taken from L. Chen et al. (2006) where $U_{gs}$ and $U_{ls}$ are the gas and liquid superficial velocities respectively.	38
1.17	Flow pattern maps obtained by L. Chen et al. (2006), plotted as function of the gas and liquid superficial velocities (a) and as a function of the Weber number of each phase (b) for channel diameters of 4.26 mm, 2.88 mm, 2.01 mm and 1.10 mm.	39
1.18	$N_2$ - $H_2O$ flow pattern map obtained in a T-junction microchannel for pressures between 0.1 MPa and 5 MPa taken from Y. Zhao et al. (2013).	40
1.19	Dynamic phase diagrams of a $CO_2$ -liquid water system obtained at two different pressure, 8 MPa on the left and 18 MPa on the right, all other parameters being kept constant ( $d_h = 75 \mu m$ , $T = 323 K$ ) taken from Marre et al. (2009).	40
1.20	Phase diagram for $CO_2$ - $EtOH$ at 313 K and flow regime map. Superficial velocity ranges: $0.13 m s^{-1} < U_G < 0.30 m s^{-1}$ , $0.01 m s^{-1} < U_L < 0.05 m s^{-1}$ taken from Martin et al. (2018).	41
1.21	(a) In this microcapillary device [sc $CO_2$ -BMImPF <sub>6</sub> 11.5 MPa 318 K] the boundary of this peculiarly thick film is made visible due to the impact of the high gradient of dissolved $CO_2$ on the refraction coefficient in the bubble wake border; (b) With the same system and other operating conditions, a modification in the lighting allows the torroïdal recirculation in the Taylor zone to be clearly seen ( <i>unpublished J.-J. Letourneau</i> (2014)).	42
1.22	Various microchannel geometry employed in the Microfluidics litterature: (a) cross-sections (b) inlet geometries.	43
1.23	Squeezing to shearing regime from Menech et al. (2008) in a T-junction square microchannel: (a) $Ca_L = 0.004$ ; (b,c) $Ca_L = 0.035$ ; (d) $Ca_L = 0.05$ .	44
1.24	Rough sketch of possible streamlines. Taken from Taylor (1961) where m is the dimensionless number $(U_B - U_{TP})/U_B$ .	47



1.25	Liquid slug streamlines obtained by CFD simulations at different capillary numbers ( $Ca_B =$ ) in the work of Taha et al. (2004). (a) $Ca_B = 0.03$ (b) $Ca_B = 0.10$ (c) $Ca_B = 0.3$ (d) $Ca_B = 1.34$ . . . . .	48
1.26	(a) Recirculation velocity $U_{rc}$ as a function of the superficial velocity ratio $\frac{U_G}{U_L}$ . (b) Recirculation velocity as a function of the two-phase superficial velocity, $U_{TP}$ . Taken from Zaloha et al. (2012). . . . .	49
1.27	Presentation of the plug flow unit-cell model. . . . .	50
1.28	Bubble decomposition in one cylindrical part and two hemispherical caps in a two-phase segmented flow. . . . .	52
1.29	$CO_2$ - $EtOH$ segmented flows at 4.3 MPa, 313 K. (a,b) the single-phase zone is reached (c) flow near the bubble point (d) flow stabilized in the gas-liquid zone, taken from Martin et al. (2018). . . . .	58
1.30	$CO_2$ - $BMimPF_6$ segmented flow at 11.4 MPa, 313 K, $\dot{V}_{BMimPF_6} = 90 \mu L \min^{-1}$ , $\dot{V}_{CO_2} = 111 \mu L \min^{-1}$ taken from Macedo Portela da Silva et al. (2014). . . . .	59
2.1	Mass transfer phenomena and pressure drop affecting the bubble size in a two-phase segmented micro-flow. . . . .	63
2.2	Expected outcome (grey boxes) of the change in bubble size in a two-phase segmented micro-flow depending on the thermodynamics of the binary system and the pressure drop. . . . .	64
2.3	$CO_2$ dissolution behaviour of the three types of binary systems. (a) $CO_2$ - $H_2O$ and Bromophenol blue at 10 MPa, 303 K, $\dot{V}_{H_2O} = 150 \mu L \min^{-1}$ , $\dot{V}_{CO_2} = 50 \mu L \min^{-1}$ . (b) $CO_2$ - $EtOH$ at 4.3 MPa, 313 K, $\dot{M}_{EtOH} = 2.32 g h^{-1}$ , $\dot{M}_{CO_2} = 2.0 g h^{-1}$ from Martin (2016). (c) $CO_2$ - $BMimPF_6$ at 11.4 MPa, 313 K, $\dot{V}_{BMimPF_6} = 90 \mu L \min^{-1}$ , $\dot{V}_{CO_2} = 111 \mu L \min^{-1}$ from Silva (2014). . . . .	66
2.4	Pressure-composition diagram of the binary system $CO_2$ - $H_2O$ at 298.1 K and 323 K for pressures between 0.1 MPa and 70 MPa. The figures have been taken from the work of Aasen et al. (2017) where a thermodynamic model is compared with experimental data from the literature. . . . .	67
2.5	Equilibrium molar fraction of $CO_2$ ( $x_{CO_2}^*$ ) in a $H_2O$ -rich phase at 303 K, 313 K and 323 K for pressures between 0.1 MPa and 20 MPa calculated with the model of Enick et al. (1990). The model is compared with experimental data from Briones et al. (1987), Koschel et al. (2006) and Hou et al. (2013). . . . .	67
2.6	Comparison of experimental vapor-liquid equilibrium data for $CO_2$ (1)- $EtOH$ (2): (♦) Tsivintzelis et al. (2004) (313.2 K); (□) Jennings et al. (1991) (314.5 K); (*) Suzuki et al. (1990) (313.4 K); (◇) Joung et al. (2001) (313.4 K); (△) Chang et al. (1997) (313.15 K). Figure taken from Tsivintzelis et al. (2004). . . . .	69
2.7	Equilibrium molar fraction of $CO_2$ ( $x_{CO_2}^*$ ) in a $EtOH$ -rich phase at 313 K and 328 K for pressures between 1.6 MPa and 9.42 MPa from the work of Tsivintzelis et al. (2004). . . . .	69
2.8	Equilibrium molar fraction of $CO_2$ ( $x_{CO_2}^*$ ) in a $BMimPF_6$ -rich phase at 308 K, 313 K and 318 K for pressures between 2.3 MPa and 35 MPa from the work of Adamou et al. (2006). . . . .	70
2.9	Density values of pure $H_2O$ at 308 K, 313 K and 318 K for pressures between 0.1 MPa and 30 MPa based on the work of Wagner et al. (2002). . . . .	72

---

2.10	Density values of pure <i>EtOH</i> at 308 K, 313 K and 318 K for pressures between 0.1 MPa and 30 MPa based on the work of Gonçalves et al. (2010). . . . .	72
2.11	Density values of pure <i>BMimPF<sub>6</sub></i> at 0.1 MPa and for temperatures between 308 K and 318 K from the work of Adamou et al. (2006). . . . .	72
2.12	Density values of pure <i>CO<sub>2</sub></i> at 308 K, 313 K and 318 K for pressures between 0.1 MPa and 30 MPa calculated with the Span et al. (1996) equation of state. . . . .	73
2.13	Viscosity of <i>H<sub>2</sub>O</i> at 308 K, 313 K and 318 K for pressures between 0.1 MPa and 30 MPa based on the work of Wagner et al. (2002). . . . .	74
2.14	Viscosity of <i>EtOH</i> at 298 K and 323 K for pressures between 0.1 MPa and 27.56 MPa from the work of Assael et al. (1994). . . . .	74
2.15	Viscosity of <i>BMimPF<sub>6</sub></i> at 0.1 MPa and for temperatures between 298 K and 323 K from the work of Adamou et al. (2006). . . . .	74
2.16	Viscosity of <i>CO<sub>2</sub></i> at 308 K, 313 K and 318 K for pressures between 0.1 MPa and 30 MPa based on the work of Fenghour et al. (1998). . . . .	75
2.17	Interfacial tension of <i>H<sub>2</sub>O</i> , <i>H<sub>2</sub>O + EtOH</i> and <i>EtOH</i> saturated with <i>CO<sub>2</sub></i> at 313 K for pressures between 0.1 MPa and 27 MPa taken from Dittmar et al. (2002). . . . .	76
2.18	Interfacial tension of <i>BMimPF<sub>6</sub></i> saturated with <i>CO<sub>2</sub></i> at 308 K, 313 K and 318 K for pressures between 0.1 MPa and 30.5 MPa based on the work of Adamou et al. (2006). . . . .	76
2.19	<i>H<sub>2</sub>O-CO<sub>2</sub></i> liquid mixture density versus the molar fraction of <i>CO<sub>2</sub></i> at 303 K for pressures between 6 MPa and 12 MPa based on the work of Bachu et al. (2003) and Garcia (2001). For each pressure, the mixture density is calculated from pure <i>H<sub>2</sub>O</i> up to the density of the mixture when thermodynamic equilibrium is reached. . . . .	77
2.20	<i>EtOH -CO<sub>2</sub></i> liquid mixture density versus the equilibrium molar fraction of <i>CO<sub>2</sub></i> at 313 K and 328 K from the work of Tsivintzelis et al. (2004). . . . .	77
2.21	<i>CO<sub>2</sub>-BMimPF<sub>6</sub></i> mixture density versus the equilibrium molar fraction of <i>CO<sub>2</sub></i> at 308 K and 318 K from the work of Adamou et al. (2006). . . . .	78
2.22	Ratio of liquid mixture volume saturated with <i>CO<sub>2</sub></i> over the volume of the pure liquid as a function of pressure, where the liquid is <i>H<sub>2</sub>O</i> , <i>EtOH</i> and <i>BMimPF<sub>6</sub></i> . . . . .	78
2.23	<i>CO<sub>2</sub>-H<sub>2</sub>O</i> non-saturated mixture viscosity versus the molar fraction of <i>CO<sub>2</sub></i> at 294 K and 322 K with pressures of 15 MPa and 30 MPa based on the work of McBride-Wright et al. (2015). . . . .	81
2.24	<i>CO<sub>2</sub>-EtOH</i> mixture viscosity versus the equilibrium molar fraction of <i>CO<sub>2</sub></i> at 303 K and 313 K from the work of Sih et al. (2008). . . . .	81
2.25	<i>CO<sub>2</sub>-BMimPF<sub>6</sub></i> mixture viscosity at 308 K and 318 K for pressures between 0.1 MPa and 30 MPa from the work of Adamou et al. (2006). . . . .	81
2.26	[Left] Three contributions of the two-phase mass transfer of a component A: diffusion in phase 1, convection at the interface and diffusion in phase 2. $N_A$ corresponds to the combined molar flux (diffusion + convection). [Right] Two phase mass transfer of <i>CO<sub>2</sub></i> from a <i>CO<sub>2</sub></i> pure phase to a <i>H<sub>2</sub>O</i> -rich phase. No diffusion in the <i>CO<sub>2</sub></i> pure phase. . . . .	83

2.27	Two-film model with mass transfer in both directions (a) and fluid to liquid only (b) where $y_{CO_2}$ is the molar fraction of $CO_2$ in the bulk of $CO_2$ -rich phase, $y_{CO_2,i}$ is the molar fraction of $CO_2$ at the interface in equilibrium with $x_{CO_2,i}$ and $y_{CO_2}^*$ is the molar fraction of $CO_2$ in the $CO_2$ -rich phase in equilibrium with the liquid phase with the molar fraction of $CO_2$ in the bulk, $x_{CO_2}$ . Adapted from Bird (2002). . . . .	84
2.28	Presentation of the unit-cell model, which is composed of one $CO_2$ segment with volume $V_b$ and delimited by the surface $S_b$ , and one $H_2O$ -rich liquid segment of volume $V_L$ , which is delimited by its surface $S_L$ composed of $S_{cap}$ , $S_{in}$ and $S_{out}$ . . . . .	86
2.29	(a) Unit-cell and combined molar flux of $CO_2$ transferring through the $H_2O$ -rich liquid slug surface. (b) Unit-cell and normal vectors of each $H_2O$ -rich liquid slug surfaces. (c) $CO_2$ -rich bubble shrinkage where $\mathbf{v}_b^i$ is the bubble interface velocity vector. . . . .	87
3.1	Fabrication steps of the microreactor made of fused silica capillary tubes able to resist high pressure. . . . .	95
3.2	3D view and dimensions of the microreactor frame. . . . .	99
3.3	Cross-section of the optical access window in the microreactor. . . . .	100
3.4	Ferrule-sleeve-nut assembling. . . . .	100
3.5	Coaxial injection inside the microreactor. . . . .	101
3.6	Assembly of the capillary tubes to form two channel types (a) where two fluids can be mixed (b) for single fluid. . . . .	101
3.7	Photo of the microreactor after the fabrication steps. The final dimensions of the reactor are 50.2 cm×8.0 cm×2.0 cm. . . . .	102
3.8	Reactor fabrication Gantt chart. The red symbol corresponds to the tasks related to the work on the reactor and the grey corresponds to drying periods. . . . .	103
3.9	Reactor fabrication Gantt chart of two reactors simultaneously. The red bars corresponds to the tasks related to the first reactor, the blue ones to the second reactor and the grey ones corresponds to drying periods. . . . .	103
3.10	Top view of the temperature-controlled chamber with the reactor placed inside. . . . .	104
3.11	(Left) Temperature-controlled chamber closure with a simple screw system. (Right) Cracked PMMA due to the screw system closure. . . . .	105
3.12	Temperature-controlled chamber closure with a screw-nut assembling. The mechanical stress is applied on the nut instead of the PMMA wall. . . . .	105
3.13	Top view of the entire microfluidic system, the reactor and the temperature-controlled chamber able to resist pressure up to 25 MPa and temperature up to 333 K. . . . .	106
3.14	Broken glass slides observation due to a dilatation difference between the glass, the PMMA and the epoxy resin at 333 K. . . . .	106
3.15	Coloured water leaking through the T-junction (left) and at the union of the parts of the microreactor due to a poor epoxy glue quality. . . . .	107

---

4.1	Raman spectroscopy technique applied to the measurement of mass transfer coefficient in two phase segmented flow at high pressure. . . . .	112
4.2	Different light interaction with matter when the photons are not absorbed by the medium. . . . .	114
4.3	Rayleigh, Stokes and anti-Stokes radiation and Raman spectroscopy technique.	114
4.4	Example of a Raman spectroscopy calibration method for a binary system composed of molecules A and molecules B. . . . .	115
4.5	(a) Raman spectra of $CO_2$ measured at 35 °C from 4 to 10 MPa from N. Liu (2013). . . . .	117
4.6	Raman spectra of $H_2O$ measured at 30 °C and 10 MPa with the measurement setup used in this thesis work. . . . .	118
4.7	Raman spectra of $CO_2$ - $H_2O$ mixture measured at 30 °C and 10 MPa with the measurement setup used in this thesis work. . . . .	118
4.8	Schematic diagram and photo of the experimental setup used to determine mass transfer coefficients in high-pressure two-phase flows. . . . .	119
4.9	Conditioning block and temperature regulation. . . . .	120
4.10	Pressure variation in the reverse pump (ISCO 260D) after six hours at 10 MPa, 303 K, $\dot{V}_{H_2O} = 110 \mu L min^{-1}$ and $\dot{V}_{CO_2} = 85 \mu L min^{-1}$ . The error bar corresponds to 0.5 % of the pump full scale. . . . .	122
4.11	Operating conditions in term of Reynolds number for the $H_2O$ flow rate (L) and $CO_2$ flow rate (F). . . . .	123
4.12	Schematic overview of the Raman spectroscopy measurement part of the experimental setup . . . . .	124
4.13	Schematic diagram of the Raman spectroscopy setup for obtaining spectra in a single phase of a segmented two-phase flow. . . . .	125
4.14	Oscilloscope visualisation of the photo-detector signal and the signal from the pulse generator. . . . .	125
4.15	Raman spectra of the $H_2O$ -rich phase at different axis location from the contacting point in the micro capillary. The operating conditions are $P = 10$ MPa, $T = 303$ K, $\dot{V}_{H_2O} = 110 \mu L min^{-1}$ and $\dot{V}_{CO_2} = 61.5 \mu L min^{-1}$ . . . . .	126
4.16	$CO_2$ normalized concentration in the $H_2O$ -rich phase at different normalized axis location. The operating conditions are $P = 10$ MPa, $T = 303$ K and $\dot{V}_{H_2O} = 110 \mu L min^{-1}$ . The error bar corresponds to $\pm 3$ standard deviation. . . . .	128
4.17	$CO_2$ normalized concentrations in the $H_2O$ -rich phase at different normalized axis locations and FFT filtered curves. The operating conditions are $P = 10$ MPa, $T = 303$ K, $\dot{V}_{H_2O} = 110 \mu L min^{-1}$ . The average deviation between the fitted concentration profiles and the experimental points are 0.7%, 0.5%, 0.3%, 0.4% and 0.5%. . . . .	130
4.18	Normalized fitted concentrations profiles of $CO_2$ in the $H_2O$ -rich phase as a function of the normalized $z$ -axis position at 8 MPa and 303 K where $\dot{V}_{CO_2} = 40.5 \mu L min^{-1}$ (top) and $\dot{V}_{H_2O} = 200 \mu L min^{-1}$ (bottom). . . . .	131
4.19	Normalized fitted concentrations profiles of $CO_2$ in the $H_2O$ -rich phase as a function of the normalized $z$ -axis position at 9 MPa and 303 K where $\dot{V}_{CO_2} = 38.2 \mu L min^{-1}$ (top) and $\dot{V}_{H_2O} = 170 \mu L min^{-1}$ (bottom). . . . .	132

4.20	Normalized fitted concentrations profiles of $CO_2$ in the $H_2O$ -rich phase as a function of the normalized $z$ -axis position at 10 MPa and 303 K where $\dot{V}_{CO_2} = 49.2 \mu L \min^{-1}$ (top) and $\dot{V}_{H_2O} = 110 \mu L \min^{-1}$ (bottom).	132
4.21	Volumetric liquid mass transfer coefficient profiles versus the normalized $z$ -axis position at 8 MPa and 303 K where $\dot{V}_{CO_2} = 40.5 \mu L \min^{-1}$ (top) and $\dot{V}_{H_2O} = 200 \mu L \min^{-1}$ (bottom).	134
4.22	Volumetric liquid mass transfer coefficient profiles versus the normalized $z$ -axis position at 9 MPa and 303 K where $\dot{V}_{CO_2} = 38.2 \mu L \min^{-1}$ (top) and $\dot{V}_{H_2O} = 170 \mu L \min^{-1}$ (bottom).	135
4.23	Volumetric liquid mass transfer coefficient profiles versus the normalized $z$ -axis position at 10 MPa and 303 K where $\dot{V}_{CO_2} = 49.2 \mu L \min^{-1}$ (top) and $\dot{V}_{H_2O} = 110 \mu L \min^{-1}$ (bottom).	135
4.24	Image of bubbles at $z/D = 42$ and $z/D = 583$ at 10 MPa, 303 K, $\dot{V}_{CO_2} = 73.7 \mu L \min^{-1}$ and $\dot{V}_{H_2O} = 110 \mu L \min^{-1}$ . Note that the spherical bubble is deformed in the vertical direction because of the light refraction between the glass of the cylindrical capillary and the air. However, there is no deformation of the bubble diameter in line with the tube axis and of the outer diameter of the capillary. The bubble shrinkage is presented in yellow.	136
5.1	Colorimetric technique applied to the measurement of mass transfer coefficient in two-phase segmented flow at high pressure.	140
5.2	Schematic diagram of the experimental setup used to determine mass transfer coefficients in high-pressure two-phase flows.	141
5.3	Photos of the experimental setup used to determine mass transfer coefficients in high-pressure two-phase flows.	141
5.4	$CO_2$ volumetric flow rates computed in the microreactor (at 10 MPa and 303 K) from the volumetric flow-rate in the ISCO pump and $CO_2$ density change between the $CO_2$ pump and the reactor (blue line). $CO_2$ volumetric flow rate computed (at 10 MPa and 303 K) with the mass flow rates measurements (black points) and linear interpolation of these measurement values (black line).	144
5.5	Operating conditions in term of Reynolds number for the $H_2O$ flow rate (L) and the $CO_2$ flow rate (F).	145
5.6	Schematic overview of the optical measurement setup. A translating system makes it possible to acquire images at the different measurement spots.	146
5.7	Relative spectra power of the different CXB3590 LED types as a function of the wavelength.	147
5.8	Images of an air bubble placed inside the microreactor filled with water when the lighting system is not equipped with reflectors (a) and when the lighting system is equipped with two reflectors (b).	147
5.9	Scheme describing the camera shutter.	149
5.10	Scheme of two bubble pictures inside a micro-capillary when the shutter of the camera is adapted (a) and when the shutter of the camera is too high (b).	149
5.11	Visible absorbance spectra (Agilent Technologies Cary 8454) of pH buffer aqueous solutions (citric acid + sodium tri-citrate) with a bromophenol blue concentration equals to $0.03 \text{ mmol L}^{-1}$ .	151

---

5.12	Visible absorbance spectra (Agilent Technologies Cary 8454) of a pH buffer solution (citric acid + sodium tri-citrate) at different BPB concentrations (in $\text{mmol.L}^{-1}$ ). The pH of the buffer solution is 3.63. . . . .	152
5.13	Calibration curve linking the pH of the pH buffer solutions (citric acid + sodium tri-citrate) with the grey level of the images of these solutions placed inside the microreactor.[BPB]=0.8 $\text{mmol.L}^{-1}$ , shutter=300 $\mu\text{s}$ . . . . .	153
5.14	Diagram of the image processing and analysis performed in the Matlab program.	154
5.15	(a)Image of a two-phase segmented flow of $\text{CO}_2 + \text{H}_2\text{O} + \text{BPB}$ at 10 MPa and 303 K. (b) blank image in the bubble generation zone (spot 1). (c) Averaged image of the 1800 images taken in spot 1. . . . .	155
5.16	Average in the z-direction of the negative average image when the image is not straightened (a) and when the image is straightened (b). . . . .	156
5.17	Determination of the capillary edges. A test image is displayed in order to verify the capillary limit detected by the Matlab program. . . . .	157
5.18	Overlay of the extracted test (a) and blank (b) images when they are not well superimposed (c) and when they are well superimposed (d). . . . .	157
5.19	Successive steps for the acquisition of the bubble geometry and the greyscale in the liquid slugs. (a) test image. (b) 255-(blank image-test image). (c) Binarization with a variable threshold and opening (erosion + dilatation). (d) Convexity filter and gap filling. (e) and (f) visual verification. . . . .	158
5.20	Successive steps for the acquisition of the bubble geometry and the greyscale in the liquid slugs. (a) Detection of the bubble positions. (b) Detection of the unit-cell positions. (c) Greyscale at the capillary center inside the liquid slugs.	159
5.21	Greyscale at the center of the capillary inside the liquid slugs along the entire microreactor. The operating conditions are $P = 10 \text{ MPa}$ , $T = 303 \text{ K}$ , $\dot{V}_{\text{H}_2\text{O}} = 150 \text{ }\mu\text{L min}^{-1}$ and $\dot{V}_{\text{CO}_2} = 58.9 \text{ }\mu\text{L min}^{-1}$ . The color level is the number of greyscale values obtained at a certain distance $z$ . The darker the color, the more values were obtained for the point displayed in the figure. The dashed blue line corresponds to an exponential type model for the greyscale along the microreactor weighted with the color density. The number of greyscale values is equal to 1767540. . . . .	160
5.22	Greyscale profiles obtained in the $\text{H}_2\text{O}$ -rich slugs versus the $z$ -axis position at 10 MPa and 303 K where $\dot{V}_{\text{CO}_2} = 58.9 \text{ }\mu\text{L min}^{-1}$ . . . . .	161
5.23	pH profiles obtained in the $\text{H}_2\text{O}$ -rich slugs versus the $z$ -axis position at 10 MPa and 303 K where $\dot{V}_{\text{CO}_2} = 58.9 \text{ }\mu\text{L min}^{-1}$ . . . . .	162
5.24	pH as a function of $\text{CO}_2$ concentrations in the $\text{H}_2\text{O}$ -rich phase, calculated from Equation 5.13 and experimental values from Peng et al. (2013). . . . .	164
5.25	Normalized fitted concentrations profiles of $\text{CO}_2$ in the $\text{H}_2\text{O}$ -rich phase versus the normalized $z$ -axis position at 10 MPa and 303 K where $\dot{V}_{\text{CO}_2} = 58.9 \text{ }\mu\text{L min}^{-1}$ .	165
5.26	Characteristics of two-phase segmented flow in the microreactor. $L_B$ is the bubble length, $L_S$ the liquid slug length and $L_{UC}$ the unit-cell length. . . . .	166
5.27	Bubble velocity $U_B$ measured at different positions along the microreactor at 10 MPa and 303 K for $\dot{V}_{\text{CO}_2} = 58.9 \text{ }\mu\text{L min}^{-1}$ and $\dot{V}_{\text{H}_2\text{O}} = 250 \text{ }\mu\text{L min}^{-1}$ . . . . .	166
5.28	Comparison of the bubble velocity $U_B$ and the two-phase velocity $U_{TP}$ for each experiment at 10 MPa and 303 K. . . . .	167

5.29	Bubble length $L_B$ measured at different positions along the microreactor at 10 MPa and 303 K for $\dot{V}_{CO_2} = 58.9 \text{ } \mu\text{L min}^{-1}$ and $\dot{V}_{H_2O} = 250 \text{ } \mu\text{L min}^{-1}$ . The bubble length $L_B$ decreases from 372 $\mu\text{m}$ to 250 $\mu\text{m}$ . . . . .	168
5.30	Liquid slug length $L_S$ measured at different positions along the microreactor at 10 MPa and 303 K for $\dot{V}_{CO_2} = 58.9 \text{ } \mu\text{L min}^{-1}$ and $\dot{V}_{H_2O} = 250 \text{ } \mu\text{L min}^{-1}$ . . .	169
5.31	Liquid slug length $L_S$ measured at different positions along the microreactor at 10 MPa and 303 K for $\dot{V}_{CO_2} = 82.5 \text{ } \mu\text{L min}^{-1}$ and $\dot{V}_{H_2O} = 110 \text{ } \mu\text{L min}^{-1}$ . . .	169
5.32	Unit-cell length $L_{UC}$ measured at different positions along the microreactor at 10 MPa and 303 K for $\dot{V}_{CO_2} = 58.9 \text{ } \mu\text{L min}^{-1}$ and $\dot{V}_{H_2O} = 250 \text{ } \mu\text{L min}^{-1}$ . . .	170
5.33	Specific surface $a_L$ measured at different positions along the microreactor at 10 MPa and 303 K for $\dot{V}_{CO_2} = 58.9 \text{ } \mu\text{L min}^{-1}$ and $\dot{V}_{H_2O} = 250 \text{ } \mu\text{L min}^{-1}$ . . .	170
5.34	Bubble length $L_B$ at $z = 2.95 \text{ cm}$ at 10 MPa and 303 K as a function of the volumetric flow rate ratio $\dot{V}_{CO_2}/\dot{V}_{H_2O}$ . . . . .	171
5.35	Slug length $L_S$ at $z = 2.95 \text{ cm}$ at 10 MPa and 303 K as a function of the volumetric flow rate ratio $\dot{V}_{H_2O}/\dot{V}_{CO_2}$ . . . . .	172
5.36	Specific surface $a_L$ at $z = 2.95 \text{ cm}$ at 10 MPa and 303 K as a function of the volumetric flow rate ratio $\dot{V}_{CO_2}/\dot{V}_{H_2O}$ . . . . .	172
5.37	Evolution of the greyscale in the bubble generation zone at 10 MPa and 303 K for $\dot{V}_{CO_2} = 58.9 \text{ } \mu\text{L min}^{-1}$ and $\dot{V}_{H_2O} = 250 \text{ } \mu\text{L min}^{-1}$ . . . . .	173
5.38	Zoom in a liquid slug in the bubble generation zone at 10 MPa and 303 K for $\dot{V}_{CO_2} = 58.9 \text{ } \mu\text{L min}^{-1}$ and $\dot{V}_{H_2O} = 250 \text{ } \mu\text{L min}^{-1}$ . The triangular-shaped zone of higher greyscale intensity (in yellow) shows the mass transfer of $CO_2$ inside the liquid slug . . . . .	173
5.39	Flow evolution in the bubble generation zone at 10 MPa and 303 K for $\dot{V}_{CO_2} = 58.9 \text{ } \mu\text{L min}^{-1}$ and $\dot{V}_{H_2O} = 250 \text{ } \mu\text{L min}^{-1}$ . . . . .	174
5.40	Normalized fitted concentrations profiles of $CO_2$ in the $H_2O$ -rich phase versus the normalized $z$ -axis position at 10 MPa and 303 K at $\dot{V}_{CO_2} = 58.9 \text{ } \mu\text{L min}^{-1}$ . . . . .	175
5.41	Normalized fitted concentrations profiles of $CO_2$ in the $H_2O$ -rich phase versus the normalized $z$ -axis position at 10 MPa and 303 K at $\dot{V}_{H_2O} = 350 \text{ } \mu\text{L min}^{-1}$ . . . . .	175
5.42	Normalized fitted concentrations profiles of $CO_2$ in the $H_2O$ -rich phase versus the normalized $z$ -axis position at 10 MPa and 303 K at $\dot{V}_{CO_2} = 82.5 \text{ } \mu\text{L min}^{-1}$ . . . . .	176
5.43	Volumetric liquid mass transfer coefficient profiles versus the normalized $z$ -axis position at 10 MPa and 303 K at $\dot{V}_{CO_2} = 58.9 \text{ } \mu\text{L min}^{-1}$ . . . . .	177
5.44	Volumetric liquid mass transfer coefficient profiles versus the normalized $z$ -axis position at 10 MPa and 303 K at $\dot{V}_{H_2O} = 350 \text{ } \mu\text{L min}^{-1}$ . . . . .	177
5.45	Volumetric liquid mass transfer coefficient profiles versus the normalized $z$ -axis position at 10 MPa and 303 K at $\dot{V}_{CO_2} = 82.5 \text{ } \mu\text{L min}^{-1}$ . . . . .	178
A.1	Scheme describing the drilling speeds. . . . .	193
A.2	Dimensions of the microreactor divided in part 1 and part 2. Each dimensions are given in mm. . . . .	194
A.3	Drilling depth for the microreactor. . . . .	195

---

B.1	The first four steps of the Fast Fourier Transform (FFT). The operating conditions are $P = 10$ MPa, $T = 303$ K, $\dot{V}_{H_2O} = 110$ $\mu\text{L min}^{-1}$ and $\dot{V}_{CO_2} = 49$ $\mu\text{L min}^{-1}$ .	198
B.2	Experimental data points of $CO_2$ concentrations and FFT fitting for different number of frequencies selected. The operating conditions are $P = 10$ MPa, $T = 303$ K, $\dot{V}_{H_2O} = 110$ $\mu\text{L min}^{-1}$ and $\dot{V}_{CO_2} = 49$ $\mu\text{L min}^{-1}$ .	199
B.3	Determination of the number of frequencies for the FFT fitting. The operating conditions are $P = 10$ MPa, $T = 303$ K, $\dot{V}_{H_2O} = 110$ $\mu\text{L min}^{-1}$ and $\dot{V}_{CO_2} = 49$ $\mu\text{L min}^{-1}$ .	199
D.1	Standardized class distributions of molar ratios in the $H_2O$ -rich phase (blue) and standardized normal distribution (red) for all data and for each couple of pressure/temperature.	204
D.2	Sketches of the laser passing through the capillary tube when the laser is not well focused inside the capillary (left) and when the laser is well focused (right).	205
D.3	Standardized class distribution of greyscale values of all the measurement spots at 10 MPa, 303 K, $\dot{V}_{CO_2} = 58.9$ $\mu\text{L min}^{-1}$ and $\dot{V}_{H_2O} = 150$ $\mu\text{L min}^{-1}$ .	206
D.4	pH class distribution at $z=33.7$ mm, 10 MPa, 303 K, $\dot{V}_{CO_2} = 58.9$ $\mu\text{L min}^{-1}$ and $\dot{V}_{H_2O} = 150$ $\mu\text{L min}^{-1}$ .	207
E.1	Calibration curves linking pH of the buffer solutions (citric acid + sodium tri-citrate) with the greyscale of the images of these solutions placed inside the microreactor. [BPB]=0.2 mmol L <sup>-1</sup> and shutters=[100 $\mu\text{s}$ , 200 $\mu\text{s}$ , 300 $\mu\text{s}$ , 400 $\mu\text{s}$ , 500 $\mu\text{s}$ ].	210
E.2	Calibration curves linking pH of the buffer solutions (citric acid + sodium tri-citrate) with the greyscale of the images of these solutions placed inside the microreactor. [BPB]=0.8 mmol L <sup>-1</sup> and shutters=[100 $\mu\text{s}$ , 200 $\mu\text{s}$ , 300 $\mu\text{s}$ , 400 $\mu\text{s}$ , 500 $\mu\text{s}$ ].	211
E.3	Calibration curves linking pH of the buffer solutions (citric acid + sodium tri-citrate) with the greyscale of the images of these solutions placed inside the microreactor. [BPB]=2 mmol L <sup>-1</sup> and shutters=[100 $\mu\text{s}$ , 200 $\mu\text{s}$ , 300 $\mu\text{s}$ , 400 $\mu\text{s}$ , 500 $\mu\text{s}$ ].	211
E.4	Output file of the Matlab program containing the data on the bubbles of each image: the number of the working image (ima), the number of the bubble in this image (drop), a boolean which is true if the bubble touches the edge of the image (Dout), the coordinates (in pixel) of the ends of the bubble (Lx, Ly, Rx, Ry, Bx, By, Tx, Ty) where L is for left, R for right, B for bottom and T for top. It also contains the perimeter (per2D) and surface (surf2D) of the bubble on the image, as well as the surface (surfrev) and volume (volrev) of the real bubble obtained by the Guldin's theorem.	212
E.5	Output file of the Matlab program containing the number of the image (image), a position in pixels (x) and an associated greyscale (Greylevel).	213
E.6	Images of two-phase segmented flow of $CO_2$ and $H_2O$ at the first measurement spot for 10 MPa and 303 K where $\dot{V}_{CO_2} = 58.9$ $\mu\text{L min}^{-1}$ : (a) $\dot{V}_{H_2O} = 150$ $\mu\text{L min}^{-1}$ , (b) $\dot{V}_{H_2O} = 200$ $\mu\text{L min}^{-1}$ and (c) $\dot{V}_{H_2O} = 300$ $\mu\text{L min}^{-1}$ .	214
E.7	Images of two-phase segmented flow of $CO_2$ and $H_2O$ at the first measurement spot for 10 MPa and 303 K where $\dot{V}_{H_2O} = 350$ $\mu\text{L min}^{-1}$ : (a) $\dot{V}_{CO_2} = 76.6$ $\mu\text{L min}^{-1}$ , (b) $\dot{V}_{CO_2} = 94.2$ $\mu\text{L min}^{-1}$ and (c) $\dot{V}_{CO_2} = 111.9$ $\mu\text{L min}^{-1}$ .	214



---

E.8	Images of two-phase segmented flow of $CO_2$ and $H_2O$ at the first measurement spot for 10 MPa and 303 K where $\dot{V}_{CO_2} = 82.5 \text{ } \mu\text{L min}^{-1}$ : (a) $\dot{V}_{H_2O} = 110 \text{ } \mu\text{L min}^{-1}$ , (b) $\dot{V}_{H_2O} = 150 \text{ } \mu\text{L min}^{-1}$ , (c) $\dot{V}_{H_2O} = 200 \text{ } \mu\text{L min}^{-1}$ and (d) $\dot{V}_{H_2O} = 300 \text{ } \mu\text{L min}^{-1}$ . . . . .	215
E.9	Images of a two-phase segmented flow evolution of $CO_2$ and $H_2O$ at the first measurement spot for 10 MPa and 303 K where $\dot{V}_{CO_2} = 82.5 \text{ } \mu\text{L min}^{-1}$ and $\dot{V}_{H_2O} = 300 \text{ } \mu\text{L min}^{-1}$ (1/600 second between each image). . . . .	215



# List of Tables

1	Objectives of the thesis work. . . . .	20
1.1	Critical points of usual chemical compounds (Smith et al. (2013)) . . . . .	23
1.2	Density, viscosity and diffusivity order of magnitude for gas, liquid and super-critical fluids (Smith et al. (2013)). . . . .	23
1.3	Scale change effect on geometry, forces and transport properties between conventional macro scale systems and microfluidic systems. The term " $\propto$ " means "proportional to". Adapted from Silva (2014). . . . .	29
1.4	Dimensionless numbers employed in gas-liquid microfluidic studies. The subscript $\Phi$ corresponds to the investigated phase, gas or liquid. . . . .	39
1.5	Theoretical model, empirical model and dimensionless regression of the liquid mass transfer coefficient in a gas-liquid Taylor flow in microchannel ( <i>order of publication date</i> ). . . . .	56
1.6	Theoretical model, empirical model and dimensionless regression of the liquid mass transfer coefficient in a gas-liquid Taylor flow in microchannel ( <i>order of publication date</i> ). . . . .	57
2.1	Comparison of dimensionless numbers in the liquid phase along the micro-channel. As an example, $Re^*$ is calculated with the liquid mixture properties when thermodynamic equilibrium is reached, and $Re$ with the pure liquid properties at the inlet. The superficial velocities and the interfacial tensions are supposed constant. . . . .	82
2.2	Basic notations for the investigation of molar transport in a multicomponent system, adapted from Bird (2002). The introduction of the local molar average velocity $\mathbf{v}^*$ enables the molar fluxes to be written with respect to stationary axes and an average molar velocity. This simplification makes it easier to switch between Euler and Lagrangian modelling approaches. . . . .	84
2.3	Combined molar $CO_2$ flux expressions, $N_{CO_2}$ , where $C_{CO_2,i}^L$ , $C_{CO_2,i}^F$ are the $CO_2$ molar concentrations at the interface in the liquid and fluid sides, respectively, and $C_{CO_2}^{L,*}$ , $C_{CO_2}^{F,*}$ are the $CO_2$ molar concentration at thermodynamic equilibrium in the liquid and fluid phases, respectively. The units of the mass transfer coefficients are $m.s^{-1}$ . . . . .	85

---

3.1	Types of capillary tubes required for the microreactor and suppliers. ID (inner diameter). OD (outer diameter). . . . .	97
3.2	Listing of the 1/16" fittings employed to manufacture the microreactor. . . .	97
3.3	Glue, fluids and raw materials employed in the fabrication steps. . . . .	98
3.4	Tools used for the different fabrication steps. . . . .	98
4.1	Molecular bond vibrations of $CO_2$ and their characteristics. Wave numbers are taken from Hollas (2013). . . . .	116
4.2	Molecular bond vibrations of $H_2O$ and their characteristics. Wave numbers are taken from Shimanouchi et al. (1978). . . . .	117
4.3	Dimensions of the capillary tubes used ( $\mu m$ ). ID=inner diameter, OD=outer diameter. . . . .	120
4.4	Pressure drop in different tubes of the system with $\dot{V}_{H_2O} = 400 \mu L \min^{-1}$ and $\dot{V}_{CO_2} = 150 \mu L \min^{-1}$ . The viscosities of $CO_2$ and $H_2O$ are computed at 8 MPa and 303 K with the models presented in Chapter 2. $\mu_{CO_2}=56.4 \mu Pa s$ , $\mu_{H_2O}=799.2 \mu Pa s$ . . . . .	122
5.1	Pressure drop in different tubes of the system with $\dot{V}_{H_2O} = 350 \mu L \min^{-1}$ and $\dot{V}_{CO_2} = 112 \mu L \min^{-1}$ . The viscosities of $CO_2$ and $H_2O$ are computed at 10 MPa and 303 K with the models presented in Chapter 2. $\mu_{CO_2}=66.3 \mu Pa s$ , $\mu_{H_2O}=796.7 \mu Pa s$ . . . . .	143
A.1	Drill parameters used for the frame fabrication with the digital milling machine (TL-01). . . . .	193
C.1	Operating conditions employed in the Raman spectroscopy method at 303 K.	202
E.1	Operating conditions employed in the colorimetric method at 10 MPa and 303 K. . . . .	209

# Bibliography

- (Aasen et al., 2017) A. Aasen, M. Hammer, G. Skaugen, J. P. Jakobsen, and Ø. Wilhelmsen. “Thermodynamic models to accurately describe the PVTxy-behavior of water / carbon dioxide mixtures”. In: *Fluid Phase Equilibria* 442 (June 25, 2017), pp. 125–139 (cit. on pp. 58, 66, 67).
- (Abadie, 2013) T. Abadie. “Hydrodynamics of gas-liquid Taylor flow in microchannels”. PhD thesis. Nov. 14, 2013 (cit. on pp. 45, 46, 131, 133, 176).
- (Abolhasani et al., 2015) M. Abolhasani, E. Kumacheva, and A. Günther. “Peclet Number Dependence of Mass Transfer in Microscale Segmented Gas Liquid Flow”. In: *Industrial & Engineering Chemistry Research* 54.36 (Sept. 16, 2015), pp. 9046–9051 (cit. on p. 55).
- (Adamou et al., 2006) A. Adamou, J.-J. Letourneau, É. Rodier, R. David, J. Fages, and P. Guiraud. “Properties measurement of the binary ionic liquid bmimPF<sub>6</sub>/SC-CO<sub>2</sub> : 1 -Solubility and density”. In: *ISSF 2006 -8th International Symposium on Supercritical Fluids*. Kyoto, Japan: Kumamoto University, Nov. 2006, 6 p. (Cit. on pp. 70–72, 74, 76, 78, 81).
- (Akbar et al., 2002) M. K. Akbar, D. A. Plummer, and S. M. Ghiaasiaan. “Gas-Liquid Two-Phase Flow Regimes in Microchannels”. In: (Jan. 1, 2002), pp. 527–534 (cit. on pp. 38, 39, 41).
- (Albrand et al., 2020) P. Albrand, C. Julcour, V. Gerbaud, and A.-M. Billet. “Accurate hydrogenated vegetable oil viscosity predictions for monolith reactor simulations”. In: *Chemical Engineering Science* 214 (Mar. 16, 2020), p. 115388 (cit. on pp. 28, 30).
- (Andersen et al., 1992) G. Andersen, A. Probst, L. Murray, and S. Butler. “An Accurate PVT Model for Geothermal Fluids as Represented by H<sub>2</sub>O-NaCl-CO<sub>2</sub>”. In: *Mixtures, Proceedings 17th Workshop on Geothermal Reservoir Engineering*. 1992, pp. 239–248 (cit. on p. 79).
- (Anderson, 1977) G. R. Anderson. “The Raman spectra of carbon dioxide in liquid water and water-d<sub>2</sub>”. In: *The Journal of Physical Chemistry* 81.3 (Feb. 1, 1977), pp. 273–276 (cit. on p. 127).

- 
- (Andersson et al., 2016) M. Andersson, K. Hjort, and L. Klintberg. “Fracture strength of glass chips for high-pressure microfluidics”. In: *Journal of Micromechanics and Microengineering* 26.9 (2016), p. 095009 (cit. on p. 32).
- (Andersson et al., 2018) M. Andersson, I. Rodriguez-Meizoso, C. Turner, K. Hjort, and L. Klintberg. “Dynamic pH determination at high pressure of aqueous additive mixtures in contact with dense CO<sub>2</sub>”. In: *The Journal of Supercritical Fluids* 136 (June 1, 2018), pp. 95–101 (cit. on pp. 32, 93, 138).
- (Ari et al., 2020) J. Ari, G. Louvet, Y. Ledemi, F. Célarié, S. Morais, B. Bureau, S. Marre, V. Nazabal, and Y. Messaddeq. “Anodic bonding of mid-infrared transparent germanate glasses for high pressure - high temperature microfluidic applications”. In: *Science and Technology of Advanced Materials* 21.1 (Jan. 31, 2020). Publisher: Taylor & Francis \_eprint: <https://doi.org/10.1080/14686996.2019.1702861>, pp. 11–24 (cit. on p. 32).
- (Arora et al., 2020) D. Arora, R. Sedev, C. C. Beh, C. Priest, and N. R. Foster. “Precipitation of Drug Particles Using a Gas Antisolvent Process on a High-Pressure Microfluidic Platform”. In: *Industrial & Engineering Chemistry Research* 59.25 (June 24, 2020). Publisher: American Chemical Society, pp. 11905–11913 (cit. on p. 36).
- (Assael et al., 1994) M. J. Assael and S. K. Polimatidou. “Measurements of the viscosity of alcohols in the temperature range 290–340 K at pressures up to 30 MPa”. In: *International Journal of Thermophysics* 15.1 (Jan. 1, 1994), pp. 95–107 (cit. on p. 74).
- (Assmann et al., 2012) N. Assmann, S. Kaiser, and P. Rudolf von Rohr. “Supercritical extraction of vanillin in a microfluidic device”. In: *The Journal of Supercritical Fluids* 67 (July 1, 2012), pp. 149–154 (cit. on pp. 31–34).
- (Aussillous et al., 2000) P. Aussillous and D. Quéré. “Quick deposition of a fluid on the wall of a tube”. In: *Physics of Fluids* 12.10 (Sept. 6, 2000). Publisher: American Institute of Physics, pp. 2367–2371 (cit. on p. 46).
- (Avila et al., 2005) P. Avila, M. Montes, and E. E. Miró. “Monolithic reactors for environmental applications: A review on preparation technologies”. In: *Chemical Engineering Journal* 109.1 (May 1, 2005), pp. 11–36 (cit. on p. 30).
- (Bachu et al., 2003) S. Bachu and J. J. Adams. “Sequestration of CO<sub>2</sub> in geological media in response to climate change: capacity of deep saline aquifers to sequester CO<sub>2</sub> in solution”. In: *Energy Conversion and Management* 44.20 (Dec. 1, 2003), pp. 3151–3175 (cit. on pp. 75, 77).
- (Balac, 2011) S. Balac. « La transformée de Fourier vue sous l’angle du calcul numérique ». In : (1<sup>er</sup> jan. 2011) (cit. on p. 197).
- (Basire et al., 2017) M. Basire, F. Mouhat, G. Fraux, A. Bordage, J.-L. Hazemann, M. Louvel, R. Spezia, S. Bonella, and R. Vuilleumier. “Fermi resonance in CO<sub>2</sub>: Mode assignment and quantum nuclear effects from first principles molecular dynamics”. In: *The Journal of Chemical Physics* 146.13 (Apr. 3, 2017). Publisher: American Institute of Physics, p. 134102 (cit. on p. 116).
- (Baten et al., 2004) J. M. van Baten and R. Krishna. “CFD simulations of mass transfer from Taylor bubbles rising in circular capillaries”. In: *Chemical Engineering Science* 59.12 (June 1, 2004), pp. 2535–2545 (cit. on pp. 49, 53–55, 176).

- (Batzle et al., 1992) M. Batzle and Z. Wang. “Seismic properties of pore fluids”. In: *GEO-PHYSICS* 57.11 (Nov. 1, 1992), pp. 1396–1408 (cit. on p. 79).
- (Bercic et al., 1997) G. Bercic and A. Pintar. “The role of gas bubbles and liquid slug lengths on mass transport in the Taylor flow through capillaries”. In: *Chemical Engineering Science* 52.21 (Nov. 1, 1997), pp. 3709–3719 (cit. on pp. 52–54).
- (Bird, 2002) L. Bird Stewart. “Transport phenomena”. In: *Applied Mechanics Reviews* 55.1 (Jan. 1, 2002). Publisher: American Society of Mechanical Engineers Digital Collection, R1–R4 (cit. on p. 84).
- (Blanch-Ojea et al., 2012) R. Blanch-Ojea, R. M. Tiggelaar, J. Pallares, F. X. Grau, and J. G. E. Gardeniers. “Flow of CO<sub>2</sub>-ethanol and of CO<sub>2</sub>-methanol in a non-adiabatic microfluidic T-junction at high pressures”. In: *Microfluidics and Nanofluidics* 12.6 (May 1, 2012), pp. 927–940 (cit. on pp. 33, 41).
- (Blom et al., 2001) M. T. Blom, E. Chmela, J. G. E. Gardeniers, J. W. Berenschot, M. Elwenspoek, R. Tjissen, and A. v. d. Berg. “Local anodic bonding of Kovar to Pyrex aimed at high-pressure, solvent-resistant microfluidic connections”. In: *Journal of Micromechanics and Microengineering* 11.4 (2001), p. 382 (cit. on p. 33).
- (Bretherton, 1961) F. P. Bretherton. “The motion of long bubbles in tubes”. In: *Journal of Fluid Mechanics* 10.2 (Mar. 1961). Publisher: Cambridge University Press, pp. 166–188 (cit. on pp. 46, 87).
- (Briones et al., 1987) J. A. Briones, J. C. Mullins, M. C. Thies, and B. .-.-U. Kim. “Ternary phase equilibria for acetic acid-water mixtures with supercritical carbon dioxide”. In: *Fluid Phase Equilibria* 36 (Oct. 2, 1987), pp. 235–246 (cit. on p. 67).
- (Campos Domínguez et al., 2016) C. Campos Domínguez and T. Gamse. “Process intensification by the use of micro devices for liquid fractionation with supercritical carbon dioxide”. In: *Chemical Engineering Research and Design*. The 15th European Conference on Mixing 108 (Apr. 1, 2016), pp. 139–145 (cit. on pp. 31–35).
- (Chambers et al., 2007) R. D. Chambers, M. A. Fox, G. Sandford, J. Trmcic, and A. Goeta. “Elemental fluorine: Part 20. Direct fluorination of deactivated aromatic systems using microreactor techniques”. In: *Journal of Fluorine Chemistry* 128.1 (Jan. 1, 2007), pp. 29–33 (cit. on p. 32).
- (Chang et al., 1997) C. J. Chang, C.-Y. Day, C.-M. Ko, and K.-L. Chiu. “Densities and P-x-y diagrams for carbon dioxide dissolution in methanol, ethanol, and acetone mixtures”. In: *Fluid Phase Equilibria* 131.1 (May 15, 1997), pp. 243–258 (cit. on p. 69).
- (J.-D. Chen, 1986) J.-D. Chen. “Measuring the film thickness surrounding a bubble inside a capillary”. In: *Journal of Colloid and Interface Science* 109.2 (Feb. 1, 1986), pp. 341–349 (cit. on p. 46).
- (L. Chen et al., 2006) L. Chen, Y. S. Tian, and T. G. Karayiannis. “The effect of tube diameter on vertical two-phase flow regimes in small tubes”. In: *International Journal of Heat and Mass Transfer* 49.21 (Oct. 1, 2006), pp. 4220–4230 (cit. on pp. 38, 39).

- 
- (Choi et al., 2011) C. Choi, D. I. Yu, and M. Kim. “Surface wettability effect on flow pattern and pressure drop in adiabatic two-phase flows in rectangular microchannels with T-junction mixer”. In: *Experimental Thermal and Fluid Science* 35.6 (Sept. 1, 2011), pp. 1086–1096 (cit. on p. 43).
- (Couto et al., 2014) R. Couto, S. Chambon, C. Aymonier, E. Mignard, B. Pavageau, A. Erriguible, and S. Marre. “Microfluidic supercritical antisolvent continuous processing and direct spray-coating of poly(3-hexylthiophene) nanoparticles for OFET devices”. In: *Chemical Communications* 51.6 (Dec. 18, 2014). Publisher: The Royal Society of Chemistry, pp. 1008–1011 (cit. on p. 36).
- (Dang et al., 2013) M. Dang, J. Yue, G. Chen, and Q. Yuan. “Formation characteristics of Taylor bubbles in a microchannel with a converging shape mixing junction”. In: *Chemical Engineering Journal* 223 (May 1, 2013), pp. 99–109 (cit. on p. 43).
- (Deleau et al., 2020) T. Deleau, M. H. H. Fechter, J.-J. Letourneau, S. Camy, J. Aubin, A. S. Braeuer, and F. Espitalier. “Determination of mass transfer coefficients in high-pressure two-phase flows in capillaries using Raman spectroscopy”. In: *Chemical Engineering Science* 228 (Dec. 31, 2020), p. 115960 (cit. on pp. 20, 217).
- (Diamond et al., 2003) L. Diamond and N. Akinfiev. *Solubility of CO<sub>2</sub> in water from -1.5 to 100 Celsius degree and from 0.1 to 100 MPa: Evaluation of literature data and thermodynamic modelling*. Vol. 208. June 1, 2003. 265 pp. (cit. on p. 58).
- (Diaz et al., 2009) M. S. Diaz and E. A. Brignole. “Modeling and optimization of supercritical fluid processes”. In: *The Journal of Supercritical Fluids*. 20th Year Anniversary Issue of the Journal of Supercritical Fluids 47.3 (Jan. 1, 2009), pp. 611–618 (cit. on p. 21).
- (Dietrich et al., 2013) N. Dietrich, K. Loubière, M. Jimenez, G. Hébrard, and C. Gourdon. “A new direct technique for visualizing and measuring gas–liquid mass transfer around bubbles moving in a straight millimetric square channel”. In: *Chemical Engineering Science*. 11th International Conference on Gas-Liquid and Gas-Liquid-Solid Reactor Engineering 100 (Aug. 30, 2013), pp. 172–182 (cit. on p. 55).
- (Dittmar et al., 2002) D. Dittmar, S. B. Oei, and R. Eggers. “Interfacial Tension and Density of Ethanol in Contact with Carbon Dioxide”. In: *Chemical Engineering & Technology* 25.1 (Jan. 1, 2002), pp. 23–27 (cit. on p. 76).
- (Ehrfeld et al., 2000) W. Ehrfeld, V. Hessel, S. Kiese-walter, H. Löwe, T. Richter, and J. Schiewe. “Implementation of Microreaction Technology in Process Engineering”. In: *Microreaction Technology: Industrial Prospects*. Ed. by W. Ehrfeld. Berlin, Heidelberg: Springer, 2000, pp. 14–34 (cit. on p. 28).
- (Enick et al., 1990) R. M. Enick and S. M. Klara. “CO<sub>2</sub> Solubility in water and brine under reservoir conditions”. In: *Chemical Engineering Communications* 90.1 (Apr. 1, 1990), pp. 23–33 (cit. on pp. 67, 68, 79, 163).
- (Eskin et al., 2012) D. Eskin and F. Mostowfi. “A model of a bubble train flow accompanied with mass transfer through a long microchannel”. In: *International Journal of Heat and Fluid Flow* 33.1 (Feb. 1, 2012), pp. 147–155 (cit. on p. 55).



- (Fenghour et al., 1998) A. Fenghour, W. A. Wakeham, and V. Vesovic. “The Viscosity of Carbon Dioxide”. In: *Journal of Physical and Chemical Reference Data* 27.1 (Jan. 1, 1998). Publisher: American Institute of Physics, pp. 31–44 (cit. on p. 75).
- (Fouilland et al., 2010) T. S. Fouilland, D. F. Fletcher, and B. S. Haynes. “Film and slug behaviour in intermittent slug-annular microchannel flows”. In: *Chemical Engineering Science* 65.19 (Oct. 1, 2010), pp. 5344–5355 (cit. on p. 43).
- (Fries et al., 2008a) D. M. Fries, F. Trachsel, and P. R. von Rohr. “Segmented gas-liquid flow characterization in rectangular microchannels”. In: *International Journal of Multiphase Flow* 34.12 (Dec. 2008). WOS:000261281100002, pp. 1108–1118 (cit. on p. 54).
- (Fries et al., 2008b) D. M. Fries, F. Trachsel, and P. R. von Rohr. “Segmented gas-liquid flow characterization in rectangular microchannels”. In: *International Journal of Multiphase Flow* 34.12 (Dec. 1, 2008), pp. 1108–1118 (cit. on p. 46).
- (Ganapathy et al., 2014) H. Ganapathy, A. Shooshtari, S. Dessiatoun, M. Alshehhi, and M. Ohadi. “Fluid flow and mass transfer characteristics of enhanced CO<sub>2</sub> capture in a minichannel reactor”. In: *Applied Energy* 119 (Apr. 15, 2014), pp. 43–56 (cit. on p. 55).
- (Garcia, 2001) J. E. Garcia. “Density of aqueous solutions of CO<sub>2</sub>”. In: (Oct. 10, 2001) (cit. on pp. 77, 79).
- (Garstecki et al., 2006) P. Garstecki, M. J. Fuerstman, H. A. Stone, and G. M. Whitesides. “Formation of droplets and bubbles in a microfluidic T-junction—scaling and mechanism of break-up”. In: *Lab on a Chip* 6.3 (2006), pp. 437–446 (cit. on pp. 43, 44, 49, 131, 171).
- (Gavoille et al., 2019) T. Gavoille, N. Pannacci, G. Bergeot, C. Marliere, and S. Marre. “Microfluidic approaches for accessing thermophysical properties of fluid systems”. In: *Reaction Chemistry & Engineering* 4.10 (Sept. 27, 2019). Publisher: The Royal Society of Chemistry, pp. 1721–1739 (cit. on p. 37).
- (Gonçalves et al., 2010) F. A. M. M. Gonçalves, A. R. Trindade, C. S. M. F. Costa, J. C. S. Bernardo, I. Johnson, I. M. A. Fonseca, and A. G. M. Ferreira. “PVT, viscosity, and surface tension of ethanol: New measurements and literature data evaluation”. In: *The Journal of Chemical Thermodynamics* 42.8 (Aug. 1, 2010), pp. 1039–1049 (cit. on p. 72).
- (Günther et al., 2004) A. Günther, S. A. Khan, M. Thalmann, F. Trachsel, and K. F. Jensen. “Transport and reaction in microscale segmented gas-liquid flow”. In: *Lab on a Chip* 4.4 (July 19, 2004). Publisher: The Royal Society of Chemistry, pp. 278–286 (cit. on p. 48).
- (Haase et al., 2016) S. Haase, D. Y. Murzin, and T. Salmi. “Review on hydrodynamics and mass transfer in minichannel wall reactors with gas-liquid Taylor flow”. In: *Chemical Engineering Research and Design* 113 (Sept. 1, 2016), pp. 304–329 (cit. on p. 49).
- (Han et al., 2009) Y. Han and N. Shikazono. “Measurement of liquid film thickness in micro square channel”. In: *International Journal of Multiphase Flow* 35.10 (Oct. 1, 2009), pp. 896–903 (cit. on p. 43).
- (Hassim et al., 2019) N. Hassim, M. Markom, M. I. Rosli, and S. Harun. “Scale-up criteria and economic analysis for supercritical fluid extraction of *Phyllanthus niruri*”. In: *Chemical Engineering and Processing - Process Intensification* 139 (May 1, 2019), pp. 14–22 (cit. on pp. 7, 21, 26).

- 
- (Heiszwolf et al., 2001) J. J. Heiszwolf, M. T. Kreutzer, M. G. van den Eijnden, F. Kapteijn, and J. A. Moulijn. “Gas-liquid mass transfer of aqueous Taylor flow in monoliths”. In: *Catalysis Today*. Structured Catalysts and Reactors 69.1 (Sept. 15, 2001), pp. 51–55 (cit. on pp. 53, 54).
- (Heuven et al., 1963) J. W. van Heuven and W. J. Beek. “Gas absorption in narrow gas lifts”. In: *Chemical Engineering Science* 18.7 (July 1, 1963), pp. 377–389 (cit. on p. 52).
- (Hollas, 2013) J. M. Hollas. *High Resolution Spectroscopy*. Google-Books-ID: Pbn8BAAAQBAJ. Butterworth-Heinemann, Oct. 22, 2013. 655 pp. (cit. on p. 116).
- (Hou et al., 2013) S.-X. Hou, G. C. Maitland, and J. P. M. Trusler. “Measurement and modeling of the phase behavior of the (carbon dioxide+water) mixture at temperatures from 298.15K to 448.15K”. In: *The Journal of Supercritical Fluids* 73 (Jan. 1, 2013), pp. 87–96 (cit. on p. 67).
- (Iglesia et al., 2007) O. de la Iglesia, V. Sebastián, R. Mallada, G. Nikolaidis, J. Coronas, G. Kolb, R. Zapf, V. Hessel, and J. Santamaría. “Preparation of Pt/ZSM-5 films on stainless steel microreactors”. In: *Catalysis Today*. “Topical Applications of Micro-reactor Engineering” held at AIChE Spring Conference, Orlando, Florida, USA, April 23-27, 2006 125.1 (July 15, 2007), pp. 2–10 (cit. on p. 32).
- (Irlandoust et al., 1992) S. Irlandoust, S. Ertlé, and B. Andersson. “Gas-liquid mass transfer in taylor flow through a capillary”. In: *The Canadian Journal of Chemical Engineering* 70.1 (Feb. 1, 1992), pp. 115–119 (cit. on pp. 49, 52).
- (Jaouhari et al., 2020) T. Jaouhari, F. Zhang, T. Tassaing, S. Fery-Forgues, C. Aymonier, S. Marre, and A. Erriguible. “Process intensification for the synthesis of ultra-small organic nanoparticles with supercritical CO<sub>2</sub> in a microfluidic system”. In: *Chemical Engineering Journal* 397 (Oct. 1, 2020), p. 125333 (cit. on p. 36).
- (Jennings et al., 1991) D. W. Jennings, R. J. Lee, and A. S. Teja. “Vapor-liquid equilibria in the carbon dioxide + ethanol and carbon dioxide + 1-butanol systems”. In: *Journal of Chemical & Engineering Data* 36.3 (July 1, 1991). Publisher: American Chemical Society, pp. 303–307 (cit. on p. 69).
- (Jia et al., 2016) H. W. Jia and P. Zhang. “Investigation of the Taylor bubble under the effect of dissolution in microchannel”. In: *Chemical Engineering Journal* 285 (Feb. 1, 2016), pp. 252–263 (cit. on p. 54).
- (Joung et al., 2001) S. N. Joung, C. W. Yoo, H. Y. Shin, S. Y. Kim, K.-P. Yoo, C. S. Lee, and W. S. Huh. “Measurements and correlation of high-pressure VLE of binary CO<sub>2</sub>-alcohol systems (methanol, ethanol, 2-methoxyethanol and 2-ethoxyethanol)”. In: *Fluid Phase Equilibria*. Proceedings of the 14th symposium on thermophysical properties 185.1 (July 30, 2001), pp. 219–230 (cit. on p. 69).
- (Kashid et al., 2011) M. N. Kashid, A. Renken, and L. Kiwi-Minsker. “Gas-liquid and liquid-liquid mass transfer in microstructured reactors”. In: *Chemical Engineering Science* 66.17 (Sept. 1, 2011), pp. 3876–3897 (cit. on p. 49).

- (Kawahara et al., 2002) A. Kawahara, P. M. .-Y. Chung, and M. Kawaji. “Investigation of two-phase flow pattern, void fraction and pressure drop in a microchannel”. In: *International Journal of Multiphase Flow* 28.9 (Sept. 1, 2002), pp. 1411–1435 (cit. on p. 54).
- (Keybl et al., 2011) J. Keybl and K. F. Jensen. “Microreactor System for High-Pressure Continuous Flow Homogeneous Catalysis Measurements”. In: *Industrial & Engineering Chemistry Research* 50.19 (Oct. 5, 2011), pp. 11013–11022 (cit. on p. 32).
- (Klima et al., 2019) T. C. Klima and A. S. Braeuer. “Vapor-liquid-equilibria of fuel-nitrogen systems at engine-like conditions measured with Raman spectroscopy in micro capillaries”. In: *Fuel* 238 (Feb. 15, 2019), pp. 312–319 (cit. on p. 37).
- (Kockmann, 2007) N. Kockmann. *Transport Phenomena in Micro Process Engineering*. Google-Books-ID: 40fQkEDXiQ0C. Springer Science & Business Media, Nov. 12, 2007. 382 pp. (cit. on p. 93).
- (Kolb et al., 1991) W. B. Kolb and R. L. Cerro. “Coating the inside of a capillary of square cross section”. In: *Chemical Engineering Science* 46.9 (Jan. 1, 1991), pp. 2181–2195 (cit. on p. 46).
- (Koschel et al., 2006) D. Koschel, J.-Y. Coxam, L. Rodier, and V. Majer. “Enthalpy and solubility data of CO<sub>2</sub> in water and NaCl(aq) at conditions of interest for geological sequestration”. In: *Fluid Phase Equilibria* 247.1 (Sept. 15, 2006), pp. 107–120 (cit. on p. 67).
- (Kreutzer et al., 2005) M. T. Kreutzer, F. Kapteijn, J. A. Moulijn, and J. J. Heiszwolf. “Multi-phase monolith reactors: Chemical reaction engineering of segmented flow in microchannels”. In: *Chemical Engineering Science*. 7th International Conference on Gas-Liquid and Gas-Liquid-Solid Reactor Engineering 60.22 (Nov. 1, 2005), pp. 5895–5916 (cit. on pp. 42, 54).
- (Kuhn et al., 2012) S. Kuhn and K. F. Jensen. “A pH-Sensitive Laser-Induced Fluorescence Technique To Monitor Mass Transfer in Multiphase Flows in Microfluidic Devices”. In: *Industrial & Engineering Chemistry Research* 51.26 (July 4, 2012), pp. 8999–9006 (cit. on p. 54).
- (Lebedev et al., 2015) A. E. Lebedev, A. M. Katalevich, and N. V. Menshutina. “Modeling and scale-up of supercritical fluid processes. Part I: Supercritical drying”. In: *The Journal of Supercritical Fluids*. Aerogels: synthesis and applications 106 (Nov. 1, 2015), pp. 122–132 (cit. on pp. 7, 21, 26).
- (Leclerc et al., 2010) A. Leclerc, R. Philippe, V. Houzelot, D. Schweich, and C. de Bellefon. “Gas-liquid Taylor flow in square micro-channels: New inlet geometries and interfacial area tuning”. In: *Chemical Engineering Journal* 165.1 (Nov. 15, 2010), pp. 290–300 (cit. on p. 43).
- (Lefortier et al., 2012) S. G. R. Lefortier, P. J. Hamersma, A. Bardow, and M. T. Kreutzer. “Rapid microfluidic screening of CO<sub>2</sub> solubility and diffusion in pure and mixed solvents”. In: *Lab on a Chip* 12.18 (Aug. 14, 2012), pp. 3387–3391 (cit. on p. 55).
- (Leung et al., 2010) S. S. Y. Leung, Y. Liu, D. F. Fletcher, and B. S. Haynes. “Heat transfer in well-characterised Taylor flow”. In: *Chemical Engineering Science* 65.24 (Dec. 15, 2010), pp. 6379–6388 (cit. on pp. 133, 176).

- 
- (Li et al., 2014) C. Li, C. Zhu, Y. Ma, D. Liu, and X. Gao. “Experimental study on volumetric mass transfer coefficient of CO<sub>2</sub> absorption into MEA aqueous solution in a rectangular microchannel reactor”. In: *International Journal of Heat and Mass Transfer* 78 (Nov. 1, 2014), pp. 1055–1059 (cit. on p. 42).
- (D. Liu et al., 2008) D. Liu and S. Wang. “Hydrodynamics of Taylor flow in noncircular capillaries”. In: *Chemical Engineering and Processing: Process Intensification* 47.12 (Nov. 1, 2008), pp. 2098–2106 (cit. on p. 43).
- (D. Liu et al., 2011) D. Liu and S. Wang. “Gas Liquid Mass Transfer in Taylor Flow through Circular Capillaries”. In: *Industrial & Engineering Chemistry Research* 50.4 (Feb. 16, 2011), pp. 2323–2330 (cit. on p. 54).
- (N. Liu et al., 2012) N. Liu, C. Aymonier, C. Lecoutre, Y. Garrabos, and S. Marre. “Microfluidic approach for studying CO<sub>2</sub> solubility in water and brine using confocal Raman spectroscopy”. In: *Chemical Physics Letters* 551 (Nov. 1, 2012), pp. 139–143 (cit. on p. 37).
- (N. Liu, 2013) N. Liu. “Supercritical Microfluidics for understanding CO<sub>2</sub> / water systems under pressure and temperature : Application to the sustainable management of the anthropogenic CO<sub>2</sub>”. In: (Nov. 22, 2013) (cit. on pp. 116, 117).
- (Luther et al., 2014) S. K. Luther, S. Will, and A. Braeuer. “Phase-specific Raman spectroscopy for fast segmented microfluidic flows”. In: *Lab on a Chip* 14.16 (July 14, 2014), pp. 2910–2913 (cit. on p. 124).
- (Luther et al., 2012) S. K. Luther and A. Braeuer. “High-pressure microfluidics for the investigation into multi-phase systems using the supercritical fluid extraction of emulsions (SFEE)”. In: *The Journal of Supercritical Fluids* 65 (May 1, 2012), pp. 78–86 (cit. on pp. 31, 93).
- (Luther et al., 2015) S. K. Luther, S. Stehle, K. Weihs, S. Will, and A. Braeuer. “Determination of Vapor–Liquid Equilibrium Data in Microfluidic Segmented Flows at Elevated Pressures Using Raman Spectroscopy”. In: *Analytical Chemistry* 87.16 (Aug. 18, 2015), pp. 8165–8172 (cit. on p. 32).
- (Macedo Portela da Silva et al., 2014) N. Macedo Portela da Silva, J.-J. Letourneau, F. Espitalier, and L. Prat. “Transparent and Inexpensive Microfluidic Device for Two-Phase Flow Systems with High-Pressure Performance”. In: *Chemical Engineering & Technology* 37.11 (2014), pp. 1929–1937 (cit. on pp. 33, 59, 94).
- (Marre et al., 2009) S. Marre, C. Aymonier, P. Subra, and E. Mignard. “Dripping to jetting transitions observed from supercritical fluid in liquid microflows”. In: *Applied Physics Letters* 95.13 (Sept. 28, 2009), p. 134105 (cit. on pp. 40, 41, 58, 73).
- (Marre et al., 2012) S. Marre, Y. Roig, and C. Aymonier. “Supercritical microfluidics: Opportunities in flow-through chemistry and materials science”. In: *The Journal of Supercritical Fluids*. Special Edition on the Occasion of Gerd Brunner’s 70th Birthday 66 (June 1, 2012), pp. 251–264 (cit. on pp. 33, 34).
- (Marre et al., 2010) S. Marre, A. Adamo, S. Basak, C. Aymonier, and K. F. Jensen. “Design and Packaging of Microreactors for High Pressure and High Temperature Applications”. In: *Industrial & Engineering Chemistry Research* 49.22 (Nov. 17, 2010), pp. 11310–11320 (cit. on pp. 30, 32, 33, 93).

- (Martin, 2016) A. Martin. “Conception d’un dispositif microfluidique résistant à la pression pour la caractérisation de l’hydrodynamique de mélanges en conditions proches du domaine supercritique : étude du binaire partiellement miscible CO<sub>2</sub>-Ethanol”. PhD thesis. Nov. 22, 2016 (cit. on pp. 4, 5, 17, 19, 66, 70).
- (Martin et al., 2018) A. Martin, S. Camy, and J. Aubin. “Hydrodynamics of CO<sub>2</sub>-ethanol flow in a microchannel under elevated pressure”. In: *Chemical Engineering Science* 178 (Mar. 16, 2018), pp. 297–311 (cit. on pp. 41, 42, 45, 58, 133).
- (Martin et al., 2016) A. Martin, S. Teychené, S. Camy, and J. Aubin. “Fast and inexpensive method for the fabrication of transparent pressure-resistant microfluidic chips”. In: *Microfluidics and Nanofluidics* 20.6 (June 1, 2016), p. 92 (cit. on pp. 31–33).
- (Maurice et al., 2020) A. Maurice, J. Theisen, and J.-C. P. Gabriel. “Microfluidic lab-on-chip advances for liquid–liquid extraction process studies”. In: *Current Opinion in Colloid & Interface Science* 46 (Apr. 1, 2020), pp. 20–35 (cit. on p. 30).
- (Mazurczyk et al., 2008) R. Mazurczyk, G. El Khoury, V. Dugas, B. Hannes, E. Laurenceau, M. Cabrera, S. Krawczyk, E. Souteyrand, J. P. Cloarec, and Y. Chevolot. “Low-cost, fast prototyping method of fabrication of the microreactor devices in soda-lime glass”. In: *Sensors and Actuators B: Chemical* 128.2 (Jan. 15, 2008), pp. 552–559 (cit. on p. 32).
- (McBride-Wright et al., 2015) M. McBride-Wright, G. C. Maitland, and J. P. M. Trusler. “Viscosity and Density of Aqueous Solutions of Carbon Dioxide at Temperatures from (274 to 449) K and at Pressures up to 100 MPa”. In: *Journal of Chemical & Engineering Data* 60.1 (Jan. 8, 2015). Publisher: American Chemical Society, pp. 171–180 (cit. on p. 81).
- (Menech et al., 2008) M. D. Menech, P. Garstecki, F. Jousse, and H. A. Stone. “Transition from squeezing to dripping in a microfluidic T-shaped junction”. In: *Journal of Fluid Mechanics* 595 (Jan. 2008), pp. 141–161 (cit. on pp. 39, 44).
- (Mo et al., 2020) Y. Mo, Z. Lu, G. Rughoobur, P. Patil, N. Gershenfeld, A. I. Akinwande, S. L. Buchwald, and K. F. Jensen. “Microfluidic electrochemistry for single-electron transfer redox-neutral reactions”. In: *Science* 368.6497 (June 19, 2020). Publisher: American Association for the Advancement of Science Section: Report, pp. 1352–1357 (cit. on p. 28).
- (Molla et al., 2013) S. Molla, D. Eskin, and F. Mostowfi. “Two-Phase Flow in Microchannels: The Case of Binary Mixtures”. In: *Industrial & Engineering Chemistry Research* 52.2 (Jan. 16, 2013), pp. 941–953 (cit. on p. 54).
- (Mukhopadhyay, 2020) S. Mukhopadhyay. “Short Review on Microfluidic Lab-on-a-Chip Systems for Future Applications in Space Technology”. In: *Journal of Nanoscience Nanotechnology and Applications* 10.1 (June 11, 2020). Number: 1, pp. 26–30 (cit. on p. 30).
- (Müller et al., 2005) A. Müller, V. Cominos, V. Hessel, B. Horn, J. Schürer, A. Ziogas, K. Jähnisch, V. Hillmann, V. Großer, K. A. Jam, A. Bazzanella, G. Rinke, and M. Kraut. “Fluidic bus system for chemical process engineering in the laboratory and for small-scale production”. In: *Chemical Engineering Journal*. Proceedings of the XVI International Conference on Chemical Reactors 107.1 (Mar. 15, 2005), pp. 205–214 (cit. on p. 33).
- (Musterd et al., 2015) M. Musterd, V. v. Steijn, C. R. Kleijn, and M. T. Kreutzer. “Calculating the volume of elongated bubbles and droplets in microchannels from a top view image”. In: *RSC Advances* 5.21 (Feb. 2, 2015), pp. 16042–16049 (cit. on p. 54).

- 
- (Nijhuis et al., 2001) T. A. Nijhuis, M. T. Kreutzer, A. C. J. Romijn, F. Kapteijn, and J. A. Moulijn. “Monolithic catalysts as efficient three-phase reactors”. In: *Chemical Engineering Science*. 16th International Conference on Chemical Reactor Engineering 56.3 (Feb. 1, 2001), pp. 823–829 (cit. on p. 30).
- (Nittis et al., 2001) V. Nittis, R. Fortt, C. H. Legge, and A. J. d. Mello. “A high-pressure interconnect for chemical microsystem applications”. In: *Lab on a Chip* 1.2 (2001), pp. 148–152 (cit. on p. 33).
- (Nosenko et al., 2018) V. V. Nosenko, G. Y. Rudko, A. M. Yaremko, V. O. Yukhymchuk, and O. M. Hreshchuk. “Anharmonicity and Fermi resonance in the vibrational spectra of a CO<sub>2</sub> molecule and CO<sub>2</sub> molecular crystal: Similarity and distinctions”. In: *Journal of Raman Spectroscopy* 49.3 (2018), pp. 559–568 (cit. on p. 116).
- (Ogden et al., 2014) S. Ogden, R. Bodén, M. Do-Quang, Z. G. Wu, G. Amberg, and K. Hjort. “Fluid behavior of supercritical carbon dioxide with water in a double-Y-channel microfluidic chip”. In: *Microfluidics and Nanofluidics* 17.6 (Dec. 1, 2014), pp. 1105–1112 (cit. on pp. 32, 33, 58).
- (Ohashi et al., 2011) A. Ohashi, M. Sugaya, and H.-B. Kim. “Development of a microfluidic device for measurement of distribution behavior between supercritical carbon dioxide and water”. In: *Analytical Sciences: The International Journal of the Japan Society for Analytical Chemistry* 27.6 (2011), pp. 567–569 (cit. on p. 32).
- (Oosterbroek et al., 2006) R. E. Oosterbroek, D. C. Hermes, M. Kakuta, F. Benito-Lopez, J. G. E. Gardeniers, W. Verboom, D. N. Reinhoudt, and A. v. d. Berg. “Fabrication and mechanical testing of glass chips for high-pressure synthetic or analytical chemistry”. In: *Microsystem Technologies* 12.5 (Apr. 1, 2006), pp. 450–454 (cit. on pp. 31, 32).
- (Pattekar et al., 2003) A. V. Pattekar and M. V. Kothare. “Novel microfluidic interconnectors for high temperature and pressure applications”. In: *Journal of Micromechanics and Microengineering* 13.2 (2003), p. 337 (cit. on p. 33).
- (Peles et al., 2004) Y. Peles, V. T. Srikar, T. S. Harrison, C. Protz, A. Mracek, and S. M. Spearing. “Fluidic packaging of microengine and microrocket devices for high-pressure and high-temperature operation”. In: *Journal of Microelectromechanical Systems* 13.1 (Feb. 2004), pp. 31–40 (cit. on p. 33).
- (Peng et al., 2013) C. Peng, J. P. Crawshaw, G. C. Maitland, J. P. Martin Trusler, and D. Vega-Maza. “The pH of CO<sub>2</sub>-saturated water at temperatures between 308K and 423K at pressures up to 15MPa”. In: *The Journal of Supercritical Fluids* 82 (Oct. 1, 2013), pp. 129–137 (cit. on pp. 163, 164, 207).
- (Pohar et al., 2009) A. Pohar and I. Plazl. “Process Intensification through Microreactor Application”. In: *Chemical and Biochemical Engineering Quarterly* 23.4 (Dec. 23, 2009). Publisher: Hrvatsko društvo kemijskih inženjera i tehnologa, pp. 537–544 (cit. on p. 28).
- (Proctor et al., 1967) B. A. Proctor, I. Whitney, and J. W. Johnson. “The strength of fused silica”. In: *Proc. R. Soc. Lond. A* 297.1451 (Mar. 21, 1967), pp. 534–557 (cit. on p. 119).

- (Quitain et al., 2018) A. T. Quitain, E. G. Mission, Y. Sumigawa, and M. Sasaki. “Supercritical carbon dioxide-mediated esterification in a microfluidic reactor”. In: *Chemical Engineering and Processing - Process Intensification* 123 (Jan. 1, 2018), pp. 168–173 (cit. on pp. 35, 36).
- (R. Murphy et al., 2007) E. R. Murphy, T. Inoue, H. R. Sahoo, N. Zaborenko, and K. F. Jensen. “Solder-based chip-to-tube and chip-to-chip packaging for microfluidic devices”. In: *Lab on a Chip* 7.10 (2007), pp. 1309–1314 (cit. on pp. 32, 33).
- (Reverchon et al., 1997) E. Reverchon and C. Marrone. “Supercritical extraction of clove bud essential oil: isolation and mathematical modeling”. In: *Chemical Engineering Science* 52.20 (Oct. 1, 1997), pp. 3421–3428 (cit. on pp. 7, 21, 26).
- (Santana et al., 2018) H. S. Santana, M. G. M. Lopes, J. L. Silva, and O. P. Taranto. “Application of Microfluidics in Process Intensification”. In: *International Journal of Chemical Reactor Engineering* 16.12 (Oct. 19, 2018). Publisher: De Gruyter Section: International Journal of Chemical Reactor Engineering (cit. on p. 93).
- (Sattari-Najafabadi et al., 2018) M. Sattari-Najafabadi, M. Nasr Esfahany, Z. Wu, and B. Sundén. “Mass transfer between phases in microchannels: A review”. In: *Chemical Engineering and Processing - Process Intensification* 127 (May 1, 2018), pp. 213–237 (cit. on p. 49).
- (Shao et al., 2008) N. Shao, W. Salman, A. Gavrilidis, and P. Angeli. “CFD simulations of the effect of inlet conditions on Taylor flow formation”. In: *International Journal of Heat and Fluid Flow* 29.6 (Dec. 1, 2008), pp. 1603–1611 (cit. on p. 43).
- (Shimanouchi et al., 1978) T. Shimanouchi, H. Matsuura, Y. Ogawa, and I. Harada. “Tables of molecular vibrational frequencies”. In: *Journal of Physical and Chemical Reference Data* 7.4 (Oct. 1, 1978). Publisher: American Institute of Physics, pp. 1323–1444 (cit. on p. 117).
- (Sih et al., 2008) R. Sih, M. Armenti, R. Mammucari, F. Dehghani, and N. R. Foster. “Viscosity measurements on saturated gas-expanded liquid systems—Ethanol and carbon dioxide”. In: *The Journal of Supercritical Fluids* 43.3 (Jan. 1, 2008), pp. 460–468 (cit. on p. 81).
- (Silva, 2014) N. M. P. d. Silva. « Développement d’un système micro/millifluidique sous pression pour l’étude et la mesure de propriétés d’écoulement diphasique : application au binaire CO<sub>2</sub> supercritique - BMimPF<sub>6</sub> ». Thèse de doct. Ecole des Mines d’Albi-Carmaux, 28 mar. 2014 (cit. on pp. 4, 5, 17, 19, 29, 66, 86).
- (Smith et al., 2013) R. Smith, H. Inomata, and C. Peters. *Introduction to Supercritical Fluids: A Spreadsheet-based Approach*. Google-Books-ID: 8HyEDhiKhz8C. Newnes, Dec. 8, 2013. 764 pp. (cit. on p. 23).
- (Sobieszuk et al., 2012) P. Sobieszuk, J. Aubin, and R. Pohorecki. “Hydrodynamics and Mass Transfer in Gas-Liquid Flows in Microreactors”. In: *Chemical Engineering & Technology* 35.8 (Aug. 1, 2012), pp. 1346–1358 (cit. on pp. 49, 50).

- 
- (Song et al., 2012) Y. Song, J. Wang, J. Yang, Y. Wu, N. Li, N. Gong, X. Pan, Y. Sun, and D. Li. “Algae Detection and Ship’s Ballast Water Analysis by a Microfluidic Lab-on-Chip Device”. In: *Instrumentation Science & Technology* 40.4 (July 1, 2012). Publisher: Taylor & Francis \_eprint: <https://doi.org/10.1080/10739149.2012.673199>, pp. 305–315 (cit. on p. 30).
- (Span et al., 1996) R. Span and W. Wagner. “A New Equation of State for Carbon Dioxide Covering the Fluid Region from the Triple-Point Temperature to 1100 K at Pressures up to 800 MPa”. In: *Journal of Physical and Chemical Reference Data* 25.6 (Nov. 1, 1996), pp. 1509–1596 (cit. on pp. 68, 73).
- (Srinivasan et al., 2004) V. Srinivasan, V. K. Pamula, and R. B. Fair. “An integrated digital microfluidic lab-on-a-chip for clinical diagnostics on human physiological fluids”. In: *Lab on a Chip* 4.4 (July 19, 2004). Publisher: The Royal Society of Chemistry, pp. 310–315 (cit. on p. 30).
- (Steijn et al., 2007) V. van Steijn, M. T. Kreutzer, and C. R. Kleijn. “micro-PIV study of the formation of segmented flow in microfluidic T-junctions”. In: *Chemical Engineering Science*. 8th International Conference on Gas-Liquid and Gas-Liquid-Solid Reactor Engineering 62.24 (Dec. 1, 2007), pp. 7505–7514 (cit. on pp. 44, 45, 131, 171).
- (Stishov et al., 2003) S. M. Stishov and A. E. Petrova. “A Method for the Hermetic Connection of High-Pressure Tubing to a High-Pressure Apparatus”. In: *Instruments and Experimental Techniques* 46.5 (Sept. 1, 2003), pp. 719–720 (cit. on p. 33).
- (H. Sun et al., 2020) H. Sun, Y. Jia, H. Dong, D. Dong, and J. Zheng. “Combining additive manufacturing with microfluidics: an emerging method for developing novel organs-on-chips”. In: *Current Opinion in Chemical Engineering* 28 (June 1, 2020), pp. 1–9 (cit. on p. 28).
- (R. Sun et al., 2011) R. Sun and T. Cubaud. “Dissolution of carbon dioxide bubbles and microfluidic multiphase flows”. In: *Lab on a Chip* 11.17 (Sept. 7, 2011), pp. 2924–2928 (cit. on p. 54).
- (Suzuki et al., 1990) K. Suzuki, H. Sue, M. Itou, R. L. Smith, H. Inomata, K. Aria, and S. Saito. “Isothermal vapor–liquid equilibrium data for binary systems at high pressures; Carbon dioxide-methanol, carbon dioxide-ethanol, carbon dioxide-1-propanol, methane-ethanol, methane-1-propanol, ethane-ethanol, and ethane-1-propanol systems”. In: *Journal of Chemical and Engineering Data; (USA)* 35:1 (Jan. 1, 1990) (cit. on p. 69).
- (Tabeling, 2015) P. Tabeling. *Introduction à la microfluidique*. Google-Books-ID : fRSWD-gAAQBAJ. Humensis, 20 juil. 2015. 257 p. (cit. on pp. 8, 27).
- (Taha et al., 2004) T. Taha and Z. F. Cui. “Hydrodynamics of slug flow inside capillaries”. In: *Chemical Engineering Science* 59.6 (Mar. 1, 2004), pp. 1181–1190 (cit. on p. 48).
- (Tan et al., 2012) J. Tan, Y. C. Lu, J. H. Xu, and G. S. Luo. “Mass transfer characteristic in the formation stage of gas–liquid segmented flow in microchannel”. In: *Chemical Engineering Journal* 185-186 (Mar. 15, 2012), pp. 314–320 (cit. on pp. 54, 55, 176).
- (Taylor, 1961) G. I. Taylor. “Deposition of a viscous fluid on the wall of a tube”. In: *Journal of Fluid Mechanics* 10.2 (Mar. 1961). Publisher: Cambridge University Press, pp. 161–165 (cit. on pp. 46, 47).



- (Thulasidas et al., 1997) T. C. Thulasidas, M. A. Abraham, and R. L. Cerro. "Flow patterns in liquid slugs during bubble-train flow inside capillaries". In: *Chemical Engineering Science* 52.17 (Sept. 1, 1997), pp. 2947–2962 (cit. on pp. 47, 48).
- (Tiggelaar et al., 2007) R. M. Tiggelaar, F. Benito-López, D. C. Hermes, H. Rathgen, R. J. M. Egberink, F. G. Mugele, D. N. Reinhoudt, A. van den Berg, W. Verboom, and H. J. G. E. Gardeniers. "Fabrication, mechanical testing and application of high-pressure glass microreactor chips". In: *Chemical Engineering Journal* 131.1 (July 1, 2007), pp. 163–170 (cit. on pp. 32, 33).
- (Toews et al., 1995) K. L. Toews, R. M. Shroll, C. M. Wai, and N. G. Smart. "pH-Defining Equilibrium between Water and Supercritical CO<sub>2</sub>. Influence on SFE of Organics and Metal Chelates". In: *Analytical Chemistry* 67.22 (Nov. 15, 1995). Publisher: American Chemical Society, pp. 4040–4043 (cit. on p. 163).
- (Trachsel et al., 2005) F. Trachsel, A. Günther, S. Khan, and K. F. Jensen. "Measurement of residence time distribution in microfluidic systems". In: *Chemical Engineering Science* 60.21 (Nov. 1, 2005), pp. 5729–5737 (cit. on p. 48).
- (Trachsel et al., 2008) F. Trachsel, C. Hutter, and P. R. von Rohr. "Transparent silicon/glass microreactor for high-pressure and high-temperature reactions". In: *Chemical Engineering Journal*. Microreaction Technology IMRET 9: Proceedings of the Ninth International Conference on Microreaction Technology 135 (Jan. 15, 2008), S309–S316 (cit. on p. 33).
- (Triplett et al., 1999) K. A. Triplett, S. M. Ghiaasiaan, S. I. Abdel-Khalik, and D. L. Sadowski. "Gas-liquid two-phase flow in microchannels Part I: two-phase flow patterns". In: *International Journal of Multiphase Flow* 25.3 (Apr. 1, 1999), pp. 377–394 (cit. on pp. 38, 39).
- (Tsivintzelis et al., 2004) I. Tsivintzelis, D. Missopolinou, K. Kalogiannis, and C. Panayiotou. "Phase compositions and saturated densities for the binary systems of carbon dioxide with ethanol and dichloromethane". In: *Fluid Phase Equilibria* 224.1 (Sept. 15, 2004), pp. 89–96 (cit. on pp. 69, 70, 77).
- (Ullah et al., 1992) U. Ullah, S. P. Waldram, C. J. Bennett, and T. Truex. "Monolithic reactors: mass transfer measurements under reacting conditions". In: *Chemical Engineering Science*. Twelfth International Symposium on Chemical Reaction Engineering Today 47.9 (June 8, 1992), pp. 2413–2418 (cit. on p. 30).
- (Vandu et al., 2005) C. O. Vandu, H. Liu, and R. Krishna. "Mass transfer from Taylor bubbles rising in single capillaries". In: *Chemical Engineering Science*. 7th International Conference on Gas-Liquid and Gas-Liquid-Solid Reactor Engineering 60.22 (Nov. 1, 2005), pp. 6430–6437 (cit. on pp. 49, 53, 54).
- (Verboom, 2009) W. Verboom. "Selected Examples of High-Pressure Reactions in Glass Microreactors". In: *Chemical Engineering & Technology* 32.11 (Nov. 1, 2009), pp. 1695–1701 (cit. on p. 35).
- (Völkel, 2009) N. Völkel. "Design and characterization of gas-liquid microreactors". PhD thesis. Dec. 4, 2009 (cit. on pp. 45, 171).

- 
- (Waelchli et al., 2006) S. Waelchli and P. Rudolf von Rohr. “Two-phase flow characteristics in gas–liquid microreactors”. In: *International Journal of Multiphase Flow* 32.7 (July 1, 2006), pp. 791–806 (cit. on p. 38).
- (Wagner et al., 2002) W. Wagner and A. Pruß. “The IAPWS Formulation 1995 for the Thermodynamic Properties of Ordinary Water Substance for General and Scientific Use”. In: *Journal of Physical and Chemical Reference Data* 31.2 (June 1, 2002). Publisher: American Institute of Physics, pp. 387–535 (cit. on pp. 72, 74).
- (Wehner et al., 2016) M. Wehner, R. L. Truby, D. J. Fitzgerald, B. Mosadegh, G. M. Whitesides, J. A. Lewis, and R. J. Wood. “An integrated design and fabrication strategy for entirely soft, autonomous robots”. In: *Nature* 536.7617 (Aug. 2016). Number: 7617 Publisher: Nature Publishing Group, pp. 451–455 (cit. on p. 28).
- (Whitesides, 2006) G. M. Whitesides. “The origins and the future of microfluidics”. In: *Nature* 442.7101 (July 2006). Number: 7101 Publisher: Nature Publishing Group, pp. 368–373 (cit. on pp. 8, 27).
- (Windisch et al., 2012) C. F. Windisch, V.-A. Glezakou, P. F. Martin, B. P. McGrail, and H. T. Schaef. “Raman spectrum of supercritical C18O2 and re-evaluation of the Fermi resonance”. In: *Physical Chemistry Chemical Physics* 14.8 (Feb. 1, 2012). Publisher: The Royal Society of Chemistry, pp. 2560–2566 (cit. on p. 116).
- (Wong et al., 1995) H. Wong, C. J. Radke, and S. Morris. “The motion of long bubbles in polygonal capillaries. Part 1. Thin films”. In: *Journal of Fluid Mechanics* 292 (June 1995). Publisher: Cambridge University Press, pp. 71–94 (cit. on p. 46).
- (Yao et al., 2014a) C. Yao, Z. Dong, Y. Zhao, and G. Chen. “An online method to measure mass transfer of slug flow in a microchannel”. In: *Chemical Engineering Science* 112 (June 14, 2014), pp. 15–24 (cit. on p. 55).
- (Yao et al., 2014b) C. Yao, Z. Dong, Y. Zhao, and G. Chen. “The effect of system pressure on gas-liquid slug flow in a microchannel”. In: *AIChE Journal* 60.3 (Mar. 1, 2014), pp. 1132–1142 (cit. on p. 32).
- (Yao et al., 2014c) C. Yao, Z. Dong, Y. Zhao, and G. Chen. “The effect of system pressure on gas-liquid slug flow in a microchannel”. In: *AIChE Journal* 60.3 (Mar. 1, 2014), pp. 1132–1142 (cit. on pp. 45, 58).
- (Yao et al., 2015) C. Yao, Z. Dong, Y. Zhao, and G. Chen. “Gas-liquid flow and mass transfer in a microchannel under elevated pressures”. In: *Chemical Engineering Science* 123 (Feb. 17, 2015), pp. 137–145 (cit. on pp. 49, 55, 58).
- (Yao et al., 2017) C. Yao, K. Zhu, Y. Liu, H. Liu, F. Jiao, and G. Chen. “Intensified CO2 absorption in a microchannel reactor under elevated pressures”. In: *Chemical Engineering Journal* 319 (July 1, 2017), pp. 179–190 (cit. on pp. 32, 134).
- (Yen et al., 2005) B. K. H. Yen, A. Günther, M. A. Schmidt, K. F. Jensen, and M. G. Bawendi. “A Microfabricated Gas–Liquid Segmented Flow Reactor for High-Temperature Synthesis: The Case of CdSe Quantum Dots”. In: *Angewandte Chemie* 117.34 (Aug. 26, 2005), pp. 5583–5587 (cit. on p. 33).

- (Yi et al., 2017) H.-G. Yi, H. Lee, and D.-W. Cho. “3D Printing of Organs-On-Chips”. In: *Bioengineering* 4.1 (Mar. 2017). Number: 1 Publisher: Multidisciplinary Digital Publishing Institute, p. 10 (cit. on p. 28).
- (Yue et al., 2007) J. Yue, G. Chen, Q. Yuan, L. Luo, and Y. Gonthier. “Hydrodynamics and mass transfer characteristics in gas–liquid flow through a rectangular microchannel”. In: *Chemical Engineering Science* 62.7 (Apr. 1, 2007), pp. 2096–2108 (cit. on p. 54).
- (Yue et al., 2009) J. Yue, L. Luo, Y. Gonthier, G. Chen, and Q. Yuan. “An experimental study of air–water Taylor flow and mass transfer inside square microchannels”. In: *Chemical Engineering Science* 64.16 (Aug. 15, 2009), pp. 3697–3708 (cit. on p. 54).
- (Yun et al., 2010) J. Yun, Q. Lei, S. Zhang, S. Shen, and K. Yao. “Slug flow characteristics of gas–miscible liquids in a rectangular microchannel with cross and T-shaped junctions”. In: *Chemical Engineering Science* 65.18 (Sept. 15, 2010), pp. 5256–5263 (cit. on p. 43).
- (Zaloha et al., 2012) P. Zaloha, J. Kristal, V. Jiricny, N. Völkel, C. Xuereb, and J. Aubin. “Characteristics of liquid slugs in gas–liquid Taylor flow in microchannels”. In: *Chemical Engineering Science* 68.1 (Jan. 22, 2012), pp. 640–649 (cit. on pp. 48, 49, 133, 176).
- (Zhang, 2019) F. Zhang. “Intensification du procédé antisolvant supercritique (SAS) par l’usage de microréacteur sous pression”. These de doctorat. Bordeaux, Nov. 29, 2019 (cit. on p. 26).
- (Zhang et al., 2020) F. Zhang, S. Marre, and A. Erriguible. “Mixing intensification under turbulent conditions in a high pressure microreactor”. In: *Chemical Engineering Journal* 382 (Feb. 15, 2020), p. 122859 (cit. on p. 26).
- (X. Zhao et al., 2020) X. Zhao, F. Bian, L. Sun, L. Cai, L. Li, and Y. Zhao. “Microfluidic Generation of Nanomaterials for Biomedical Applications”. In: *Small* 16.9 (2020), p. 190 (cit. on p. 28).
- (Y. Zhao et al., 2013) Y. Zhao, G. Chen, C. Ye, and Q. Yuan. “Gas–liquid two-phase flow in microchannel at elevated pressure”. In: *Chemical Engineering Science* 87 (Jan. 14, 2013), pp. 122–132 (cit. on pp. 32, 40, 41, 58).
- (Zhu et al., 2014) C. Zhu, C. Li, X. Gao, Y. Ma, and D. Liu. “Taylor flow and mass transfer of CO<sub>2</sub> chemical absorption into MEA aqueous solutions in a T-junction microchannel”. In: *International Journal of Heat and Mass Transfer* 73 (June 1, 2014), pp. 492–499 (cit. on pp. 42, 55, 58).
- (Zhukov, 2020) D. V. Zhukov. “Facilitating Miniaturized Bioanalytical Assays in Microfluidic Devices”. PhD thesis. California Institute of Technology, 2020 (cit. on p. 30).

## Abstract

### Mass transfer and thermodynamics phenomena in high pressure two-phase microflows

The aim of the thesis concerns the study of mass transfer performance under high-pressure ( $P > 7$  MPa) within a two-phase segmented flow comprising carbon dioxide. Mass transfer is determined indirectly by measuring the  $CO_2$  transferred between the two phases along the microreactor. Calculation of the mass transfer coefficient allows the performances in such two-phase systems to be quantified. However, a literature study has shown that the models formulated under ambient conditions for calculating the mass transfer coefficients are not well adapted to high pressure flows. This is due to the fact that the physical properties of the fluids change with pressure. In this thesis work, a microfluidic platform was fabricated that allows two-phase flow at high pressure to be studied using optical techniques. Two experimental methods - a colorimetric method and a Raman spectroscopy method - have been developed in order to indirectly measure the amount of  $CO_2$  exchanged between the two phases along a two-phase flow. The classical model for calculating mass transfer coefficients has been adapted to take into account the effects of pressure. This model and the experimental methods were applied to the  $CO_2$ - $H_2O$  system to determine the local liquid-side mass transfer coefficient.

**Keywords:** Mass transfer, Taylor flow, High-pressure, Microreactors

---

## Résumé

### Étude d'un couplage thermodynamique/transfert de matière dans un écoulement diphasique sous haute pression en microsystème

L'objectif général de la thèse concerne l'étude des performances de transfert de matière sous haute pression ( $P > 7$  MPa) au sein d'un écoulement diphasique comportant du dioxyde de carbone, par une mesure indirecte des quantités de soluté et/ou de  $CO_2$  échangées entre les deux phases et ceci le long du microréacteur. Le calcul de coefficients de transfert de matière permet de quantifier ces performances dans de tels systèmes diphasiques. Cependant, une étude bibliographique a montré que les modèles de calcul de ces coefficients, formulés à des conditions ambiantes, ne sont pas adaptables à la haute pression, du fait du changement des propriétés physiques des fluides en présence. Lors de cette thèse, une plateforme microfluidique permettant l'étude d'écoulement diphasique à haute pression, tout en gardant un accès optique à l'écoulement, a été fabriquée. Deux méthodes expérimentales ont été développées, une méthode de colorimétrie et une méthode de spectroscopie Raman, afin de mesurer de manière indirecte les quantités de  $CO_2$  échangées entre les deux phases le long d'un écoulement diphasique. Le modèle classique de calcul de coefficients de transfert de matière a été repensé pour prendre en compte les effets de la pression. Ce modèle ainsi que les méthodes expérimentales ont été appliquées au binaire  $CO_2$ - $H_2O$  afin de déterminer le coefficient de transfert de matière dans la phase liquide de l'écoulement et au long du microcanal.

**Mots-clés :** Transfert de matière, Taylor flow, Haute pression, Microréacteurs